University of South Australia

Antibiotic-alternative Therapies for the Treatment of Infected Wounds

Nikki Black

(Bachelor of Science (Biomedical Science) (Honours))

Submitted for the degree of

Doctor of Philosophy

(Biomaterials Engineering and Nanomedicine)

Submitted in Partial Fulfilment of the Requirements

for the Degree of Doctor of Philosophy

November 2024

Future Industries Institute

School of Clinical and Health Sciences

University of South Australia

Table of Contents

List of Figures v
List of Tables viii
List of Abbreviations ix
Declaration xii
Acknowledgements xiii
Project Summary xiv
Chapter One – Introduction 1
1.1. Skin 2
1.2. Wound Healing 3
1.3. Wound Infection 7
1.4. Antimicrobial Resistance 8
1.5. Chronic Wounds 10
1.6. Diabetes Mellitus 13
1.7. Antibiotic-Alternative Approaches for Wound Infection 17
1.7.1. Flightless I 17
1.7.2. Porous Silicon Nanoparticles (pSiNPs) 21
1.7.3. Antimicrobial Peptides 24
1.7.4. Photodynamic Therapy 29
1.7.5. Summary 35
1.8. Aims and Hypotheses 36
1.8.1. Aims 37
1.8.2. Hypothesis 37
Chapter Two – Materials and Methods 38
2.1. Chemicals 39
2.2. Solutions 39
2.2.1. Cellular 39
2.2.2. Bacterial 39
2.2.3. Histological Staining 40
2.3. General Animal Techniques 41
2.3.1. General Husbandry 41
2.3.2. Anaesthetic Protocols 41
2.3.3. Daily Monitoring 42
2.3.4. Wounding 43
2.3.5. Wound Infection 43
2.3.6. Wound Collection 44
2.3.7. Bacterial Colony Forming Units (CFUs) 44

2.4. Wound Analysis 44
2.4.1. Macroscopic Measurements 44
2.4.2. IVIS Analysis 45
2.4.3. Tissue Fixation and Processing 46
2.4.4. Histological Staining 47
2.4.5. Microscopic Measurements 48
2.4.6. Masson's Trichrome Staining 49
2.4.7. Immunohistochemistry (IHC) 52
2.5. General Techniques 55
2.5.1. Cell Culture 55
2.5.2. Cytotoxicity Assay 55
2.5.3. Proliferation Assay 56
2.5.4. Migration Assay 56
2.6. Statistical Analysis 57
Chapter Three – Neutralising Flightless I in a Diabetic Infected Excisional Wound Model 58
3.1. Background 59
3.2. Methods 61
3.2.1. Fabrication of Porous Silicon Nanoparticles (pSiNPs) 61
3.2.2. Thermal Oxidation Functionalisation of Porous Silicon Nanoparticles 61
3.2.3. Formulation of FnAb pSiNPs 62
3.2.4. The FnAb pSiNP Animal Trial 62
3.2.5. Investigation of pSiNPs Auto-luminescence 64
3.3. Results 65
3.3.1. Neutralising FnAb did not improve the rate of wound healing in the presence of infection. 65
3.3.2. Neutralising FnAb did not alleviate the bacterial burden of the wounds. 70
3.3.3. Neutralising FnAb had no effect on collagen deposition or Flightless I, PCNA or F4/80 and YM-1 expression in *S. aureus*-infected diabetic wounds. 74
3.3.4. Wounds treated with porous silicon nanoparticles exhibited increased luminescence at the injection sites. 80
3.3.5. Potential migration of *S. aureus* from the wound to the intradermal injection sites. 84
3.3.6. Porous silicon nanoparticles show auto-luminescence when topically applied but not when intradermally injected. 87
3.4. Discussion 89
Chapter Four – Pexiganan Delivered in Porous Silicon Nanoparticles in an Infected Excisional Wound Model 94
4.1. Background 95
4.2. Methods 99

4.2.1. Fabrication of pSiNPs 99
4.2.2. Hydrosilylation Functionalisation of pSiNPs 99
4.2.3. Loading Pexiganan into the pSiNPs 100
4.2.4. Hydrogels 100
4.2.5. Pexiganan pSiNP Treatment of *S. aureus* Infected Mouse Wounds 101
4.3. Results 103
4.3.1. Pexiganan is not cytotoxic to keratinocytes at low doses 103
4.3.2. Porous silicon nanoparticles improved the efficacy of pexiganan on wound healing in an infected excisional wound model 107
4.3.3. Pexiganan had no effect on neutrophil recruitment to the wound bed or on the proliferation of keratinocytes. 113
4.3.4. Pexiganan had no effect on collagen deposition at seven days post-injury. 113
4.3.5. Pexiganan had no significant effect on infection compared to the vehicle control regardless of delivery method. 117
4.3.6. The antibiotic treatment control showed the efficacy of the infected excisional wound model. 120
4.4. Discussion 123
Chapter Five – Photodynamic Therapy Using Methylene Blue-Antibody Conjugates in an Infected Excisional Wound Model: A Pilot Study 128
5.1. Background 129
5.2. Methods 131
5.2.1. The LED Light 131
5.2.2. Conjugation 133
5.2.3. Western Blots 136
5.2.4. The PAT Pilot Study 137
5.3. Results 139
5.3.1. Conjugating Photosensitisers to an antibody specific to bacteria using EDC/NHS chemistry 139
5.3.2. Methylene Blue alone is not cytotoxic to keratinocytes or fibroblasts over a 2-hour period. 142
5.3.3. Methylene Blue only control shows toxicity to keratinocytes and fibroblasts after a 24-hour period while the light only control does not. 144
5.3.4. Determine safe dose of MB-PDT *in vitro.* 146
5.3.5. Photo-Antibody Therapy is a safe therapy for the treatment of infected wounds. 148
5.3.6. MB-Ab Photo-Antibody Therapy showed no significant effects on wound healing in infected excisional wounds in a pilot study of 12 mice. 152
5.3.7. MB-Ab Photo-Antibody Therapy showed no significant effects on wound infection using an infected excisional murine model 160
5.4. Discussion 163

Chapter Six –Discussion 168
6.1. Project Significance 169
6.2. Key Results and Discussion: FnAb 170
6.3. Key Results and Discussion: Pexiganan 172
6.4. Key Results and Discussion: Photodynamic Therapy 174
6.5. Porous silicon nanoparticles cannot be intradermally injected in the presence of infection 176
6.6. Limitations and Future Directions 178
6.6.1. Optimising the Wound Model 178
6.6.2. Optimising Treatments 179
6.6.3. Delivery method 180
6.6.4. IVIS vs CFUs 181
6.6.5. Additional wound models 182
6.6.6. COVID-19 183
6.7. Conclusion 184
References 185

List of Figures

Figure 1.1. Schematic representation of the structure of the skin 2
Figure 1.2. The four main stages of wound healing. (1) haemostasis (2) inflammation (3) proliferation (4) re-modelling 4
Figure 1.3. Examples of an acute wound and a chronic wound. 10
Figure 1.4. The key differences in the healing process between an acute wound and a chronic wound. (A) An acute wound successfully progressing through the wound healing process (B) A chronic wound that is failing to resolve inflammation, clear infection, and re-epithelialise 11
Figure 1.6. Excisional wounds in Wildtype (WT), Flii Under-Expressing mice (Flii $^{+/-}$) and Flii Over-Expressing mice (Flii $^{tg/tg}$) 7 days post-wounding with key findings noted..... 18
Figure 1.7. Methods of pore formation by antimicrobial peptides to kill bacteria. 25
Figure 1.8. A typical photodynamic treatment of an infected excisional wound model..... 29
Figure 1.9. The basic mechanisms of how photosensitisers produce reactive oxygen species and singlet oxygen. 31
Figure 1.10. A murine skin abrasion model four days post-injury, infected with MRSA and treated with PDT (Left) and untreated (Right)..... 32
Figure 1.11. A human diabetic foot ulcer trial utilising combined Methylene Blue (MB) and Toluidine Blue O (TBO) PDT. 34
Figure 2.1. The general timeline for the infected excisional wound model. 42
Figure 2.2. The macroscopic wound area and wound gape measurements. 45
Figure 2.3. The IVIS Lumina S5 Imaging System measuring bioluminescence to monitor infection. (A) The IVIS Lumina S5 Imaging System (B) A representative photo of wounds infected with bioluminescent *S. aureus* (C) The same photo with regions of interest (ROI) drawn around the wounds..... 45
Figure 2.4. The microscopic wound measurements on haematoxylin and eosin (H&E)-stained wound samples. 49
Figure 3.1. A schematic representation of the treatment groups used for the infected diabetic excisional wound model used in the Flightless I trial. 64
Figure 3.2. The diabetic wound size significantly decreases between the day of surgery (Day 0) and Day 1 prior to treatment. 66
Figure 3.3. FnAb-pSiNPs did not improve healing compared to pSiNP controls in infected diabetic wounds..... 67
Figure 3.4. FnAb trended towards improved healing compared to the saline control in infected diabetic wounds. 68
Figure 3.5. All diabetic wounds were almost completely healed at 14 days post-surgery. 69
Figure 3.6. Equal bacterial burden in diabetic wounds at Day 1 post-bacterial inoculation. 71
Figure 3.7. The treatment groups that received pSiNPs showed higher rates of bioluminescence.73
Figure 3.8. Equal amounts of total collagen measured by Masson's Total Collagen Trichrome Stain in Day 14 infected diabetic infected wounds..... 75
Figure 3.9. Analysis of Flightless I expression in the wound bed in Day 14 infected diabetic wounds..... 76
Figure 3.10. Analysis of proliferating cell nuclear antigen (PCNA)-positive cells in Day 14 infected diabetic wounds. 77
Figure 3.11. Analysis of macrophage infiltration in Day 14 infected diabetic wounds..... 79
Figure 3.12. Daily macroscopic and bioluminescent images of Mouse 46 over the 14-day trial. ... 81
Figure 3.13. Daily macroscopic and bioluminescent images of Mouse 52 over the 14-day trial. ... 82
Figure 3.14. Daily macroscopic and bioluminescent images of Mouse 38 over the 14-day trial. ... 83

Figure 3.15. The bacterial burden of the three pSiNPs groups showing the bacteria potentially leaving the wound and inhabiting the intradermal injection sites. 86
Figure 3.16. Porous silicon nanoparticles showed negligible auto-luminescence when intradermally injected into mice posthumously. 88
Figure 4.1. Analysis of the porous silicon nanoparticles used to encapsulate pexiganan. 96
Figure 4.2. Cellular cytotoxicity of the porous silicon nanoparticles and pexiganan on L929 fibroblasts. (A) Cytotoxicity of the HS-pSiNPs and pexi-HSpSiNPs. 97
Figure 4.3. Antimicrobial activity of pexi-pSiNPs against *S. aureus* and *P. aeruginosa*. 98
Figure 4.4. A schematic representation of the treatment groups and the infected excisional wound model used in the pexiganan trial. 102
Figure 4.5. Low dose pexiganan is non-cytotoxic and increased proliferation of HaCaTs. 104
Figure 4.6. Pexiganan negatively effects the migration of keratinocytes at higher doses. 106
Figure 4.7. The wound size decreased between the day of surgery (Day 0) and the day of treatment (Day 1). 108
Figure 4.8. Pexi-pSiNPS improved wound healing over the 7-day trial. 110
Figure 4.9. Wounds treated with pexi-pSiNPs trended towards higher rates of re-epithelialisation indicating improved wound healing. 112
Figure 4.10. Analysis of proliferating cell nuclear antigen (PCNA)-positive cells in Day 7 wounds. 114
Figure 4.11. Analysis of neutrophil infiltration in Day 7 infected wounds. 115
Figure 4.12. Equal amounts of total collagen measured by Masson's Total Collagen Trichrome Stain in Day 7 infected wounds. 116
Figure 4.13. Equal bacterial burden in wounds at Day 1 post-bacterial inoculation. 118
Figure 4.14. Pexiganan did not significantly control the infection. 119
Figure 4.15. The ciprofloxacin treatment group showed the success of the infected excisional wound model. 122
Figure 5.1. A diagrammatic representation of the LED setup used in this study. 131
Figure 5.2. The LED light assembly for treating a 96-well plate (Left) and for treating mice (Right). 133
Figure 5.3. The timeline and treatment groups for the infected excisional wound model used in the Photo-Antibody Therapy pilot study. 138
Figure 5.4. The creation of the photosensitiser-antibody conjugates. 141
Figure 5.5. Effect of methylene blue on the viability of keratinocytes and fibroblasts two hours post-treatment. 143
Figure 5.6. The effect of the LED light and methylene blue separately on keratinocytes and fibroblasts 24 hours post-treatment. 145
Figure 5.7. The effect of MB-PDT on the viability of keratinocytes and fibroblasts 24 hours post-treatment. (A) HaCaTs (B) HFFs. 147
Figure 5.8. The health of the mice during the pilot study. 150
Figure 5.9. Representative histological sections of the five major organs taken at Day 7 of the trial and stained with H&E. 151
Figure 5.10. The initial macroscopic measurements of the wound gape and wound area on Day 0 and Day 1. 154
Figure 5.11. The macroscopic wound size over the 7-day trial. 156
Figure 5.12. The histological analysis of the wounds excised at Day 7. 158
Figure 5.13. Masson's Trichrome Total Collagen Stain showing MB-AB-PAT had no effect on collagen deposition on Day 7. 159
Figure 5.14. Bacterial burden significantly increased between the day of surgery (Day 0) and the following day prior to treatment (Day 1). 161

Figure 5.15. The bacterial burden over the course of the study. 162

List of Tables

Table 2.1. The overnight processing protocol for paraffin tissue preservation. 46
Table 2.2. The haematoxylin and eosin staining protocol. 48
Table 2.3. The Masson's Trichrome Total Collagen Stain Protocol. 51
Table 2.4. The immunohistochemistry (IHC) protocol. 53
Table 2.5. The primary and secondary antibodies used for immunohistochemistry (IHC). 54
Table 5.1. LED light equipment used in this study and their specifications. 132
Table 5.2. The calculated exposure times for the various light fluences tested. 133
Table 5.3. Selected photosensitisers for this study with their key characteristics. 134
Table 5.4. The modified photosensitisers purchased for the conjugation chemistry. 134

List of Abbreviations

Ab – antibody

AEC – animal ethics committee

AGES – advanced glycation end products

ANOVA – analysis of variance

BGL – blood glucose level

C - carbon

CAF – Core Animal Facility

CFUs – colony forming units

CRS – critical recording sheet

DMEM – Dulbecco's Modified Eagle Media

ECM – extracellular matrix

EDC – 1-Ethyl-3-(3-dimethylaminopropyl)carbodiimide

EtOH – ethanol

FCS – foetal calf serum

FDA – food and drug administration

Flii – flightless I

FnAb – flightless neutralising antibody

H - hydrogen

H and E – haematoxylin and eosin

HaCaT – human keratinocyte cell line

HF – hydrofluoric acid

HFF – human fibroblast cell line

HIF – hypoxia inducible factor

HK – humanely kill

HS – hydrosilylated

IBC – institutional biosafety committee

ID – intradermal

IL – interleukin

Inf MB-PDT – methylene blue photodynamic therapy in an infected excisional wound model

Inf MB-Ab-PAT – methylene blue-antibody conjugate photo-antibody therapy in an infected excisional wound model

IP – intraperitoneal

MB – methylene blue

MB-Ab – methylene blue-antibody conjugate

MB-Ab-PAT – methylene blue-antibody-mediated photodynamic therapy

MB-PDT – methylene blue-mediated photodynamic therapy

MHC – major histocompatibility complex

MIC – minimum inhibitory concentration

mIgG – monoclonal immunoglobulin g

MMP – matrix metalloproteinases

NFκB – nuclear factor kappa b

NGS – normal goat serum

NHS – N-hydroxysuccinimide

NO – nitric oxide

NOD – non-obese diabetic

O - oxygen

P. aeruginosa – pseudomonas aeruginosa

PAT – photo-antibody therapy

PBS – phosphate buffered solution

PCNA – proliferating cell nuclear antigen

PDGF – platelet derived growth factor

PDT – photodynamic therapy

Pexi – pexiganan

Pexi-pSiNPs – pexiganan-loaded porous silicon nanoparticles

pSi – porous silicon

pSiNPs – porous silicon nanoparticles

ROS – reactive oxygen species

SEM – standard error of the mean

Si - silicon

S. aureus – staphylococcus aureus

STZ – streptozotocin

TBS – tris buffered saline

TGF – transforming growth factor

TNF – tumour necrosis factor

TO – thermally oxidised

TRS – target retrieval solution

TSA – tryptic soy agar

TSB – tryptic soy broth

UnInf MB-PDT – methylene blue photodynamic therapy in an uninfected excisional wound model

UniSA – University of South Australia

UniVet – university veterinarian

UV - ultraviolet

VEGF – vascular endothelial growth factor

Declaration

I declare that:

this thesis presents work carried out by myself and does not incorporate without acknowledgment any material previously submitted for a degree or diploma in any university; to the best of my knowledge it does not contain any materials previously published or written by another person except where due reference is made in the text; and all substantive contributions by others to the work presented, including jointly authored publications, is clearly acknowledged.



Acknowledgements

First and foremost, I would like to extend my heartfelt gratitude to my supervisors, Professor Allison Cowin, Dr. Chris Turner, Dr. Xanthe Strudwick, and Dr. Zlatko Kopecki. Thank you for the opportunity to undertake this PhD and for all of your hard work and guidance throughout the process.

A special thanks to everyone in the Regenerative Medicine Lab, particularly Dr. Tahlia Kennewell, who has always been there to answer my unending questions, and Kiralee Janusaitis, without whose expertise I would be lost. I would also like to express my appreciation to Amanda and Lora in the Micro Lab for their assistance with the bacterial work.

I would like to acknowledge the facilities, scientific and technical assistance of Microscopy Australia at the University of South Australia, a facility that is funded by the University of South Australia, the State and Federal Governments. In particular, I would like to give a big thank you to Sofia Hassiotis from Adelaide Microscopy for her endless support with all things histology.

This work would not have been possible without the financial support from my scholarships: The University of South Australia Postgraduate Research Award and the Australian Government Research Training Program (RTP) Scholarship.

Above all, I'm immensely grateful to my husband, Toby. The only thing more unending than this PhD has been your love and support. All the "end of PhD" celebrations you planned over the years, only to be met with awkward silence, and yet you still retained unwavering, foolish optimism. I will always be grateful.

For my dear son, Iggy, you are the greatest distraction I will never regret. Thank you for all the purpose and love you have inspired me with. I hope to inspire you with my passion for learning and foolish perseverance. It is a long life ahead of us and I look forward to every chapter with you.

Project Summary

Chronic wounds are wounds that fail to heal within six weeks, posing a significant global health challenge that often leads to amputation or even death. As a wound remains open, the risk of infection increases, typically in the form of a biofilm, which further hinders the healing process. While current treatments primarily rely on antibiotics, the growing issue of antimicrobial resistance is diminishing their effectiveness. This highlights the need for antibiotic-alternative treatments for infected wounds. These antibiotic-alternative approaches aim to either eliminate infection allowing wound healing to progress, or by promoting healing, and thereby supporting the immune system's ability to control infection. In this study, three antibiotic-alternative methods of treating infected wounds were investigated.

The first approach investigated was the delivery of a monoclonal antibody to neutralise Flightless I – a negative regulator of wound healing – in porous silicon nanoparticles to promote wound healing in an infected wound. Flightless I is a negative regulator of wound healing whose overexpression has been shown to delay wound healing and under expression shown to accelerate wound healing. Previously, Flightless I has been successfully neutralised using anti-Flightless I siRNA and the Flightless I neutralising antibody (FnAb), with positive wound healing outcomes in uninfected incisional and excisional wounds. In this study, FnAb, is delivered in porous silicon nanoparticles to an infected diabetic murine wound model. The additional burdens of infection and diabetes creates an extremely hostile environment that degrades monoclonal antibodies. The use of porous silicon nanoparticles functions to protect the FnAb from the hostile environment while allowing for a slow, sustained release. While no conclusions could be drawn in terms of efficacy of the treatments, the delivery of the treatments has been optimised for future studies. This study revealed that porous silicon nanoparticles cannot be intradermally injected around an infected wound as this promotes the infection spread from the wound to the injection sites. It was found that porous silicon nanoparticles may be contraindicated in infected wounds as they may be a potential niche for additional infection.

The second approach investigated was one examining the antibacterial efficacy of the antimicrobial peptide, pexiganan, when delivered in porous silicon nanoparticles. Pexiganan has been proven to be an excellent antimicrobial against a wide array of micro-organisms and was able to promote wound healing in diabetic foot ulcers through the

clearance of infection. In this study, pexiganan was shown to be safe and even beneficial to keratinocytes *in vitro* at 20 µg/mL or lower but cytotoxic and with negative effects on the proliferation and migration of keratinocytes at higher concentrations. For the treatment of infected wounds, pexiganan was delivered in porous silicon nanoparticles to allow for a slow sustained release of treatment thereby avoiding cytotoxicity. Porous silicon nanoparticles also protect the treatment from degradation by the exacerbated inflammatory response and high number of proteases created in the infected wound. In the animal trial, no antibacterial effect from pexiganan was observed but evidence of improved wound healing was found. Pexiganan delivered in porous silicon nanoparticles accelerated wound healing over both the pexiganan and the porous silicon nanoparticle groups, indicating that porous silicon nanoparticles are an effective delivery method for pexiganan. While pexiganan alone was shown to impair wound healing compared to the porous silicon nanoparticles control. Further investigation suggested an increase in keratinocyte proliferation on Day 7 post-wounding, supporting an effect on wound healing through keratinocytes independent of antibacterial properties.

The third approach investigated was Photo-Antibody Therapy (PAT) that utilises photosensitiser-antibody conjugates to clear infection in the wound. Photodynamic therapy has been proven to be an excellent method of killing bacteria. However, the lack of specificity in the photosensitiser means that healthy tissue is killed along with the bacteria. Conjugating the photosensitiser to an antibody specific to bacteria increases the photosensitiser's specificity for bacteria over healthy mammalian tissue, increasing its efficacy, and allowing a reduced dose thereby decreasing unwanted negative side effects. In this study, the photosensitiser Methylene Blue was conjugated to an antibody specific to gram-negative bacteria and tested *in vivo* in a pilot study of 12 mice with infected wounds. No statistical significance is found in wound healing or infection due to the small sample size, however, the safety of this novel Photo-Antibody Therapy is demonstrated. Additionally, the results found are promising, indicating no difference in wound healing or infection control between the conjugated and unconjugated Methylene Blue despite the much smaller concentration of the conjugated Methylene Blue being used, and both treatments trending to efficacy than the untreated control.

In this study, three different approaches were tested for the treatment of infected wounds and while they all revealed new information, there was minimal success in preclinical infection models. This highlights the difficulty of developing antibiotic-alternative antimicrobial approaches for the treatment of infected wounds.

Chapter One – Introduction

1.1. Skin

The skin is the largest organ of the body, providing a barrier against the outside world and maintaining homeostasis. The skin consists of three main layers – the epidermis, the dermis, and the hypodermis (also known as the subcutaneous layer) (Figure 1.1) [1]. The epidermis consists of stratified squamous epithelium, consisting primarily (90%) of keratinocytes. These keratinocytes are organised into five layers of strata. They differentiate from basal cells attached to the basement membrane through to corneocytes (dead keratinocytes) at the surface of the skin and are the primary protection against UV light and infection. Cells also present in the epidermis include melanocytes which carry the pigment melanin and protect the skin from ultraviolet (UV) damage, Langerhans cells which help with the immune response, and Merkel cells which form the afferent nerves response for our sense of touch [2].

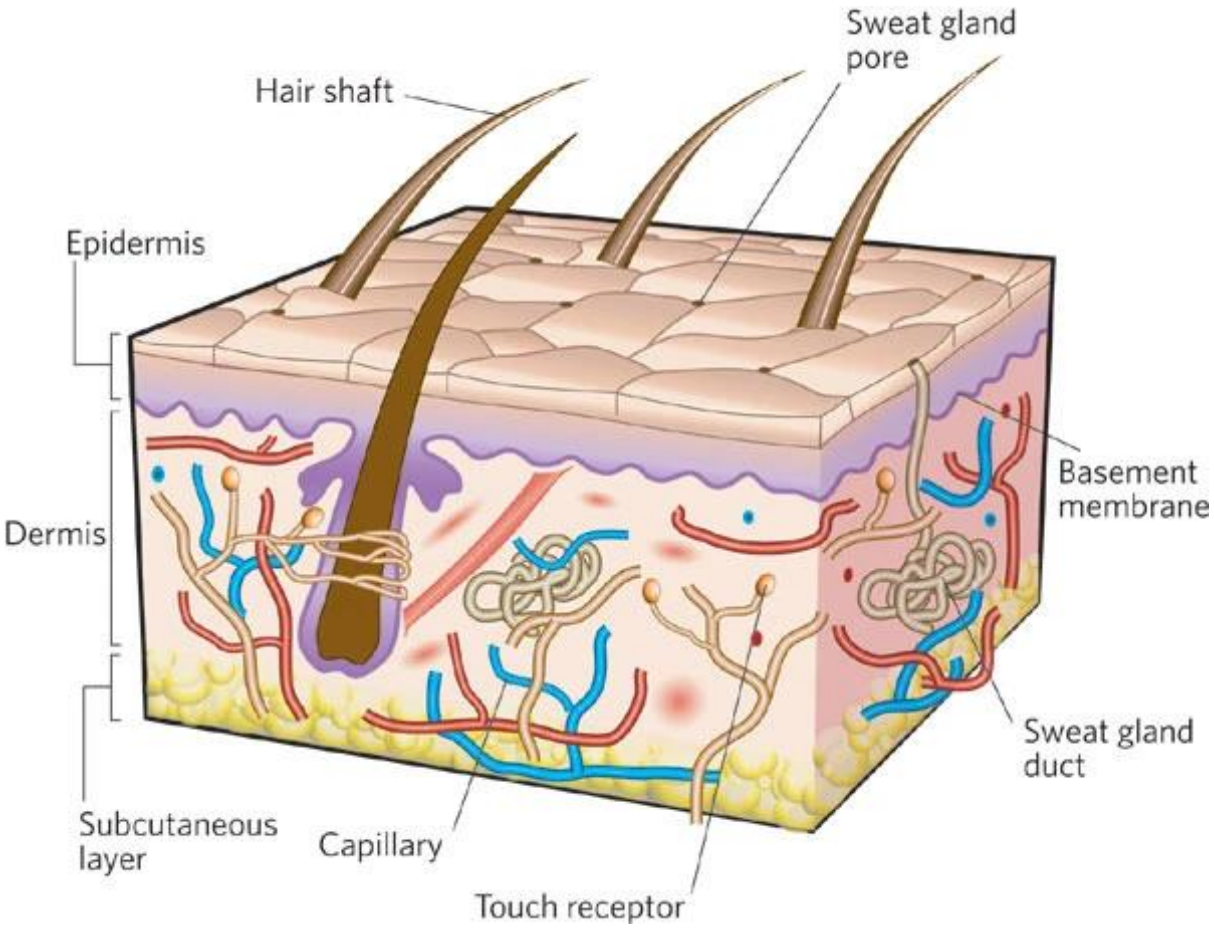

Figure 1.1. Schematic representation of the structure of the skin [3].

As the basal keratinocytes proliferate, they move up the strata, changing shape and composition as they undergo multiple stages of differentiation and become anucleated. During this process, the keratinocytes become highly organised, and desmosomes form attachments between the cells. Keratinocytes help protect epithelial cells from damage and stress by secreting keratin proteins, and contribute to the extracellular matrix through the production of lipids [3, 4]. The basement membrane connects the epidermis to the dermis and consists mostly of laminin and collagen IV. Anchoring filaments tether the hemidesmosomes and basal keratinocytes to the membrane while anchoring and collagen fibrils connect the basement membrane to the dermis. Fibroblasts and keratinocytes synthesise many of the components of the basement membrane [5, 6].

The dermis consists of two layers – the papillary layer and the reticular layer. The papillary layer consists of nerves, glands and capillaries. While the reticular layer consists largely of fibroblasts which synthesise collagen and other components of the extracellular matrix. Approximately 70% of the reticular layer consists of collagen bundles woven into a fibrous network interspersed with elastin fibres. This network forms the structure of the skin and allows for limited stretching [1, 2]. Beneath the dermis is the hypodermis which is comprised of connective tissue and fat, which attaches the skin to the underlying muscle and bone, and consists of loose connective tissue and elastin. The main cell types include fibroblasts, macrophages and adipocytes [2, 7].

1.2. Wound Healing

A wound is an injury that compromises the integrity of the skin. Superficial wounds affect the epidermal layer, partial-thickness wounds affect the epidermis and the dermis, while full-thickness wounds affect the epidermis, dermis and the underlying fat and tissues [8]. There are four main overlapping phases in the wound healing process including; haemostasis, inflammation, proliferation, and tissue remodelling (Figure 1.2).

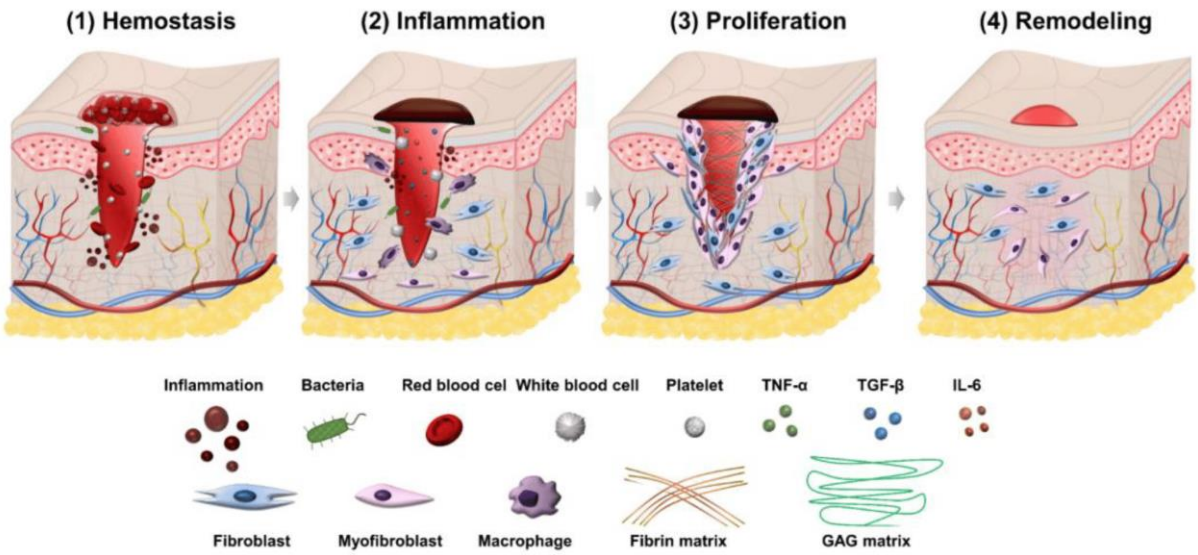

Figure 1.2. The four main stages of wound healing. (1) haemostasis (2) inflammation (3) proliferation (4) re-modelling [9].

The first phase, haemostasis, involves the creation of a blood clot within a few minutes of injury to prevent blood loss. Platelets from the blood come into contact with collagen in the extracellular matrix which triggers the platelets to degranulate and aggregate to form a temporary fibrin clot [10]. The clot consists of aggregated platelets held together with a mesh of cross-linked fibrin fibres supplemented with actin and myosin filaments [11]. In addition to preventing blood loss, the fibrin clot also serves as a barrier against infection, and as a scaffold for migrating immune cells. The activated platelets within the clot release platelet derived growth factor (PDGF) and transforming growth factor (TGF)-β1 which attract the first infiltration of neutrophils, monocytes which differentiate into macrophages, and stimulates migration and proliferation of smooth muscle cells and fibroblasts [12].

Haemostasis is rapidly followed by the inflammatory phase which is crucial for clearing foreign pathogens and can last 7-10 days post-injury [13]. Mast cells come into contact with collagen and degranulate, and produce prostaglandins and histamine which supports the migration of inflammatory cells into the wound by increasing the dilation and permeability of the surrounding vessels and capillaries [14]. Additionally, resident keratinocytes produce a plethora of cytokines and growth factors with different functions in innate and adaptive immunity responses during wound repair including during inflammation, healing, and the

ability to fight pathogens. Some of the main cytokines include: interleukin (IL)-1, tumour necrosis factor (TNF), TGF-β1, IL-8 which promote inflammation [15, 16].

Neutrophils are one of the first immune cells that enter the wound. At day one post-injury, 50% of the cells in the wound are neutrophils [17]. The neutrophils are recruited by the recognition of damage associated molecular patterns (DAMPs) and pattern associated molecular patterns (PAMPs) by toll like receptors (TLRs). Neutrophils have many roles in wound healing including clearing pathogens, as well as regulating and promoting inflammation. These roles are achieved through the production of reactive oxygen species (ROS), proteases, TNF, antimicrobial peptides (AMPs) and vascular endothelial growth factor A (VEGF-A) [18, 19].

Monocytes arrive in the wound within 48 hours of injury, and are recruited by TGF-β1 and monocyte chemoattractant protein (MCP)-1 produced by fibroblasts, epithelial, endothelial, and smooth muscle cells [20-22]. The monocytes then differentiate into either M1 or M2 macrophages [23]. The pro-inflammatory M1 macrophages are stimulated by lipopolysaccharide (LPS) and interferon (IFN)-γ, and release ROS, IL-12, IL-1 β, IL-6, TNFα, PDGF and VEGFA. The main role of M1 macrophages is to promote inflammation and clear the wound of debris and bacteria. Neutrophils are replaced by M1 macrophages as the major mediators of inflammation once the apoptotic neutrophils have been phagocytosed by the M1 macrophages. Anti-inflammatory M2 macrophages play a key role in the resolution of the inflammation phase. M2 macrophages release IL-4, IL-18, IL-13, and arginase which help resolve the inflammation phase. M2 macrophages also promote the repair of the extracellular matrix by producing TGF-β1 and PDGF to recruit fibroblasts [24]. M2 macrophages are further classified based on what they are stimulated by – M2a macrophages are stimulated by IL-4 and IL-13, M2b macrophages are stimulated by LPS and immune complexes, and M2c macrophages are stimulated by IL-10 and TGF- β1 [25].

The third phase of wound healing is the proliferation phase. If the inflammation or infection in the wound has not resolved, then this stage will be delayed and may progress sub-optimally. The main cell types involved in this process are endothelial cells, fibroblasts, and keratinocytes. This stage consists of three key processes including; angiogenesis, the reformation of the extracellular matrix, and re-epithelialisation.

Angiogenesis is the formation of new blood vessels restoring vasculature to the tissue. Low oxygen in the wound triggers the production of hypoxia inducible factor (HIF)-1 and then VEGFA from endothelial cells, fibroblasts, cardiac smooth muscle and monocytes [26, 27]. VEGFA binds to VEGF receptor (VEGFR) on endothelial cells which causes the endothelial cells to proliferate and migrate. The proliferating endothelial cells release matrix metalloproteinases (MMPs) to degrade the basement membrane as they migrate into the granulation tissue. As the vasculature is restored, the oxygen in the wound increases, resulting in decreased HIF-1 and VEGFA production, resulting in negative regulation and cessation of the angiogenesis process.

The extracellular matrix begins repair when M2 macrophages release PDGF and TGF-β1 which attract fibroblasts to the wound approximately 3 days after wounding [24]. Once in the matrix, fibroblasts synthesise collagen III which is organised into bundles and acts as a temporary scaffold for further cellular movement. Fibroblasts deposit most of the key components used to repair the extracellular matrix including collagen and elastin [28, 29]. Restoration of the extracellular matrix allows the key process of closing the wound through re-epithelialisation. At the edges of the dermis, keratinocytes produce MMPs to degrade the fibrin clot created during the first stage of wound healing. As the fibrin clot is degraded, the keratinocytes proliferate and migrate across the newly formed dermal matrix to create a new epithelial layer, forming the new cutaneous barrier, and closure of the wound [30, 31].

The final stage of wound healing is tissue remodelling. Triggered by PDGF and TGF- β, fibroblasts can differentiate into myofibroblasts which are contractile and contribute to the contraction of the wound [32]. This process of contraction can continue for up to 4 weeks post-injury in human skin [33]. Tissue remodelling can continue for years post-injury, and involves fibroblasts producing MMPs to break down collagen III and replace it with collagen I. As more bundles of collagen I are deposited, the tensile strength of the tissue increases [34]. However, the tensile strength of the tissue only recovers to approximately 80% of the original [11]. Collagen synthesis proceeds for 4-5 weeks post-injury and collagen redistribution can continue for years [11].

Once the wound has completely re-epithelialised, a scar often remains consisting of scar tissue. This scar tissue consists of denser connective tissue, is less elastic, has decreased vasculature, and an altered ratio of collagen [35]. Re-epithelialisation may be the most

crucial step to wound healing, restoring the skin's primary function – to protect what lies underneath. Unfortunately, while the wound is open and exposed, infection is likely to occur [36]. The slower the wound heals, the greater the chance of infection.

1.3. Wound Infection

Communities of micro-organisms reside on top of the skin, and it is due to this natural microbiota that all cutaneous wounds are susceptible to bacterial contamination, though not all of them will progress to the development of clinical infection. There are five stages of wound infection; contamination, colonisation, critical colonisation, local infection, and systemic infection [37]. All wounds experience the contamination and colonisation stages of bacterial infection but most often the immune system is able to control the infection so it does not develop beyond this stage. Critical colonisation occurs when the infection has exceeded beyond what the host immune system can control, which is generally when pathogen colonisation exceeds 1×10^5 bacteria/g of tissue [38]. When this occurs, colonisation can develop into a local infection where inflammation is exacerbated and damage to the host tissue occurs. Systemic infection can subsequently occur where the bacteria can infiltrate into the surrounding tissues and induce a systemic inflammatory response, which can lead to organ dysfunction, and death [39].

The immune system may fail to control the infection at the critical colonisation stage due to the development of bacterial biofilms [40]. Biofilms are layers of bacteria that are formed when planktonic bacteria adhere to a surface and begin secreting extracellular polymeric substances (EPS) to form an extracellular matrix. This extracellular matrix protects the bacteria from desiccation, phagocytosis from the immune cells, and can protect the bacteria from antibodies and even antibiotics [41]. The bacteria then replicate into micro-colonies which proliferate while the biofilm matures. The biofilm can then produce more planktonic bacteria which can spread and cause the formation of biofilms elsewhere in the body [42].

A common bacteria found in the skin microbiota that causes infection is *Staphylococcus aureus*, a gram-positive bacteria that is a commensal and an opportunistic pathogen [38]. Within the first week post-wounding, gram-positive bacteria dominate, with *S. aureus* being the most common pathogen found in wounds [43-45]. This changes to gram-negative

bacteria within the second week, with *Pseudomonas aeruginosa* being the most common gram-negative bacteria found in infected wounds [43]. One study of 239 patients between 2017 and 2019 showed that 75.3% of the wound infections were a monoculture and 24.7% were polymicrobial. Of all the bacteria strains isolated, 57.9% were gram-negative, with 40.2% *P. aeruginosa*, and 36.6% were gram-positive, with 79.4% *S. aureus* [43]. Bacteria can not only cause infection but also produce a range of proteases that inhibit wound healing. For instance, *S. aureus* can produce autolysin, staphopain A and B, and staphylococcal serine protease which can contribute to complement inactivation and degradation of the extracellular matrix [42].

The initial steps of treating a wound involves debridement, antiseptics and antibiotics. Wound debridement cleans the wound and provides a 72-hour therapeutic window for antiseptics and antibiotics to work [46, 47]. Antiseptics are used to inhibit the growth of bacteria, preventing infection and re-infection, but do not kill bacteria or treat infection [48, 49]. Common antiseptics used against *S. aureus* and *P. aeruginosa* is hydrogen peroxide and sodium hypochlorite respectively [46, 50]. While some antiseptics are capable of disrupting biofilm formation by degrading extracellular polymeric substances, antibiotics are relied on to treat infection [46]. Unfortunately, in addition to negative side effects on wound healing and the patient, bacteria are increasingly gaining resistance to antibiotics.

1.4. Antimicrobial Resistance

Antibiotic resistance (AMR) is a bacteria's ability to develop resistance to a particular antibiotic, though a bacterium may become resistant to multiple antibiotics over time [51]. The first case of antibiotic resistance was recorded in the 1940s, as cases of penicillin-resistant *S. aureus* emerged. The first case of the well-known methicillin-resistant *Staphylococcus aureus* (MRSA) was in 1961 [9, 10], however, *S. aureus* has since become resistant to multiple other antibiotics. Bacteria that have developed antibiotic resistance include *Enterococcus faecium*, *S. aureus*, *Klebsiella pneumoniae*, *Acinetobacter baumanii*, *P. aeruginosa*, and Entero*bacter* strains. Together, these make up the "ESKAPE" pathogens [52]. In one study of bacterial isolates taken from the wounds of 239 patients over a two year period, 88.2% of isolates was found to be resistant to at least one antibiotic, and 29.2%

of isolates were resistant to at least six antimicrobials. Some *S. aureus* isolates were resistant to 12 different antimicrobials [43].

The continued treatment of infection with antibiotics, regardless of whether the bacteria are already resistant to one or more antibiotics, exacerbates the problem by leading to further antibiotic resistance. Over prescription and misuse of antibiotics has worsened this clinical problem. Using antibiotics as minimally as possible is a start to solving antibiotic resistance alongside better antimicrobial stewardship approaches, however, antibiotic-alternative methods of eradicating bacterial wound infections need to be developed [53].

In 2024, an estimated 4.71 million deaths were associated with bacterial AMR, with 1.14 million deaths directly caused by bacterial AMR. Of these deaths, 550,000 were associated with MRSA and 130,000 deaths directly caused by MRSA [54]. In the community, 85-90% of *S. aureus* strains are resistant to penicillin, and community-acquired infections now dominate over hospital-acquired infections [55]. As antimicrobial resistance increases, treatment options decrease. This leads to an increase not only in infectious related deaths, but also amputations, sepsis, and death.

Antimicrobial resistance can be innate, acquired through mutation or horizontal gene transfer, or acquired through a need to adapt to the environment [56]. There are four main mechanisms of resistance. The first is through alteration, where the bacteria produce enzymes that irreversibly neutralise antibiotics. For instance, the production of β-lactamases to inhibit the action of β-lactam antibiotics, like penicillin [57]. The second is through the modification of drug binding sites to prevent anti-microbials from interacting with bacteria. Examples of this include target enzyme modifications, ribosomal target site alterations, and cell wall precursor alterations [56, 57]. The third mechanism is reduced cell permeability which involves a reduction of porins capable of allowing the antimicrobial to enter the cell. The fourth mechanism is through biofilm formation where bacteria can proliferate and mutate at an increased rate, and transfer antibiotic resistance genes to each other. Bacteria are also less susceptible to antibiotics when in a biofilm, only further worsening the problem [42, 58]. As the use of antibiotics becomes increasingly ineffective, new methods of clearing infection are urgently sought.

This is particularly important in wound healing as in the presence of infection, wounds may fail to progress from the inflammatory stage of wound healing, leading to the formation of

a chronic wound – a wound that fails to heal. Over 60-80% of chronic wounds are found to have a biofilm [42, 59]. Biofilms allow the exchange of resistance genes with polymicrobial biofilms showing intrinsic genotypic resistances, phenotypic resistance, and tolerance to antimicrobial drugs [43, 60, 61]. A wound may also become chronic due to underlying pathologies, further increasing the risk of infection.

1.5. Chronic Wounds

There are two main types of wounds: chronic and acute. Acute wounds are wounds that continue through the stages of wound healing resulting in a healed and closed wound within a designated time (Figure 1.3). Chronic wounds often fail to progress to the inflammatory stage of wound healing and are termed “chronic” if they fail to close within six weeks [62-65]. Chronic wounds are often exacerbated by the presence of an infection and which affects their ability to pass the inflammatory stage of wound healing until the infection is cleared [59, 62] (Figure 1.4). If chronic wounds persist, they can lead to amputation, disability, or sepsis. Chronic wounds affect 450,000 Australians every year and incur a cost to the healthcare budget of approximately $6.6 billion [66].

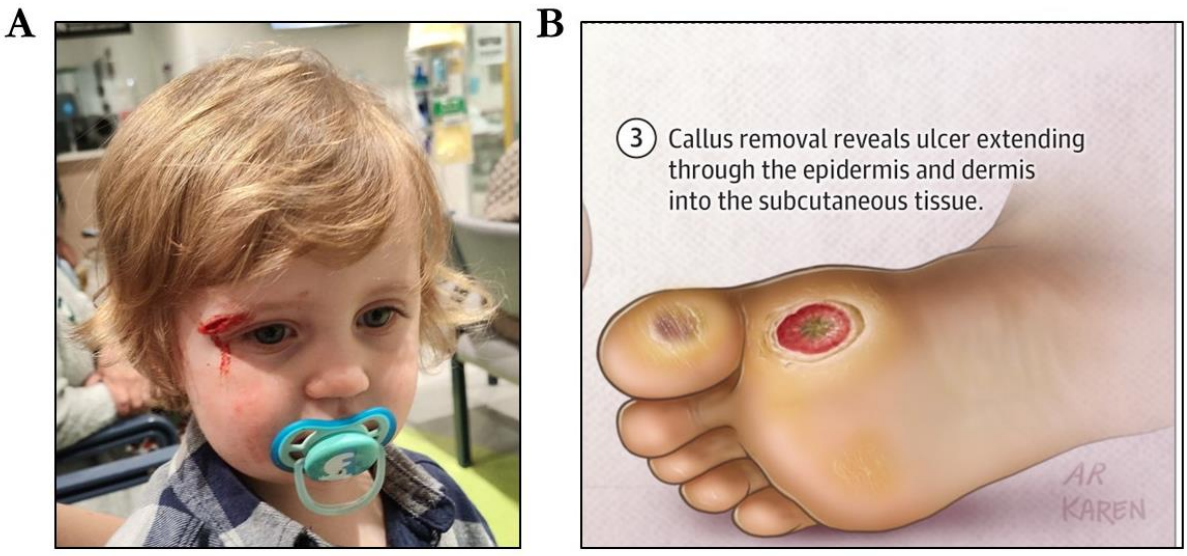

Figure 1.3. Examples of an acute wound and a chronic wound. (A) A most handsome young man with an acute wound on his eyebrow, attained after not listening to his mother **(B)** A chronic wound - a diabetic foot ulcer [67].

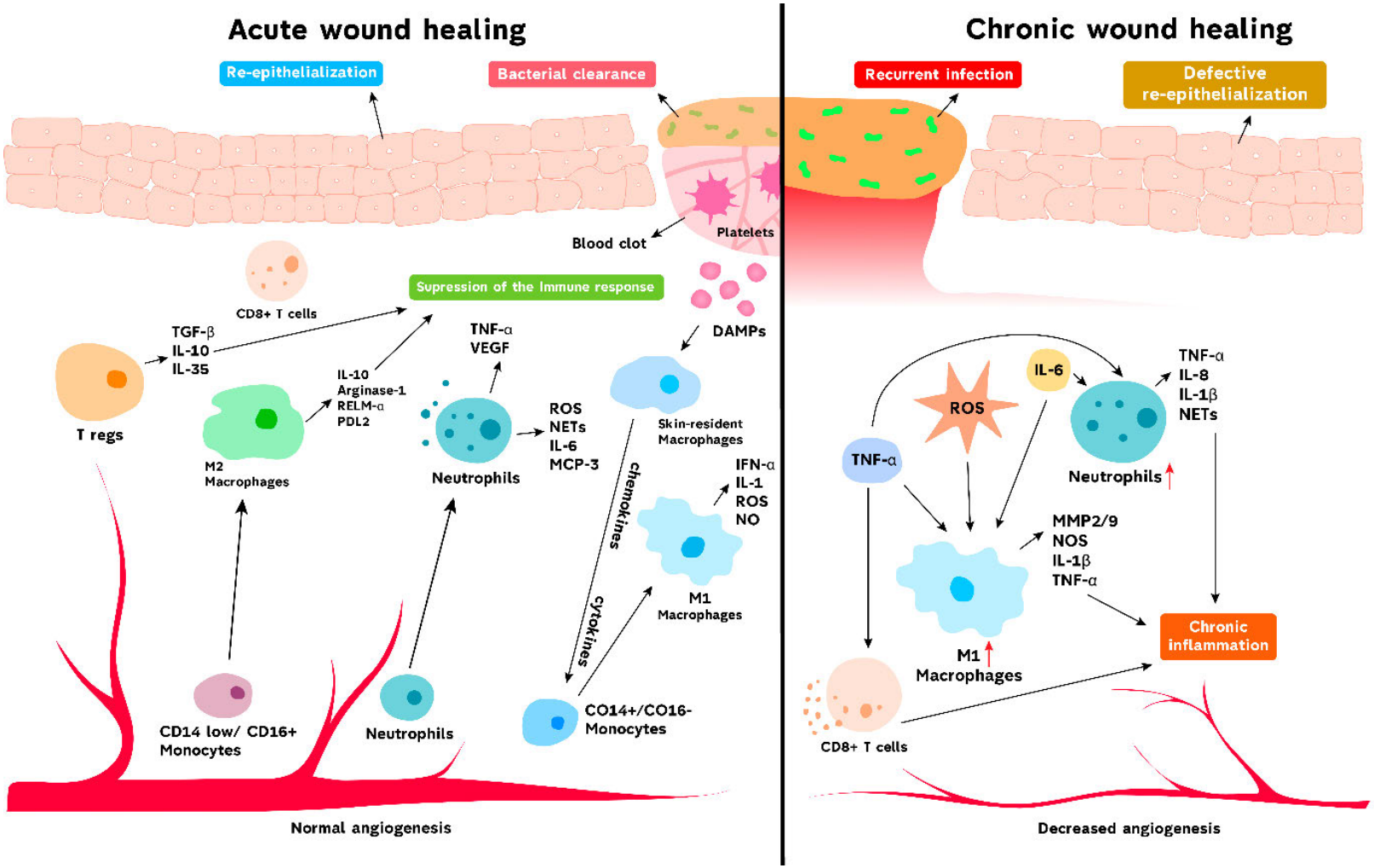

Figure 1.4. The key differences in the healing process between an acute wound and a chronic wound. (A) An acute wound successfully progressing through the wound healing process **(B)** A chronic wound that is failing to resolve inflammation, clear infection, and re-epithelialise [68].

The current treatment for an infected wound begins with debridement, the surgical or chemical removal of non-viable tissues from within and surrounding the wound. Once this is achieved, the next focus is to control for infection and therefore inflammation. This is often done through the use of topical antibiotics and antiseptics. Finally, the wounds are covered by a dressing to maintain a moist environment to facilitate wound healing to occur hence providing an integral barrier to the external environment, preventing the wound from further bacterial contamination [37, 63].

The treatment of infected wounds is also limited by the harsh environment of the chronic wound. Chronic wounds have a prolonged inflammatory response which results in a large number of proteases that are capable of breaking down many therapeutic treatments [62]. A growing number of studies are investigating the delivery of drugs in nanoparticles in order to protect the drug from this harsh environment [69-71]. Treatments of infected chronic wounds may work by removing the infection so the wound can progress through the healing stages, or focus on stimulating the wound healing process so the body is better able to fight off the infection and heal.

In addition to preventing the wound healing process from progressing, excessive inflammation can damage host tissue. The exacerbated neutrophil presence results in high levels of ROS being produced, resulting in damage to cell membranes and the extracellular matrix. In particular, neutrophil collagenase MMP-8 degrades elastase in host tissue which degrades growth factors like PDGF and TGF-β1. Increased production of MMP-2 and MMP-9 results in a decreased expression of tissue inhibitor of metalloproteinases (TIMPs) which inhibit MMPs. This results in disproportionate collagen degradation [62, 72, 73].

The inflammatory cells in a chronic wound continue to act on each other, causing the population to increase and accumulate, which perpetuates the prolonged inflammatory storm. This further leads to increased production of proteases and pro-inflammatory mediators IL-1, IL-6 and TNF. In chronic wounds, pro-inflammatory M1 macrophages are the predominant macrophages present with M2 macrophages being necessary for the resolution of the inflammatory phase [74-76]. Chronic wounds may also result from reduced blood flow which leads to increased necrotic debris and impaired immune responses. In addition to infection, chronic wounds can be caused or exacerbated by underlying pathologies like diabetes. Diabetic wounds are also more prone to infection.

1.6. Diabetes Mellitus

One of the most prevalent types of chronic wounds are diabetic wounds. Diabetes melittus is a disease characterised by sustained high blood sugar levels which results in hyperglycaemia [77]. Type I diabetes is an autoimmune disorder that involves the destruction of the insulin-producing β cells in the pancreas, resulting in limited insulin production. Type II diabetes involves the development of insulin resistance resulting in insulin overproduction in order to compensate which leads to β cell death and impaired ability to produce insulin. Both pathologies impair the wound healing process at every stage, and this begins with the structure of the skin. Diabetic skin has been found to be similar to aged skin with decreased lipid content, decreased hydration and increased advanced glycation end products (AGEs) [78-81]. Diabetes has many comorbidities including neuropathy, hyperglycaemia and atherosclerosis. Autonomic neuropathy results in reduced sweat gland activity which can leave skin cracked and dry, increasing the risk of itch and infection. Motor neuropathy increases pressure on the plantar surface of the foot which in combination with reduced neuron density can lead to tissue ischemia and death [82]. Additionally, diabetic skin is also subject to an increase in free radical damage due to reduced activity of the antioxidants glutathione reductase and superoxide dismutase [83] and an increase in ROS production [82].

An impaired skin barrier and a decrease in the production of antimicrobial peptides (AMP) causes diabetics to be more prone to skin infection. This is exacerbated by the hyperglycaemic environment of the wound that promotes bacterial growth. *S aureus* in particular has an increased prevalence of colonisation in diabetic skin and is a high contributor to the development of diabetic foot ulcers [84].

Diabetic wounds are one of the most prevalent types of chronic wound and involve a non-resolving inflammatory phase with an increased number of neutrophils and macrophages in the wound bed [72, 85, 86], and a chronic release of IL-1, IL-6, TNFα and plasma C reactive protein [72, 85, 87, 88]. The pro-inflammatory M1 macrophage phenotype dominates in the diabetic wound [86, 89, 90], and diabetic murine macrophages show a decreased secretion of growth factors [91].

Diabetic wounds also have decreased vasculature due to a decreased capillary density leading to insufficiency in the supply of blood factors [92]. This decrease in vasculature can

be due to the many comorbidities associated with diabetes. Atherosclerosis limits blood supply and prevents nutrients from reaching the wound [93]. Peripheral arterial disease is associated with increased severity and an increased risk of limb amputation. The hypoxic environment of the diabetic wound results in poor circulation, and differential gene expression of various cell populations [77].

Furthermore, HIF-1 signalling is impaired in diabetes [94]. The hyperglycaemic environment interferes with the stabilisation of HIF-1 impairing its protective ability against proteasomal degradation [95], impairing angiogenesis and revascularisation of the wound. Endothelial cells are also impaired by the hyperglycaemic environment via increased oxidative stress and inflammation, reduced VEGFA activity, and increased ROS production [96, 97].

Further impeding the later stages of wound healing, hyperglycaemia disrupts protein synthesis, migration and proliferation of keratinocytes and fibroblasts [78, 98-100]. Myofibroblasts produce MMPs to reconstitute the extracellular matrix, and replace collagen III with collagen I [22]. Myofibroblasts also produce tissue inhibitor of metalloproteinases (TIMPs) which block MMPs to balance the degradation of the extracellular matrix [101]. Hyperglycaemia results in a higher production of MMPs and a decreased production of TIMPs resulting in abnormal healing of the extracellular matrix [101, 102]. Diabetic wounds have fewer myofibroblasts, decreased secretion of the extracellular matrix and weakened wound contraction [76, 103, 104]. Without myofibroblasts there is no extracellular matrix for keratinocytes to migrate across and the wound cannot re-epithelialise [103].

In 2021, 1.3 million Australians were found to be living with diabetes [105], with diabetic foot disease affecting approximately 50,000 Australians every year, and resulting in 4,400 amputations every year [105] [106]. The five-year survival rate for diabetic foot ulcers is 70%, while the 1 and 5 year survival rate for those that receive a major amputation from diabetic foot ulcers is 41.7% and 8.3% respectively [107, 108]. Between 2020 and 2021, 11% of all hospitalisations were associated with diabetes, and in 2021, diabetes contributed to approximately 19,300 deaths [105]. Diabetic patients also have a higher risk of infection and colonisation by MRSA [109-113]. Infection can cause sepsis if bacteria enter the lymphatic system and blood vessels [43]. Over a 25-year period, sepsis occurred in 12.5 million people, with diabetes reported in 17% of cases [109, 114]. Patients with diabetes have higher sepsis-related morbidity, mortality, and post-sepsis complications [109-113].

Diabetes is currently one of the top ten leading causes of death in Australia [105] and research which addresses the complications of diabetic healing is of high priority.

There are many murine models of diabetes all looking at various pathologies like delayed wound healing, retinopathy, nephropathy, and neuropathy [115]. Each diabetic model has its benefits and limitations. The diabetic model chosen for a study should represent the aspect of diabetes being studied e.g. neuropathy, nephropathy [116]. Generally, models that involve the removal of the pancreas or destruction of the pancreatic β cells are good models for Type 1 Diabetes, while models that involve obesity and insulin resistance are good models for Type 2 Diabetes [115, 116].

There are two main categories of diabetic murine models: genetic models and chemically induced models. Of the genetic models, non-obese diabetic (NOD) mice and Akita mice are most commonly used and the most representative of human Type 1 diabetes. NOD mice are created through a series of mutations in the orthologues of major histocompatibility complex (MHC) molecules resulting in polyuria, weight loss, and lymphocytic infiltration of the islets of the pancreas [117]. Akita mice are created through a missense mutation in the *Insulin 2* gene causing insulin to accumulate in the β cells of the pancreas leading to cell death and hyperglycaemia [118, 119]. Obese db/db mice are a genetic model for Type II diabetes. These animals are created through a mutation in the leptin receptor which increases hunger and dysregulates glucose homeostasis resulting in obesity and hyperglycaemia [120-122].

Chemically-induced murine diabetic models are commonly created through the administration of alloxan or streptozotocin (STZ), both of which are models of Type 1 diabetes [115, 120]. Alloxan is a cytotoxic glucose analogue that inhibits glucokinase causing death of pancreatic β cells resulting in hyperglycaemia [116, 120, 121]. STZ is a cytotoxic alkylating agent that is highly selective to pancreatic β cells. STZ can be administered as either one high dose (the high dose method) or spread out over five consecutive days (the low dose method) [123]. The high dose method is directly cytotoxic to pancreatic β cells, rapidly causing diabetes. The low dose method only partially damages the pancreatic islets triggering an inflammatory response that causes further β cell death, resulting in insulin deficiency and hyperglycaemia [116, 123].

Additionally, the low dose STZ method may more closely resemble human Type 1 diabetes due to the contribution of autoimmunity. The multiple low-dose method only partially damages the pancreas, triggering inflammation and further β cell death. Hyperglycaemia occurs with lymphocytes infiltrating the pancreatic islets, causing apoptosis of the β cells, insulitis, and then insulin deficiency [123].

Many of the Type 1 diabetic models result in weight loss. This is due to increased urination as the kidneys work harder to filter out the excess glucose, increasing thirst, and the body beginning to burn muscle for energy [124]. This is reflective of Type 1 diabetes in humans. The high dose STZ model, in particular, weight loss can also cause weight loss due to the sudden onset of diabetes, fasting prior to STZ administration and STZ toxicity to the kidneys, liver, and intestines [125].

In addition to these models, diabetes can also be induced through a high fat diet, leading to obesity and insulin resistance, or through a pancreatectomy – the partial or complete removal of the pancreas [126, 127]. These models in particular allow for a wide range of animals to be used as diabetic models, including rats, rabbits, pigs, and monkeys, though mice are the most commonly utilised [121]. Chemical models allow for other genetic backgrounds to be investigated and allows some consistency between different animals e.g. going from mice to pigs to humans.

Wound healing has been investigated in the context of diabetes. Wound models for these investigations can include incisional wounds, excisional wounds, or burns, and can utilise mice, rats, rabbits or pigs [128]. Mice are often the first utilised in wound healing investigations due to their ease of use, though the wound healing process of pigs is more similar to that of humans [129]. Investigations often begin in mice and then extend into pigs before extending into humans.

Models of infected wounds are more complicated, and no model exists that is truly representative of an infected human chronic wound. The best model for an infected wound that currently exists is simply an excisional wound inoculated with bacteria [130]. Bioluminescent bacteria can be used to allow for daily monitoring of the infection over time [131]. Bacteria often used for the inoculation is *S. aureus*, one of the most common pathogens found in infected wounds [44, 45] and one of the most resistant bacteria developing [54].

While this is the best infected wound model currently used, it is not reflective of an infected human wound. Human wounds are often polymicrobial, varying in bacterial burden, population variety and burden. Chronic wounds in particular need time for the infection to establish itself and develop biofilms [36, 59].

1.7. Antibiotic-Alternative Approaches for Wound Infection

1.7.1. Flightless I

The Flightless I (Flii) protein was first discovered in 1993, in the *Drosophilia melanogaster* fruit fly when mutations in the gelsolin domain of the indirect flight muscles prevented them from being able to fly. Flii is a highly conserved protein with 95% homology between mice and humans [132].

A member of the gelsolin family, the protein consists of a series of Leucine Rich Repeats (LRR) followed by a series of gelsolin domains (Figure 1.5). Both segments are capable of binding different proteins, and some proteins interact with both segments. The LRR domain promotes protein-protein interactions as a nuclear co-activator involved in cellular signalling. While the gelsolin segment is responsible for binding the actin proteins [133-135].

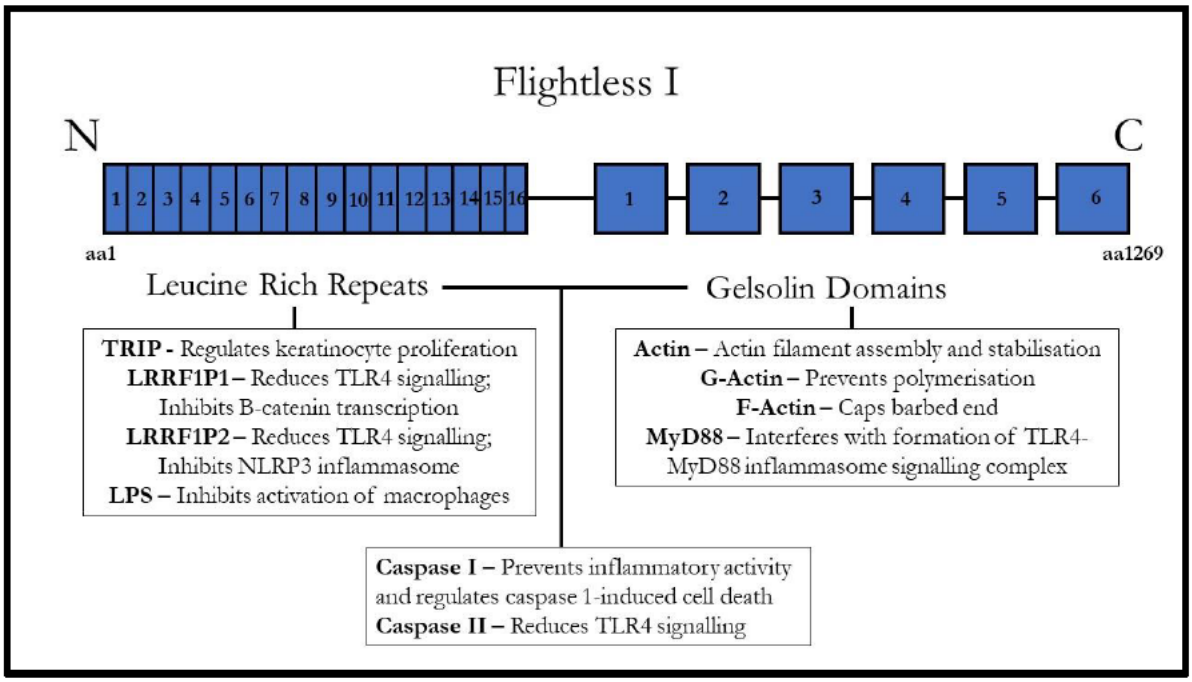

Figure 1.5. A schematic diagram of Flightless I with key binding partners and interactions.

1.7.1.1. Flightless I and Wound Healing

Flii has negligible expression in unwounded skin but is upregulated upon wounding in mice [136]. Increased levels of Flii have been shown to impair wound healing in murine incisional wounds, excisional wounds, and burn models. Impaired healing associated with aging and diabetes has also been shown to be exacerbated by increased Flii expression [137, 138].

In murine studies, the role of Flii is studied using two genetic models of Flii expression (Figure 1.6). One is a Flii under-expressing model, Flii $^{+/-}$, a heterozygous knockout (KO) where only one copy of the Flii gene has been deleted. A double knockout is not possible as it results in embryonic death [139]. The other is a Flii over-expressing model, Flii $^{tg/tg}$, where an additional copy of the Flii gene has been added. Combined with a wildtype (WT), this allows wound healing to be studied at various levels of Flii expression. Flii has also been knocked down using siRNA in order to create Flii under-expressing mice [140, 141].

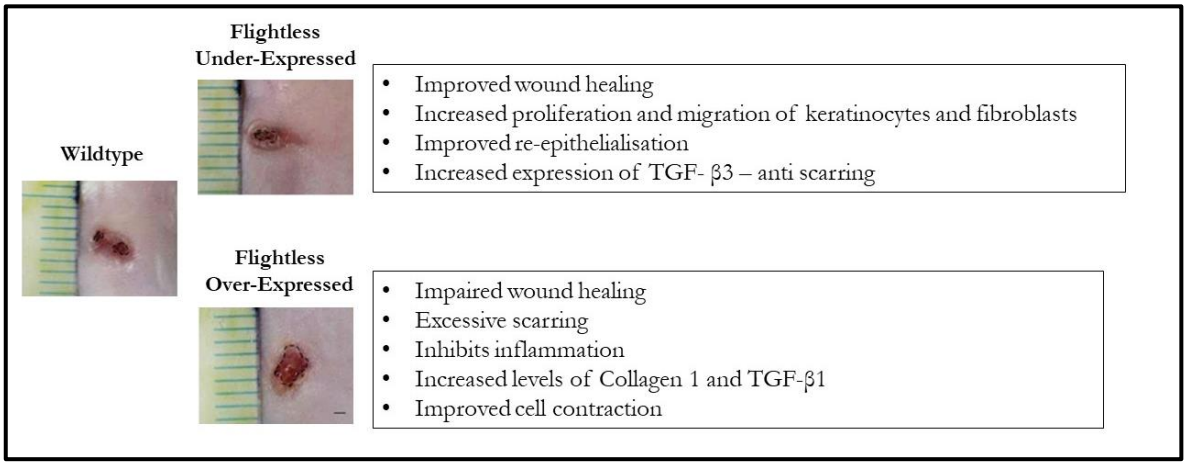

Figure 1.6. Excisional wounds in Wildtype (WT), Flii Under-Expressing mice (Flii $^{+/-}$) and Flii Over-Expressing mice (Flii $^{tg/tg}$) 7 days post-wounding with key findings noted [138].

Flightless I is considered to be necessary for the inflammatory stage of wound healing but detrimental to the later stages of wound healing [132]. Reducing Flii expression has been shown to accelerate wound healing with improved wound healing outcomes, while Flii overexpression has been shown to delay wound healing with poorer wound healing and more excessive scar formation [136, 138, 140-147].

Flii under-expressing mice show increased rates of re-epithelialisation due to the increased proliferation and migration of fibroblasts and keratinocytes, while the over-expression of Flii results in impaired adhesion in both keratinocytes and fibroblasts [148]. Flightless I negatively regulates proliferation through the negative regulation of the Wnt pathway responsible for the expression of proliferative genes, which results in delayed wound closure [149]. siRNA knockdown of Flii *in vitro* in both fibroblasts and keratinocytes resulted in increased proliferation, while cells from Flii over-expressing mice showed an impaired ability to proliferate [140]. However, proliferation is enhanced in tenocytes isolated from Flii overexpressing mice [150].

Angiogenesis is negatively regulated by Flii through the downregulation of VEGF. Flii under-expressing mice show an upregulation in VEGFA expression, as well as increased numbers of endothelial cells and pericytes in diabetic murine wounds [136, 151]. Meanwhile, Flii overexpressing mice show reduced micro vessel sprouting and decreased formation of tight junctions in the endothelial cells of diabetic wounds [136].

Flightless is also associated with impaired wound contraction. The skin of Flii overexpressing mice is significantly thinner than WT and showed reduced tensile strength [148]. Flii under-expressing wounds appear more contracted and have an increased number of myofibroblasts on the wound [140], and Flii attenuated burns show a decrease in the number of myofibroblasts [146]. Fibroblast-specific Flii overexpression showed a reduction in collagen I and an increased number of myofibroblasts [144]. This suggests that the effect of Flightless on myofibroblasts is independent of fibroblasts.

In addition to worse wound healing outcomes, Flii is associated with more severe scarring, with Flii expression increased in human burns and hypertrophic scars [146]. This is reflected in the TGF-β pathway where TGF-β1 and TGF-β2 increase the severity of scarring while TGF-β3 reduces it. Increasing Flii expression resulted in higher scarring, an increased number of myofibroblasts and an elevated collagen I/III ratio which is indicative of fibrosis [146]. Flii KO results in a decrease in TGF-β1 and TGF-β2 expression, and an increase in the expression of TGF- β3 [152]. Reducing Flii expression in fibroblasts using siRNA resulted in reduced expression of TGF-β1 [137]. In Flii deficient cells, TGF-β1 mRNA expression was decreased, but increased in Flii over-expressing fibroblasts [152]. In a scald burn model of Flii under-expressing mice, TGF-β3 expression was increased and a decrease in scarring was observed [142]. Collagen I contributes to excessive scarring, and Flii over-expression is associated

with increased granulation tissue formation and collagen deposition [140]. In fibroblasts treated with Flii siRNA, collagen I expression and secretion is reduced [140] and the siRNA knockdown of Flii inhibited the estrogen-mediated collagen I secretion by fibroblasts [142].

1.7.1.2. Flightless and Diabetes

Flii expression is increased in diabetic wounds, with high Flii expression being found in human diabetic wound tissue samples and fluid [136, 138]. Additionally, Flii expression is upregulated in unwounded diabetic skin compared to non-diabetic skin [136]. This may contribute to the overall impaired wound healing associated with diabetes. In a murine STZ model of diabetes, Flii expression peaked at 5 days post-injury in Flii under-expressing mice, and at 7 days post-injury in WT and Flii over-expressing mice. Reduced levels of Flii increased M2 macrophages and fewer macrophages overall in the wound. Reducing Flii expression improved wound repair in diabetic excisional wounds [147].

1.7.1.3. Flightless I Neutralising Antibody

Flightless I neutralising antibody (FnAb) is a monoclonal antibody that neutralises Flii by binding extracellular Flii to reduce its local activity. FnAb has been shown to improve wound healing, particularly in the later stages of repair in murine incisional wounds [145], excisional wounds [145], scald burns [142], developing scars [146], and porcine excisional wounds [153].

In a murine scald burn model, intradermal injections of FnAb improved wound healing and downregulated TGF-β1 and upregulated TGF-β3, indicating reduced scarring. A decrease in the myofibroblast marker α-smooth muscle antigen (αSMA) was also observed in the scar, showing increased wound contraction [142]. FnAb injected directly into the developing scars of mice, created through bleomycin resulted in a reduction in scarring, decreased dermal thickness, and a decreased ratio of collagen I/III [146].

In a STZ murine model of diabetes, FnAb intradermally injected into excisional wounds showed a decrease in TLR4 expression, but not Nuclear Factor kappa B (NFκB) expression. This indicates the FnAb decreases the inflammatory response during wound healing by inactivating the TLR4 pathway, however, the lack of change in NFκB expression shows some

inflammatory pathways remain active [138]. Intradermal injections of FnAb into excisional wounds was also found to upregulate expression of VEGFA within the wound, indicating improved angiogenesis [136].

Porous silicon nanoparticles have been investigated as a delivery system for FnAb and were found to protect the FnAb from being degraded by proteases in the wound microenvironment while allowing for a long, slow, sustained release into the wound bed. When treated with proteases, *in vitro,* FnAb pSiNPs showed intact and functional antibody release for up to 7 days post-treatment. FnAb pSiNPs were shown *in vitro* to increase the proliferation and migration of keratinocytes. A single dose of FnAb pSiNPs injected intradermally into murine incisional wounds resulted in smaller wound area compared to wounds treated with unloaded pSiNPs. In a STZ murine model of diabetes, FnAb pSiNPs injected intradermally into excisional wounds resulted in wound closure two days earlier than the unloaded pSiNPs [145]. FnAb has not yet been tested in the context of an infected wound.

1.7.2. Porous Silicon Nanoparticles (pSiNPs)

Porous silicon (pSi) is a silicon formulation discovered in the 1950s that has nanopores created in its microstructure [154]. pSi has four main chemical features: Si-H and Si-Si bonds with strong reducing power, a nanostructure high surface area with a fragile nature, the relative stability of Si-O, Si-N, Si-C surface bonds, and the photochemical activity of the material, derived from the semiconducting nature of silicon and quantum confinement effect in nanostructures [155].

Porous silicon is prepared through the electrochemical etching of a crystalline silicon wafer using hydrofluoric acid (HF) to introduce pores [156]. The pSi film is then detached and turned into nanoparticles through ultra-sonication, ball milling, or micro-fluidation [157]. The porosity, pore size, pore pattern and particle size can all be controlled through the fabrication parameters: HF concentration, current density, electrolyte composition, and wafer (dopant type, dopant density, crystallographic orientation) [154].

Porous silicon nanoparticles (pSiNPs) a are capable of being loaded with a drug which protects the load from degradation and allows for a slow sustained release [157]. This slow sustained release occurs through diffusion from the pores and degradation of the

nanoparticles. The rate of release can be altered by changing the pore size with larger pores allowing for a faster release, and by altering the degradation profile of the nanoparticles [156]. pSiNPs have shown no toxicity or inflammatory responses through oral, subcutaneous, or intravenous administration [158]. These nanoparticles are being used for a wide range of biological applications as a drug delivery system due to their high loading yield, biocompatibility, and safe degradation into the non-toxic orthosilicic acid which is excreted through the urine [159, 160]. pSiNPs can degrade within a few hours [156] or within a few days [160] and surface modifications can increase the stability of the nanoparticles.

Porous silicon nanoparticles have silicon hydroxide (Si-OH) functionality with silicon hydride (Si-H) and silicon-oxide bridges (Si-O-Si) which allow for surface modifications to be made. Surface modifications can include increasing the hydrophilicity to enhance substrate loading and water solubility, controlling the release rate of the substrate from the pore, targeting specific cell/organ/bacteria through the addition of homing moieties (e.g. peptides, ligands), or imaging agents (e.g. fluorophores) to allow for *in vivo* tracking [156].

There are three main surface modification methods including: hydrosilylation, oxidation, and hydrolytic condensation [154]. Hydrosilylation increases the stability of the pSi by creating Si-C bonds from Si-H and maintains the pore structure, allowing for further functionalisation [154].

Oxidation is the formation of an oxide-layer on the surface of the pSi to increase hydrophilicity. Increasing the hydrophilicity enhances the loading yield of positively-charged substrates, enhances their biocompatibility, increases their stability, and allows for further functionalisation (e.g. chemical conjugation) [157]. Oxidation also enhances the quantum confinement effects on the surface of the pSi which exacerbates the auto-luminescent properties of the porous silicon [154, 161]. pSiNPs are auto-luminescent which is detectable *in vivo* using an *In Vivo* Imaging System (IVIS) [155, 160]. Thermal oxidation exacerbates the auto-luminescence by passivating the surface [161]. This results in the pSiNPs displaying a strong orange to near-infrared (NIR) photo luminescence at room temperature which is attributed to the quantum confinement effects in the silicon cores and the localised Si-SiO2 interfacial defects [161-164].

Hydrolytic condensation creates new Si-O-Si bonds on the surface of the pSi which allows for further surface modification [154]. Hydrolytic condensation also improves the hydrophilicity and in doing so helps control the degradation rate and increases the substrate yield [157].

Due to their biocompatibility, pSiNPs are being explored in a wide range of biomedical applications. pSiNPs are broadly being investigated as a delivery mechanism for a wide range of drugs [165] but have also been explored as a potential wound healing treatment. Silica nanoparticles and orthosilicic acid were found to increase the metabolic activity, proliferation and migration of human skin fibroblasts at 50 μM and 100 μM [166]. A silicon dioxide wound dressing improved wound healing and increased re-epithelialisation in an excisional wound murine model [167]. In an incisional murine model, self-luminating pSiNPs were used as a tissue adhesive that promoted angiogenesis and epidermal regeneration [160]. In the same study, orthosilicic acid, the degradation product of pSiNPs, was found to promote the tube formation of Human Umbilical Vein Endothelial Cells (HUVECs) [160], indicating that orthosilicic acid may also be beneficial to the wound healing process. While no inherent antibacterial properties have been reported for pSi, pSiNPs produce singlet oxygen under visible light irradiation indicating potential use as a photosensitiser in photodynamic therapy [161].

Other nanoparticles have been explored as drug delivery systems, with some nanoparticles having antimicrobial properties (e.g. silver, gold, zinc), and some having beneficial effects on wound healing (e.g. can promote re-epithelialisation) [168]. No such effects have been reported for pSiNPs. This allows the investigation of the treatment protected from hostile biological environments without the possible addition of synergistic effects from more active nanoparticles.

1.7.3. Antimicrobial Peptides

Antimicrobial peptides (AMPs) are small peptides with antimicrobial and immunomodulating properties. These peptides are produced by humans, animals, and bacteria to control and eliminate infection [169, 170]. Synthetic peptides can be made which often mimic naturally occurring ones. For instance, the AMP, DRGN-1, is a synthetic peptide inspired by the histone H1-derived peptide from the Komodo dragon [171].

Many AMPs have been shown to be antimicrobial. This has been shown to occur through the disruption of the cell membrane at various points of contact (Figure 1.7). The peptide accumulates on the surface of the membrane, before forming a structure, and creating a pore through the membrane. This is often achieved through toroidal pore formation or the barrel-stave method which leads to thinning of the membrane and eventually cell death [172].

While many AMPS have been shown to have antimicrobial properties through simple minimum inhibitory concentration (MIC) assays with planktonic cultures, AMPs have also shown great anti-biofilm properties [173]. AMPs have been shown to inhibit biofilm formation through the down regulation of quorum sensing, inhibiting nucleic acid synthesis, and by reducing the expression of binding transport genes necessary for the development of a biofilm. They can also eradicate biofilms by acting on the membrane potential of bacteria leading to the degradation of the extracellular polymeric substance [174-176]. Nisin A can disturb the membrane potential of MRSA leading to the degradation of the biofilm [174].

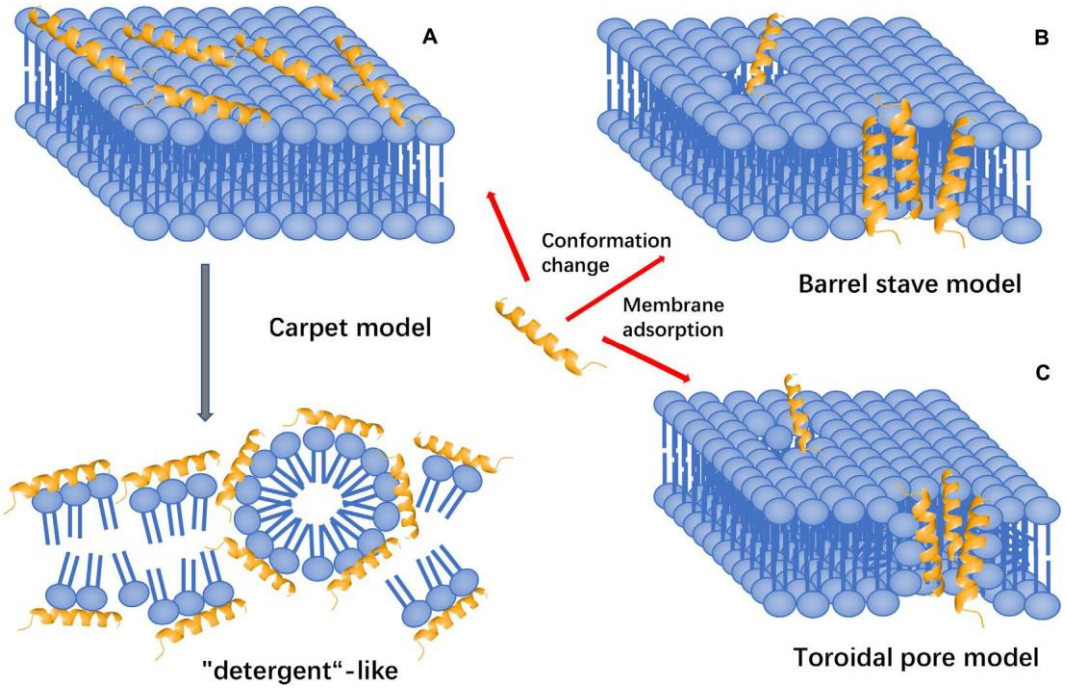

Figure 1.7. Methods of pore formation by antimicrobial peptides to kill bacteria. (A) Carpet model **(B)** Barrel stave model **(C)** Toroidal pore model [172].

Several AMPs have been investigated as treatments for infected wounds *in vivo*. The antimicrobial peptide, LL-37, improved angiogenesis in full thickness excisional wound models [177]. Tiger 17 is a cyclic peptide derived from the AMP tigerinin isolated from the skin secretions of the *Fejervarya cancrivona* frog with a MIC of 256 µg/mL against *S. aureus* [178]. In a full thickness skin wound murine model, Tiger 17 improved wound healing, with more macrophages in the wound bed, and activation of the MAP kinase pathways, stimulating the release of IL-6 and TGF-β1 in murine macrophages. Tiger 17 has also promoted the proliferation and migration of keratinocytes and fibroblasts [179, 180], and has been shown to accelerate clotting [178].

Tylotoin is a short peptide derived from the C terminus of a cathelicidin extracted from the skin of a salamander. Tylotoin has shown no antimicrobial activity but improved wound healing in a full thickness excisional murine model. *In vivo*, Tylotoin promoted the expression of TGF-β1 and IL-6. *In vitro*, Tylotoin promoted the proliferation and migration of vascular endothelial cells, fibroblasts and keratinocytes [179, 181]. A topical solution of the synthetic AMP, SHAP-1, at just 1 µM accelerated wound closure in full thickness excisional murine wound models [182]. Epinecidin-1 enhanced wound closure and decreased the MRSA bacterial load in both a murine model and a porcine model.

The effect of AMPs on the inflammatory phase of wound healing has been explored. Epinecidin-1, Tiger 17 and Tylotoin have been shown to increase the recruitment of macrophages to the wound in murine excisional wounds [180, 181, 183] while CW49 reduced macrophage recruitment [184], and Epinecidin also promoted the recruitment of neutrophils [183]. IDR-1018 and Cathelicidin-WA have been shown to drive the macrophage phenotype switch from the pro-inflammatory M1 phenotype to the anti-inflammatory M2 phenotype *in vitro* [185, 186]. The expression of pro-inflammatory cytokines is decreased by WR12, F1-P(R)P(R)P(L), Epinecidin-1, and CW49 [183, 184, 187-189]. TCP-25 has been shown to decrease the overall inflammatory response by reducing NFκB/activator protein (AP)-1 activation [190]. The expression of pro-inflammatory cytokines is increased by Tylotoin, Tiger 17 and AH90 [180, 181, 191]. In murine models, AH90 was shown to work through the NFκB and JNK pathways, while Tiger 17 was shown to function through its effects mediated by the ERK, MAPK and JNK signalling pathways [180, 191].

Keratinocytes are important for wound closure and are affected by a wide range of AMPs. The AMPs DRGN-1, Esclulentin, LL-37, Pep 19-2.5, Pep 19-4LF, SHAP-1, and Temporins A&B have all been shown to promote the migration of keratinocytes *in vitro* [171, 182, 192-195]. While the AMPs A5G81, Melittin and Tiger 17 have been shown to promote both the migration and proliferation of keratinocytes *in vitro* [180, 196, 197]. This is often through the activation of the epidermal growth factor receptor (EGFR) pathway [169, 179].

AMPs can support the formation of granulation tissue through their effect on fibroblasts. The proliferation and migration of fibroblasts is promoted by Tiger 17 and SR-0379 *in vitro* [180, 198]. Both AH90 and Tylotoin promote the differentiation of fibroblasts into myofibroblasts, supporting wound contraction, *in vitro* and *in vivo* respectively [181, 191]. Additionally, Tiger 17 has been shown to promote collagen synthesis in murine excisional wounds [180]. CW49 and WRL3 both support angiogenesis by increasing the expression of VEGFA in murine diabetic wounds [184, 199]. SR-0379 and Tylotoin promote angiogenesis by increasing the proliferation of endothelial cells, and endothelial tube formation, respectively both *in vitro* and *in vivo* [181, 198].

1.7.3.1. Pexiganan

Pexiganan, also known as MSI-78, is a synthetic antimicrobial peptide that has shown broad-spectrum efficacy against bacteria and viruses. Pexiganan is an analogue of Magainin 2, which is found in the skin of the African clawed frog, *Xenopus laevis*. Magainin 2 was discovered in 1987 when the frog was placed into infected water with incisions on the frog's skin, but the wounds did not become infected [200]. Pexiganan is 23 amino acids long, has an α helical structure, and is unstructured in solution and then forms structure when it encounters the bacterial cell membrane. Pexiganan accumulates on the membrane and eventually forms a toroidal pore, disrupting the membrane [201].

Pexiganan was the first AMP investigated as a treatment for infected skin wounds [169]. In 1997, two consecutive phase III FDA trials took place totalling 835 participants. All patients had mildly infected diabetic foot ulcers and received either pexiganan, or ofloxacin. The patients that received the pexiganan treatment topically applied as a 1% pexiganan acetate cream twice a day, while those that received the antibiotic, received 200 mg ofloxacin orally twice a day. The minimum treatment period was 14 days, but the investigators could extend the treatment for up to 28 days if necessary. Wound closure occurred in 10-15% of patients after 4 weeks, and 18-30% after six weeks. Clinical cure or improvement was achieved in ~90% of patients and microbial eradication in 42-47% of patients treated with either the pexiganan or the ofloxacin, with no statistical significance found between the two treatments [202]. The pexiganan cream did not receive FDA approval as there was no statistical significance between the pexiganan treatment and the standard ofloxacin treatment being used at the time. However, antimicrobial resistance to ofloxacin was observed in the ofloxacin-treated patients while no resistance was observed in the pexiganan-treated patients. There was also no statistical significance in side effects or patient withdrawal from the study between the two treatments [202, 203].

From the FDA trials, 2515 isolates were taken from the infected diabetic foot ulcers at various time points during the trial, and their MICs determined *in vitro*. The study included gram positive, gram negative, anaerobic and aerobic bacteria, all of which were found to have an MIC_{90} of 16 µg/mL or less. *S. aureus* (375 isolates), in particular, was shown to have an MIC_{90} of 16 µg/mL and MIC_{50} of 8 µg/mL [204]. The bactericidal effect of pexiganan was shown to be increased by increasing the pH, while temperature had no effect [205]. This study also showed that pexiganan was non-toxic up to 50 µg/mL on HeLa cells [205].

Research to date has focused on investigating different delivery systems and synergistic effects with other AMPS. The AMPs, pexiganan and nisin were incorporated into a biogel and used to control both planktonic and biofilm *S. aureus* and *P. aeruginosa* cultures isolated from a diabetic foot ulcer. This study also explored the antibacterial efficacy of pexiganan against *S. aureus, P. aeruginosa*, and combined *S. aureus* and *P. aeruginosa* planktonic cultures and biofilms. Higher concentrations of pexiganan were needed for the *P. aeruginosa* and combined cultures, and for the biofilms [206]. Pexiganan and Tiger 17 have been loaded into nanocrystalline-reinforced poly(vinyl alcohol) electrospun mats [178]. A wound dressing of nanofibers loaded with pexiganan was successfully used against *S. aureus in vitro* but did show cell cytotoxicity [207]. A modified variant of pexiganan was created which contained an additional nitric oxide donor moiety on lysine residues that could self-assemble upon a pH shift, forming a hydrogel [208].

A lack of cross-resistance has also been shown between pexiganan and other antibiotics. This was likely due to the membrane-targeted mechanism of action [204, 209, 210], and the rapid bactericidal mechanism of action [204, 210]. Unfortunately, pexiganan has been shown to have cytotoxic effects on various cell populations at higher concentrations [178, 205, 207, 211]. Modifications and delivery systems have been explored to mitigate this cytotoxicity.

AMPs have shown reduced efficacy when topically applied due to the peptide's susceptibility to an alkaline pH, proteolysis, hydrolysis, oxidation and haemolysis [169, 212]. An arginine-rich variant of pexiganan was shown to be more resistant to proteases and enhanced anti-parasitic activity *in vitro* [213]. Pexiganan nanoparticles enhanced the adherence to gastric mucosa in mice, resulting in a prolonged stay in the stomach and improved *Helicobacter pylori* clearance [214]. Nanoparticles containing pexiganan with silver nanoparticles attached to the outside enhanced anti-bacterial activity against bacteria residing within macrophages compared to free pexiganan *in vivo* [215].

1.7.4. Photodynamic Therapy

Photodynamic Therapy (PDT) is an antibiotic-alternative method of killing bacteria. PDT involves the administration of a light-activated chemical, a photosensitiser, followed by activation with light irradiation to produce reactive oxygen species (ROS) to kill nearby bacteria/cells [216] (Figure 1.8). PDT has been approved for clinical treatments since 1993 [217], including skin cancers, acne vulgaris, rheumatoid arthritis, and age-associated macular degeneration [218].

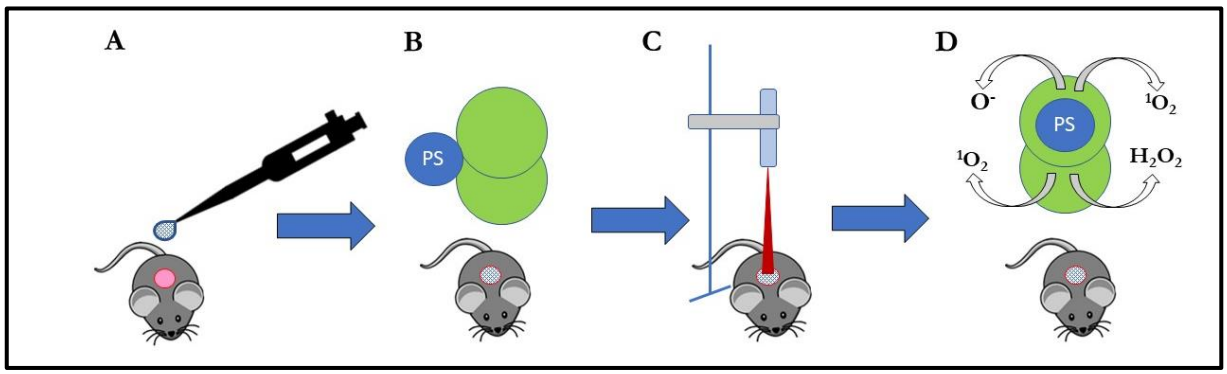

Figure 1.8. A typical photodynamic treatment of an infected excisional wound model. A. The photosensitiser is administered topically to the infected wound. **B.** The photosensitiser enters the bacteria. **C.** The wound is irradiated with an LED light to activate the photosensitiser. **D.** The activated photosensitiser produces reactive oxygen species (ROS) and singlet oxygen ($^1O_2$) to kill the bacteria from within.

Photodynamic therapy dates back thousands of years, however in 1900 it was Raab's observations that acridine dyes when exposed to light were able to treat single-celled protists, *paramecia*, that the technique was re-introduced into the modern world [218]. However, the therapy was put on the back burner as a method of clearing infection as antibiotic treatments were discovered and increased in use. With the emergence of antibiotic resistance in 1961, researchers started looking into photodynamic therapy again as an alternative approach for the management of wound infection.

There are two key components of PDT; the photosensitiser and the light. Photosensitisers are light-activated dyes capable of producing singlet oxygen ($^1O_2$) and/or ROS when activated. There are a wide range of photosensitisers varying in characteristics including structure, composition, toxicity, efficacy and the activation wavelength. Despite these

differences, photosensitisers produce singlet oxygen or reactive oxygen species the same way (Figure 1.9). When the photosensitiser is irradiated at the correct wavelength, the photosensitiser gains energy, and transitions from the ground state to an excited singlet state. The photosensitiser can then transition even higher to an excited triplet state where it interacts with biomolecules through either Type I or Type II pathways. The Type I pathway involves electron-transfer reactions with an organic substrate molecule of the cells to produce free radicals which can interact with endogenous molecular oxygen to produce reactive oxygen species. The Type II pathway involves the triplet state photosensitiser interacting with oxygen to produce singlet oxygen, and is the main pathway through which photodynamic therapy occurs [219, 220].

Due to the short radius of action of singlet oxygen, where the photosensitiser localises inside the cell is very important and effects the concentration of photosensitiser required. For instance, if a photosensitiser localises at the cell membrane the damage from the singlet oxygen or ROS can tear open the cell membrane and cause cellular leakage, while photosensitisers that localise in the endoplasmic reticulum or cytoplasm may need to cause more damage before the cell dies, and therefore a higher concentration of photosensitiser within the cell. Photosensitisers that localise in the mitochondria or endoplasmic reticulum induce apoptosis while those that localise in the lysosome or plasma membrane cause necrosis [221-224].

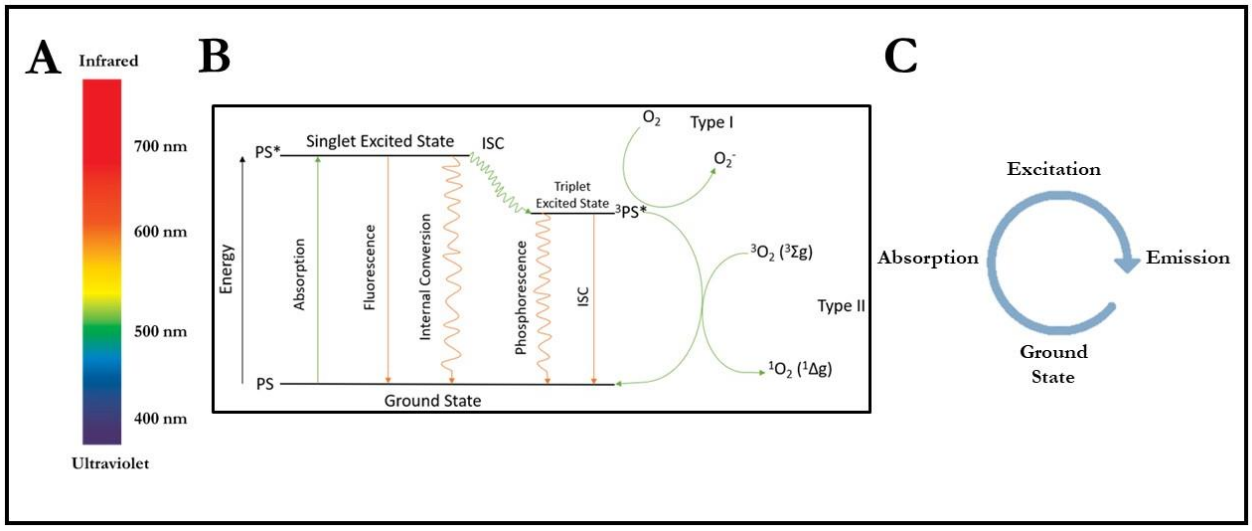

Figure 1.9. The basic mechanisms of how photosensitisers produce reactive oxygen species and singlet oxygen. (A) The light spectrum that may be used to activate photosensitisers **(B)** A Jablonski diagram showing the energy transitions of a photosensitiser being activated (green) and the ways in which the photosensitiser may lose its excitation (orange). Adapted from Pye [225]. **(C)** The basic cycle of a photosensitiser being activated.

Most commonly, photosensitisers are activated with green (520 - 560 nm) or red (635 - 700 nm) light, though various photosensitisers can also be activated at other wavelengths including infrared or near-infrared wavelengths. Light of longer wavelengths are often preferred as longer wavelengths penetrate deeper into tissues, allowing the treatment to penetrate further into the body. One review reported that optical penetration is 1.8 mm for 660 nm, 2.2 mm for 750 nm and 2.4 mm at 850 nm [226].

Light sources used to activate the photosensitiser include lamps, lasers, and light emitting diodes (LEDs). LEDs are a common choice as they are inexpensive, and with the use of optic fibres, LEDs allow the applications of PDT to not be limited to just the skin. The light dose differs amongst photosensitisers and the surrounding conditions, and often a higher light fluence is needed *in vivo* compared to *in vitro*.

Photodynamic therapy has been studied extensively in the context of infection, with many photosensitisers being proven to kill planktonic bacteria *in vitro*, although fewer studies are reported *in vivo*. PDT treatment utilising a specific photosensitiser is often denoted as

photosensitiser-PDT. While there has been significant research on PDT and infection, there are relatively few studies focusing on the use of PDT in wound healing.

One study used a murine skin abrasion model that consisted of methicillin resistant *S. aureus* (MRSA)-infected scratch wounds on the back of mice treated with polythethylamine-ce6-mediated PDT activated by red light which increased the rate of wound repair by 8.6 days and caused a 2.7-log reduction of MRSA based on bioluminescence (Figure 1.10) [227]. RLP068/Cl (Zinc Phthalocyanine)-mediated PDT at 60 J/cm^2 was successfully used to treat murine MRSA-infected chronic leg ulcerations, causing a 3-log reduction in bacteria 2 days post-infection and complete re-epithelialisation for the PDT treatment group on Day 9 [228]. A further study showed ALA-mediated PDT successfully accelerated wound healing and decreased bacterial counts in murine MRSA-infected leg ulcers [229].

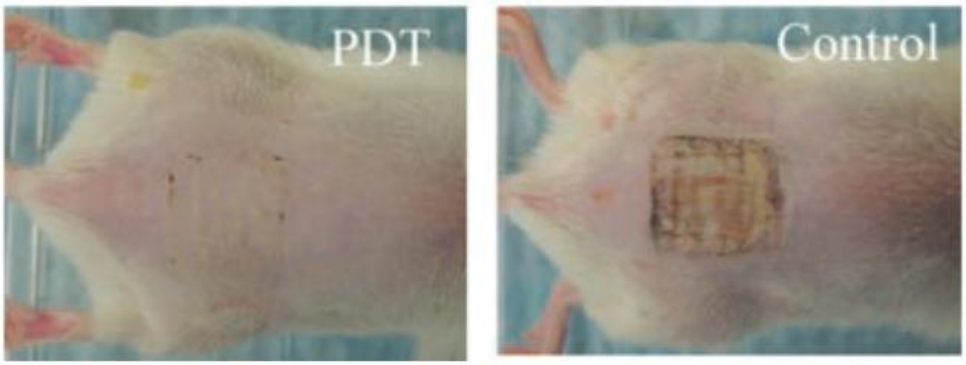

Figure 1.10. A murine skin abrasion model four days post-injury, infected with MRSA and treated with PDT (Left) and untreated (Right) [227].

Only one paper suggested that PDT may delay wound healing. Third degree murine burn wounds infected with *S. aureus* were treated with 500 µL PTMPP (porphyrin) and 25% DMSO, and up to 423 J/cm^2. The delay in healing was observed in both the PDT and light only treatment groups. 98% of the bacteria was eradicated in the presence of PTMPP at 210 J/cm^2, however, bacterial regrowth was observed, and higher concentrations of photosensitiser and light were required *in vivo* than *in vitro* to achieve similar results [230].

In a murine model of bacterial arthritis using MRSA, MB-PDT was shown to decrease the bacterial burden at 100 µM and 50, 80 and 120 J/cm^2 (light fluences tested: 5-160 J/cm^2).

MB-PDT resulted in an increased accumulation of neutrophils which corresponded with the resolution of infection. However, at the highest dose tested 160 J/cm^2, damage to the synovial micro vessels and an increase in red blood cells, indicative of tissue damage, was observed. The antibacterial effects of MB-PDT gradually decreased past 50 J/cm^2. Additionally, treating the mice with MB-PDT at 100 µM and 50 J/cm^2 one day prior to infection showed a reduction in bacterial burden over the seven-day period. This suggests that MB-PDT has the ability to suppress the development of an infection as a preventative treatment [231].

1.7.4.1. Methylene Blue

Methylene Blue (MB) is a photosensitiser that has been widely researched for PDT due to its desirable activation wavelength, charge and water solubility compared to other photosensitisers. Methylene Blue has previously been conjugated to gold nanoparticles [232-234], silver nanoparticles [235], hydrogel nanoparticles [236], dextran-capped gold nanoparticles [237], and oligonucleotides [238], but not to antibodies.

MB-PDT has shown efficacy against more than 20 strains of *S. aureus* at 3 mM and 26.3 J/cm^2 *in vitro* [239]. MRSA has been successfully treated *in vitro* at 100 µM and 20 J/cm^2, and at 300 µg/mL and 60 J/cm^2 [240, 241]. Additionally, the same approach was effective in treating polymicrobial biofilms consisting of MRSA and *P. aeruginosa in vitro* using 500 µg/mL and 108 J/cm^2 [242]. In murine models of infection, MB-PDT has been used to treat *C. albicans* at 450-500 µg/mL, and a MRSA biofilm at 100 µM and 50 J/cm^2 [231, 243].

PDT using a combination of MB and Toluidine Blue-O (TBO) was successfully used to treat human diabetic foot ulcers (Figure 1.11). Wounds in the PDT treatment group were either irrigated or injected with a solution of equal parts MB and TBO and then irradiated with either a lamp at 30 J/cm^2 or an optical fibre at 6 J/cm^2. The differences in treatment were dependent on the presence or absence of an open fistula in the wound. The PDT treatment underwent treatment twice a week initially then once a week. In the PDT treatment group, only one of the 18 patients went on to have an amputation, while all 16 patients in the control group that received antibiotics went on to receive amputations [244]. In another clinical case, multiple treatments of a 1% MB solution and 37 J/cm^2 successfully cleared two patients with infected skin ulcers [245].



Figure 1.11. A human diabetic foot ulcer trial utilising combined Methylene Blue (MB) and Toluidine Blue O (TBO) PDT. (A) An example of a DFU being irrigated with the combined photosensitiser treatment **(B)** A diabetic foot ulcer at the beginning of the trial **(C)** The same diabetic foot ulcer as in **(B)** at the end of the trial [244].

1.7.4.2. Photo-Antibody Therapy

Photo-Antibody Therapy (PAT), also known as Antibody-Directed Phototherapy, is the use of antibody conjugates to increase the specificity of the photosensitiser, and is a largely unexplored field, especially in its application against infection. In 2002, Embleton *et al.* conjugated the photosensitiser tin chlorin e6 (SnCe6) to Immunoglobulin (Ig)G to direct the photosensitiser to Protein A in the cell wall of *S. aureus.* The treatment was effective *in vitro*, though strain-specific and growth phase dependent [246]. This was improved upon in 2004 when the same photosensitiser was attached to an antibody raised against MRSA capsular polysaccharides, particularly polysaccharides 5 and 8 [247]. Chlorin e6 was also conjugated to poly-L-lysine and tested *in vivo* against *S. aureus* with success and showed that the conjugate was more effective than the free Ce6 [248]. Studies on conjugates that are antibody-specific and target infection are very few, as cancer has often been the focus and other conjugates have been explored like oligonucleotides, peptides, and chitosan.

1.7.5. Summary

Clearing infected wounds can take two different approaches. The first focuses on clearing infection so wound healing can progress. The second approach is to enhance wound healing so the body's natural antimicrobial defences can clear the infection itself. Photo-Antibody Therapy and pexiganan pSiNPs treatments focuses on clearing infection while the FnAb pSiNPs treatment focuses on encouraging wound healing in an infected wound.

Antibiotic-alternative methods of clearing infected wounds are similarly met with a host of challenges. One such challenge is being able to target the bacteria over the healthy mammalian tissue as to not further damage the wound area and impede the cells necessary for wound healing to occur. Photo-Antibody Therapy may be a solution to this problem, allowing for the bacteria to be targeted with minimal damage incurred to the wound, allowing for successful wound healing to occur.

Another challenge to treating infected wounds is the hostility of the wound exacerbated by infection and pathologies such as diabetes, degrading therapeutic treatments [69-71]. Porous silicon nanoparticles are an effective drug delivery system that may improve the efficacy of existing treatments in more hostile wound environments [157]. The antimicrobial peptide, pexiganan, and the monoclonal antibody, FnAb, may have improved efficacy through the use of porous silicon nanoparticles and therefore be effective treatments for infected wounds. Additionally, the slow-release profile of the porous silicon nanoparticles may reduce the cytotoxic effects of pexiganan while still promoting wound healing.

1.8. Aims and Hypotheses

With the increase of antimicrobial resistance, antibiotic-alternative methods of clearing infected wounds are needed. This thesis explores three alternative treatments for the resolution of infected wounds; Photo-Antibody Therapy, pexiganan pSiNPs, and FnAb pSiNPs.

Photodynamic therapy is a promising antibiotic-alternative treatment with a wide range of photosensitisers and adaptability. However, in the context of an infected wound, the lack of specificity in PDT can lead to tissue damage which may further impair wound healing outcomes. Photo-Antibody Therapy may solve this limitation by conjugating a photosensitiser to an antibody specific to gram-positive bacteria reducing the concentration of the photosensitiser that may be required to clear infection and potentially limiting the damage to the healthy tissue. Increasing the specificity this way may also result in more effective treatments of harder to kill organisms and biofilms.

Another antibiotic-alternative method of clearing infection is the utilisation of the antimicrobial peptide, pexiganan. Despite showing potential in clinical trials, the efficacy of pexiganan is limited due to the hostile nature of the wound and its cytotoxicity to mammalian cells. Delivering pexiganan to the wound using porous silicon nanoparticles (pSiNPs) is likely to protect the peptide from degradation and allow for its slow release resulting in better anti-bacterial and wound healing outcomes.

Monoclonal antibodies (mAbs) can neutralise proteins that contribute to poor wound healing. Flii neutralising antibody (FnAb) has been shown to have reduced efficacy in a diabetic model of wound healing, possibly due to the degradation of FnAb by proteases. Infection exacerbates the hostile wound environment further contributing to further degradation. Delivering the FnAb in pSiNPs may protect the FnAb from degradation and allow for slow release of the antibody over the course of the wound healing process. While FnAb-pSiNPs has been shown to improve wound healing in a diabetic model, efficacy has not been proven in the presence of infection, and it is not known if FnAb can promote healing despite the presence of infection.

Overall, this thesis investigates the efficacy of three novel antibiotic-alternative strategies for the management of infected wounds.

1.8.1. Aims

Aim One: To determine if conjugating Methylene Blue to an antibody specific to gram positive bacteria will improve the specificity of Methylene Blue, and result in a safer and more effective photodynamic therapy treatment of infected wounds.

Aim Two: Determine if encapsulating pexiganan in pSiNPs protects the pexiganan from proteolytic degradation and reduces cytotoxicity in an *in vivo* infection wound healing model and assess if this leads to improved wound healing outcomes.

Aim Three: To investigate the wound healing effect of Flii neutralising antibody (FnAb) delivered in pSiNPs in an infected excisional diabetic murine model.

1.8.2. Hypothesis

The bacterial burden and wound healing of infected excisional wounds will be improved by increasing the specificity and durability of existing antibiotic-alternative treatments through the use of antibody conjugation or porous silicon nanoparticles.

Chapter Two – Materials and Methods

2.1. Chemicals

All chemicals utilised in protocols were purchased from Sigma Aldrich (Castle Hill, NSW, Australia) unless stated otherwise.

2.2. Solutions

2.2.1. Cellular

Cell Culture Media: 5 mL Penicillin/Streptomycin (1%) and 50 mL Foetal Calf Serum (FCS) (10%) was added to 445 mL Dulbecco's Modified Eagle Medium (DMEM) (L-Glutamine added) (Gibco, ThermoFisher Scientific, Scoresby, VIC, Australia).

Freezing Media: 1 mL of freezing media (10% Dimethyl Sulfoxide (DMSO), 30% FCS, 60% DMEM Media) was used per confluent flask (5 x 10^6 cells/mL) and aliquoted into a cryogenic vial. The cryogenic vials were placed into either a CoolCell Container or Mr Frosty at -80˚C overnight before being moved into liquid nitrogen storage.

Resazurin: 110 µg/mL Resazurin was mixed in Dulbecco's Phosphate Buffered Solution (DPBS) and filtered with a 0.2 µM pore filter via syringe. Resazurin was stored in a glass bottle at 4˚C. The resazurin was diluted 1 in 10 in media for use.

2.2.2. Bacterial

Tryptic Soy Agar (TSA) Plates: 7.5 g Technical Agar and 15 g Tryptic Soy Broth (TSB) was mixed in 500 mL distilled water and autoclaved. Once cool enough to handle, the solution was poured into the plates in a biosafety cabinet. The plates were used within a month. The unused agar solution was allowed to set in the bottle and used within six months, heated to 100˚C, cooled to 50˚C and then poured.

Tryptic Soy Broth (TSB): 15 g Tryptic Soy Broth was mixed in 500 mL distilled water and autoclaved. The broth was used within six months.

Supplemented with kanamycin: 200 µg/mL kanamycin = 100 mg kanamycin per 500 mL of TS agar/broth.

2.2.3. Histological Staining

Acid Alcohol – 10 mL Hydrochloric Acid + 700 mL Ethanol + 290 mL MilliQ Water.

Bicarbonate Solution – 5 g Sodium Bicarbonate in 1 L MilliQ water.

Celestine Blue – 0.25 g Celestine Blue in 50 mL MilliQ water + 0.25 g Iron Alum in 50 mL MilliQ water – mix the two solutions together.

Fuchsin Ponceau – 2 g Xylidene Ponceau, 1 g Acid Fuchsin in 99 mL MilliQ water + 1 mL acetic acid.

Phosphotungstic Acid – 5 g Phosphotungstic in 100 mL MilliQ water.

Acetic Acid – 1 mL Acetic Acid + 99 mL MilliQ water.

Light Green – 2 g Light Green in 100 mL MilliQ water.

Target Retrieval Solution (TRS) – 2.1 g Citric Acid, 3.76 g Glycine, 0.376 g Ethylenediaminetetraacetic acid (EDTA) in 1 L MilliQ water, pH 5.9.

20X PBS – 160 g Sodium Chloride, 4 g Potassium Chloride, 28.8 g Disodium Hydrogen Orthophosphate, 4.8 g Potassium Phosphate Monobasic in 1 L MilliQ water, pH 7.4.

2.3. General Animal Techniques

2.3.1. General Husbandry

All animal studies were approved by the University of South Australia (UniSA) animal ethics committee and carried out at the Core Animal Facility (CAF) in keeping with the Australian Code of Practice for the Care and Use of Animals for Scientific Purposes. Specific ethics approval information is included in the respective chapters.

Mice were group caged upon arrival and allowed to acclimatise for 7 days before the commencement of the trials. Upon commencement, the mice were single housed in individually ventilated cages (IVC) in the infectious suite at the CAF. Food (Meat Free Rat and Mouse Diet (SF00-100), Western Australia) and water were provided ad libitum, and the mice were on a 12-hour day cycle with red lighting being utilised between 7pm and 7am. The mice were also provided with physical enrichment including animal hides and paper bedding.

2.3.2. Anaesthetic Protocols

All animals were wounded under general anaesthesia on heat pads to maintain core body temperature. Mice were administered Buprenorphine (Temgesic) via subcutaneous injection (MSD, Macquarie Park, NSW, Australia) 30 minutes prior to wounding, and 6-8 hours post-wounding. Additional analgesic was administered via subcutaneous injection as needed based on signs of distress or discomfort, or more than 10% weight loss.

Anaesthesia was induced by 4% isoflurane (Abbott Australasia, Macquarie Parl, NSW, Australia) mixed with oxygen (1-4 L/min), and anaesthesia maintained with 2-3% isoflurane mixed with oxygen (0.4 L/min). Surgical anaesthetic depth was confirmed by the absence of the pedal reflex.

2.3.3. Daily Monitoring

All mice were monitored daily, and details recorded on approved Clinical Record Sheets (CRS). The daily monitoring involved weighing the mice and checking for signs of pain or distress. The main signs of pain and distress include a reluctance to move, hunching, grimace, a ruffled coat, abnormal breathing, sunken eyes, skin tenting (dehydration), and injury. Each of these signs is a score of 1; a score of 2 or more resulted in additional checks and notifying the UniVets. Additional Buprenorphine would be administered under advice from the UniVet based on these observations. Weight loss is a crucial indicator of distress. Exceeding 10% weight loss would result in an additional Buprenorphine administration, with a humane endpoint of 15% weight loss.

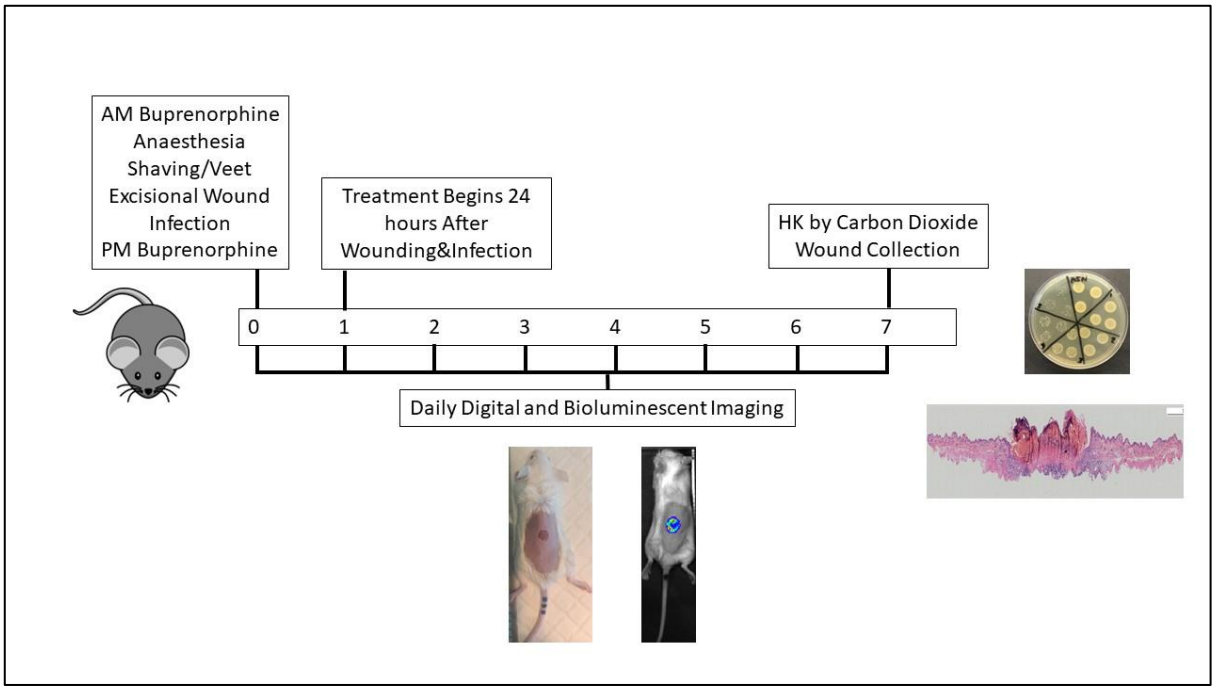

Figure 2.1. The general timeline for the infected excisional wound model.

2.3.4. Wounding

Under anaesthesia, the backs of the mice were shaved and treated with Veet Hair Removal Cream Sensitive (Veet, commercially available) to remove the hair. The skin was then washed with water and sterilised with ethanol. Full thickness excisional wounds were created on the backs, one wound per mouse, using a biopsy punch (AcuPunch, Bydand Medical, NSW, Australia) to create an imprint, and curved surgical scissors and forceps to cut out the skin. A digital photo of the wound was then taken for macroscopic measurements, with a ruler visible in the photograph in order to calibrate measurements.

2.3.5. Wound Infection

The bioluminescent strain of *S. aureus* (ATCC12600; Xen29) (PerkinElmer, UK) used, possesses a copy of the *Photorhabdus luminescens* lux operon "luxABCDE" on the bacterial chromosome which encodes genes to produce luminescent proteins by metabolically active bacteria. This operon was inserted at a single integration site. This *S. aureus* strain was derived from the parental strain *S. aureus* 12600, a pleural fluid isolate. *The* use of genetically modified bacteria was approved by the UniSA Institutional Biosafety Committee (IBC) under application IBC#0286.

A single colony of bioluminescent *S. aureus* was grown in TSB supplemented with kanamycin for 24 hours prior to the trial on a shaking platform at 37°C. The morning of use, the bacteria level was measured using a spectrophotometer at 660 nm to determine the optical density (OD). An OD of 0.5 equates to 5 $x10^8$ CFUs. The bacteria were centrifuged at 4,500 x g for 10 minutes and washed in PBS. The bacteria were resuspended in PBS at 5 x 10^9 CFUs/mL and transported to the CAF.

Immediately after wounding, 10 µL of the bioluminescent *S. aureus* (5 x 10^7 CFUs) was pipetted onto the wound. Mice were imaged using a IVIS Lumina S5 Imaging System (Perkin Elmer, Massachusetts, USA) to measure infection. Both digital and IVIS photos were taken daily while the mice were under anaesthesia. The infected wounds were left uncovered for the entirety of the trial.

2.3.6. Wound Collection

At the conclusion of the trial, the mice were humanely killed by carbon dioxide and the wounds were collected by cutting through the skin approximately 1 cm around the wound down to the fascia. For wounds that were adhered to the spine, the sample was carefully dissected to separate the spine from the tissue above. For all trials, the wound was bisected across the animal's spine and half of the wound was collected for histological analysis by preserving the tissue samples in 10% neutral buffered Formalin for 24 hours followed by 70% ethanol for a minimum of 24 hours before further processing. Unwounded tissue was removed from the remaining wound half and transferred to PBS for CFU counts.

2.3.7. Bacterial Colony Forming Units (CFUs)

Wound tissues were collected in pre-weighed Eppendorf tubes containing 200 µL PBS, and weighed again after tissue collection. The samples were vortexed for 2 minutes, and sonicated for 2 minutes, for three cycles. The solution was then serially diluted 10-fold in a 96-well plate. On TSB with kanamycin plates, 3 x 20 µL of each dilution were spotted. The plates were then incubated overnight at 37°C and the colonies counted. The number of bacteria were then calculated using the following equation;

$$\text{CFU/mg} = \text{DF} \times \text{Average Count} \times 10/\text{Weight Change (mg)}.$$

2.4. Wound Analysis

2.4.1. Macroscopic Measurements

Macroscopic area and gape of the wounds were measured daily from time of surgery to the experimental endpoint. The wounds were measured by taking a photo of the wounded mouse next to a ruler, and measuring the area and gape, as in Figure 2.2, using Image Pro Plus (Media Cybernetics Inc, Bethesda, MD, USA). Using this program, the measurements were calibrated using the ruler in the photo. The data is presented as a percentage of the original wound on the day of treatment (Day 1).

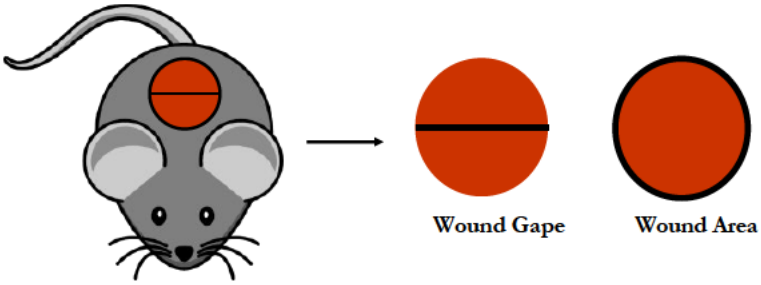

Figure 2.2. The macroscopic wound area and wound gape measurements. The wound gape is always measured across the spine, approximately halfway through the wound.

2.4.2. IVIS Analysis

The bacterial burden was quantified daily in real time following measurement of the radiance and analysis of the total flux using the IVIS Lumina S5 Imaging System (Perkin Elmer, Massachusetts, USA) as in Figure 2.3. The images were analysed by measuring the bioluminescence of a drawn region of interest (ROI), and the total flux (photons/second) quantified. The presented quantified data is normalised to the day of treatment – Day 1. Representative images were normalised to the same scale bar at the conclusion of the study.

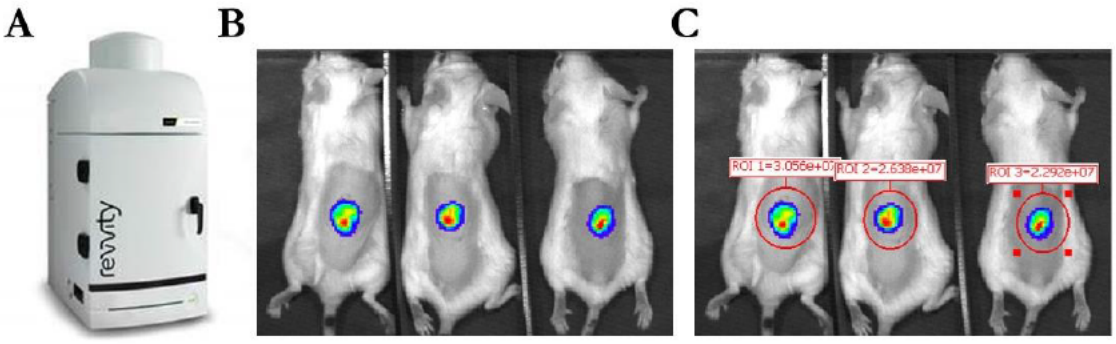

Figure 2.3. The IVIS Lumina S5 Imaging System measuring bioluminescence to monitor infection. (A) The IVIS Lumina S5 Imaging System **(B)** A representative photo of wounds infected with bioluminescent *S. aureus* **(C)** The same photo with regions of interest (ROI) drawn around the wounds.

2.4.3. Tissue Fixation and Processing

Wound samples were processed overnight using an Excelsior TM AS Tissue Processor (Thermo Fisher Scientific, Massachusetts, USA) as in Table 2.1. The samples were dehydrated through a series of ethanol solutions, cleared in xylene, and fixed with paraffin wax. Samples were embedded in paraffin, trimmed, cut into 4 µm section with a microtome (Leica Microsystems, Macquarie Park, Australia) and transferred onto microscope slides. Standard glass microscope slides (Paul Marienfeld GmBH & Co. Laude-Konigshofen, Germany) were used for haematoxylin and eosin staining, positively charged Histobond slides (Hurst Scientific, WA, Australia) were used for immunohistochemistry. Slides were dried in the oven at 50°C overnight.

Table 2.1. The overnight processing protocol for paraffin tissue preservation.

Step	Reagent	Temperature (°C)	Time
1	70% Ethanol	Room Temperature	20 minutes
2	70% Ethanol	Room Temperature	60 minutes
3	80% Ethanol	30	30 minutes
4	80% Ethanol	30	30 minutes
5	90% Ethanol	30	30 minutes
6	90% Ethanol	30	30 minutes
7	100% Ethanol	30	30 minutes
8	100% Ethanol	30	60 minutes
9	Xylene	30	30 minutes
10	Xylene	30	30 minutes
11	Xylene	30	120 minutes
12	Paraffin Wax	60	120 minutes
13	Paraffin Wax	60	120 minutes
14	Paraffin Wax	60	120 minutes

2.4.4. Histological Staining

Wound samples were stained with haematoxylin and eosin as in Table 2.2. Sections underwent two changes of xylene at 2 minutes each to remove the paraffin wax. The sections were then rehydrated through a series of ethanol changes of decreasing concentrations. Sections were then stained with Lillie Mayer's Haematoxylin (Australian Biostain, Traralgon, VIC, Australia) for 5 minutes and rinsed in tap water again. The sections were dipped in 0.25% acid alcohol eight times and washed in running tap water. The sections were blued in a 5% bicarbonate solution for 1 minute and stained with alcoholic eosin with phloxine for 2 minutes, with washes in running tap water in between. The sections were dehydrated through a series of ethanol changes of increasing concentrations before two two-minute changes of xylene. The slides were mounted with ClearVue Mountant XYL (Thermofisher Scientific, Scoresby, VIC, Australia), cover slipped and left to air dry overnight. All samples were imaged using an Olympus IX83 Fluorescence Microscope (Olympus, Tokyo, Japan).

Table 2.2. The haematoxylin and eosin staining protocol.

Step	Stain	Time	Repeats
1	Xylene	2 minutes	x 2
2	Absolute Ethanol	2 minutes	x 2
3	70% Ethanol	2 minutes	x 1
4	30% Ethanol	2 minutes	x 1
5	Tap Water	4 minutes	x 1
6	Lillie-Mayer's Haematoxylin	5 minutes	x 1
9	Running Tap Water	Rinse	x 1
10	0.25% Acid Alcohol	8 dips	x 1
11	Running Tap Water	Drain Quickly	x 1
12	5% Bicarbonate Solution	1 minute	x 1
13	Running Tap Water	Rinse	x 1
14	Alcoholic Eosin w. Phloxine	2 minutes	x 1
15	Running Tap Water	Drain Quickly	x 1
16	70% Ethanol	5-6 dips	x 1
17	Absolute Ethanol	6-8 dips	x 2
18	Xylene	2 minutes	x 2
19	Xylene	Hold	

2.4.5. Microscopic Measurements

The microscopic measurements of the wounds were performed on the images of the H&E-stained wound samples in Image Pro Plus (Media Cybernetics Inc., Bethesda, MD, USA) as in Figure 2.4. The wound length, dermal gape and re-epithelialisation were measured. The wound length was measured as the bottom of the epidermis along the dermal-epidermal junction, between the appearance of the first hair follicle on either side of the wound. The dermal gape was measured as a straight line across the dermal-epidermal junction as in Figure 2.4. The percentage of re-epithelialisation was determined by measuring the epithelial tongues, from the first hair follicle to the edge of the wound (Figure 2.4), and calculating the percentage of the total wound length they cover. The average epidermal thickness was measured by measuring along both the top and bottom of the epidermis along the total wound length and calculating the average distance between these two lines using ImagePro Plus.

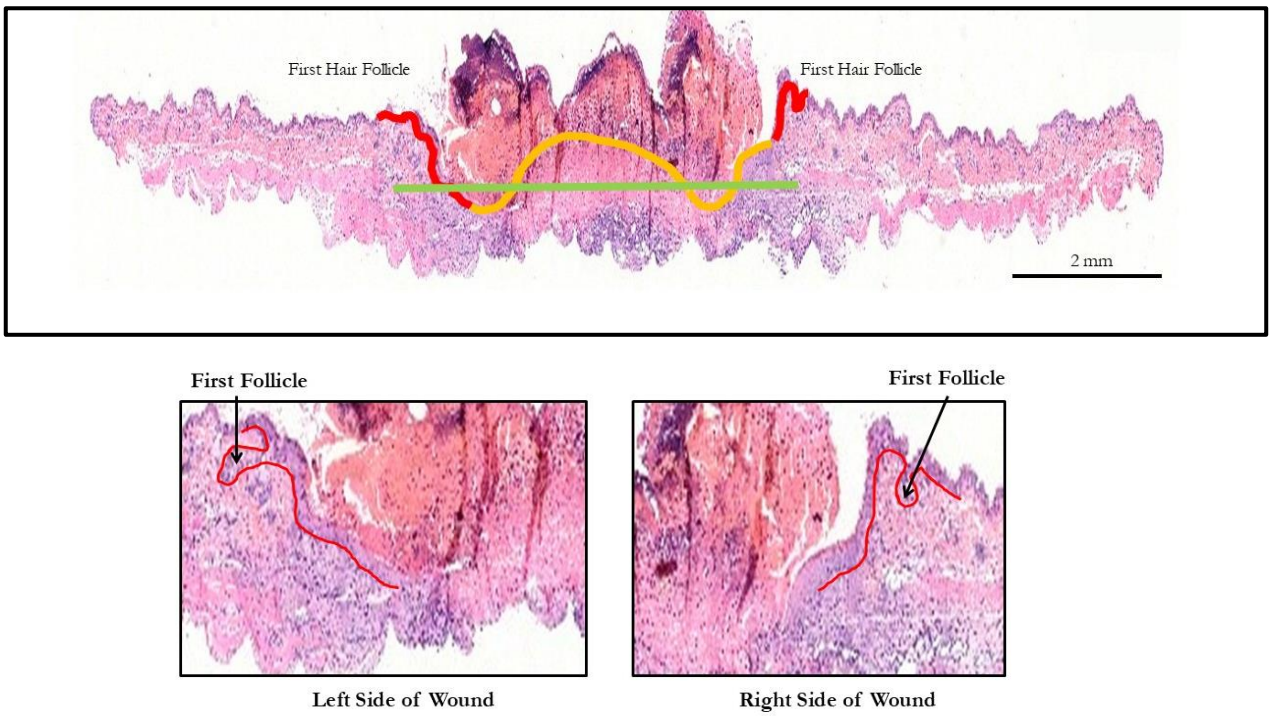

Figure 2.4. The microscopic wound measurements on haematoxylin and eosin (H&E)-stained wound samples. Top: Full wound sample. The red sections represent the epithelial tongues, the orange represents the length of the wound gape, and the green represents the dermal gape. The red and orange sections represent the total wound length. Bottom: Epithelial tongues from the above image to highlight the follicles and the epidermis in the measurements.

2.4.6. Masson's Trichrome Staining

The total collagen of the wound samples was visualised (i.e. stained green) using Masson's Total Collagen Trichrome Staining as in Table 2.3. The samples were de-paraffinised through 2 changes of xylene and rehydrated through a series of ethanol changes of decreasing concentrations. The samples were then fixed in Bouin's solution (Sigma Aldrich, Castle Hill, Australia) at 60°C for 30 minutes. After rinsing with tap water, the samples were stained with celestine blue (Sigma Aldrich, Castle Hill, Australia) for 3 minutes, before being rinsed with tap water again. Next, the samples were stained with Lillie Mayer's Haematoxylin for 3 minutes, rinsed with tap water, blued for 15 seconds in 5% bicarbonate solution, and rinsed again. The samples were then stained with fuchsin ponceau for 5 minutes, rinsed with MilliQ water, then submerged in 5% phosphotungstic acid (Sigma Aldrich, Castle Hill, Australia), then light green for 3 minutes.

One by one, the slides were quickly dipped once in acetic acid, and once in MilliQ water. The slides were then blotted with filter paper before being placed into a rack to air dry. Once the slides were dry, the slides underwent 2 x 2-minute xylene changes. The samples were mounted with ClearVue Mountant XYL, cover slipped, and left to air dry overnight. The samples were imaged using an Olympus IX83 Fluorescence Microscope (Olympus, Tokyo, Japan), with wounded skin measured in the wound bed, and unwounded skin measured on the edges of the sample either side of the wound bed.

For quantitative morphometric analysis, the trichrome slides were captured as an RGB image which was subsequently analyzed using Image J (version 1.32j) software (National Institutes of Health, USA http://rsb.info.nih.gov/ij/). The amount of fibrosis was then estimated from the RGB images with a macro written by Kennedy et al., 2006 [249] by converting pixels of the image with substantially greater (> 120%) blue than red intensity to have the new, grey scale amplitude = 1, leaving other pixels as with amplitude = 0.

Macro as follows;

- run("Brightness/Contrast..."); ***set brightness and contrast to automatic***
- run("RGB Stack"); ***convert RGB image to a stack***
- run("Convert Stack to Images"); ***split stack to three images, Red, Blue and Green***
- run("Image Calculator...", "image1=Blue operation=Divide image2=Red create 32 bit"); ***divide blue by red***
- run("Brightness/Contrast..."); ***set brightness and contrast to automatic***
- run("Subtract...", "value=1.2"); ***discard all image where blue intensity is not 120% of red intensity***
- run("Multiply...", "value=10000000"); ***convert all decimal values to integers***
- run("Brightness/Contrast..."); ***set brightness and contrast to automatic***
- run("Max...", "value=1"); ***set max value to be 1***
- run("Min...", "value=0"); ***set min value to be 0***
- run("Measure"); ***add up 1s and express as fraction of total area***

Table 2.3. The Masson's Trichrome Total Collagen Stain Protocol.

Step	Stain	Time	Repeats
1	Xylene	2 minutes	x 2
2	Absolute Ethanol	2 minutes	x 2
3	70% Ethanol	2 minutes	x 1
4	30% Ethanol	2 minutes	x 1
5	Tap Water	4 minutes	x 1
6	Bouin's Solution	30 minutes	x 1
7	Tap Water	Rinse	x 1
8	Celestine Blue	3 minutes	x 1
9	Rinse in Tap Water	Rinse	x 1
10	Lillie Mayer's Haematoxylin	3 minutes	x 1
11	Rinse in Tap Water	Rinse	x 1
12	5% Bicarb Solution	15 seconds	x 1
13	Fuchsin Ponceau	5 minutes	x 1
14	Rinse in MilliQ Water	Rinse	x 1
15	Phosphotungstic Acid	10 minutes	x 1
16	Light Green	3 minutes	x 1
17	Acetic Acid	Quick Dip	x 1
18	MilliQ Water	Quick Dip	x 1
19	Blot, Rack and Air Dry		x 1
20	Xylene	2 minutes	x 1
21	Xylene	Hold	x 1

2.4.7. Immunohistochemistry (IHC)

The wound samples were subjected to fluorescent IHC analysis as in Table 2.4. Samples were deparaffinised in Xylene twice for 5 minutes each and then rehydrated through a series of ethanol changes of decreasing concentrations before being rinsed in water and then PBS. Antigen retrieval was performed by submerging the slides in a target retrieval solution (TRS) and placing the slides into a decloaker (Biocare Medicare, USA) and heated to 90°C for 10 minutes and then cooled to 50°C. Enzyme digestions was performed with a PBS wash and then an incubation in 250 mL PBS with 0.0625 g trypsin for 3 minutes before being rinsed in PBS again. The samples were then blocked with 3% normal goat serum (NGS) for 45 minutes and washed three times with PBS, 2 minutes each. The primary antibody incubation was performed with the antibodies in Table 2.5 overnight at 4°C with 3% NGS in a dark, moist environment. After another PBS wash, the secondary antibody incubation, see Table 2.5, was performed in PBS for 1 hour at room temperature, in a dark moist environment. The samples were washed with PBS once more, before being incubated with DAPI (1:5000; 1 mg/mL stock) for 3 minutes in the dark. After a final PBS wash, the slides were mounted with Fluorescence Mounting Medium (Agilent Technologies Australia, Mulgrave, Australia), cover slipped and stored at 4°C in the dark. All slides were imaged using an Olympus IX83 Fluorescence Microscope (Olympus, Tokyo, Japan) and immunohistochemical quantification performed using CellSens (Olympus Life Science, Australia). The fluorescence was measured in the wound bed, with the wound defined as between the first hair follicle on either side and excluding the scab and muscle. For the analysis of neutrophils, macrophages, and proliferating cell nuclear antigen (PCNA) cell counts were performed, while a mask was used to quantify Flightless I expression as the mean grey intensity. All measurements were taken in the wound bed. Minimum thresholds were consistent between samples of the same study.

Table 2.4. The immunohistochemistry (IHC) protocol.

Step	Stain	Time	Repeat
1	Xylene	5 minutes	x2
2	Absolute Ethanol	2 minutes	x2
3	70% Ethanol	2 minutes	x1
4	30% Ethanol	2 minutes	x1
5	Water	Rinse	x1
6	PBS	2 minutes	x3
7	Antigen Retrieval	10 minutes	x1
8	PBS	2 minutes	x3
9	Enzyme Digestion	3 minutes	x1
10	PBS	2 minutes	x3
11	Blocking	45 minutes	x1
12	PBS	2 minutes	x3
13	Primary Antibody	Overnight	x1
14	PBS	2 minutes	x3
15	Secondary Antibody	60 minutes	x1
16	PBS	2 minutes	x3
17	DAPI	3 minutes	x1
18	PBS	2 minutes	x3
19	Fluorescent Mounting Media and Coverslip		x1

Table 2.5. The primary and secondary antibodies used for immunohistochemistry (IHC).

Target	Primary Antibody			Secondary Antibody		
	Antibody	Supplier	Working Concentration	Antibody	Supplier	Working Concentration
Macrophages	Rat anti-F4/80 #MCA497R	Bio-Rad Laboratories	5 μg/mL	Alexa Fluor goat anti-rat 488 #A11006	Invitrogen	5 μg/mL
M2 Macrophages	Rabbit anti-YM-1 #60130	Stem Cell Technologies	0.37 μg/mL	Alexa Fluor goat anti-rabbit 633 #A31577	Invitrogen	5 μg/mL
PCNA	Mouse anti-PCNA #sc-56	Santa Cruz Biotechnology	1 μg/mL	Alexa Fluor goat anti-mouse 568 #A11004	Invitrogen	5 μg/mL
Flightless I	Mouse anti-Flii (1A6)	AbRegen	10 μg/mL	Alexa Fluor goat anti-mouse 568 #A11004	Invitrogen	5 μg/mL
Neutrophils	Rat anti-NIMP-14 #sc-59338	Santa Cruz Biotechnology	0.5 μg/mL	Alexa Fluor goat anti-rat 488 #A11006	Invitrogen	5 μg/mL

2.5. General Techniques

2.5.1. Cell Culture

Commercially available cryopreserved vials of human keratinocytes (HaCaTs; CLS Cell Lines Service, 300493) and human fibroblasts (HFFs; HFF-1, ATCC® SCRC1041™) were purchased and stored in liquid nitrogen. Cryopreserved vials were defrosted in a 37˚C water bath for 2 minutes, cells pelleted, washed, and incubated in cell culture media in a T75 tissue culture flask (Corning, New York, USA) at 37°C with 5% CO_2 in an incubator (Thermo Fisher Scientific, Scoresby, VIC, Australia) at a seeding density of $5x10^6$ cells/T75 flask. The following day, the adhered cells were washed with room temperature, sterile PBS and replaced with fresh cell culture media. The cells were cultured until 80% confluent, with a media change every 2-3 days. To subculture, the cells were washed with PBS, incubated with 1 mL sterile trypsin-EDTA at 37°C, and then gently tapped until the cells become dislodged as seen under microscope. The trypsin was neutralised with 10 mL cell culture media and the entire suspension centrifuged for 5 minutes at 360 x g to form a pellet. The pellet was resuspended in fresh, warmed cell culture media, counted via haemocytometer and seeded either in a flask for culturing or plates for cellular assays.

2.5.2. Cytotoxicity Assay

In a sterile 96-well plate, 1×10^4 cells/well were incubated at 37˚C for 24 hours in culture media. The media was removed and replaced with the treatments in complete culture media at a volume of 200 µL and incubated at 37°C for 24 hours. After 24 hours, the media was removed, and the cells washed with DPBS. To each well, 100 µL Resazurin solution was added to each well and incubated for 2 hours at 37˚C. The fluorescence intensity was then measured using a FLUOstar OPTIMA plate reader (BMG LabTech, Melbourne, Australia) at 495 nm and 535 nm, and normalised to media only controls.

2.5.3. Proliferation Assay

In a sterile 96-well plate, 5 x 10^3 cells/well were incubated at 37°C for 24 hours in culture media. The media was replaced with serum-free media and incubated at 37°C for 6 hours. The media was removed and replaced with the treatments in complete culture media at a volume of 200 µL and incubated at 37°C for 24 hours. Following the incubation, 10 µL WST-1 was added to each well and incubated at 37°C for two hours. The fluorescence intensity was measured using a FLUOstar OPTIMA plate reader (BMG LabTech, Melbourne, Australia) at 450 nm and 650 nm, and normalised to media only controls.

2.5.4. Migration Assay

In a sterile 96-well plate, 2 x 10^4 cells/well were incubated in cell culture media at 37˚C for 24 hours or until confluent. Scratch wounds were made in each well using a Wound Maker (Essen Bioscience, Michigan, USA). The media was removed, and the cells washed with PBS, then the treatments added in serum free media at a volume of 200 µL. The plate was then placed into the Incucyte Imager IncuCyte (Essen BioScience, Michigan, USA) where an image was taken every 3 hours for 48 hours or until the control wounds closed.

2.6. Statistical Analysis

All statistical analysis was performed in GraphPad Prism (GraphPad, California, USA). For all statistical analyses, any p value <0.05 was considered significant. Graphical representation of significance: * = $p < 0.05$, ** = $p < 0.01$, *** = $p < 0.001$, **** = $p > 0.0001$. All *in vitro* data is displayed as mean ± SEM, while *in vivo* data is displayed as mean ± SD.

A one-way ANOVA was used to test significance between multiple groups, a two way ANOVA to test the significance between multiple groups over time. For data with missing values, a mixed effects analysis was used instead of a two way ANOVA.

Three different post hoc tests were utilised throughout these studies. Tukey's Multiple Comparisons test was used to compare all means with each other. Dunnett's Multiple Comparisons test was used to compare the means to a designated control. Sidak's Multiple Comparisons test was used to check specific means for statistical significance.

For figures with statistical significance, the statistical and post hoc tests are specified in the figure legend. All statistical analyses are specified below:

One-way ANOVA and Tukey's Multiple Comparisons Test: Figures 3.5, 3.7.C, 3.8, 3.9, 3.10, 3.11, 4.5.B, 4.9, 4.10, 4.11, 4.12, 4.14.C, 5.6.B and C, 5.11, 5.12, 5.13, 5.15.C.

One-way ANOVA and Dunnett's Multiple Comparisons Test: Figures 4.5.A and 5.6.C and D.

Two-way ANOVA and Tukey's Multiple Comparisons Test: Figure 3.2, 3.6, 4.8, 4.14.B, 5.4, 5.7, 5.8, 5.10, 5.15.B.

Two-way ANOVA and Sidak's Multiple Comparisons Test: Figures 3.4, 3.7, 4.7, 4.13, 4.15, 5.14.

Two-way ANOVA and Dunnett's Multiple Comparisons Test: Figures 3.7 and 4.6.

Mixed-Effects Analysis and Tukey's Multiple Comparisons Test: Figures 3.3.B and 5.11.

Mixed-Effects Analysis and Dunnett's Multiple Comparisons Test: Figure 3.3.A.

Chapter Three – Neutralising Flightless I in a Diabetic Infected Excisional Wound Model

3.1. Background

An alternative approach to clearing infection directly in order to treat infected wounds is to develop treatments that focus on stimulating wound healing so the body's immune system can better clear the infection and heal the wound. One protein that has been identified as a regulator of wound healing is Flightless I (Flii). Flii is expressed by fibroblasts, keratinocytes, macrophages and neutrophils, and is upregulated in response to wounding [132, 136]. High levels of Flii are found in chronic wounds, diabetic wounds, and burns, and over-expression of Flii has been shown to impair healing [136, 138, 140, 146]. Flii is considered to be important in the inflammatory phase but detrimental to the proliferative and remodelling phases [132]. Neutralising Flii activity with an antibody (FnAb) improves wound healing and reduces scarring in both murine [136, 142, 145, 146] and porcine wound models [153]. Therefore, FnAb is now being explored as a therapeutic approach for improving wound healing.

Previously, in a murine STZ-model of type I diabetes, FnAb intradermally injected into excisional wounds resulted in improved wound closure and increased angiogenesis [136]. Chronic, non-healing wounds are known to contain high levels of proteases. This increase in protease activity along with an altered pH, creates a hostile environment such that therapies like monoclonal antibodies are prone to degradation and thereby are predicted to have reduced efficacy [69, 70, 145]. To protect the antibodies from the hostile conditions of human chronic diabetic wounds, approaches have been developed to encapsulate and deliver using porous silicon nanoparticles (pSiNPs). pSiNPs additionally allow for a slow, prolonged release of treatment, thereby assisting FnAb to better capture the therapeutic window [154].

Previous studies have shown that pSiNPs are able to be loaded with clinically relevant concentrations of FnAb in a process that is highly reproducible and upscaleable [145]. Previously, pSiNPs at 161 ± 58 nm in size with a pore size of 33 ± 7 nm were generated to assess their delivery of FnAb in diabetic wounds. For the loading, 268 ± 35 µg FnAb were loaded per mg of pSiNPs. 93% of the FnAb was released after 14 days and the antibody retained its functionality. pSiNPs have shown intact and functional FnAb release for up to 7 days post-treatment when exposed to proteases, while the FnAb alone was completely degraded. *In vitro*, FnAb pSiNPs have been shown to increase the proliferation and migration of keratinocytes by 25% compared to the unloaded pSiNPs. A single dose of FnAb

pSiNPs injected intradermally into murine incisional wounds resulted in improved wound closure compared to non-specific mIgG pSiNPs at Day 6, supporting the ability of FnAb to retain functionality and effective release in a wound environment. In a STZ-model of diabetes, where increased protease load is established [123], FnAb pSiNPs intradermally injected into excisional wounds resulted in wound closure two days earlier than the unloaded pSiNPs. Critically, FnAb pSiNPs-treated wounds were 30% smaller at Day 7 than the wounds treated with FnAb alone [145]. This result supports pSiNPs as a clinically useful delivery tool to deliver functional FnAb to hostile wounds.

Chronic wounds are often infected with bacteria which not only increases the hostility of the wound environment, but also includes an additional protease burden [70, 71]. In this chapter, the capacity of pSiNPs to effectively deliver healing promoting FnAbs to diabetic wounds with the additional burden of wound infection was assessed as this is more reflective of a real world wound situation. It was hypothesised that improved healing may indirectly contribute to infection reduction. To explore this, FnAb-loaded pSiNPs were tested using diabetic excisional wound healing in the presence of infection.

3.2. Methods

3.2.1. Fabrication of Porous Silicon Nanoparticles (pSiNPs)

The pSiNPs were generated and optimised by Parham Sahandi-Zangabad and Nico Voelcker from Monash University as previously described [145], with the specific conditions selected to allow for both particle and pore size to be optimised for effective FnAb loading and release. Briefly, highly boron-doped porous silicon (pSi) wafers were anodised using 3% hydrofluoric acid:ethanol (HF:EtOH) solution and a two-step cycle consisting of a current density of 50 mA cm^{-2} for 7.3 seconds and 400 50 mA cm^{-2} for 0.4 seconds repeated for 1 hour. The etched layer was then removed from the Si substrate using electropolishing and a 1:2 HF:EtOH solution.

3.2.2. Thermal Oxidation Functionalisation of Porous Silicon Nanoparticles

The pSiNPs were functionalised to maximise loading and functional release of FnAb. Thermal oxidation at 200°C was selected as being the optimal conditions required for the loading and release of FnAb. Freshly etched pSi films placed into a quartz tube which was then placed into a Labec horizontal tube furnace where it was heated to 200°C (heating rate of 20°C/min) for 2 hours to form a SiO layer on the surface. The pSi was then slowly cooled to room temperature before removing from the furnace and sonicating in absolute ethanol.

Both the nanoparticle size and the size of the pore diameter were determined using transmission electron microscopy (TEM) (JEOL JEM-2100F) equipped with a field emission gun, operating at 200 kV. The samples were prepared by dispersing pSiNPs in ethanol (100 µg/mL). The samples were ten spotted (10 µL) onto 300-mesh copper grids and dried under nitrogen flow at room temperature. Measurements were then performed on 20 randomly selected particles using ImageJ software. This process formed nanoparticles 149 ± 25 nm in size with a pore diameter of 33 ± 7 nm.

3.2.3. Formulation of FnAb pSiNPs

FnAb was mixed with pSiNPs at a ratio of 1:10 (10 mg pSi with 1 mg FnAb – 1 mg/mL stock) and incubated at 4°C for 16 hours. The solution was then centrifuged three times for 10 minutes, with PBS washes to remove unbound FnAb. FnAb in the incubation buffer and wash samples was assessed by UV Vis (nanodrop) and compared to the unloaded FnAb stock to allow measure of the loading efficiency. Repeated load experiments (n>3) demonstrated a loading efficiency of >95%. The formula used to calculate the loading efficiency is as below;

$$M_1 = M_{stock} - M_{totalspnt}$$

$$\text{Loading Capacity} = M_1/M_{pSiNPs}$$

$$\text{Loading Efficiency (\%)} = M_1/M_{stock} \times 100$$

M_{stock} = amount of FnAb used in loading solution (µg)
$M_{totalspnt}$ = total amount of FnAb (µg) remaining in the supernatant
M_{pSiNPs} = mass of the pSiNPs used (µg)

3.2.4. The FnAb pSiNP Animal Trial

A 36 diabetic mice animal trial was conducted to test the efficacy of FnAb pSiNPs in an infected excisional diabetic wound model (Figure 3.1). The infected excisional wound model was utilised as previously described in Chapter Two (2.3), with 10 mm wounds created. The nails were trimmed at the time of surgery to limit scratching, and soaked food was provided daily due to the heavier burden placed on the mice by the diabetes. This animal trial was approved by the UniSA animal ethics committee and carried out at the core animal facility (CAF), UniSA. The animal ethics number for this animal trial is U11/22. The mice were obtained from Ozgene (Perth, Australia) and consisted of all male balb/c mice aged 8-11 weeks.

Following acclimatisation, the mice began the six-week process of diabetes induction through the streptozotocin (STZ) method. Mice were injected with STZ (50 mg/kg) daily for five consecutive days and then monitored daily for the next five weeks [123]. STZ damages the pancreas which causes impaired insulin secretion and an inability to control blood

glucose levels. This leads to increased urination, elevated thirst and impaired thermoregulation. After the final STZ injection, the blood glucose levels (BGLs) of the mice were tested at two, three, and five weeks post-injection. The mice need to have had a diabetes long enough to have developed a delayed wound healing phenotype and an elevated protease load [136, 145, 250, 251]. Blood Glucose Levels (BGLs) of >15 mM for at least two weeks is required for each mouse to be classified as diabetic. BGLs were monitored using a tail vein prick, glucose strips and a glucometer. Combination insulin (NovoMix 30 Penfill, Australia; 100U/mL; 0.5 – 1 units) was administered subcutaneously using a 31G needle based on weight loss exceeding more than 10%. Insulin was administered in the afternoon to avoid hyperglycaemia. Weight loss is more pronounced in this chronic disease state and the humane endpoint based on weight was changed to 20% to reflect this. 36 mice underwent the process of diabetes induction, however, one mouse died before the beginning of the trial, leaving 35 mice remaining. The mice were divided amongst five treatment groups to allow for equitable distribution of BGLs. Power calculations determined that a sample size of 8 mice per group will provide 97% power at the 5% level of significance to demonstrate an average reduction of 5 mm in wound size between groups with a standard deviation of 2.3, using an unpaired Student's t test. These power calculations were based on a reduction of 20% in wound size which is considered biologically significant.

The treatment groups included three pSiNPs treatments; FnAb delivered in pSiNPs (FnAb pSiNPs), pSiNPs alone (pSiNPs), and a non-specific antibody control delivered in pSiNPs (mIgG pSiNPs). Two additional treatment groups included FnAb and Saline, each delivered alone. All treatment groups were the equivalent of 200 µg FnAb and/or 2 mg pSiNPs per wound.

The mice were treated once on Day 1 of the study, 24 hours after wounding and infection. Treatments consisted of 4 intradermal injections around the wound of 50 µL each. The treatments were made up in saline. The mice were humanely killed on Day 14 and the wounds excised. Half the wounds were used for histology, one quarter for CFUs, and one quarter snap frozen in liquid nitrogen and stored at -80°C.

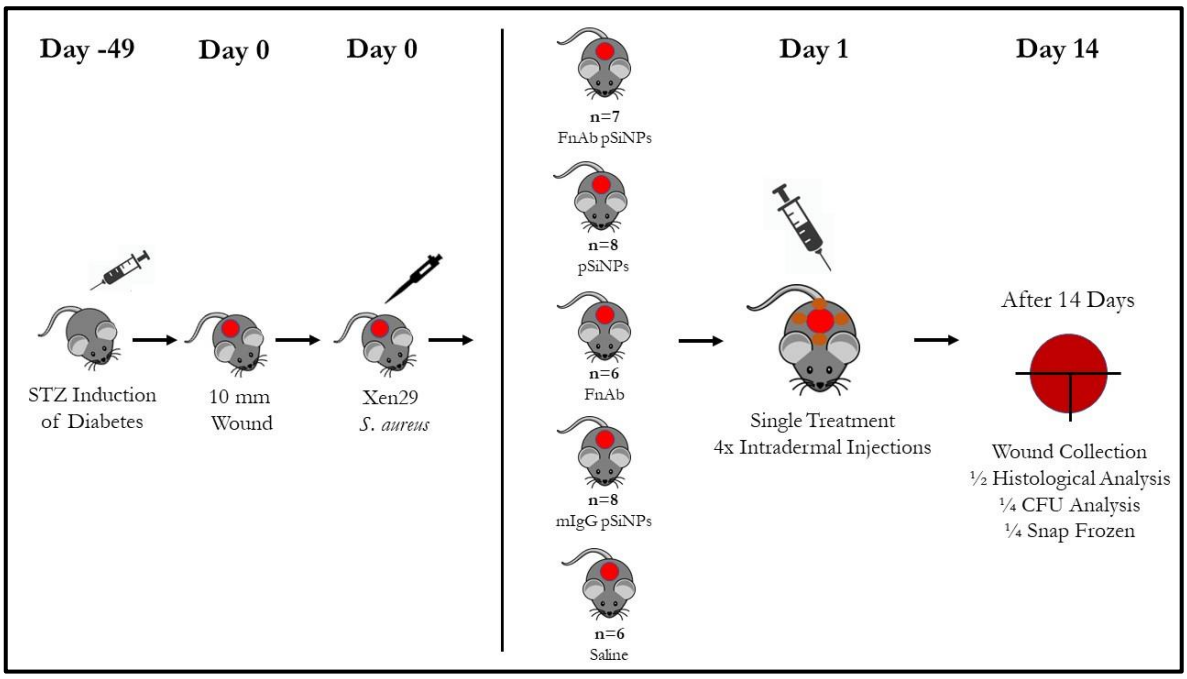

Figure 3.1. A schematic representation of the treatment groups used for the infected diabetic excisional wound model used in the Flightless I trial.

3.2.5. Investigation of pSiNPs Auto-luminescence

To investigate the potential auto-luminescence of pSiNPs, pSiNPs were administered to two mice posthumously and imaged using the IVIS Lumina S5 Imaging System (Perkin Elmer, Massachusetts, USA). Two humanely killed mice were obtained as UniSA AEC scavenged tissue notification as per the Australian Code for Care and Use of Animals for Scientific Purposes. The humanely killed ARC mice (8 weeks old) were shaved, hair removed by Veet, and four 10 mm full thickness excisional wounds created on the dorsum of each mouse. Each wound was treated with one of four pSiNP/PBS preparations; topical application of pSiNPs, intradermal (ID) injection of pSiNPs, topical application of PBS, and intradermal injection of PBS. Intradermal injections were performed with a 25G needle. The pSiNPs were prepared fresh at 10 mg/mL in saline. Each injection was 50 µL. The mice were imaged for bioluminescence using the IVIS, as in 2.5.2, and digital images taken. Intradermally injected pSiNPs and a sample of healthy skin tissue were collected in 10% formalin where it was fixed for 24 hours before being transferred to 100% ethanol. The tissue samples were processed as in 2.4.3 and stained as in 2.4.4.

3.3. Results

3.3.1. Neutralising FnAb did not improve the rate of wound healing in the presence of infection.

To investigate the efficacy of delivering FnAb in pSiNPs compared to FnAb alone in infected diabetic wounds on both wound healing and infection, excisional wounds were created in STZ-induced diabetic mice and then infected with bioluminescent *S. aureus* (ATCC12600; Xen 29). A single treatment of FnAb-pSiNPs, FnAb, mIgG pSiNPs, pSiNPs, and saline was administered by intradermal injection on Day 1 post-injury/infection and healing monitored for a total of 14 days. All treatment groups were the equivalent of 200 µg FnAb and/or 2 mg pSiNPs per wound

All mice started with no statistical differences between the treatment groups for the wound gape or wound area. There were significant differences between Day 0 and Day 1 infected wound size prior to treatment commencing at Day 1 post-injury (Figure 3.2), and since treatment occurred on Day 1, data was subsequently normalised to Day 1.

Macroscopic wound measurements were taken daily, starting immediately after surgery (Figure 3.3 and Figure 3.4). The wound area of the pSiNPs treatment groups (Figure 3.3.A) decreased steadily over the 14-day trial though no significance was found between the FnAb-pSiNPs and the control groups for either the wound gape (Figure 3.3.B) or the wound area (Figure 3.3.C). The mIgG pSiNPs performed significantly worse than the pSiNPs on Days 2, 3 and 4 for the wound gape (Figure 3.3.B) and Days 3 and 4 for the wound area (Figure 3.3.C). Overall, FnAb pSiNPs did not improve wound healing compared to the controls.

The macroscopic wound size for FnAb and saline decreased steadily over the 14 day trial (Figure 3.4.A). For both the wound gape (Figure 3.4.B) and the wound area (Figure 3.4.C), FnAb resulted in decreased but not significant wound gape and area throughout the study, compared to the saline control, with most notable differences from Day 11 onwards.

Histological measurements of the H&E-stained wound sections taken on Day 14 were analysed (Figure 3.5.A). As can be seen in Figure 3.5.B-E, there was no statistical significance between the treatment groups for the wound length, dermal gape, epidermal thickness, or percentage of re-epithelialisation. As can be seen in Figure 3.5.E, the majority of the wounds were nearly entirely re-epithelialised by Day 14.

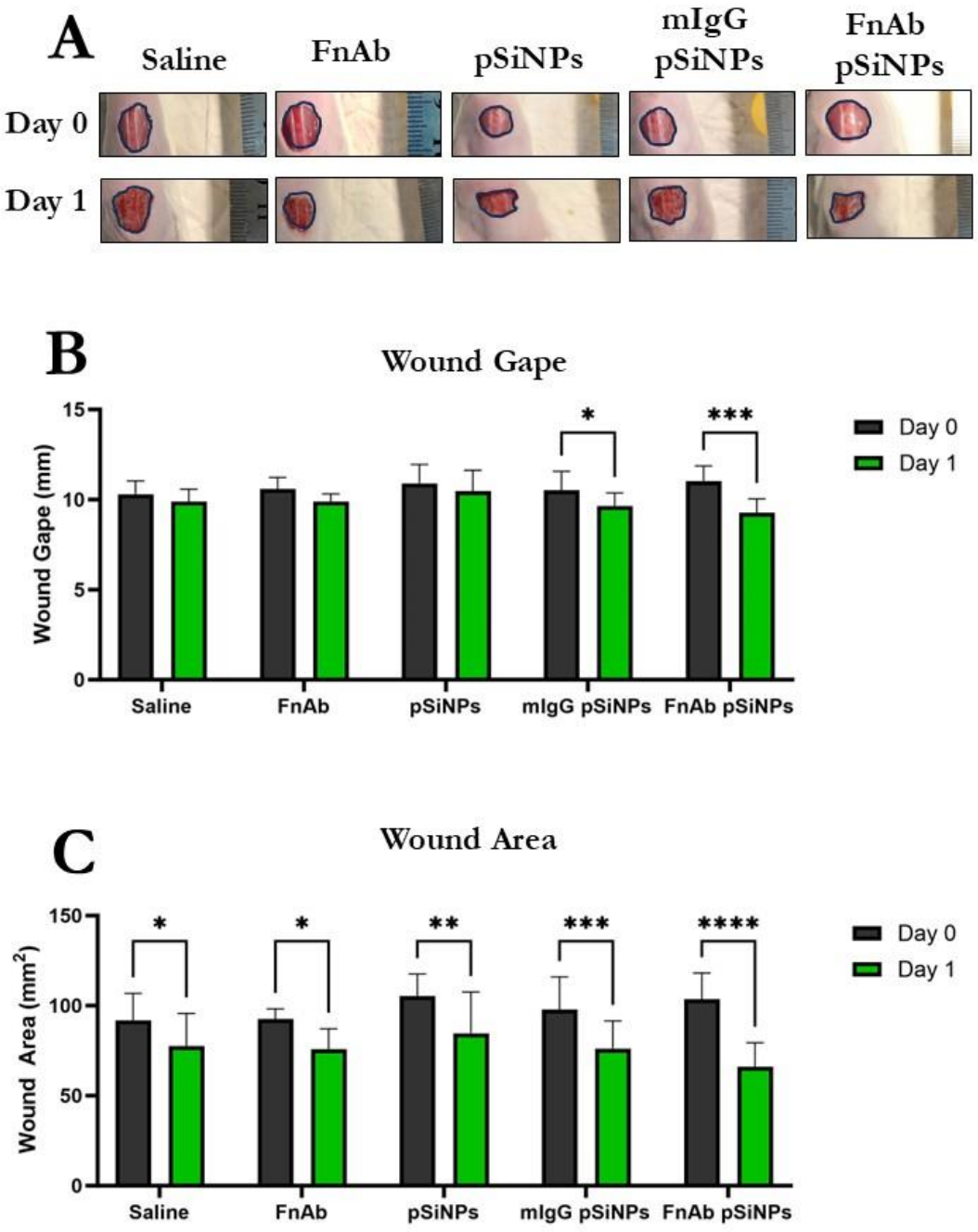

Figure 3.2. The diabetic wound size significantly decreases between the day of surgery (Day 0) and Day 1 prior to treatment. (A) Representative images of the wounds on Day 0 immediately after surgery and Day 1 prior to treatment. **(B)** The initial measurements of the Wound Gape on Day 0 and Day 1 **(C)** The initial measurements of the Wound Area on Day 0 and Day 1. Data is presented as mean ± SD (n≤8 per group). Statistical significance was achieved through a Two-way ANOVA and Tukey's Multiple Comparison's Test. * = $p<0.05$, ** = $p < 0.01$, *** = $p < 0.001$, ****= $p <0.0001$.

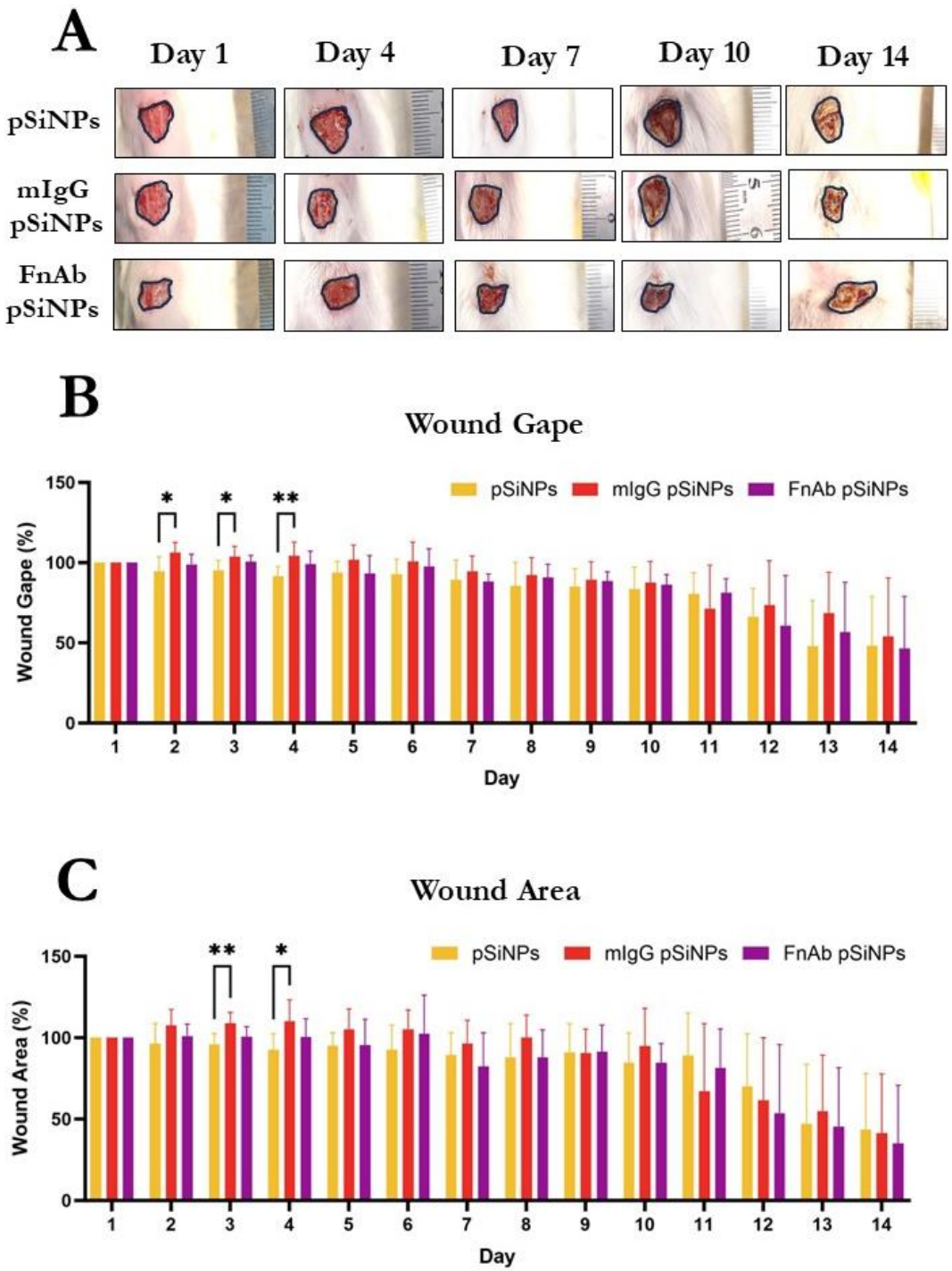

Figure 3.3. FnAb-pSiNPs did not improve healing compared to pSiNP controls in infected diabetic wounds. (A) Representative images of the wounds taken over the 14-day trial. **(B)** The Wound Gape **(C)** The Wound Area. Data was measured using ImagePro Plus. Data is normalised to the day of treatment at Day 1 and presented as mean ± SD (n≤8 per group). The statistical significance was determined through a Mixed Effects Analysis and a for **(B)** a Dunnett's Multiple Comparison Test and **(C)** Tukey's Multiple Comparison's Test. * = $p<0.05$, ** = $p<0.01$.

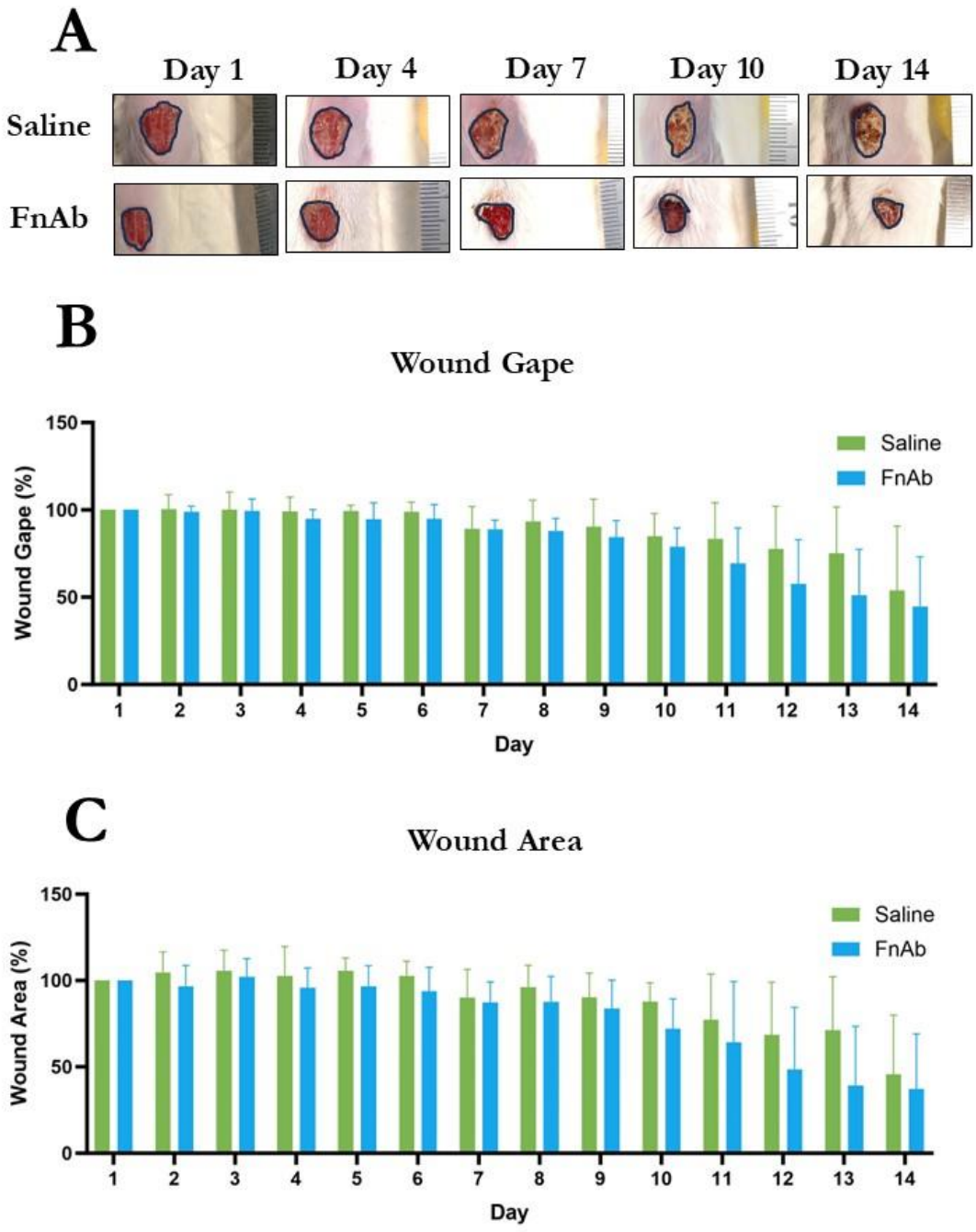

Figure 3.4. FnAb trended towards improved healing compared to the saline control in infected diabetic wounds. (A) Representative images of the wounds taken over the 14-day trial. **(B)** The Wound Gape **(C)** The Wound Area. Data was measured using ImagePro Plus. Data is normalised to the day of treatment at Day 1. Data is presented as mean ± SD (n≤8 per group).

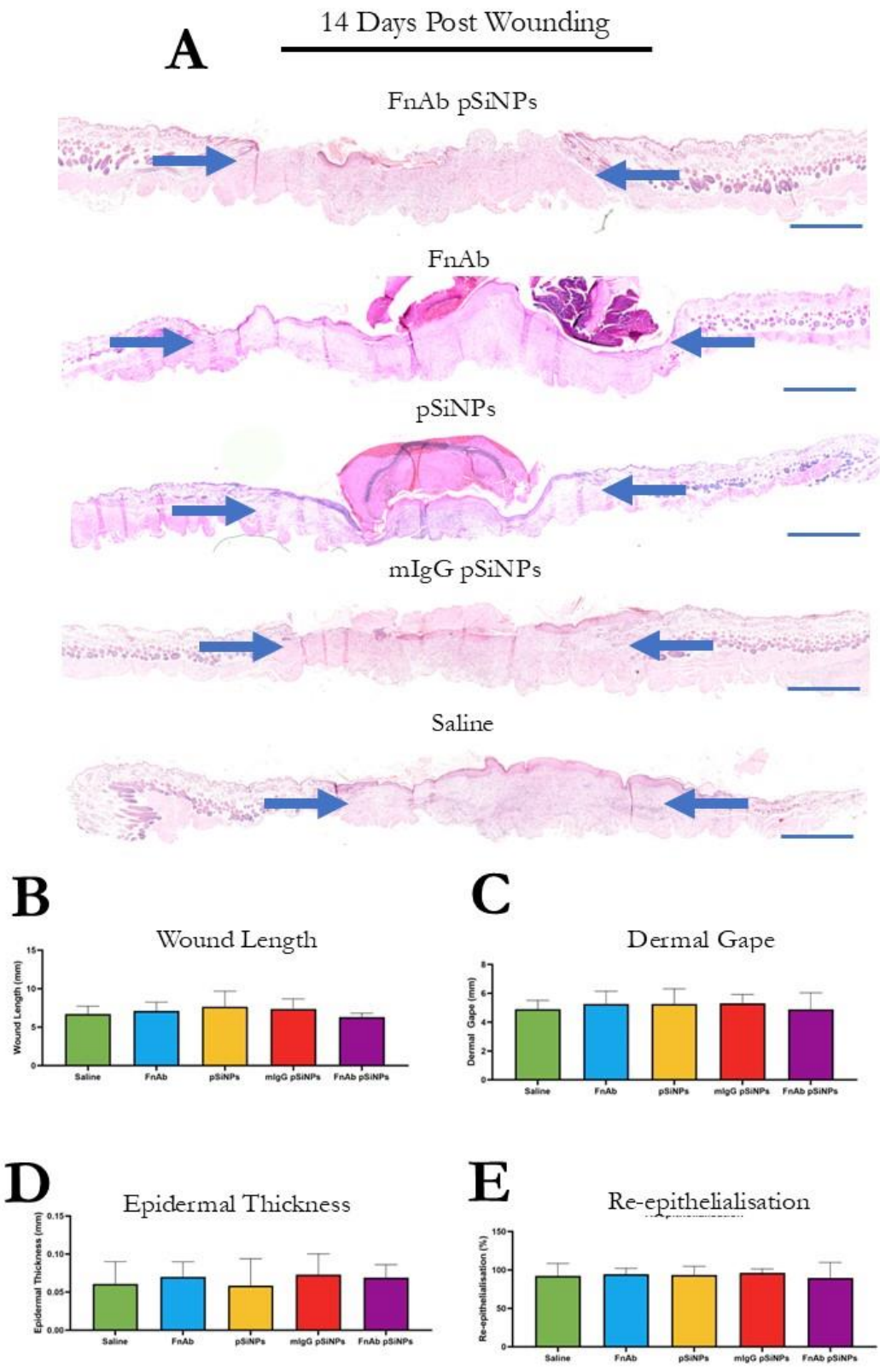

Figure 3.5. All diabetic wounds were almost completely healed at 14 days post-surgery. **(A)** Representative images of the excised wounds stained with Haematoxylin and Eosin. Arrows indicate dermal gape. Scale bar is 1 mm. **(B-E)** The histological measurements as measured using ImagePro Plus. Data is presented as mean ± SD (n≤8 per group).

3.3.2. Neutralising FnAb did not alleviate the bacterial burden of the wounds.

The bacterial burden was measured daily in real time using the IVIS Live Imaging System (Figure 3.6 and Figure 3.7). There was some variation in the initial bacterial load between the groups on Day 0 which evened out on Day 1, and all groups showed a significant decrease in infection load between Day 0 and Day 1 (Figure 3.6). The overall measure of infection was subsequently baseline corrected to Day 1 – the day of treatment – in order to account for this.

FnAb pSiNPs appeared to control the infection better than the IgG pSiNPs and pSiNPs treatment groups, but worse than the FnAb and saline controls, with a significant difference between FnAb pSiNPs and FnAb on Days 3, 4, and 5, with FnAb controlling the infection better. As observed in Figure 3.7.A, the bioluminescence measured by the IVIS decreased by the end of the trial. Notable differences were seen between the pSiNP and non-pSiNP, suggesting bacteria was elevated in response to pSiNP exposure or pSiNPs are auto-luminescent. As such, the pSiNPs and non-pSiNP treatment groups were presented separately. FnAb treated wounds showed consistently lower levels of infection than the saline control, especially on Days 3-6 (Figure 3.7.B). Notably, all treatment groups that involved pSiNPs – FnAb pSiNPs, mIgG pSiNPs, pSiNPs – showed a significant increase in the luminescence detected, beginning with a significant jump of 70-80% luminescence between Days 2 and 3 (Fig 3.7.C). The FnAb pSiNPs appeared to control the infection the best out of the three pSiNP groups, with significant improvement on Days 5 and 6 compared to pSiNPs alone (Figure 3.7.C). No statistical significance was found between the treatment groups on Day 14. This was supported by the CFUs, where there was no significant different between the treatment groups (Figure 3.7.D).

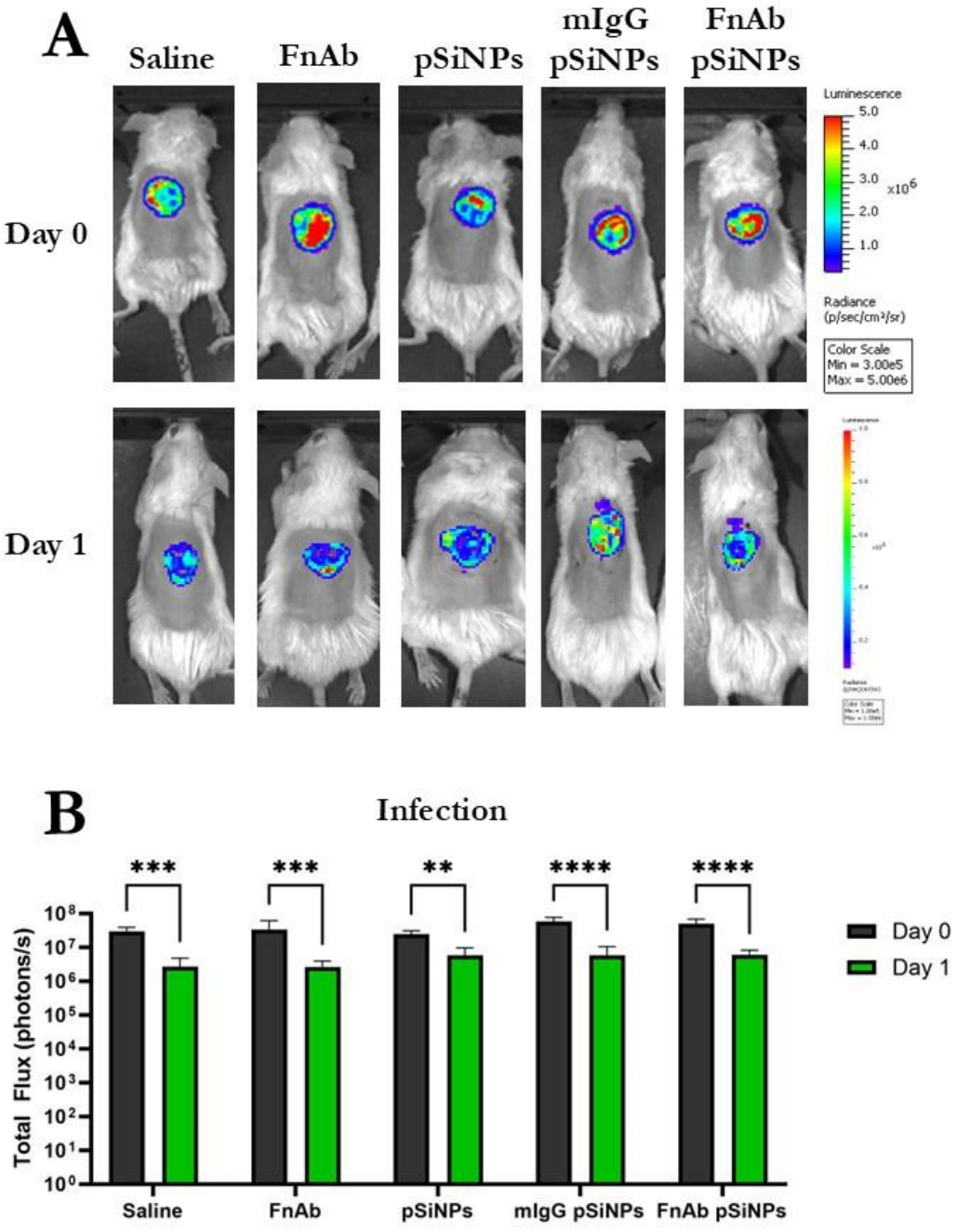

Figure 3.6. Equal bacterial burden in diabetic wounds at Day 1 post-bacterial inoculation. **(A)** Representative images showing the bioluminescence of the wounds on Day 0. **(B)** The bacterial burden on Day 0 and Day 1. Statistical significance was achieved through a Two-way ANOVA and Tukey's Multiple Comparison's Test. Data is presented at mean ± SD. n≤8. * =p<0.05, ** =p<0.01, *** =p<0.001, **** =p<0.0001.

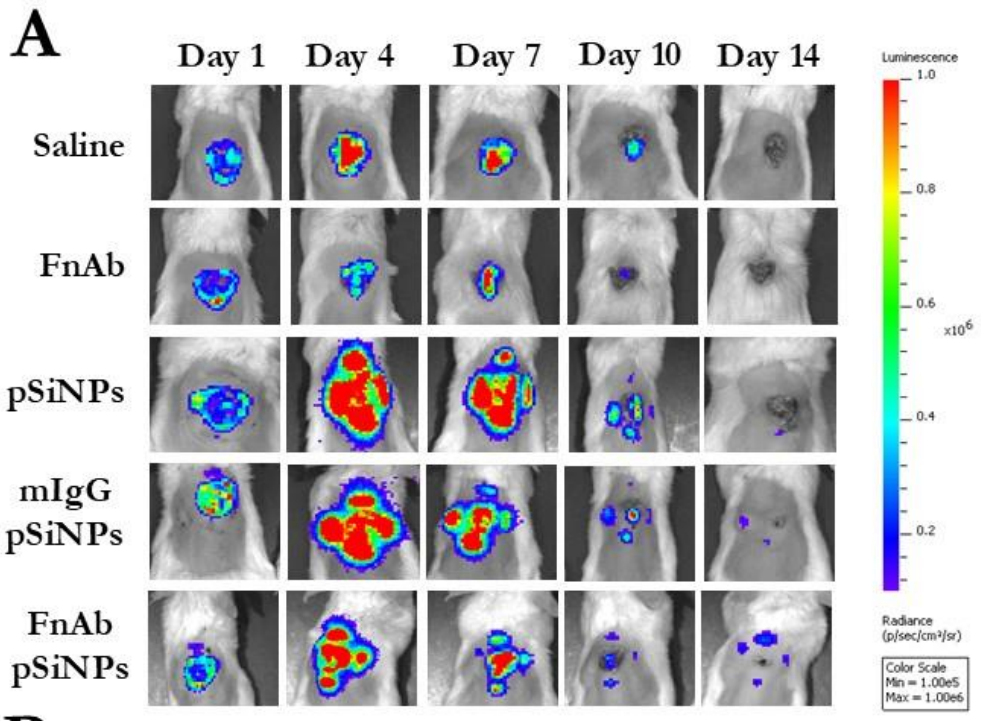
A
Day 1
Day 4
Day 7
Day 10
Day 14
Saline
FnAb
pSiNPs
mIgG pSiNPs
FnAb pSiNPs
Luminescence
1.0
0.8
0.6
x10^6
0.4
0.2
Radiance (p/sec/cm²/sr)
Color Scale
Min = 1.00e5
Max = 1.00e6

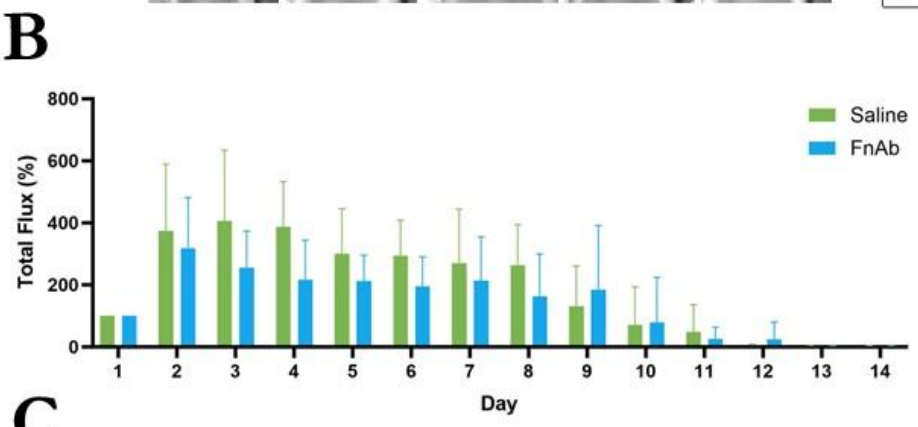
B
Saline
FnAb
Total Flux (%)
800
600
400
200
0
1
2
3
4
5
6
7
8
9
10
11
12
13
14
Day

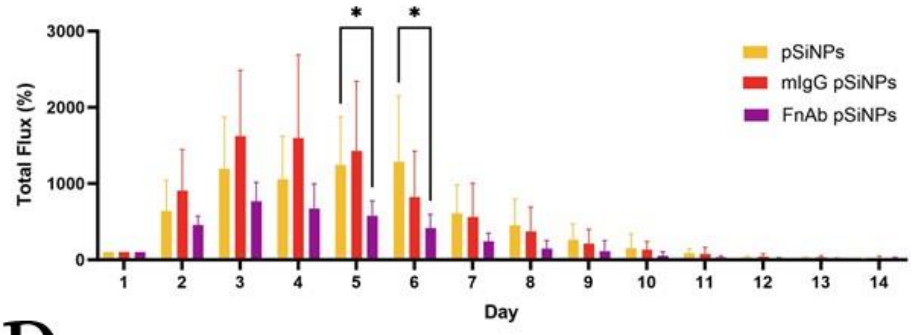
C
*
*
pSiNPs
mIgG pSiNPs
FnAb pSiNPs
Total Flux (%)
3000
2000
1000
0
1
2
3
4
5
6
7
8
9
10
11
12
13
14
Day

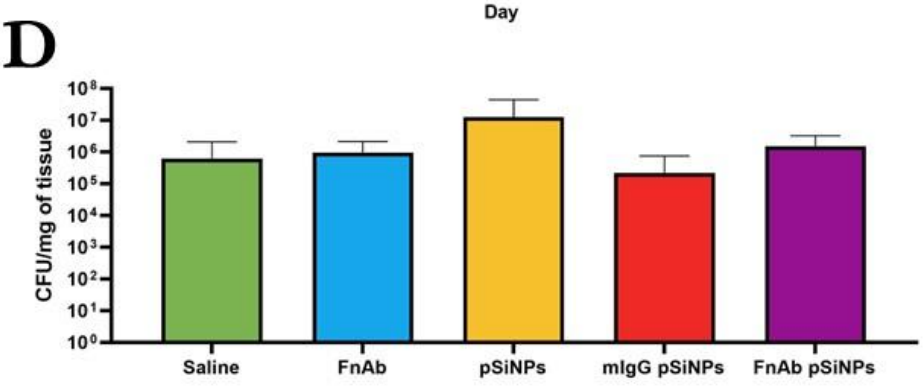
D
CFU/mg of tissue
10^8
10^7
10^6
10^5
10^4
10^3
10^2
10^1
10^0
Saline
FnAb
pSiNPs
mIgG pSiNPs
FnAb pSiNPs

Figure 3.7. The treatment groups that received pSiNPs showed higher rates of bioluminescence. (A) Representative bioluminescent images taken over the 14-day trial. **(B)** The total flux measured over the course of the study by the IVIS and normalised to the day of treatment – Day 1 for the non-pSiNPs treatment groups. **(C)** The total flux measured over the course of the study by the IVIS and normalised to the day of treatment – Day 1 for the pSiNPs treatment groups. **(D)** The CFUs measured on Day 14 at the end of the study presented as per mg or mL of sample. Data is presented as mean ± SD (n≤8 per group). The statistical significance of **(B)** and **(C)** was achieved through a two-way ANOVA and **(B)** Dunnett's Multiple Comparisons Test **(C)** Sidak's Multiple Comparison Test, and **(D)** through a one-way ANOVA and Tukey's Multiple Comparisons Test. * = $p<0.05$.

3.3.3. Neutralising FnAb had no effect on collagen deposition or Flightless I, PCNA or F4/80 and YM-1 expression in *S. aureus*-infected diabetic wounds.

Collagen deposition into the wound bed is an important part of the wound healing process, with more collagen being deposited as the wound healing process continues. Masson's Trichrome Total Collagen stain was used to assess the level of collagen deposition and the maturation of the wound. No significant difference in total collagen was observed in the granulation tissue between any of the treatment groups indicating that by Day 14 of this study, all treatment groups had reached the same stage of wound healing (Figure 3.8).

Flightless I is overexpressed in response to wounding and is associated with impaired wound healing. FnAb was used to neutralise Flightless I and therefore improve wound healing. To investigate any differences in the expression of Flightless I in the wounds between the treatment groups, the wounds were immunofluorescently stained for Flightless I (Figure 3.9.A). No significance in Flightless I expression was seen between the treatment groups (Figure 3.9.B). This may indicate that 14 days post-wounding is too late to see any differences in Flightless I expression.

Proliferating cell nuclear antigen (PCNA) expression was assessed as a measure of keratinocyte proliferation with higher PCNA expression indicating that the wound is in the proliferative phase of wound healing (Figure 3.10.A). No significance in PCNA expression was found between the treatment groups (Figure 3.10.B). Overall, the expression of PCNA was quite low. As these are Day 14 wounds, this may be indicative that the wounds have surpassed the proliferative phase of wound healing and have now entered the tissue remodelling phase.

Inflammation is crucial for both wound healing and removing infection. Macrophages in particular can express Flightless I. While M1 macrophages are indicative of inflammation when they first enter the wound, the phenotype switch from M1 to M2 indicates the resolution of the inflammatory phase with the anti-inflammatory M2 macrophages dominating. Macrophage markers F4/80 and YM-1 were quantified as a measure of macrophage recruitment into the wound, with F4/80 being a marker for all macrophages and YM-1 being a marker for M2 macrophages (Figure 3.11.A). No significance was found in either total macrophage counts (Figure 3.11.B) or in the ratio of M2 macrophages to M1 macrophages (Figure 3.11.C). This aligns with the other staining, indicating that the wounds are now in the tissue remodelling phase of wound healing.

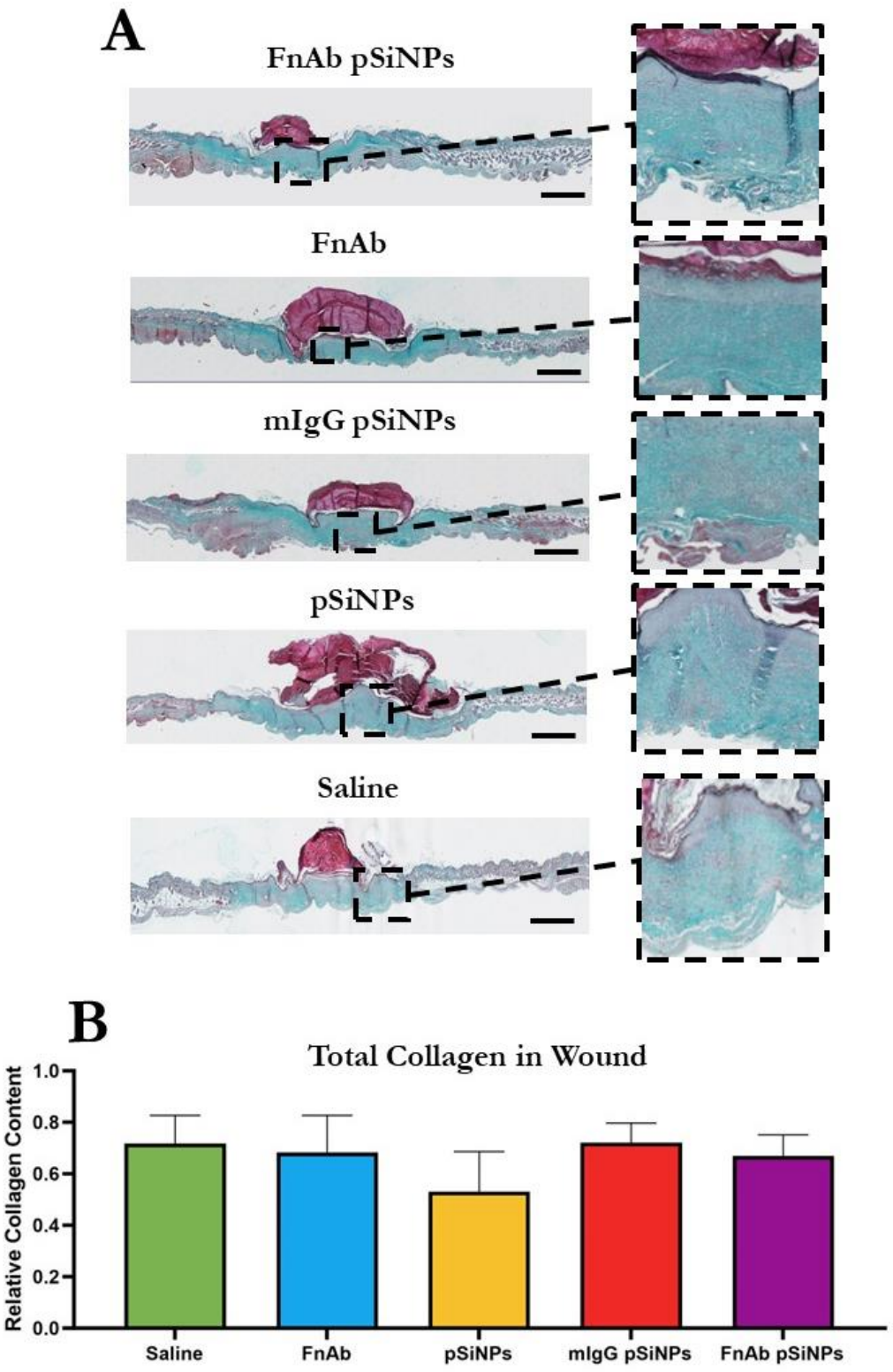

Figure 3.8. Equal amounts of total collagen measured by Masson's Total Collagen Trichrome Stain in Day 14 infected diabetic infected wounds. (A) Representative images of the excised wounds stained with Masson's Total Collagen Trichrome Stain **(B)** The total collagen in the wound measured using ImageJ. Data is presented as mean ± SD. n=4. Scale bar = 1 mm.

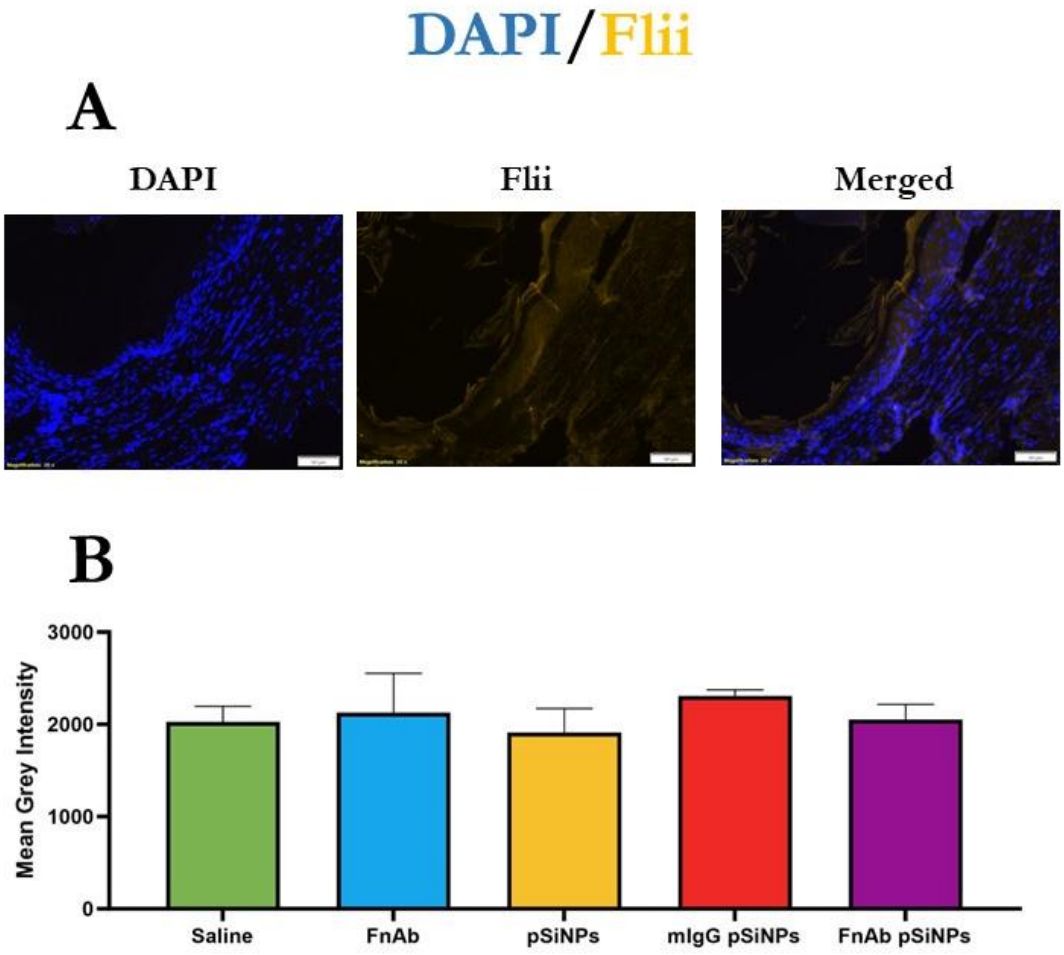

Figure 3.9. Analysis of Flightless I expression in the wound bed in Day 14 infected diabetic wounds. (A) Representative images of Flii immune-positivity in the granulation tissue of the wound bed. Flii (yellow)/DAPI (blue). **(B)** Corresponding analysis of Flii immune-positivity expressed as Mean Grey Intensity. Data shown as mean ± SD. Scale bar is 50 µm. 20x magnification. n = 4.

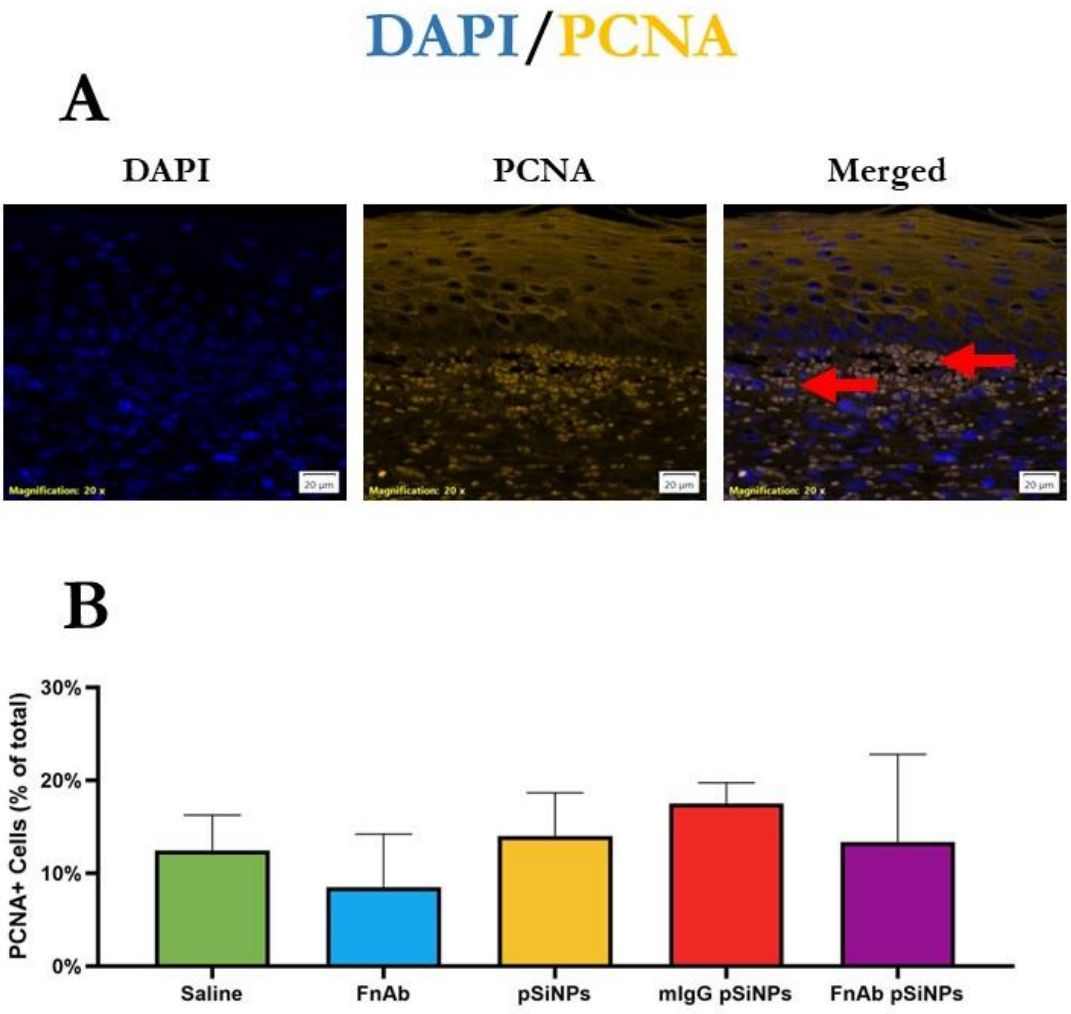

Figure 3.10. Analysis of proliferating cell nuclear antigen (PCNA)-positive cells in Day 14 infected diabetic wounds. (A) Representative images of PCNA positive cells in the wound bed. PCNA (orange)/DAPI (blue). Arrows indicate keratinocytes. **(B)** Corresponding analysis of PCNA positive cells expressed as a percentage of total cell counts. Data shown as mean ± SD. Scale bar is 20 µm. 20x magnification. n = 4.

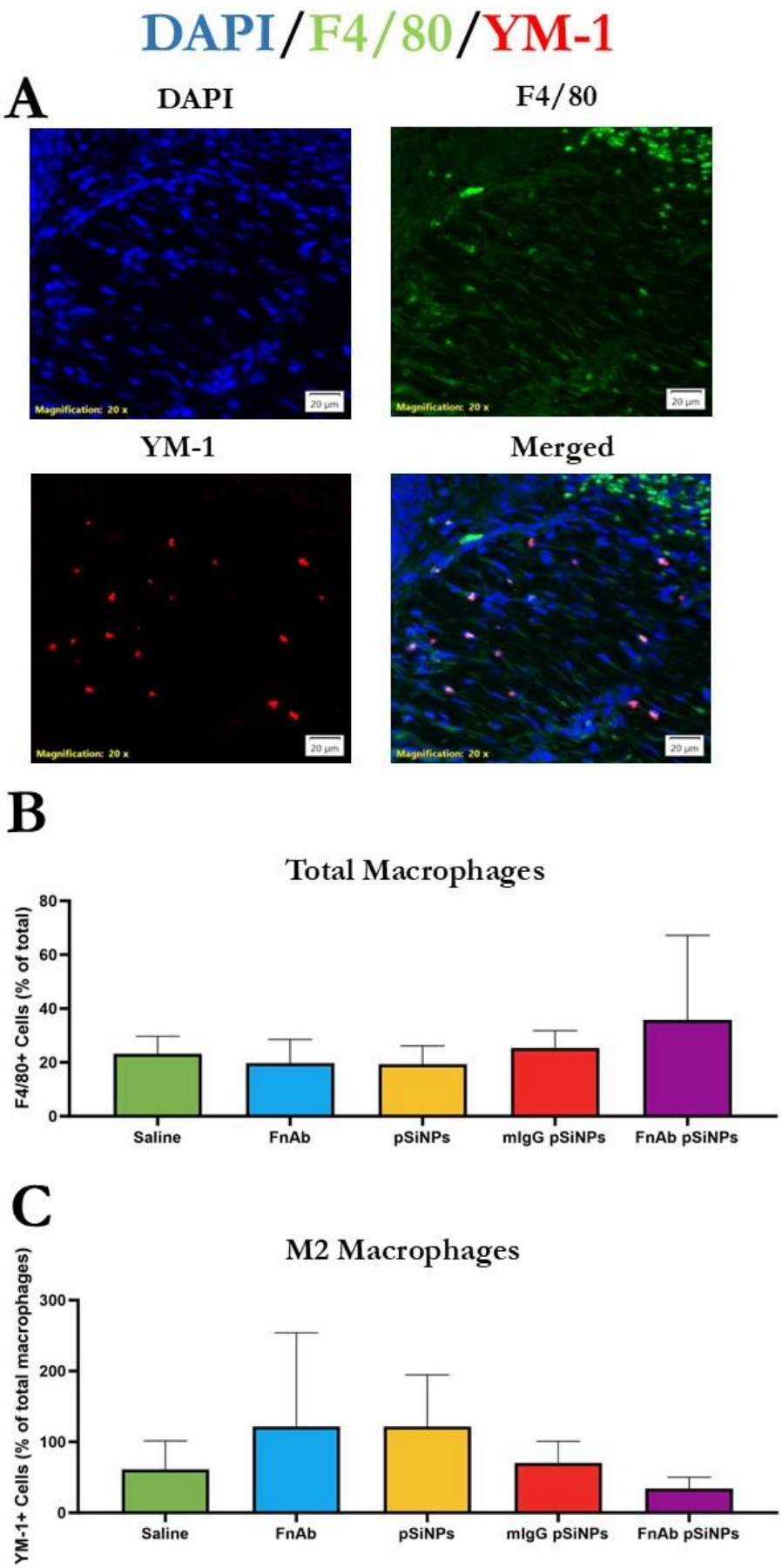
DAPI/F4/80/YM-1
A
DAPI
F4/80
YM-1
Merged
Magnification: 20 x
20 µm
B
Total Macrophages
F4/80+ Cells (% of total)
0
20
40
60
80
Saline
FnAb
pSiNPs
mIgG pSiNPs
FnAb pSiNPs
C
M2 Macrophages
YM-1+ Cells (% of total macrophages)
0
100
200
300
Saline
FnAb
pSiNPs
mIgG pSiNPs
FnAb pSiNPs

Figure 3.11. Analysis of macrophage infiltration in Day 14 infected diabetic wounds. (A) Representative images of macrophages in the granulation tissue of the wound bed. F4/80 (green)/YM-1 (red)/DAPI (blue). **(B)** Number of total macrophages **(C)** Number of M2 macrophages. Data shown as mean ± SD. Scale bar is 20 µm. 20x magnification. n = 4.

3.3.4. Wounds treated with porous silicon nanoparticles exhibited increased luminescence at the injection sites.

Upon examination of the IVIS bioluminescent images, a pattern was observed in some of the mice groups (Figure 3.12). Luminescence was detected at the intradermal injection sites, not just in the wound where the bioluminescent bacteria was applied. As the trial progressed, the bioluminescence levels reduced within the wound, with luminescence only being detected at the intradermal injection sites. Not all the mice displayed this luminescent pattern, only the mice that received pSiNPs, suggesting pSiNPs may exhibit auto-bioluminescence or attract bacteria (Figure 3.13). This is further investigated in Section 3.3.6.

Supporting bacterial attraction, the luminescence pattern corresponded to visual signs of irritation in the pSiNPs cohorts (Figure 3.12). At many of the intradermal injection sites, signs of redness, swelling and scabbing were observed (Figure 3.12). Surrounding wound erythema (redness) was seen to some extent in all the mice that received pSiNPs except one; Mouse 38 which received the FnAb pSiNPs treatment. This was the only mouse that received pSiNPs and did not display erythema or irritation as observed in the digital photos. However, the luminescence pattern across the four intradermal injection sites was still observed by the IVIS (Figure 3.14).

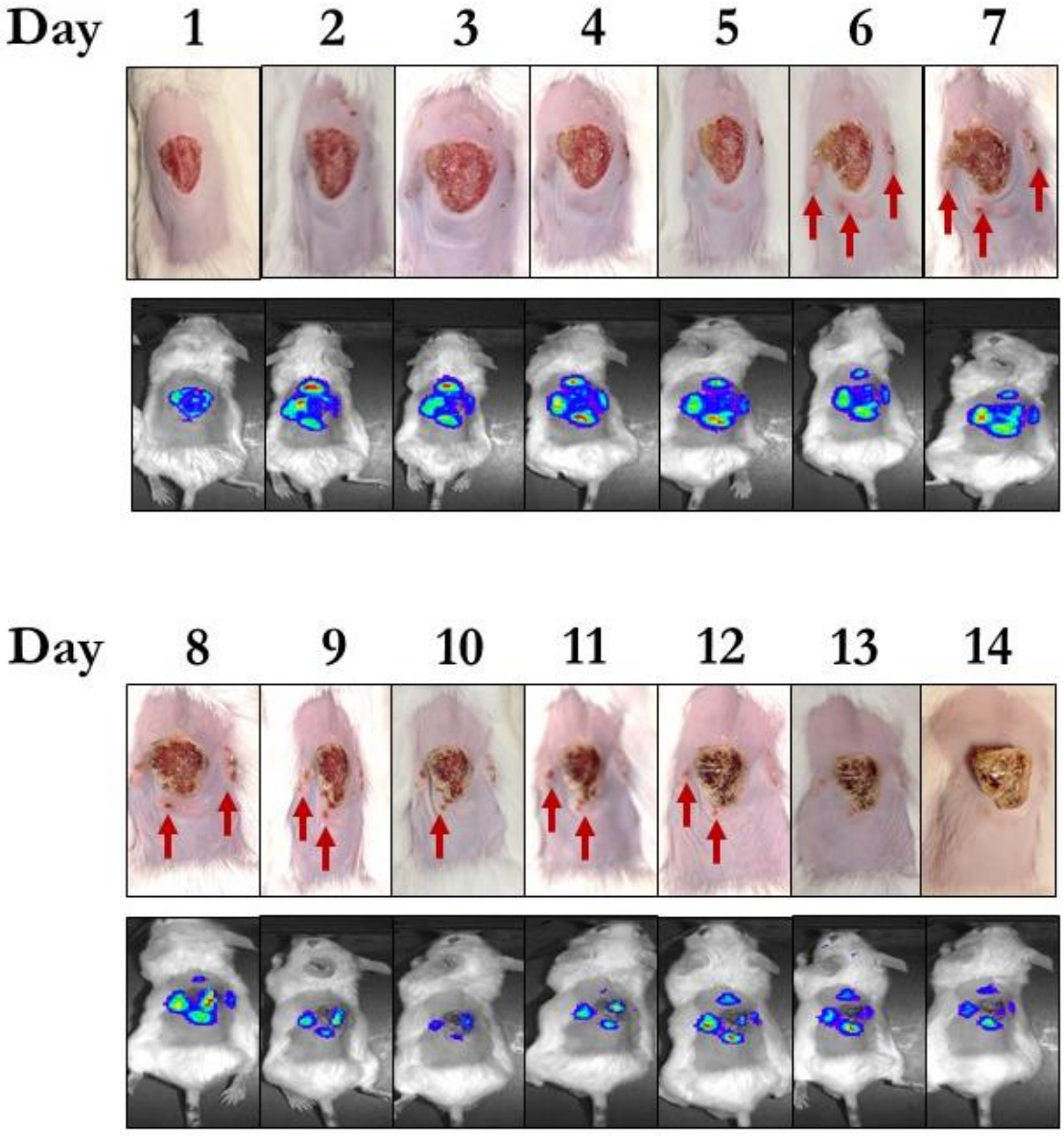

Figure 3.12. Daily macroscopic and bioluminescent images of Mouse 46 over the 14-day trial. Mouse 46 received the pSiNPs treatment. Arrows point to the potentially infected intradermal injection sites that correspond to increased luminescence.

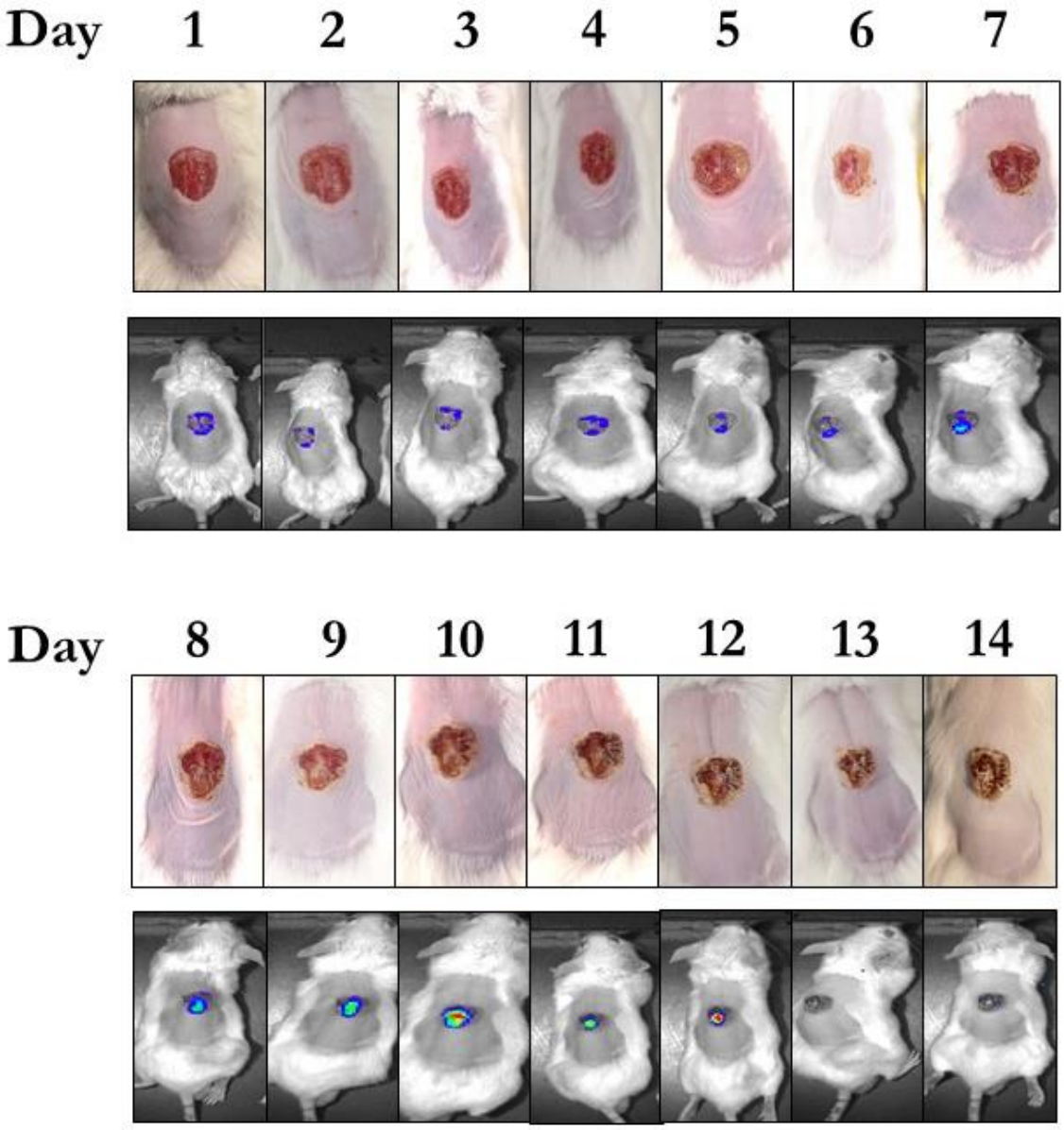

Figure 3.13. Daily macroscopic and bioluminescent images of Mouse 52 over the 14-day trial. Mouse 52 received the FnAb treatment, intradermally injected and in the absence of pSiNPs, and lacked evidence of luminescence or skin irritation at the injection sites observed for the pSiNPs cohorts.

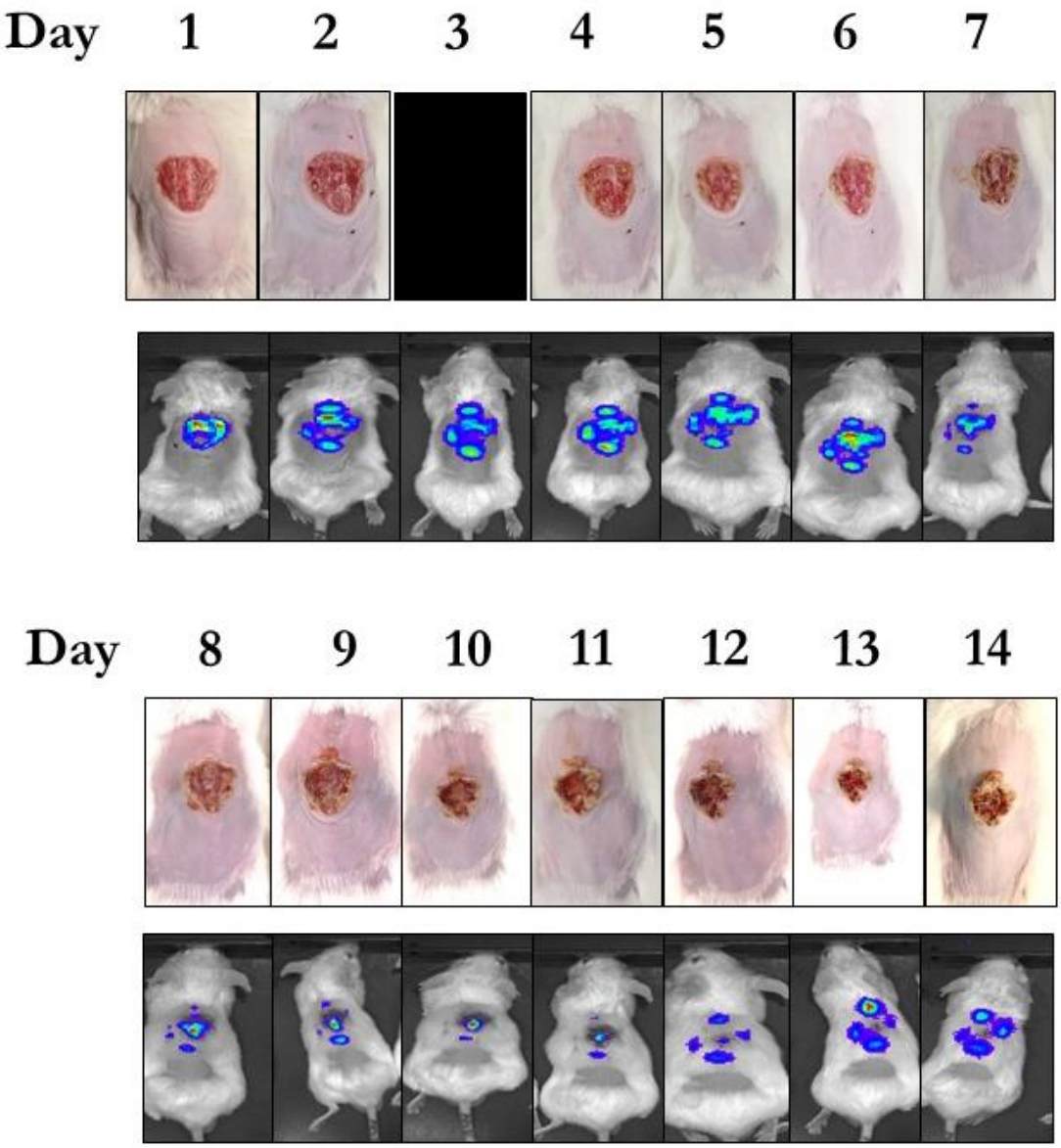

Figure 3.14. Daily macroscopic and bioluminescent images of Mouse 38 over the 14-day trial. Mouse 38 received the FnAb pSiNPs treatment. This is the only mouse in the pSiNP cohorts to lack apparent injection site agitations, although it retained an increase in luminescence. The Day 3 image for this mouse was not captured.

3.3.5. Potential migration of *S. aureus* from the wound to the intradermal injection sites.

The bioluminescence pattern observed in the pSiNPs treatment cohorts was re-assessed in more detail (Figure 3.15). The first measurement measured the entire bioluminescent pattern (Figure 3.15.A), while the second measurement measured the luminescence detected within the wound (Figure 3.15.B). The measurements were then expressed as the percentage of luminescence detected outside of the wound. As shown in Figure 3.15.C, the luminescence detected outside of the wound increased to 60-80% of the total luminescence detected on Day 2 – the first luminescent image taken of the mice post-treatment. This was maintained throughout the trial with a small dip on Day 10 followed by another increase on Day 14. This pattern was maintained even though the overall luminescence measured decreased steadily over the trial (Figure 3.15.D).

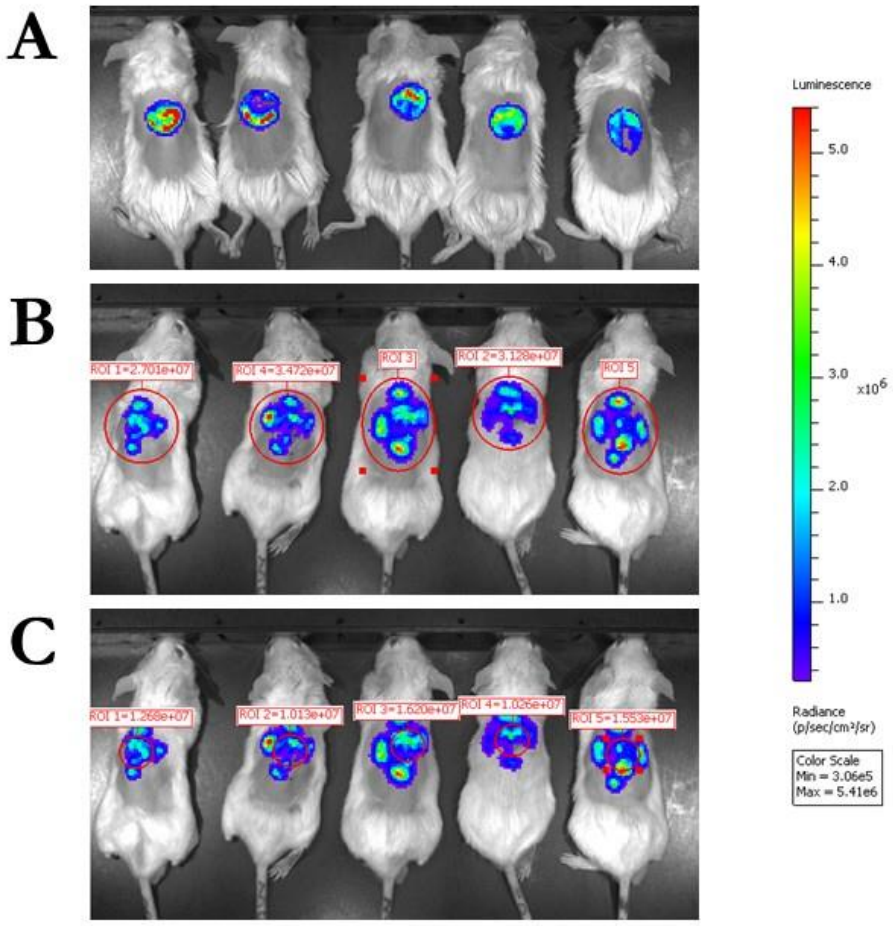
A
B
C
Luminescence
5.0
4.0
3.0
x10^6
2.0
1.0
Radiance (p/sec/cm²/sr)
Color Scale
Min = 3.06e5
Max = 5.41e6
ROI 1=2.701e+07
ROI 4=3.472e+07
ROI 3
ROI 2=3.128e+07
ROI 5
ROI 1=1.268e+07
ROI 2=1.013e+07
ROI 3=1.620e+07
ROI 4=1.026e+07
ROI 5=1.553e+07

D

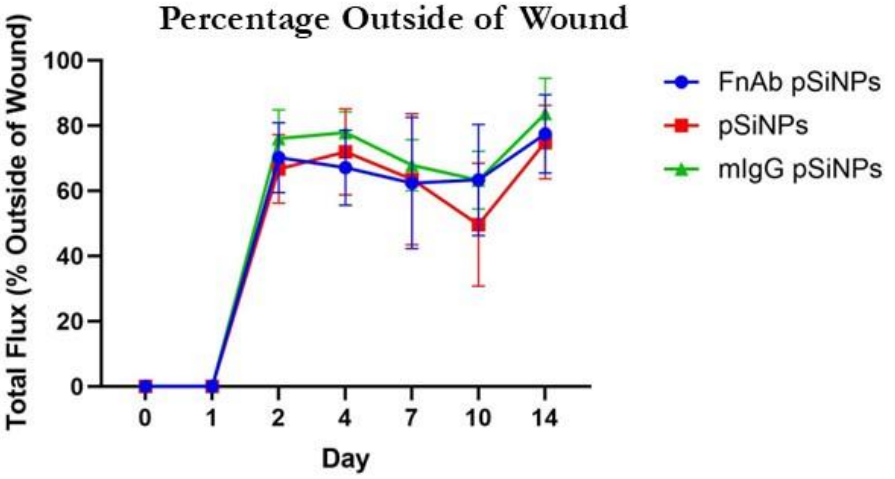
Percentage Outside of Wound
Total Flux (% Outside of Wound)
100
80
60
40
20
0
0
1
2
4
7
10
14
Day
FnAb pSiNPs
pSiNPs
mIgG pSiNPs

E

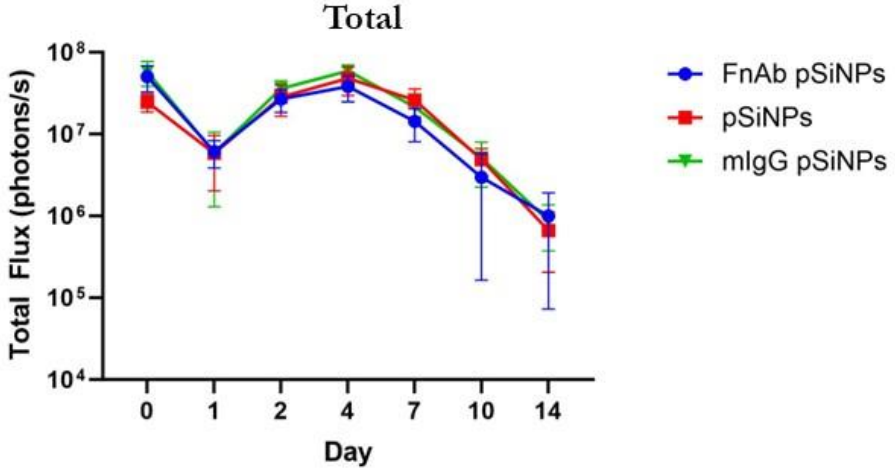
Total
Total Flux (photons/s)
10^8
10^7
10^6
10^5
10^4
0
1
2
4
7
10
14
Day
FnAb pSiNPs
pSiNPs
mIgG pSiNPs

Figure 3.15. The bacterial burden of the three pSiNPs groups showing the bacteria potentially leaving the wound and inhabiting the intradermal injection sites. (A) A representative photo showing the bioluminescence in the wound on Day 0 **(B)** A representative photo showing the entire bioluminescent pattern being measured at Day 4. **(C)** A representative photo showing only the bioluminescence of the wound being measured at Day 4. **(D)** The percentage of bioluminescence detected outside of the wound for the three pSiNPs treatment groups: FnAb pSiNPs, pSiNPs, and mIgG pSiNPs, on Days 0, 1, 2, 4, 7, 10, 14. **(E)** The total bioluminescence detected for the three pSiNPs treatment groups: FnAb pSiNPs, pSiNPs, and mIgG pSiNPs, on Days 0, 1, 2, 4, 7, 10, 14. Data is presented as mean ± SD. n≤8.

3.3.6. Porous silicon nanoparticles show auto-luminescence when topically applied but not when intradermally injected.

To investigate whether the increase in luminescence in pSiNPs treated wounds was due to infection or the auto-luminescence of pSiNPs, a study was conducted in two humanely killed mice. Post-mortem intradermal injections or topical applications of pSiNPs or saline were administered to the mice. The mice were then immediately imaged in the IVIS. As can be seen in Figure 3.16.A, the auto-exposure did record luminescence for the topically applied pSiNPs but very little for the intradermally injected pSiNPs. The areas of interest as shown in Figure 3.16.A, were measured and shown in Figure 3.16.B. The highest reading for the pSiNPs was 5×10^5 for the "leaked" pSiNPs. The topically applied pSiNPs gave readings of 2.75×10^5 and 6.953×10^5. This demonstrates that while the pSiNPs did auto-luminesce, they did not show a measurable amount of luminescence when intradermally injected. This suggests that the luminescence observed during the trial was due to infection and not pSiNPs auto-luminescence.

The intradermal injected skin of pSiNPs at the bottom of Mouse B was collected, along with a sample of healthy skin tissue. The skin samples were processed as in Chapter 2.4.3, and H&E-stained as in Chapter 2.4.4. As can be seen in Figure 3.16.C, a small amount of brown stain can be seen between the muscle and the dermis. This discolouration is not observed in the healthy skin sample and is most likely the injected pSiNPs. This suggests that the discolouration shown in the skin of some of the mice post-mortem was due to the pSiNPs.

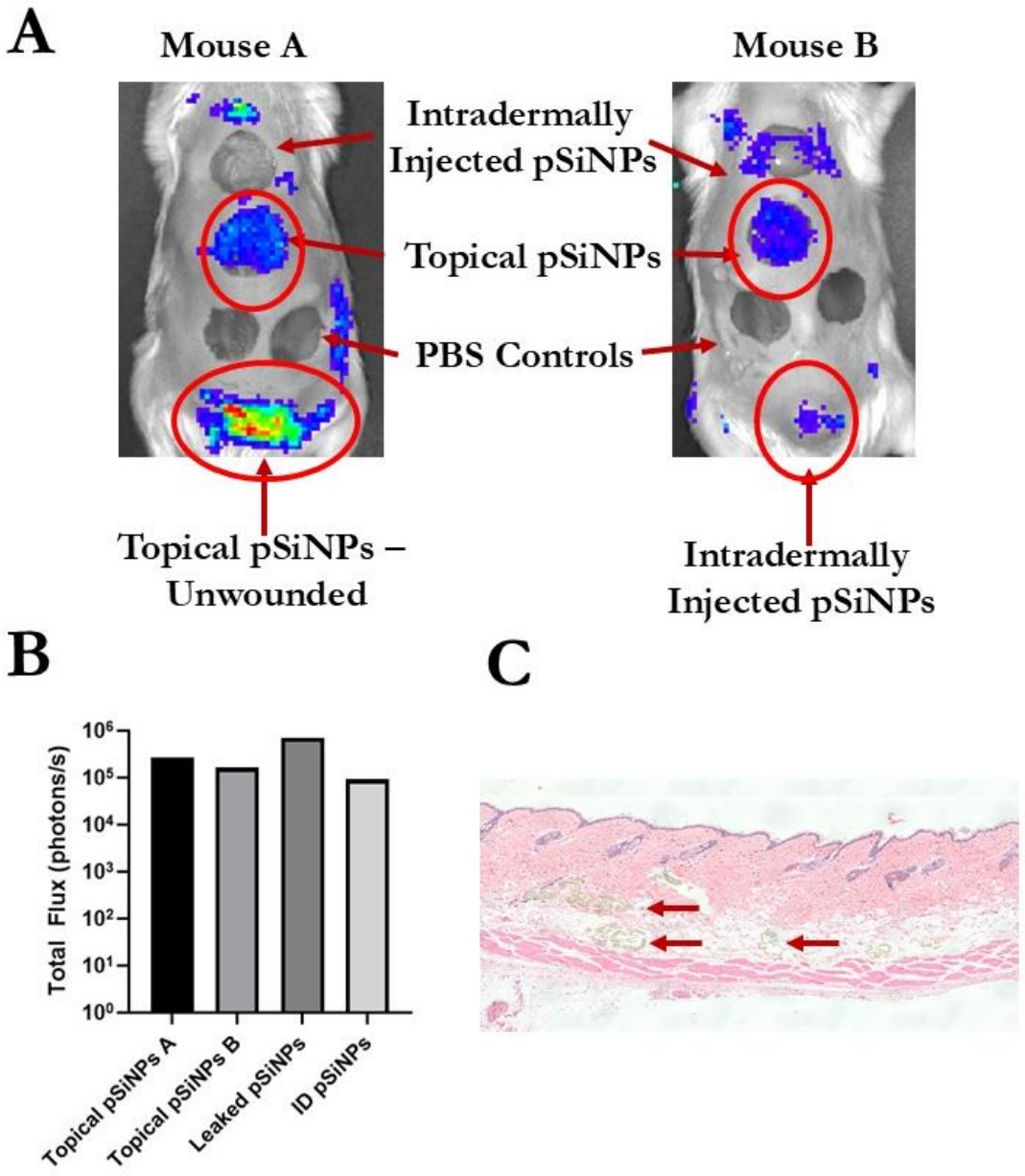

Figure 3.16. Porous silicon nanoparticles showed negligible auto-luminescence when intradermally injected into mice posthumously. (A) Bioluminescent photos of the two mice taken by the IVIS with labels indicating treatment. Four regions of interest are circled; Mouse A, top: topical pSiNPs applied to wounded skin; Mouse A, bottom: topical pSiNPs applied to unwounded skin; Mouse B, top: topical pSiNPs applied to wounded skin; Mouse B, bottom: intradermally injected pSiNPs in unwounded skin **(B)** The regions of interest circled in (A) quantified **(C)** H&E-stained analysis of the intradermally injected pSiNPs near the tail of Mouse B. Arrows indicate discolouration.

3.4. Discussion

Chronic wounds affect approximately 450,000 Australians every year, with diabetic foot disease affecting approximately 50,000 Australians every year and venous leg ulcers being the most common type of chronic wound [66, 106]. Between 60 and 80% of chronic wounds have a biofilm [59]. Infection is likely to reduce treatment efficacy in diabetic wounds due to increased protease load and an exacerbated inflammatory response [69-71]. The bacteria themselves also contribute to this hostile environment through the production of proteases that inhibit wound healing [42]. Methods of protecting treatments from the hostile wound are being explored.

FnAb is a monoclonal antibody (mAb) that has previously been shown to increase the rate of wound repair in mice [136, 142, 145, 146], and pigs [153] through the neutralisation of the negative regulator of wound healing, Flightless I (Flii). Flii is a negative regulator of wound healing with Flii under-expressing mice showing increased rates of re-epithelialisation and Flii over-expressing mice showing impaired wound healing and excessive scarring [138]. Flii expression is upregulated in diabetic skin compared to non-diabetic skin and upregulated even further in diabetic wounds [136, 138]. Flii under-expressing diabetic mice have also shown improved wound healing with excisional wounds compared to Flii over-expressing mice [147]. FnAb improves wound healing when intradermally injected into incisional wounds [145], burns [142], developing scars [146], murine excisional wounds [136], murine diabetic excisional wounds [138], and porcine excisional wounds [153].

While monoclonal antibodies are a promising new therapy, they can be rapidly degraded by proteases. Chronic wounds have been found to have a 100-fold more proteases than in acute wounds [251]. Delivery systems that provide protection from proteolytic degradation and therefore needed to overcome this limitation. One such delivery system is the use of porous silicon nanoparticles.

Porous silicon (pSi) is a widely used biocompatible material that degrades into non-toxic silicic acid. Nanoparticles made from porous silicon (pSiNPs) are capable of being loaded with drugs and provide protection it from the surrounding harsh environment. In addition. They provide a slow, sustained release [154]. pSiNPs have shown no toxicity or inflammatory responses through oral, subcutaneous, or intravenous administration [158].

To protect FnAb from degradation and allow a slow and sustained treatment, investigations have begun to test the improved efficacy of delivering FnAb using porous silicon nanocarriers. Previously, FnAb pSiNPs have been shown to improve diabetic wound healing compared to FnAb alone [145]. However, as diabetic wounds are often infected, it became important to assess the efficacy of FnAb pSiNPs in the presence of infection in diabetic wounds. The presence of infection creates an even more hostile "chronic wound like" environment that promotes the degradation of FnAb through an exacerbated inflammatory response and an increase in the production of proteases. Therefore, in this more hostile environment, the use of pSiNPs may be even more necessary. This chapter extended previous current research by investigating the FnAb pSiNPs in diabetic excisional wounds in the presence of infection. Although FnAb is not expected to directly reduce infection, by increasing the rate of wound repair and enhancing the organism's natural antimicrobial defences, infection may be more easily managed.

Previously, pSiNPs have shown intact and functional release of the Flii neutralising antibody, FnAb, for up to 7 days post-treatment. pSiNPs were used to deliver FnAb into murine diabetic excisional wounds via intradermal injection which resulted in improved wound healing. By Day 7 of this trial, the wounds treated with FnAb pSiNPs were 30% smaller than the wounds treated with FnAb alone, supporting pSiNPs as a delivery mechanism of monoclonal antibodies to chronic wounds [145].

Under these specific experimental conditions, FnAb pSiNPs had no effect on infected wound healing in diabetic animals – neither did FnAb alone. While the macroscopic size of the wounds decreased steadily over the course of the trial, no significance was found between the treatment groups. This was supported by the microscopic measurements where there was no significant difference between the treatment groups and almost all the wounds had completely re-epithelialised at day 14. This is further supported by the Masson's staining that showed no difference in total collagen deposited in the wound bed. Immunohistochemistry showed no difference in the expression of Flii, PCNA, and macrophages between the treatment groups at Day 14.

Consistent with the previous studies in diabetic mice, this study administered the treatments via intradermal injection via 4 intradermal injections around the excisional

wound. Moreover, the properties of the pSiNPs were equivalent to the prior study, suggesting the infection may have prevented the FnAb from having pro-wound healing effects observed in previous studies. This is confirmed in a recent comparative trial where FnAb pSiNPs demonstrated efficacy in non-infected compared to infected diabetic wounds [unpublished]. In that trial, FnAb pSiNPs was significantly more effective than FnAb delivered alone.

As there was no significant effect on wound healing, there was not expected to be a difference in infection. In the current study, FnAb pSiNPs had no pronounced effect on infection though FnAb pSiNPs significantly reduced bacterial burden on Day 5 and 6 compared to the pSiNPs alone. Overall, FnAb pSiNPs controlled the infection the best out of the three pSiNPs treatment groups. The CFUs measured on Day 14 of the trial showed no significance between the treatment groups. The daily measures of infection via the IVIS showed unexpected results. There was an obvious divergence, particularly on Days 2-7, between the treatment groups that received pSiNPs (FnAb pSiNPs, mIgG pSiNPs, pSiNPs) and the treatment groups that did not receive pSiNPs (FnAb, Saline). While the FnAb and Saline treatment groups trailed steadily below with no statistical significance between each other, the remaining treatment groups jumped in bioluminescence to varying degrees. Of the pSiNP groups, FnAb pSiNPs controlled the infection the best with the bacterial burden increasing to over 500% of its Day 1 measure, while pSiNPs increased to over 1000%, and mIgG pSiNPs increased to over 1500%. However, there was no statistical significance found between these three groups due to the large variation of the data.

Through the capture of daily bioluminescent images, a pattern involving the intradermal injection sites was observed in the three pSiNP treatment groups but not in the FnAb or Saline treatment groups. This pattern was investigated with two possibilities considered including the auto-luminescence of the pSiNPs, and the pSiNPs attracting and promoting infection.

Porous silicon nanoparticles are surface functionalised via various methods in order to increase the beneficial qualities (e.g. biocompatibility, drug-uptake) [157]. The pSiNPs used in this chapter were functionalised using thermal oxidation. Thermal oxidation is the heating of porous silicon to high temperatures to produce a thin layer of silicon oxide on the wafer. Thermal oxidation increases the solubility, biocompatibility, and loading yield of the pSiNPs while also allowing for decreased degradation [157]. Porous silicon

nanoparticles have inherent photoluminescent properties due to quantum confinement and surface defects [161, 164]. This auto-luminescence is exacerbated by thermal oxidation which passivates the surface, exacerbating quantum confinement and the Si-SiO_2 interfacial defects [161-164]. This results in photoluminescence in the orange-near infrared range at room temperature [161]. The auto-luminescence of the thermally oxidised pSiNPs used in this chapter was investigated using an ex vivo wound model and the IVIS live imaging system. While auto-luminescence was detected by the IVIS when the pSiNPs were topically applied, no luminescence was detected by the pSiNPs when intradermally injected. Therefore, while the auto-luminescence of the thermally oxidised pSiNPs was confirmed, it did not explain what was observed in the animal trial.

Through the daily bioluminescent images, it can be seen that in spite of the overall bioluminescence decreasing over time, from Day 2 onwards, the majority of the luminescence detected is detected outside of the original wound area. This movement from entirely within the wound to 60-80% outside the wound area took place 48 hours post-infection and 24 hours post-treatment. Along with the bioluminescent pattern matching with the injection sites, this indicates that the infection has moved from the wound to the injection sites. As the FnAb and Saline treatment groups involved intradermal injections but not pSiNPs, it may be that the combination created a hospitable niche for the bacteria to thrive in.

The ability for pSiNPs to promote infection has not been reported previously and could be investigated using *in vitro* antimicrobial assays. However, it is hypothesised that the combination of the pSiNPs being intradermally injected acted similarly to how implants can develop biofilms. This is supported by remnants of the pSiNPs being found at the injection sites posthumously. While pSiNPs are known to be biocompatible and degrade into the non-toxic orthosilicic acid, there is evidence that this degradation did not occur in some of the mice, and instead may have created an environment in which bacteria could proliferate.

The addition of infection caused problems previously unseen in this model and may require modifications in order for this model to be successful in future investigations. Future studies will investigate a topical application of the treatments instead of intradermal injections. While intradermal injections allow for an immediate, localised treatment, a topical application would ensure the infection remains localised to the wound area. A

topical application is also more applicable for clinical applications during wound management. Additionally, to help prevent contamination and further infection caused by the pSiNP treatments, the pSiNPs would need to be UV-sterilised before use. Nanoparticles with inherent antimicrobial properties, like gold and silver nanoparticles, could also be researched, both as a way to avoid this limitation and to add beneficial synergistic effects.

In addition to assessing FnAb pSiNPs using a topical delivery regimen, there are several other approaches that may improve the treatment outcomes. Treatment could begin on Day 0 instead of Day 1, the treatment dose could be increased to overcome the increased bacterial protease burden, the number of treatments could be increased (e.g. Day 0, 3, and 7), and the number of endpoints in the trial could be increased to better understand any effects on wound healing and infection. The genetic db/db model of diabetes could also be used instead of the STZ-model which more closely resembles the phenotypical features and pathology of human diabetic wounds. Studies could also be extended into porcine models which are more similar to the human wound healing processes.

In conclusion, delivering FnAb in pSiNPs did not significantly improve the healing of infected wounds under these specific trial conditions. Further studies are needed where the treatments are topically applied instead of intradermally injected in order to determine if pSiNPs improve the efficacy of FnAb in an infected diabetic wound model. Further investigations using pSiNPs will explore a topical delivery system using a hydrogel to mitigate the complications seen in this chapter.

Chapter Four – Pexiganan Delivered in Porous Silicon Nanoparticles in an Infected Excisional Wound Model

4.1. Background

Chronic wounds are wounds that fail to close within 6 weeks [64, 65]. While there are many reasons for this, one consideration is that these wounds get halted in the inflammatory phase and fail to progress to the proliferation and tissue remodelling phases of healing [68, 252]. Arrested healing is exacerbated by the presence of infection, resulting in a prolonged inflammation that impeded infection resolution [59, 62]. For the wound to heal, the infection needs to be cleared, which is most commonly achieved with antibiotics. However, with the rise of antimicrobial resistance, other methods of clearing infection are being investigated.

Antimicrobial peptides (AMPs) are small peptides with antimicrobial properties. Occurring naturally as part of the immune system of humans, animals, and bacteria, they can also be generated synthetically [171]. In addition to antimicrobial effects, AMPs have also been shown to have pro-wound healing properties. For example, epinecidin, LL-37 and SHAP-1 accelerate wound closure in excisional wound models [177, 182, 183, 253]. Tiger 17 and Tylotoin have been shown to promote the proliferation and migration of keratinocytes and fibroblasts [180, 181]. Pexiganan, is a synthetically created analogue of the naturally occurring AMP, Magainin 2, from the African clawed frog and has been shown to have an MIC_{90} of 16 μg/mL or less in 375 isolates taken from diabetic foot ulcers [204, 205]. However, the possible pro wound healing attributes are little explored. Most notably, pexiganan has been used in a human clinical trial of 835 participants to successfully treat polymicrobial diabetic foot ulcers, demonstrating equal efficacy in a 1% pexiganan cream to antibiotic control [203]. While this pexiganan treatment did not receive FDA approval as it failed to outperform the antibiotic control, interest in pexiganan is on the rise as antibiotic-alternative treatments are urgently sought.

Infected wounds can be extremely hostile, with high levels of inflammation and proteases causing damage to the host tissue and degrading therapeutic treatments. AMPs also have reduced efficacy when topically applied due to degradation in response to the hostile wound environment, being especially susceptible to alkaline pH, proteolysis, hydrolysis, oxidation and haemolysis [169, 212]. One method of protecting therapeutic treatments from the hostility of the infected wound is through the use of nanoparticles. Porous nanoparticles can be loaded with drugs, which then dissolve with a slow-release profile, thereby reducing toxicity and allowing the therapeutic treatment window to be better

captured. Porous silicon nanoparticles (pSiNPs) are biocompatible nanoparticles that degrade into non-toxic orthosilicic acid [157]. Collaborators at Monash University recently generated porous silicon formulations to maximise the loading and release of functional pexiganan for the use in wounds [unpublished]. To optimise this approach, pSiNPs were functionalised through either thermal oxidation (TO) or hydrosilylation (HS), with HS-pSiNPs selected as the preferred method for our *in vivo* study. In support, this study identified the HS-functionalised pSiNPs to have significantly higher loading efficiency than the TO-SiNPs, with a loading efficiency of more than threefold increase (37.2 ± 4.4.% and 8.8 ± 0.5% respectively) (Figure 4.1.A). The HS-functionalised pSiNPs (HS-pSiNPs) released 5.9% of the loaded pexiganan *in vitro* over 6 days, which equated to 11 µg (Figure 4.1.B).

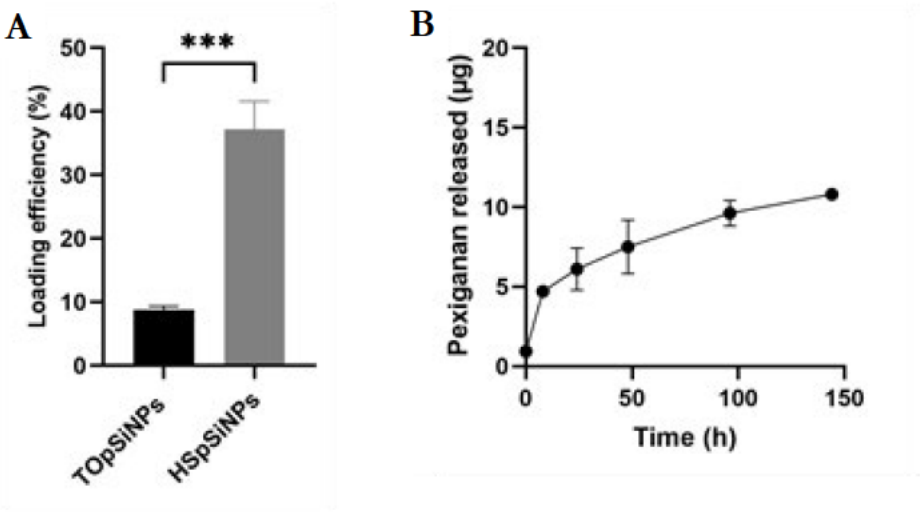

Figure 4.1. Analysis of the porous silicon nanoparticles used to encapsulate pexiganan. **(A)** The loading efficiency of pexiganan in thermally oxidised (TO) and hydrosilylated (HS) pSiNPs **(B)** The release of pexiganan from the HS-pSiNPs. Data is presented as mean ± SD (n = 3). Thermally Oxidised pSiNPs (TOpSiNPs). Hydrosilylated pSiNPs (HSpSiNPs). *** = p > 0.001. Data provided by Darren Laidin, Monash University.

The cytotoxicity of L929 fibroblasts was investigated by assessment of varying doses of pexiganan HS-pSiNPs, where 150 µg of pexiganan was loaded into 1 mg pSiNPs and then serially diluted (Figure 4.2.A). Viability decreased with increased concentration of HS-pSiNPs alone and pexiganan pSiNPs but remained at non-toxic levels for the amounts of both pSiNPs and pexiganan expected to be used in wound studies. Notably, there was no noted difference in viability between cells exposed to HS-pSiNPs alone and pexiganan pSiNPs except at 100 µg/mL (15 µg pexiganan), suggesting that observed toxicity is likely

due to the pSiNPs and only a minor contribution from pexiganan. Free pexiganan was then applied to L929 fibroblasts up to 40 µg/mL to investigate the cytotoxicity of pexiganan on mammalian cells alone (Figure 4.2.B). Cell viability was significantly decreased to below 20% at 40 µg/mL pexiganan. This further illustrates the necessity of a slow-release delivery system that can treat infection without toxicity to healthy mammalian cells.

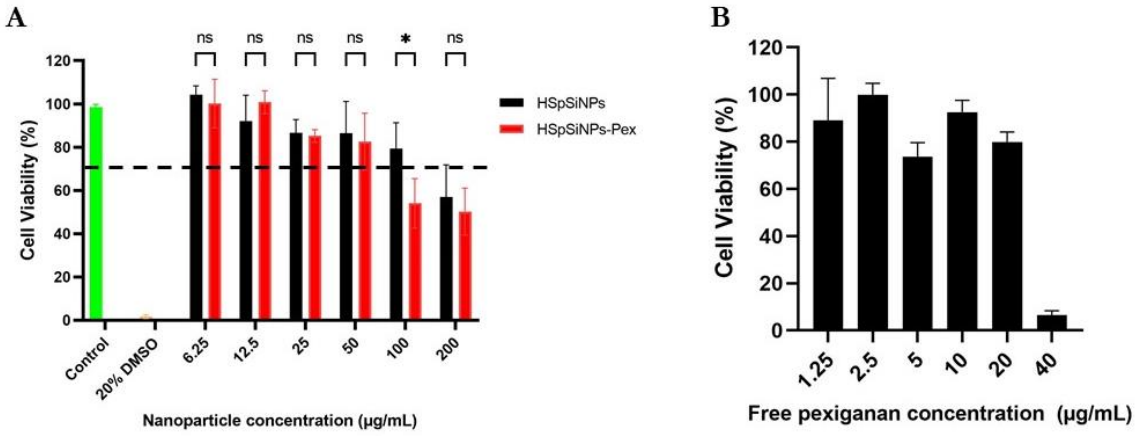

Figure 4.2. Cellular cytotoxicity of the porous silicon nanoparticles and pexiganan on L929 fibroblasts. (A) Cytotoxicity of the HS-pSiNPs and pexi-HSpSiNPs. Dotted line = 70% viability. **(B)** Cytotoxicity of free pexiganan. Data is presented as mean ± SD (n = 3). n.s. = no significance. * = $p > 0.05$. Statistics for **(B)** not included. Data provided by Darren Laidin, Monash University.

The antimicrobial effects of the pexi-pSiNPs were then explored in two laboratory bacterial strains common to infected wounds including *S aureus* and *P. aeruginosa* (Figure 4.3). In an indirect assay, the supernatant from a 96-hour incubation with pexi-pSiNPs was applied to the bacteria (Figure 4.3.A). This resulted in a 5-log reduction in *S. aureus* and a 10-log reduction in *P. aeruginosa* and confirming that pexiganan retained functionality following release from the pSiNPs. A direct assay was also performed where the pexi-pSiNPs were applied directly to the bacteria for a 24-hour incubation, further confirming initial results demonstrating a 6-log reduction in *S. aureus* and a 2-log reduction in *P. aeruginosa* (Figure 4.3.B).

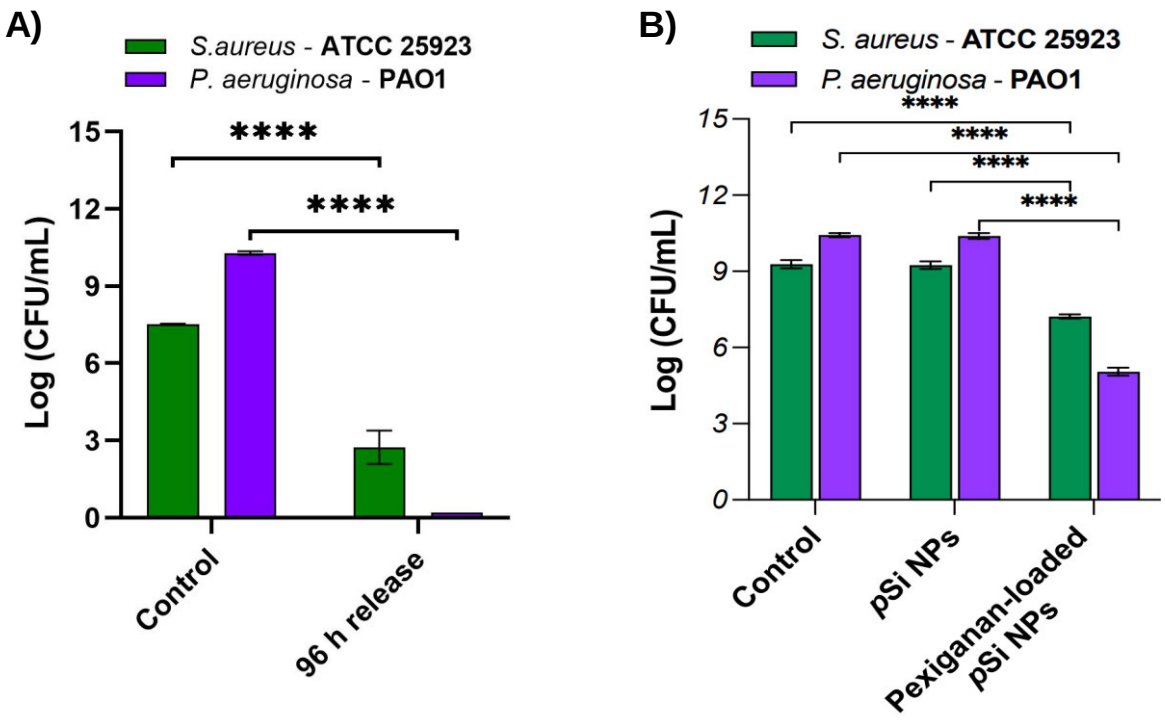

Figure 4.3. Antimicrobial activity of pexi-pSiNPs against *S. aureus* and *P. aeruginosa*. (A) Indirect assay using supernatant from a 96-hour incubation with pexi-pSiNPs **(B)** Direct assay using pSiNPs or pexi-pSiNPs (pexiganan-loaded pSiNPs). Data is shown as mean ± SD. (n=3). **** = $p < 0.0001$. Data provided by Darren Laidin, Monash University.

This chapter therefore investigates the antibacterial efficacy of pexiganan pSiNPs delivered in a hydrogel in *S. aureus*-infected excisional wounds. Moreover, the effect of pexiganan on keratinocyte toxicity was also explored through the use of *in vitro* assays and fluorescent histochemistry with the tissue samples from the animal trial.

4.2. Methods

4.2.1. Fabrication of pSiNPs

The pSiNPs were generated and optimised for pexiganan loading and release by collaborators Darren Laidin, Parham Sahandi-Zangabad and Nico Voelcker at Monash University. pSiNPs were made through the electrochemical etching of a highly boron-doped p++ type silicon wafer on an electrolyte solution consisting of 3:1 (v:v) 48% Hydrofluoric acid (HF):Ethanol (EtOH). The etching waveform consisted of a square wave in which a lower current density of 2 mA/cm^2 was applied for 370 seconds, followed by a higher current density of 184 mA/cm^2 for 0.4 seconds. This two-cycle etching step was repeated for 6 hours to produce a multilayered porous silicon (pSi) film. This film was then lifted from the silicon wafer by using a current density of 184 mA/cm^2 in 1:1 (v/v) 48% HF:EtOH for 2 minutes. The freestanding pSi films were then collected, washed 4 times with ethanol and then stored in anhydrous ethanol. The particles were then made by sonicating the pSi films using an ultrasonic system for 24 hours. The particles were then centrifuged at 16,000 rcf for 7 minutes for three cycles, followed by another three rounds of 2,000 rpm for 1 minute to obtain the size selected pSiNPs.

Both the nanoparticle size and the size of the pore diameter were determined using transmission electron microscopy (TEM) (JEOL JEM-2100F) equipped with a field emission gun, operating at 200 kV. The samples were prepared by dispersing pSiNPs in ethanol (100 µg/mL). The samples were ten spotted (10 µL) onto 300-mesh copper grids and dried under nitrogen flow at room temperature. Measurements were then performed on 20 randomly selected particles using ImageJ software. The resulting pSiNPs were 340 nm in size with a pore diameter of 10 nm.

4.2.2. Hydrosilylation Functionalisation of pSiNPs

The pSiNPs were functionalised at Monash University by mixing the pSiNPs with 10-undecenoic acid (UDA) and sparged under nitrogen for 30 minutes to eliminate any traces of oxygen within the mixture. The solution was then stirred and heated to 120°C for 20 hours using a magnetic stirrer on a hot plate. The functionalised pSiNPs were then rinsed with ethanol three times to remove any remaining UDA.

4.2.3. Loading Pexiganan into the pSiNPs

To prepare for the *in* vivo trial, pexiganan (2.5 mg) was mixed with the pSiNPs (5 mg) at 1:2 ratio to a final concentration of 2 mg pexiganan/mL pSiNPs, and incubated for 16 hours at 4°C. To wash off unloaded pexiganan, the sample was centrifuged three times at 20,000 rcf for 10 minutes with fresh PBS buffer replaced each time. The pexiganan remaining in the supernatant was measured using a Nanodrop (Thermo Scientific Nanodrop) at 220 nm and the concentration determined using a calibration curve. The loading efficiency of pexiganan into pSiNPs for this study was calculated to be ~60%. The loading efficiency and loading capacity was then calculated as follows.

$$M_1 = M_{stock} - M_{totalspnt}$$

$$\text{Loading Capacity} = M_1/M_{pSiNPs}$$

$$\text{Loading Efficiency (\%)} = M_1/M_{stock} \times 100$$

M_{stock} = amount of pexiganan used in loading solution (µg)
$M_{totalspnt}$ = total amount of pexiganan (µg) remaining in the supernatant
M_{pSiNPs} = mass of the pSiNPs used (µg)

4.2.4. Hydrogels

Pexi-pSiNPs were formulated into a thermosensitive hydrogel for topical wound healing. The hydrogel is a liquid when stored on ice allowing effective mixing and equal distribution of the pexi-pSiNPs suspension. However, when applied to skin, the increased temperature allows the hydrogel to set on the wound surface. Hydrogels provide a moist, protected environment that promote wound healing and can be loaded with treatments [254]. This hydrogel can help promote wound healing by providing a moist, protected environment that degrades to 85% of its initial weight within a week [255]. All treatment groups were administered in 100 µL hydrogel except for ciprofloxacin which was administered in PBS. Pluronic F127 hydrogels were made by mixing 19% Pluronic F127 and 10% Propylene Glycol (Sigma, Australia; W294004) in PBS then incubated overnight at 4°C. Treatments were centrifuged down and gently resuspended in the hydrogel the morning of use.

4.2.5. Pexiganan pSiNP Treatment of *S. aureus* Infected Mouse Wounds

This animal trial was approved by the UniSA animal ethics committee and carried out at the Core Animal Facility (CAF). The animal ethics number for this animal trial is U22/23. 8-10 week-old female balb/c mice were obtained from Australian Bio Resources (ABR). The infected excisional wound model was utilised as previously described in Section 2.2.4 and 2.2.5, with 10 mm wounds created. Mushy food was provided daily, and the nails trimmed at the time of surgery to limit scratching.

An animal trial of 32 mice was conducted to test the efficacy of the pexi-pSiNPs in an infected excisional wound model (Figure 4.4). Power calculations determined that a sample size of 8 mice per group will provide 97% power at the 5% level of significance to demonstrate an average reduction of 5 mm in wound size between groups with a standard deviation of 2.3, using an unpaired Student's t test. These power calculations were based on a reduction of 20% in wound size which is considered biologically significant. Four groups of 8 were designated one of the following treatments: pexiganan (pexi)-pSiNPs, pexi (pexiganan alone), Hydrogel (vehicle control), and ciprofloxacin (antibiotic control).

All treatments, except the ciprofloxacin control, were administered in a thermosensitive F127 pluronic hydrogel that is non-toxic, biocompatible and biodegradable. The pexi-pSiNPs dose was 80 µg administered to each wound, with 20 µg pexiganan expected to be released by the nanoparticles, and the pexiganan alone dose was 20 µg to match this. The ciprofloxacin treatment was at a dose of 20 µg per wound (stock: 4 mg/mL in PBS).

The mice were treated once on Day 1, 24 hours after wounding and infection. The mice were humanely killed on Day 7 and the wounds excised. Half the wounds went to histology, one quarter to quantitate CFUs, and one quarter snap frozen in liquid nitrogen and stored at -80°C.

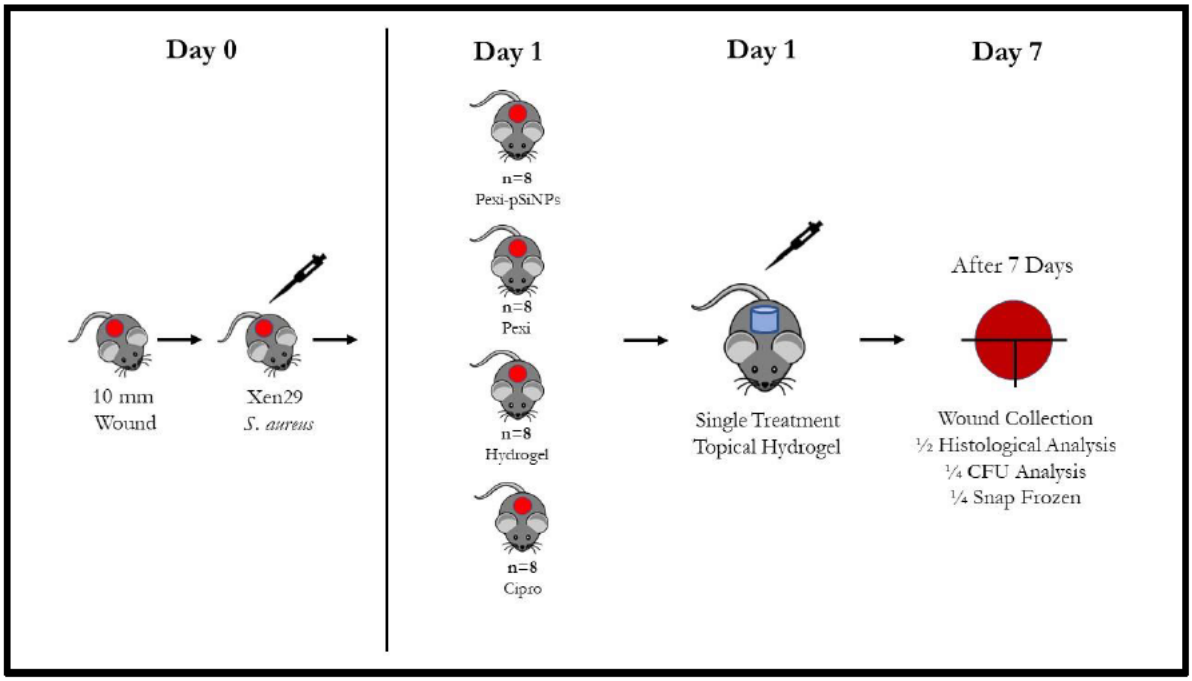

Figure 4.4. A schematic representation of the treatment groups and the infected excisional wound model used in the pexiganan trial.

4.3. Results

4.3.1. Pexiganan is not cytotoxic to keratinocytes at low doses

Treatments for infected wounds need to not be detrimental to cells integral to the wound healing process and ensure wound healing is not further impaired. Keratinocytes are important for the re-epithelialisation of the wound, allowing the wound to close over and prevent further infection or contamination. To investigate the cytotoxicity of pexiganan on keratinocytes, a series of *in vitro* assays were performed using a human keratinocyte cell line (HaCaTs).

First, a resazurin assay was performed to test the viability of the keratinocytes after a 24-hour incubation with various concentrations of pexiganan. As can be observed in Figure 4.5.A, pexiganan began to significantly reduce cell viability at 15 µg/mL. Pexiganan did not cross the cytotoxic threshold until 80 µg/mL at 70% viability, though 60 µg/mL was close at 75% cell viability. The higher doses of pexiganan at 80 µg/mL had a cell viability of 62%, and 100 µg/mL cell viability of 47%.

Next a WST-1 assay was performed to measure the effect of pexiganan on the proliferative abilities of the keratinocytes (Figure 4.5.B). Pexiganan promoted proliferation at low doses of 1 µg/mL ($p<0.01$) and 5 µg/mL ($p<0.05$) by 10% and 8% respectively. Doses between 10 and 20 µg/mL had no effect on proliferation, while proliferation significantly declined at ≥40 µg/mL ($p<0.0001$). The remaining high doses, 60, 80 and 100 µg/mL were at the cytotoxic threshold at 75%, 70% and 68% cell viability respectively.

Scratch wound assays using a wound maker and an Incucyte imaging were used to investigate the effects of pexiganan on migration (Figure 4.6). Pexiganan negatively affected migration in a dose-dependent manner, with wounds treated with 100 µg/mL pexiganan taking the longest to heal. Pexiganan had no significant effect on migration up to 20 µg/mL. Overall, this indicates that pexiganan may detrimentally impact wound healing in a time and dose dependent manner, suggesting that a slow-release delivery profile, as facilitated with the use of pSiNPs may be advantageous for *in vivo* applications.

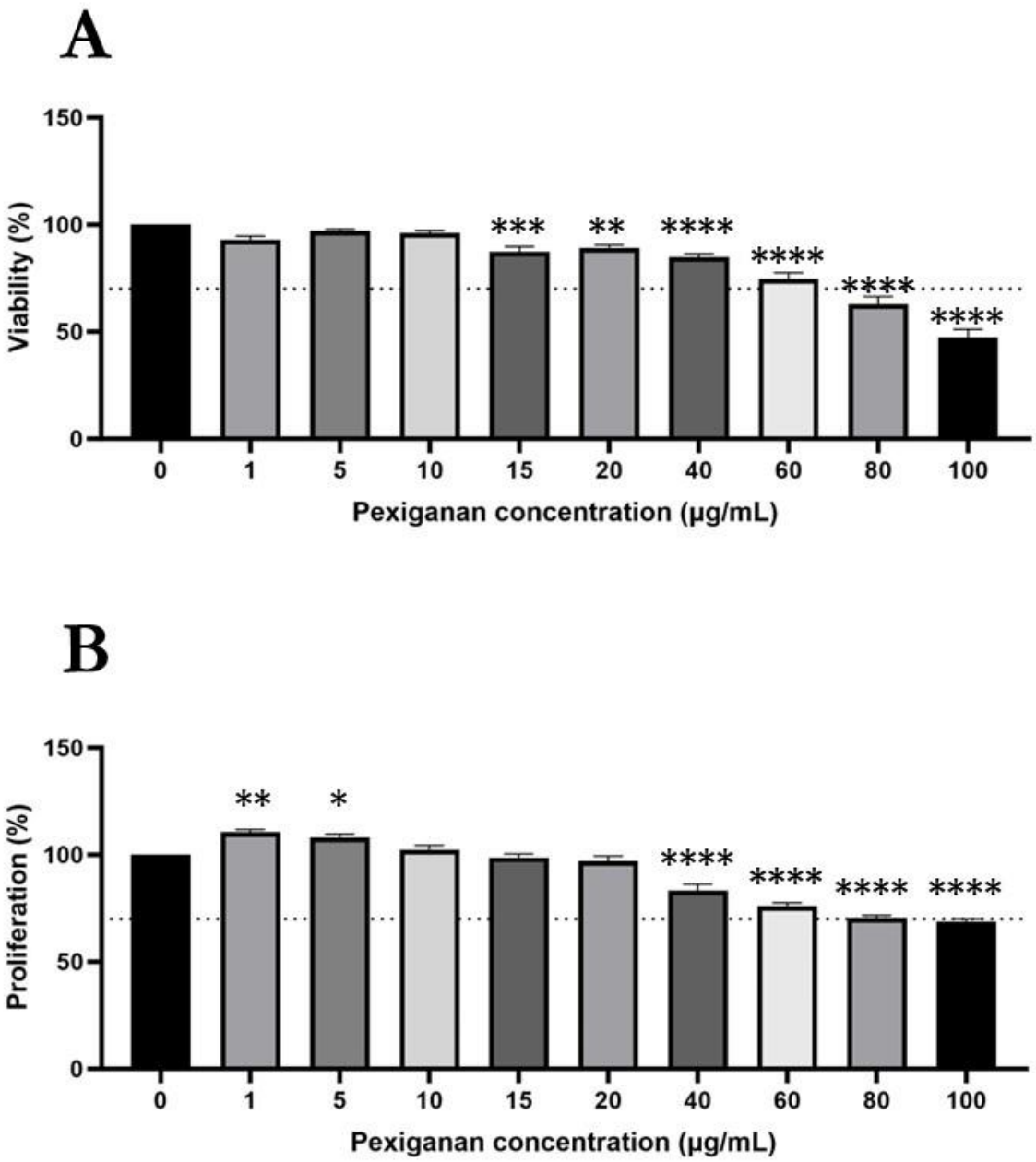

Figure 4.5. Low dose pexiganan is non-cytotoxic and increased proliferation of HaCaTs (A) The cell viability of HaCaTs 24 hours post-treatment with pexiganan. **(B)** The proliferation of keratinocytes 24 hours post-treatment with pexiganan. Data is normalised to the cells only control and is presented as mean ± SEM, n = 3. Dashed line represents 70% cell viability. Statistical significance was achieved through a One-way ANOVA and (A) Dunnett's (B) Tukey's Multiple Comparisons test. * = $p < 0.05$, ** = $p < 0.01$, *** = $p < 0.001$, ****= $p < 0.0001$.

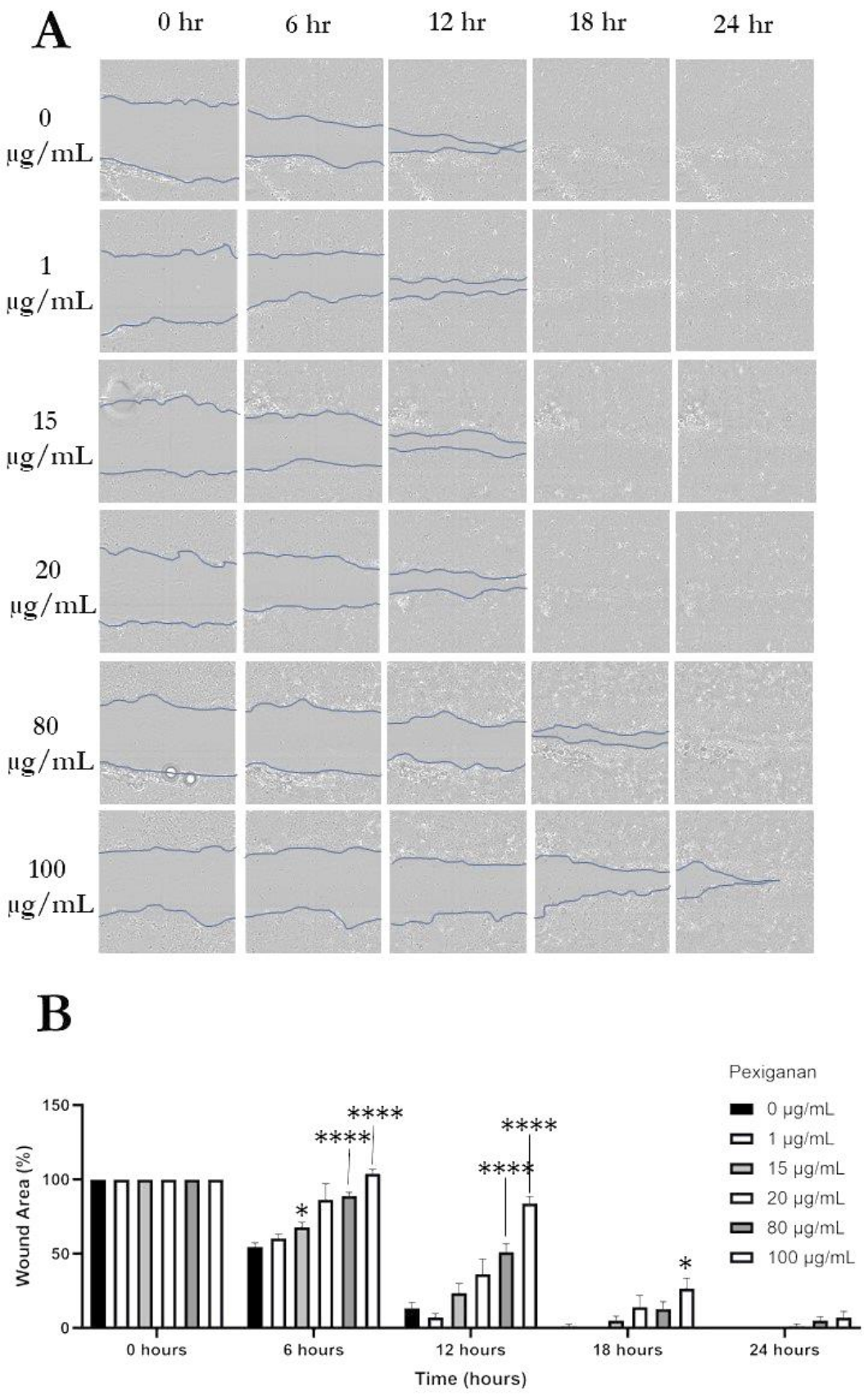
A
0 hr
6 hr
12 hr
18 hr
24 hr
0 µg/mL
1 µg/mL
15 µg/mL
20 µg/mL
80 µg/mL
100 µg/mL
B
Pexiganan
0 µg/mL
1 µg/mL
15 µg/mL
20 µg/mL
80 µg/mL
100 µg/mL
Wound Area (%)
150
100
50
0
****
****
****
****
*
*
0 hours
6 hours
12 hours
18 hours
24 hours
Time (hours)

Figure 4.6. Pexiganan negatively effects the migration of keratinocytes at higher doses. **(A)** Representative images of pexiganan-treated keratinocyte scratch wounds at 0, 6, 12, 18, and 24 hours. The wound margins are outlined. **(B)** The quantified wound area over 24 hours of pexiganan-treated keratinocytes presented as a percentage of the original wound size. The wound area was measured using Incucyte zoom software. Data is presented as mean ± SEM, n = 3. Significance shown is compared to the cells only control. Statistical significance was achieved through a Two-way ANOVA and a Dunnett's Multiple Comparisons Test. * = $p < 0.05$, **** = $p < 0.0001$.

4.3.2. Porous silicon nanoparticles improved the efficacy of pexiganan on wound healing in an infected excisional wound model

To investigate the antibacterial efficacy of pexiganan pSiNPs, a 10 mm excisional wound was created on the backs of mice and then infected with bioluminescent *S. aureus* (ATCC12600; Xen 29). A single treatment of pexi-pSiNPs, free pexiganan (pexi), or hydrogel only was administered topically on Day 1, 24 hours post-injury/infection. Treatments were administered in a topical thermosensitive hydrogel. The mice were monitored daily for seven days following surgery and infection.

All wounds created on Day 0 were uniform in size without significant variation between the treatment groups. Wounds from the vehicle and free pexi treatment groups significantly contracted 24 hours after their creation ($p<0.01$ and $p<0.001$) but not the pexi-pSiNPs group, which was accounted for by procedure variability as no wounds were yet treated at this point (Figure 4.7). However, as wounds were treated on Day 1 (following capturing wound photographs), subsequent data was expressed as a percentage of Day 1.

Digital images of the wounds were taken daily, starting immediately post-surgery (Figure 4.8.A). For both the wound gape (Figure 4.8.B) and the wound area (Figure 4.8.C), the pexi-pSiNPs performed significantly better compared to the hydrogel vehicle treatment control group, with the effect most pronounced between days 3 and 5 post-injury. Notably, healing was worse in the free pexi compared to vehicle-treated wounds (non-significant), suggesting free pexi may be cytotoxic and the pSiNPs reduced this negative effect through its slow-release kinetics release of pexiganan.

The histological measurements on Day 7 (Figure 4.9.A) did not show any statistical significance (Figure 4.9.B-E). However, there was a trend towards pexi-pSiNPs increasing the epidermal thickness (Figure 4.9.D) and re-epithelialisation (Figure 4.9.E).

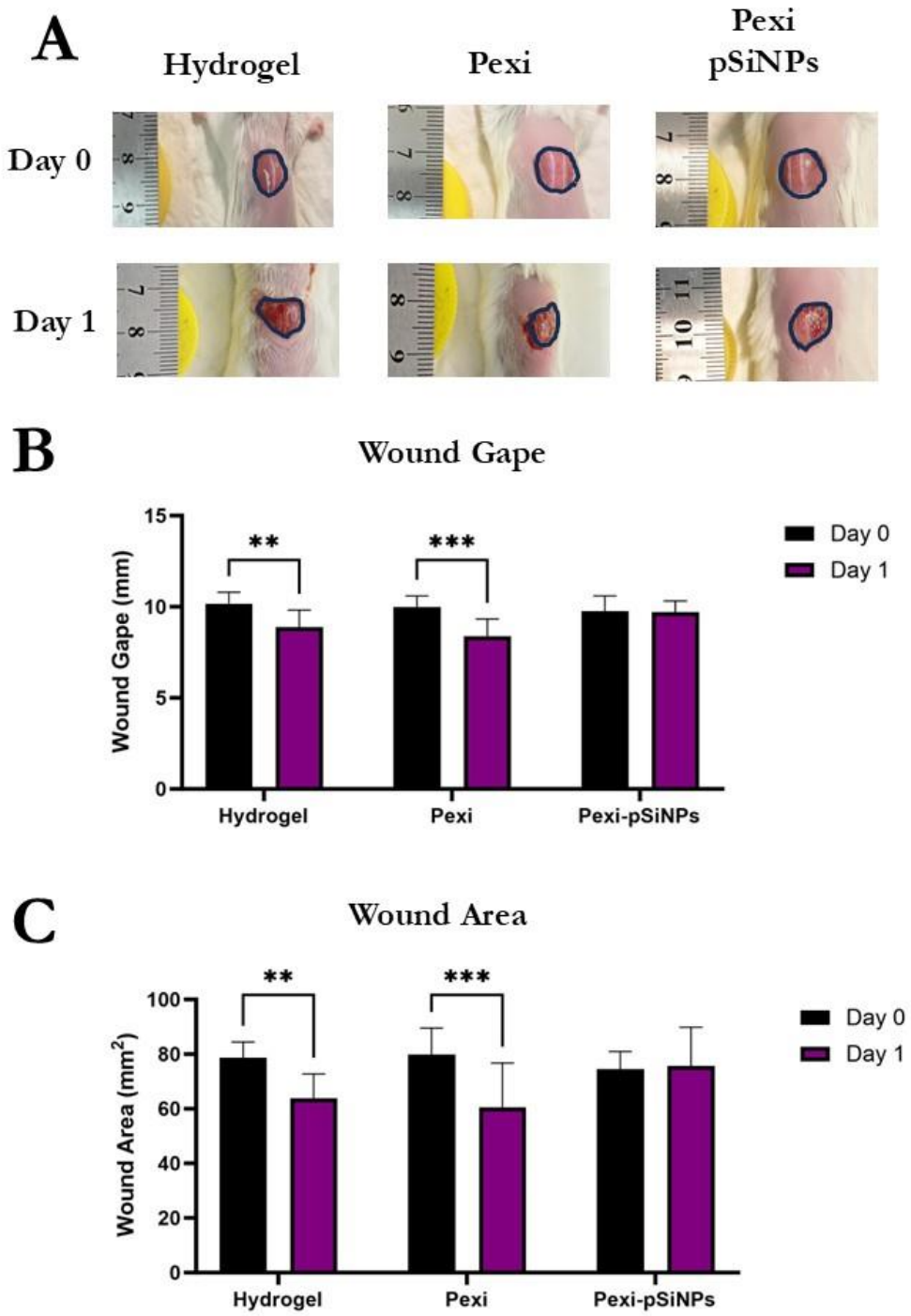

Figure 4.7. The wound size decreased between the day of surgery (Day 0) and the day of treatment (Day 1). (A) Representative images of the wounds on Day 0 immediately after surgery and Day 1 prior to treatment **(B)** The Day 0 and Day 1 measurements for Wound Gape **(C)** Comparing the Day 0 and Day 1 measurements for the Wound Area. Statistical significance was achieved through a Two-way ANOVA and Sidak's Multiple Comparisons Test. Data is presented as mean ± SD (n = 8). ** = $p < 0.01$, *** = $p < 0.001$. Pexi = pexiganan (free).

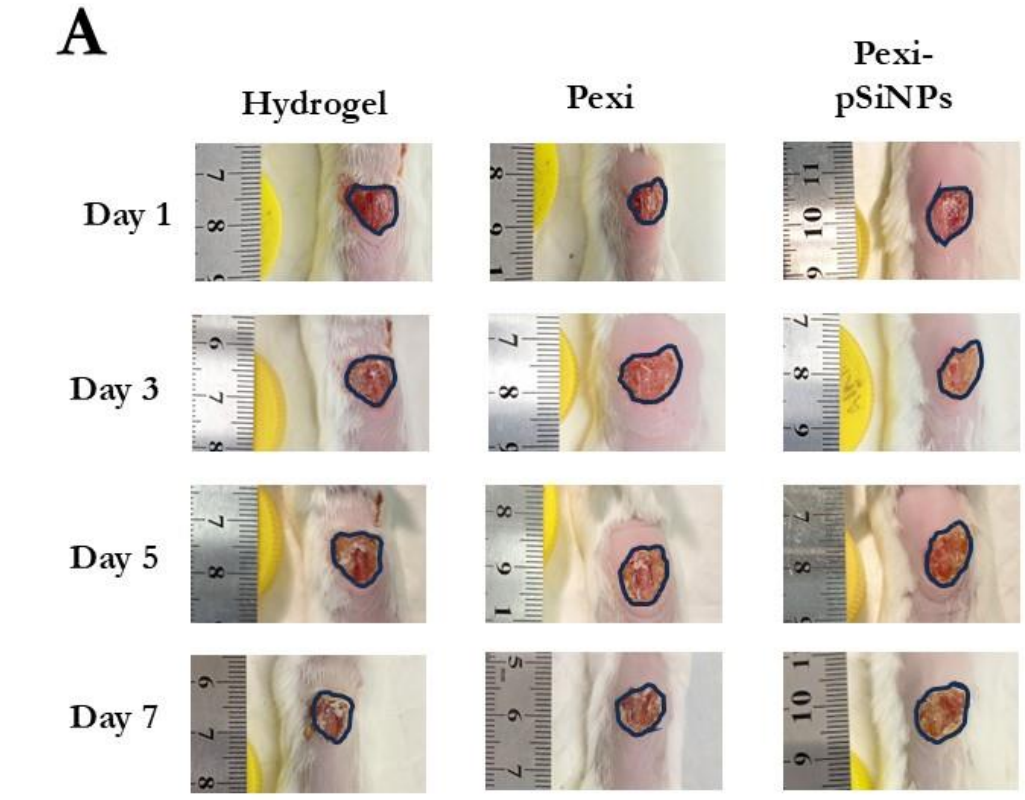
A
Hydrogel
Pexi
Pexi-
pSiNPs
Day 1
Day 3
Day 5
Day 7

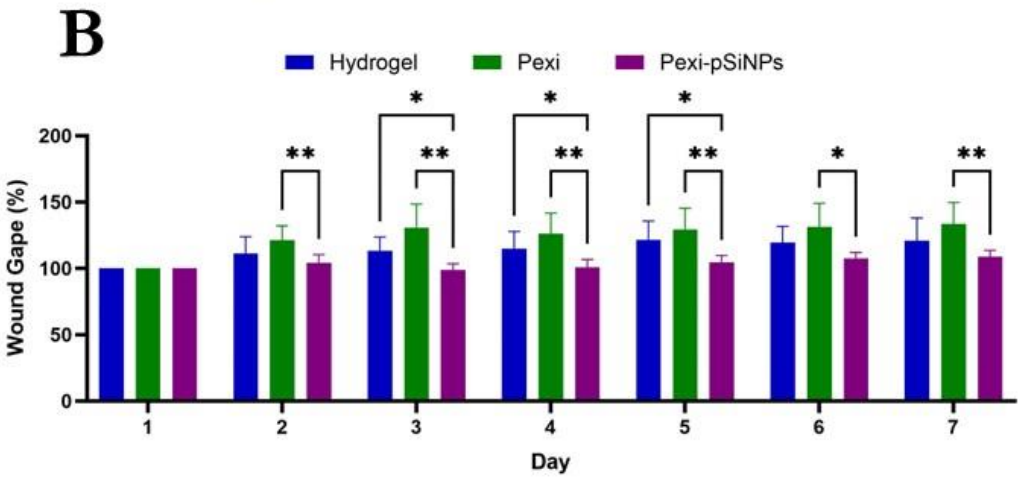
B
Hydrogel
Pexi
Pexi-pSiNPs
Wound Gape (%)
Day

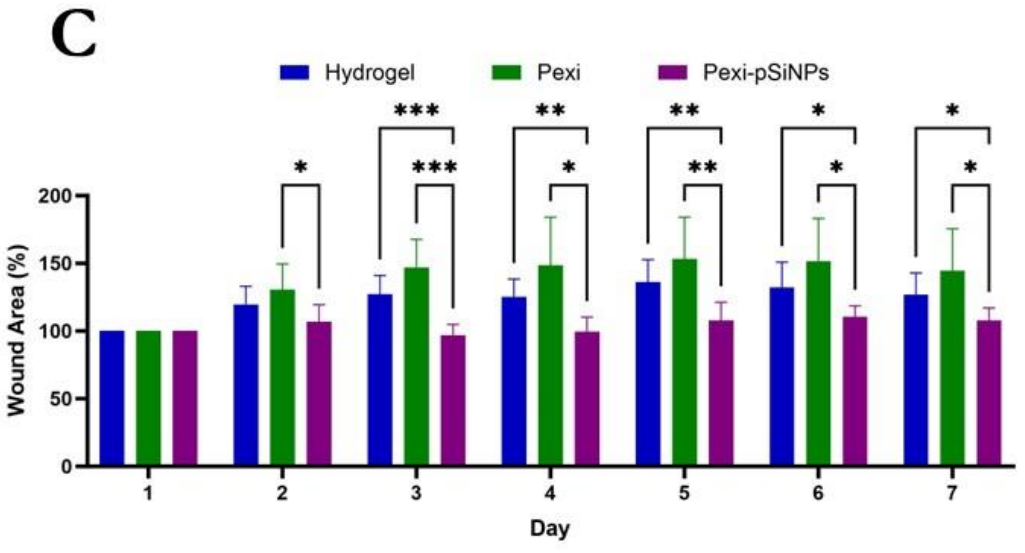
C
Hydrogel
Pexi
Pexi-pSiNPs
Wound Area (%)
Day

Figure 4.8. Pexi-pSiNPS improved wound healing over the 7-day trial. (A) Representative images of the wounds taken over the 7-day trial. **(B)** The Wound Gape **(C)** The Wound Area. Data was measured using ImagePro Plus. Data is normalised to the day of treatment at Day 1. Data is presented as mean ± SD (n = 8). Statistical significance was achieved through a Two-way ANOVA and Tukey's Multiple Comparison's Test. * = $p > 0.05$, ** = $p > 0.01$, *** = $p > 0.001$. Pexi = pexiganan (free).

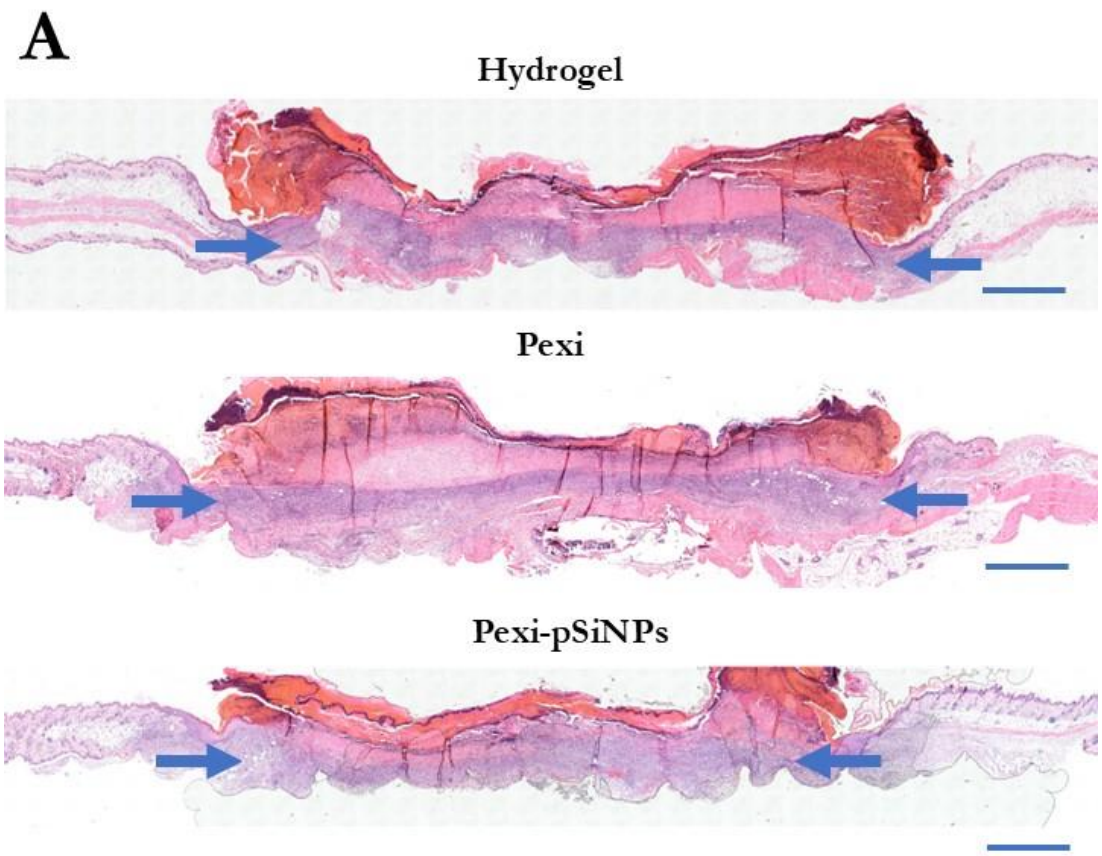
A
Hydrogel
Pexi
Pexi-pSiNPs

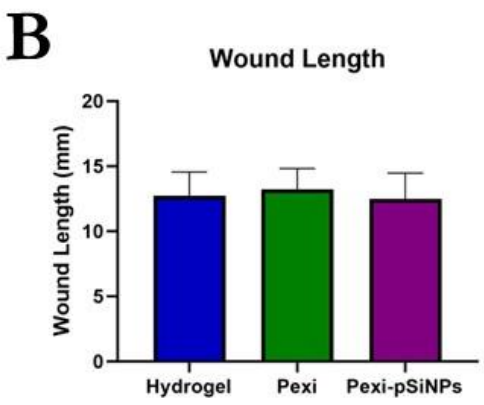
B
Wound Length
Wound Length (mm)
20
15
10
5
0
Hydrogel
Pexi
Pexi-pSiNPs

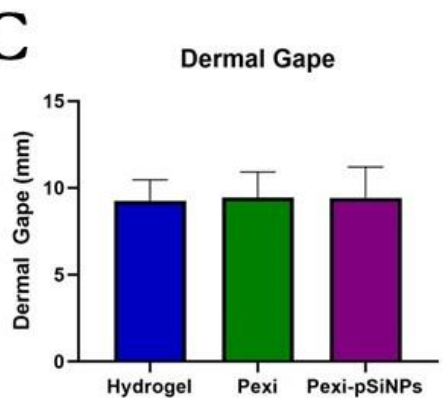
C
Dermal Gape
Dermal Gape (mm)
15
10
5
0
Hydrogel
Pexi
Pexi-pSiNPs

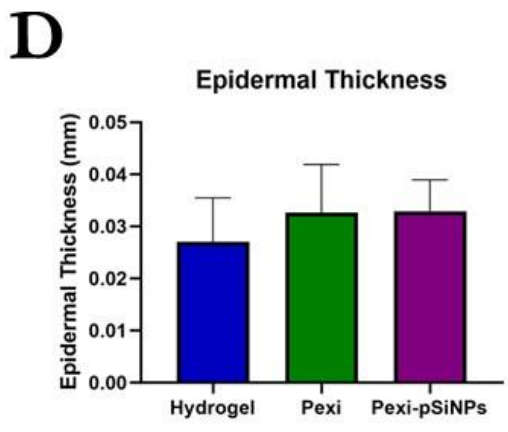
D
Epidermal Thickness
Epidermal Thickness (mm)
0.05
0.04
0.03
0.02
0.01
0.00
Hydrogel
Pexi
Pexi-pSiNPs

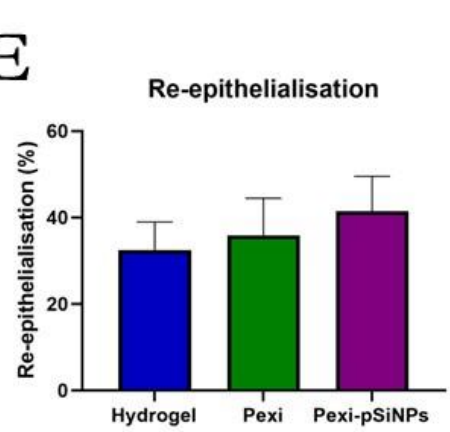
E
Re-epithelialisation
Re-epithelialisation (%)
60
40
20
0
Hydrogel
Pexi
Pexi-pSiNPs

Figure 4.9. Wounds treated with pexi-pSiNPs trended towards higher rates of re-epithelialisation indicating improved wound healing. (A) Representative images of the excised wounds at day 7 post-injury stained with Haematoxylin and Eosin. Arrows indicate dermal gape. Scale bar is 1 mm. **(B-E)** The histological measurements as measured using ImagePro Plus. Data is presented as mean ± SD (n = 8). Pexi = pexiganan (free).

4.3.3. Pexiganan had no effect on neutrophil recruitment to the wound bed or on the proliferation of keratinocytes.

Day 7 wounds were immunofluorescently stained to assess the impact of pexiganan on proliferating cell nuclear antigen (PCNA) as a measure of proliferating keratinocytes (Figure 4.10) and quantified as a percentage of total cell counts. Porous silicon nanoparticles did not appear to increase the efficacy of pexiganan with the pexiganan only treatment having the highest numbers of PCNA-positive cells and the pexi-pSiNPs having the least. This may indicate that the wounds treated with pexi have reached the proliferative phase of wound healing while the other groups are still in the inflammatory phases.

Tissue samples were stained with NIMP-R14 which binds the Ly6C and Ly6G antigens on neutrophils. NIMP-R14-positive cells counted and normalised to wound area to quantify neutrophil infiltration into the wound bed (Figure 4.11). While not statistically significant, the data trends towards the pexi-pSiNPs having the highest number of neutrophils in the wound bed and the hydrogel control with the least. This indicates the porous silicon nanoparticles increased the recruitment of neutrophils to the wound bed caused by pexiganan. However, the overall number of neutrophils in the wound bed was low. This may be due to neutrophils being more prominent in the earlier days post-wounding, though differences at Day 7 post-wounding may still indicate prolonged inflammation.

4.3.4. Pexiganan had no effect on collagen deposition at seven days post-injury.

Collagen is deposited by fibroblasts in the later stages of wound healing, with more collagen being indicative of a more mature wound. Masson's trichrome total collagen stain was used to measure the amount of collagen deposition in the wounds on Day 7 (Figure 4.12.A). There was no significant difference in collagen deposition between the treatment groups (Figure 4.12.B). While insignificant, there is a slight decrease in collagen deposition in the pexi-pSiNPs and pexiganan treatment groups compared to the hydrogel control. Overall, there appears to be a high amount of collagen in the wounds despite being only 7 days post-wounding and the wounds still being open (Figure 4.8 and Figure 4.9). This may be indicative of fibrosis, or a positive effect on fibroblasts but not keratinocytes.

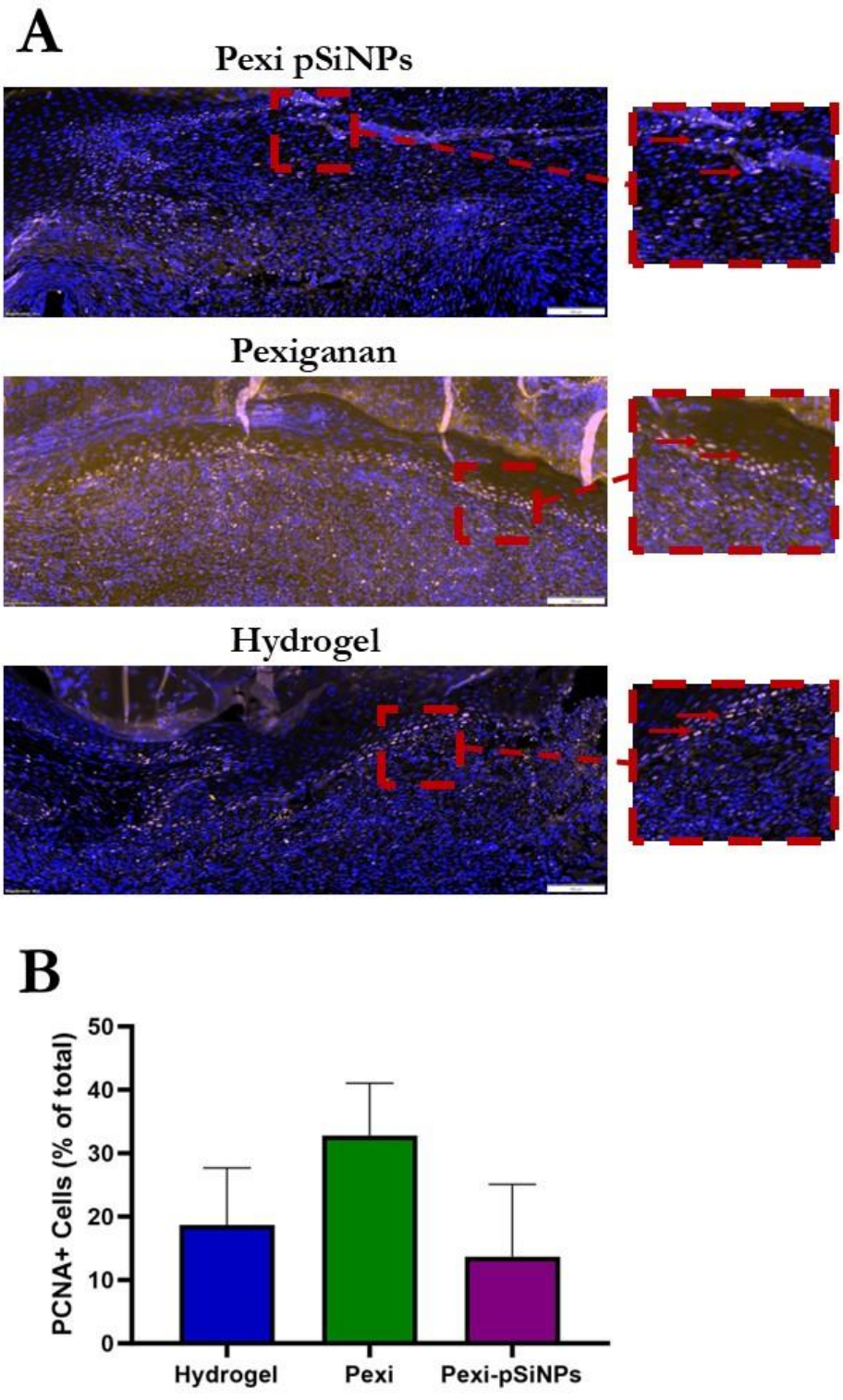

Figure 4.10. Analysis of proliferating cell nuclear antigen (PCNA)-positive cells in Day 7 wounds. (A) Representative images of PCNA positive cells in the epidermis. PCNA (orange)/ DAPI (blue). **(B)** PCNA positive cells expressed as a percentage of total cell counts. Data is presented as mean ± SD. Scale bar is 100 µM. 20x magnification. n=4.

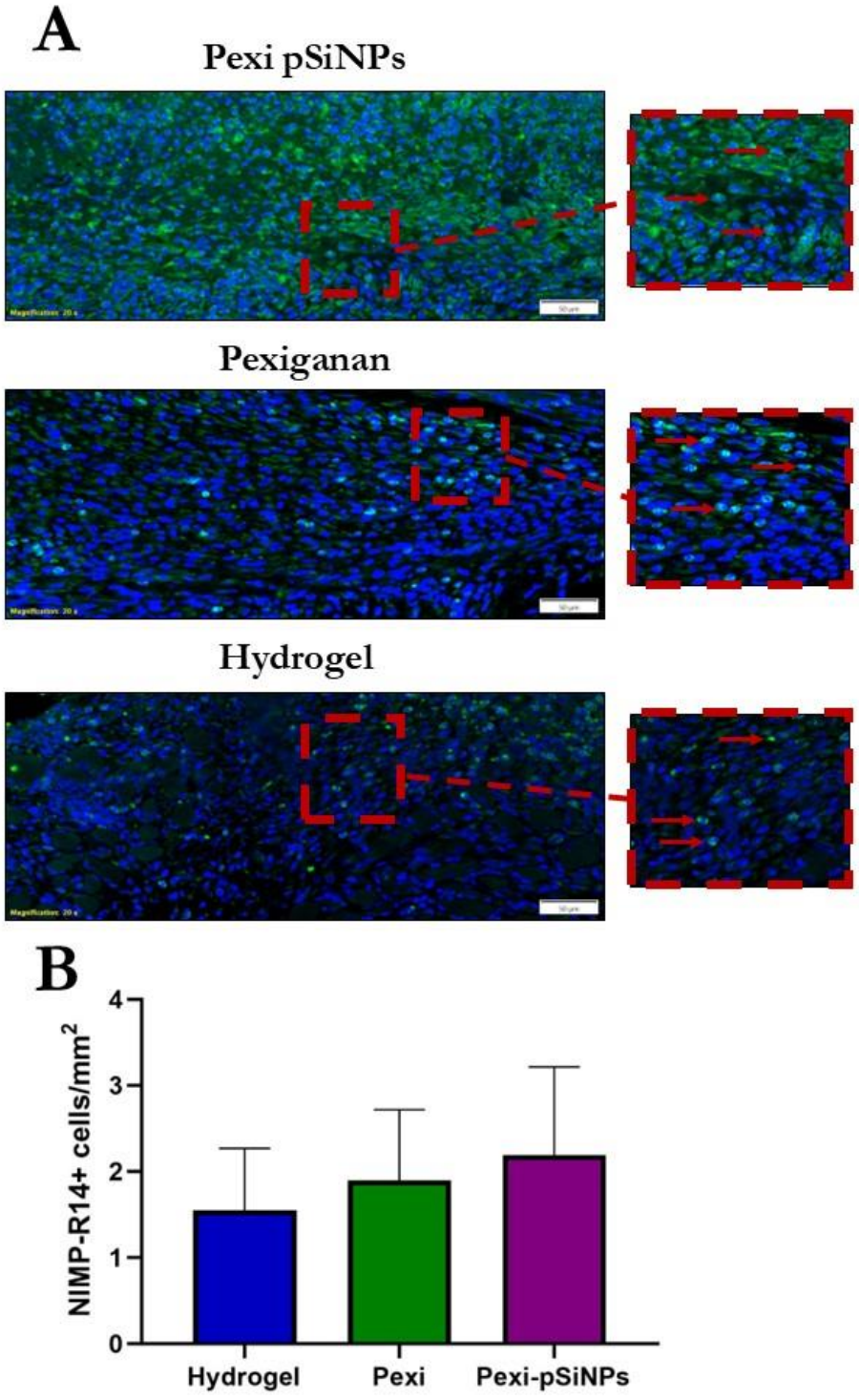

Figure 4.11. Analysis of neutrophil infiltration in Day 7 infected wounds. (A) Representative images of NIMP14 positive cells in the wound bed. NIMP14 (green)/ DAPI (blue). **(B)** NIMP14 positive cells normalised to wound area. Data is presented as mean ± SD. Scale bar is 100 µM. 20x magnification. n=4.

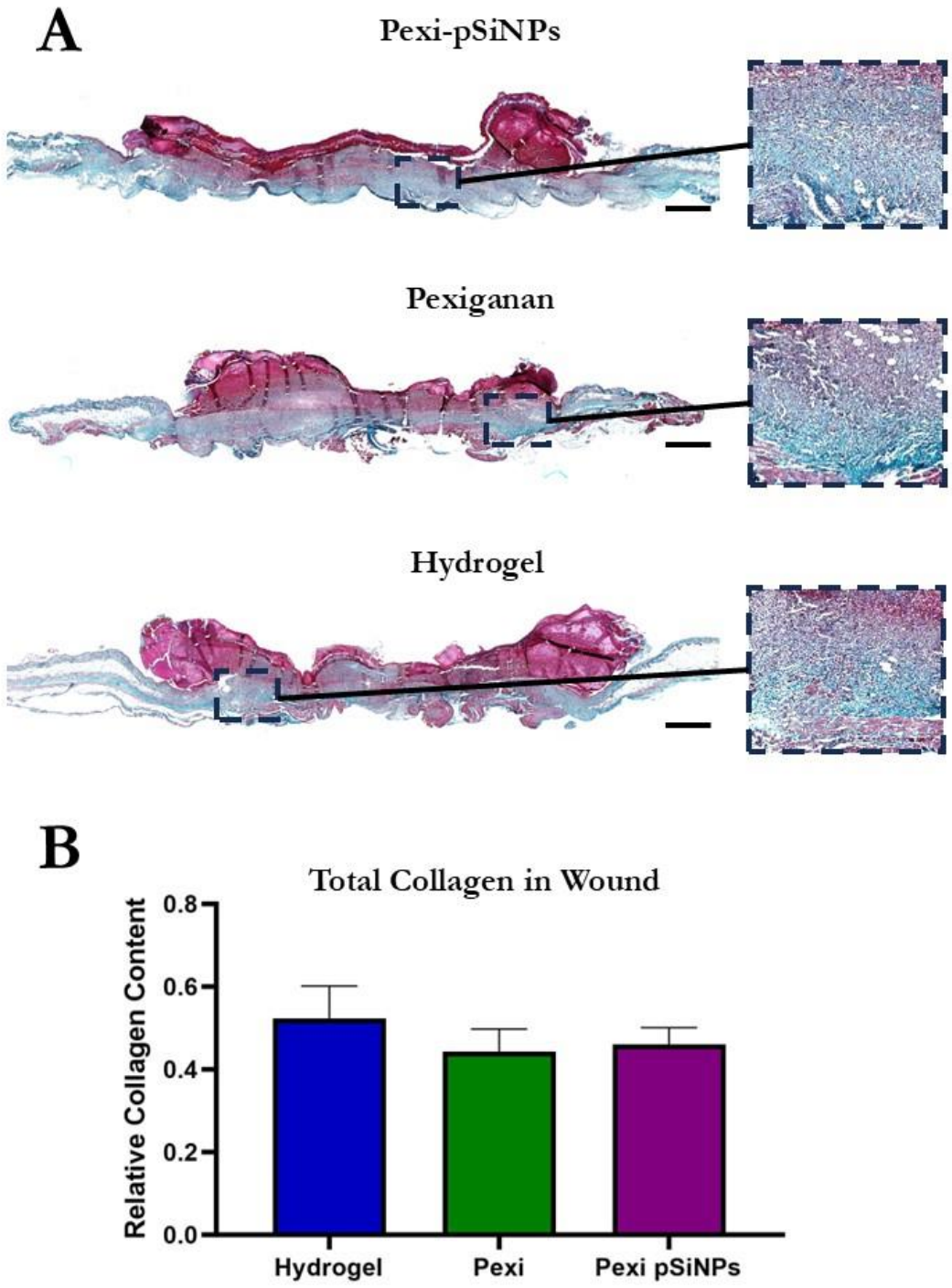

Figure 4.12. Equal amounts of total collagen measured by Masson's Total Collagen Trichrome Stain in Day 7 infected wounds. (A) Representative images of the excised wounds stained with Masson's Total Collagen Trichrome Stain. **(B)** The total collagen in the wound measured using ImageJ. Data is presented as mean ± SD. n = 4. Scale bar = 1mm.

4.3.5. Pexiganan had no significant effect on infection compared to the vehicle control regardless of delivery method.

The bacterial burden was measured daily using the IVIS Live Imaging System (Figure 4.13.A). All wounds started with an equal burden of infection on Day 0 (Figure 4.13.B). The bacterial burden remained even on Day 1 (Figure 4.13.B), however, there was a significant decrease between Day 0 – the day of inoculation – and Day 1 – prior to treatment (Figure 4.13.C). In order to account for this, data is baseline-corrected to Day 1 instead of Day 0.

As can be seen in Figure 4.14.A, the infection increased within 24 hours of treatment, regardless of treatment, with a peak on Day 3. While there was no significance between the treatment groups (Figure 4.14.B), there was a trend where pexi-pSiNPs controlled the infection better than the pexiganan alone, with a smaller peak in infection over the course of the trial. There is also a trend that from Day 5 onwards, the hydrogel alone controlled the treatment the best. However, this is not supported by the CFUs measured on Day 7 (Figure 4.14.C) where there is no significant difference between the three treatment groups.

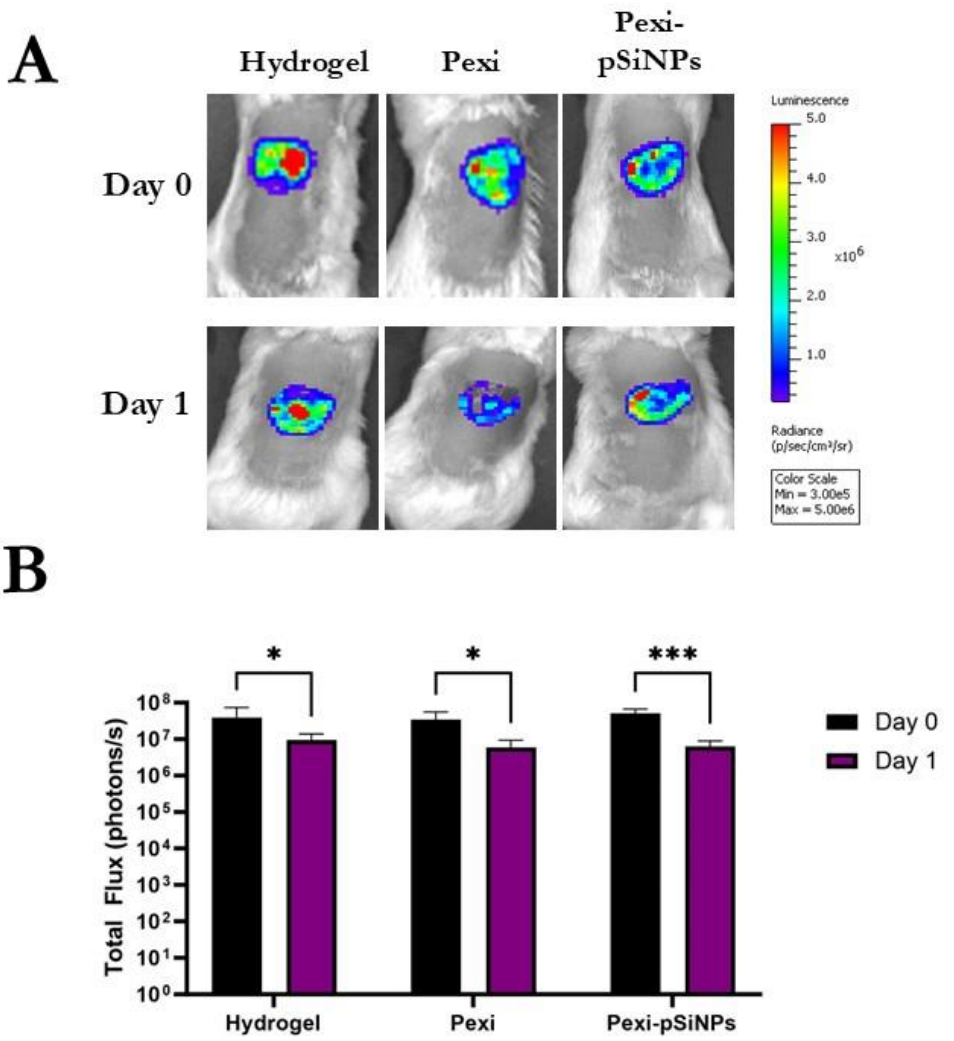

Figure 4.13. Equal bacterial burden in wounds at Day 1 post-bacterial inoculation. (A) Representative images showing the bioluminescence of the wounds on Day 0 **(B)** The bacterial burden on Day 0 and Day 1. Data is presented at mean ± SD. Statistical significance was achieved through a Two-way ANOVA and Sidak's Multiple Comparisons Test. n = 8. * =$p < 0.05$, *** =$p < 0.001$. Pexi = pexiganan (free).

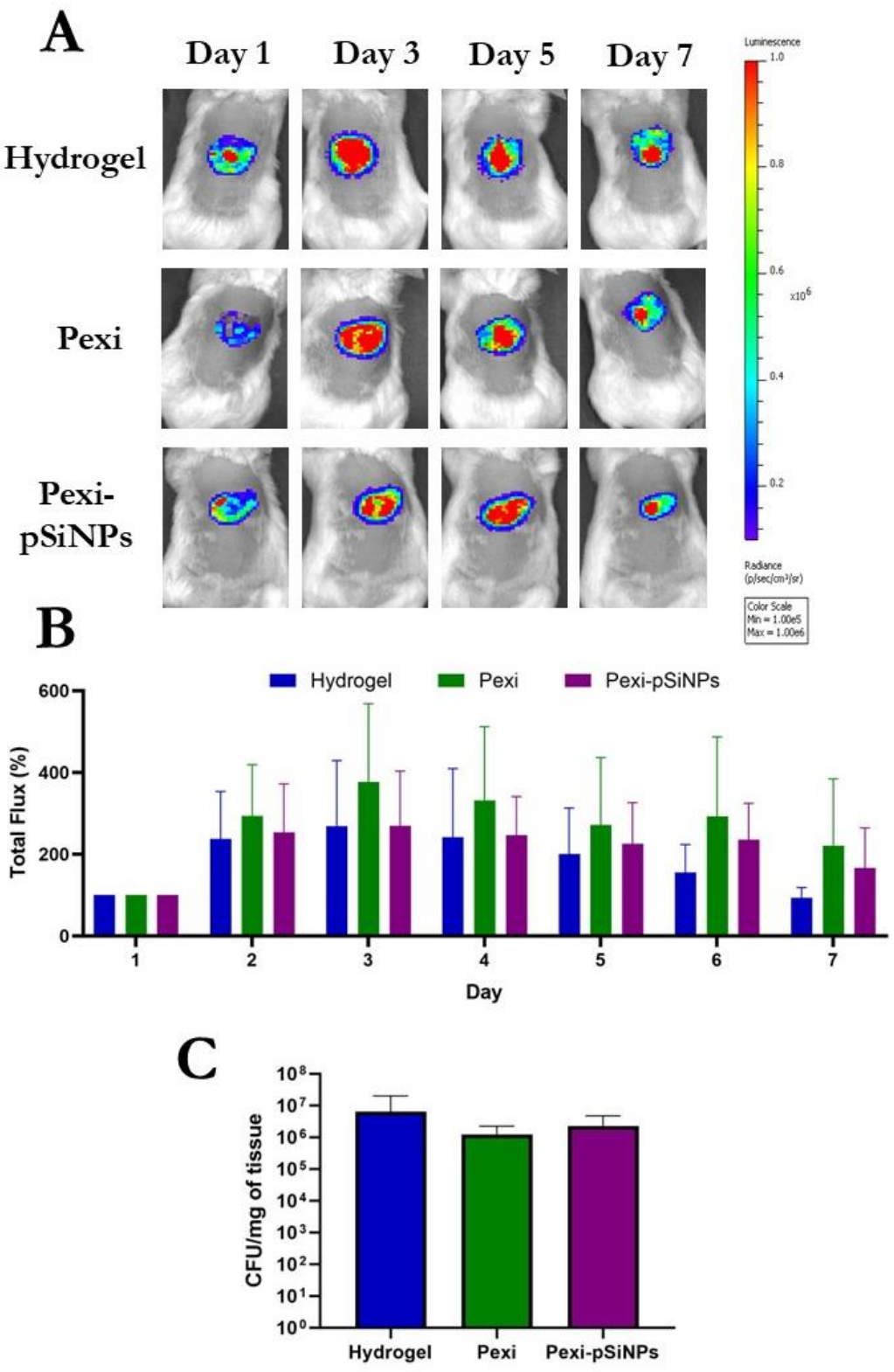

Figure 4.14. Pexiganan did not significantly control the infection. (A) Representative bioluminescent images taken over the 7-day trial. **(B)** The total flux measured over the course of the study by the IVIS and normalised to the day of treatment – Day 1. **(C)** The CFUs measured at the end of the study presented as per mg of tissue. Data is presented as mean ± SD (n = 8). Pexi = pexiganan (free).

4.3.6. The antibiotic treatment control showed the efficacy of the infected excisional wound model.

To assess the efficacy of pexi-pSiNPs, the antibacterial properties of pexi-pSiNPs was compared to an accepted treatment modality, namely an antibiotic control, ciprofloxacin. As can be seen in Figure 4.15.A, the wound size remained reasonably unchanged over the 7-day period when treated with ciprofloxacin. However, ciprofloxacin still performed better than the hydrogel control from Day 3 onwards (Figure 4.15.B and Figure 4.15.C). The ciprofloxacin treatment group had a slight decrease in wound area on Day 3 (6%), ending with a 17% decrease on Day 7. There was a significant difference between Day 1 and Day 7 for both treatment groups (Figure 4.15.C). The infection dramatically decreased over 7 days, as can be seen in Figure 4.15.D and was significant compared to the hydrogel control from Day 5 onwards (Figure 4.15.E). Overall, this confirms the efficacy of the infected excisional wound model and industry standard ciprofloxacin is effective at reducing bacterial load which subsequently improves the wound healing cascade by removing infection as a blockade.

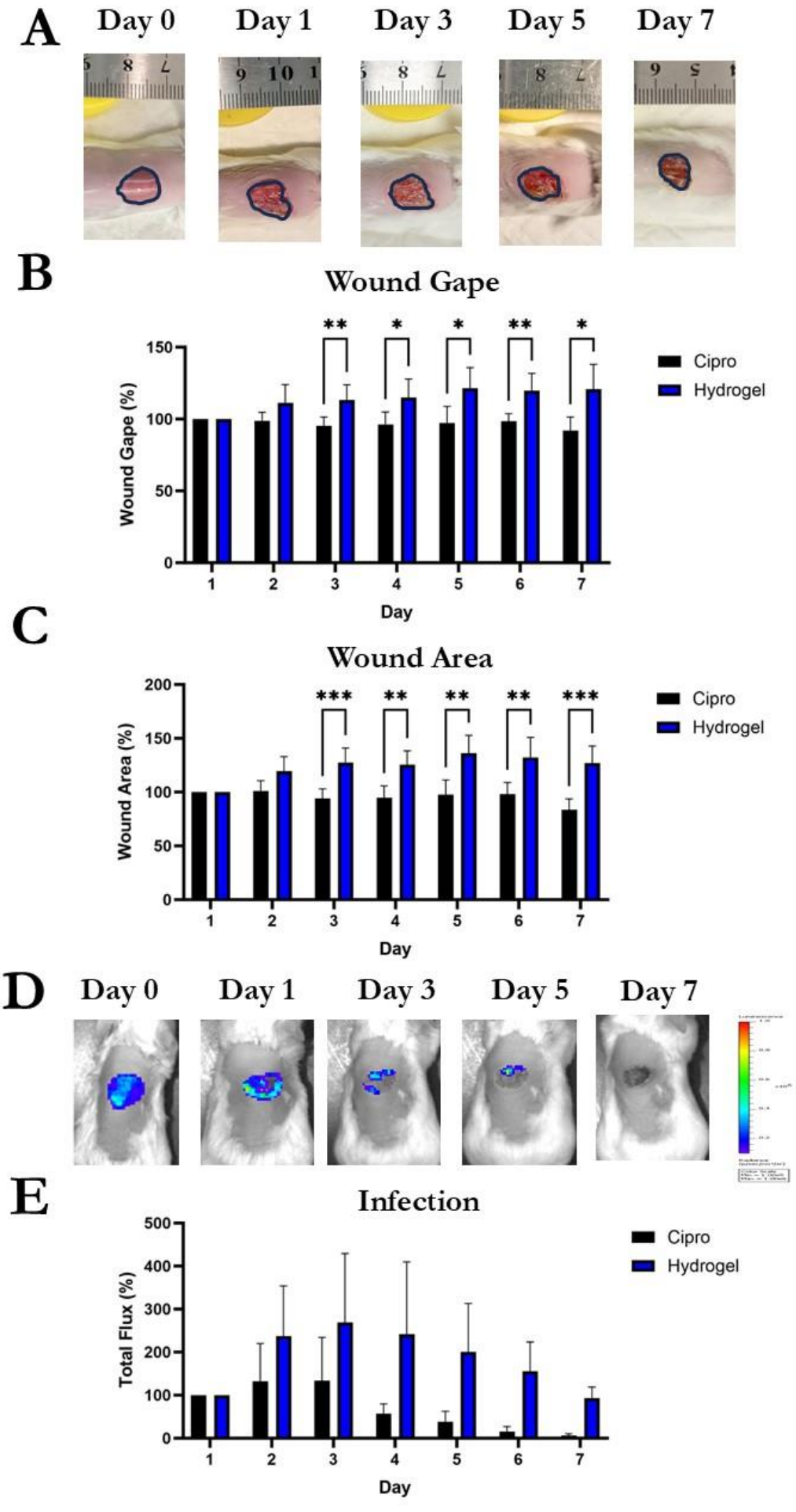
A
Day 0
Day 1
Day 3
Day 5
Day 7
B
Wound Gape
Wound Gape (%)
Day
Cipro
Hydrogel
C
Wound Area
Wound Area (%)
Day
Cipro
Hydrogel
D
Day 0
Day 1
Day 3
Day 5
Day 7
E
Infection
Total Flux (%)
Day
Cipro
Hydrogel

Figure 4.15. The ciprofloxacin treatment group showed the success of the infected excisional wound model. (A) Representative images of the macroscopic wound area **(B)** Wound Gape **(C)** Wound Area **(D)** Representative images of the bioluminescent bacterial burden **(E)** Infection. **(C-E)** Data is presented as mean ± SD (n =8). Statistical significance was achieved through a Two-way ANOVA and Sidak's Multiple Comparisons Test. * = $p<0.05$, ** = $p < 0.01$, *** = $p < 0.001$.

4.4. Discussion

Chronic wounds are exacerbated by the presence of infection [37, 63]. With antimicrobial resistance on the rise, alternative methods of clearing infection are needed. Antimicrobial peptides (AMPs) are peptides with antimicrobial properties against a wide range of bacteria [212]. Most notably, the AMP, pexiganan, has been used to successfully treat polymicrobial human diabetic foot ulcers, clearing infection and closing the wounds, as 1% cream in a clinical trial that consisted of 835 participants [203]. Pexiganan has also been shown to be effective *in vitro* against a wide range of bacteria [204]. However, AMPs like pexiganan are susceptible to degradation through proteolysis and oxidation [169, 212]. Chronic infected wounds are an extremely hostile environment with over 100-fold the proteases and a prolonged inflammatory response [70].

Porous silicon nanoparticles (pSiNPs) are biocompatible nanoparticles with a wide range of biomedical applications. pSiNPs are capable of being loaded with therapeutic agents, protecting it from degradation and allowing for a slow, sustained release [154]. Infected wounds are particularly hostile to antimicrobial peptides with an increased level of inflammation and proteases [70, 71].

Methods of increasing the stability of pexiganan have been explored, creating an arginine-rich variant of pexiganan that is more resistant to proteases [213], creating pexiganan nanoparticles [214], and using PLGA nanoparticles with silver nanoparticles attached [215]. However, the use of pSiNPs as a delivery system for pexiganan was yet to be explored. In this chapter, we investigate the efficacy of pSiNPs as a delivery mechanism for pexiganan in an infected excisional wound model.

While the antibacterial properties of pexiganan are well known, any pro-wound healing properties are little explored, focusing only on cytotoxicity and not functionality. Previously, pexiganan has shown no cytotoxicity up to 50 µg/mL to rat fibroblasts [211] and HeLa cells [205]. No cytotoxicity was observed in either murine fibroblasts or HaCaTs at concentrations of 32 µg/mL and 128 µg/mL [178]. Cytotoxicity has been observed in higher doses, with human dermal fibroblasts (HDFs) reducing to 80.1% cell viability at 512 µg/mL, 69.9% cell viability at 1024 µg/m, and 58.6% cell viability at 2048 µg/mL. Additionally, at 2048 µg/mL, the HDFs also showed morphological changes appearing smaller and rounder [207]. Consistent with these results, in this study, pexiganan was found to have a negative

effect on the cell viability, proliferation, and migration of keratinocytes at higher doses of 40-100 μg/ml. Pexiganan had a significant effect on the viability of HaCaTs starting at 15 μg/mL, pexiganan from 1-20 μg/mL was safe and may even be beneficial to the wound healing process.

No data has previously been reported on pexiganan's effect on proliferation and migration. The proliferation and migration of keratinocytes in particular is crucial for the closure of the wound. The sooner the wound has fully re-epithelialised, the sooner the wound has a physical barrier against further bacterial contamination and infection. Within this non-cytotoxic range, pexiganan at a concentration of 1 and 5 μg/mL increased the proliferation of keratinocytes. Between 10 and 20 μg/mL had no effect on proliferation, and no concentration below 20 μg/mL had an effect on the migration of keratinocytes. Concentrations higher than 40 μg/mL negatively affected the proliferation and migration of keratinocytes with scratch wounds treated with 80 μg/mL taking on average six more hours to close than the untreated, and the 100 μg/mL, an average of 12 hours more.

Overall, these results indicate that pexiganan up to 20 μg/mL is safe or even beneficial to wound healing. The MIC of pexiganan to *S. aureus* has previously been reported to be 8 μg/mL [205], 16 μg/mL [204, 256], and 20 μg/mL [211]. This suggests there is a therapeutic window where pexiganan is non-cytotoxic but is anti-bacterial. Consistent with these findings and the reported literature, the pexi-pSiNPs and pexiganan (free) treatment groups in the animal trial were the equivalent of 20 μg/mL released pexiganan, right at the therapeutic window.

In an infected excisional murine wound model, pexi-pSiNPs had no significant effect on bacterial burden or infection progression. A trend could be observed where the pexi-pSiNPs controlled the infection better than the pexiganan alone, but this was not significant. This was supported by the CFUs taken on Day 7 at the conclusion of the study where there was no significance found between the treatment groups. This may be due to the dose of pexiganan released by the pSiNPs being too low or too slowly released to have potent antimicrobial effect on the progression of infection.

There are indications that pexiganan may promote wound healing in addition to its well documented antibacterial properties. In one study, pexiganan reduced the secretion of TNFα, nitric oxide (NO), and IL-6 by LPS-stimulated macrophages *in vitro* [257], suggesting

a potential role in the resolution of the inflammatory phase. Nitric oxide (NO) released from pexiganan-loaded hydrogels was shown to promote collagen production by fibroblasts *in vitro* [208]. Electrospun mats loaded with pexiganan and another antimicrobial peptide, Tiger 17, were shown *in vitro* to be both antibacterial and accelerate blood clotting. While the accelerated blood clotting was more attributed to Tiger 17 than pexiganan, the pexiganan controls showed that pexiganan did promote blood clotting but not as much as Tiger 17 [178]. Pexiganan loaded into polycaproladone (PCL) nanofibers were used as a wound dressing to successfully inhibit bacterial growth *in vitro* [207]. In an excisional wound rat model, pexiganan delivered in a collagen matrice resulted in increased wound contraction [211]. In this chapter, Pexi-pSiNPs improved wound healing significantly more than the pexiganan alone, and the hydrogel treatment groups from Day 3 onwards. This was supported by the histological data where a trend was observed with the wounds treated with pexi-pSiNPs having an increased rate of re-epithelialisation and a thicker epidermis, however, larger studies are required to validate this finding.

Pexiganan showed higher numbers of PCNA-positive cells than the remaining groups showing an effect on the proliferation of keratinocytes *in vivo*. This effect was diminished by the porous silicon nanoparticles. Interestingly, pexiganan appeared to promote the recruitment of neutrophils into the wound bed and this effect was further increased by the use of porous silicon nanoparticles suggesting the ability to better fight infection. This could also be indicative of a prolonged inflammatory response. However, as the infection did not resolve by the end of the 7-day study, it cannot be determined if this inflammation is necessary or detrimental at this stage. Pro-inflammatory effects of pexiganan have not been explored and could be an area of further study. There were no effects on collagen deposition observed indicating no significant effect on fibroblasts function in this model.

A decreasing trend was observed in the daily quantification of bacterial load in the wounds that indicated that pSiNPs increased the antibacterial efficacy of pexiganan. However, this was not significant due to the wide variation of the data. Increasing the pexiganan dose or altering the chemistry of the pSiNPs to allow for a more rapid release of pexiganan may strengthen these trends to produce significance. Preliminary work by our collaborators (Figure 4.1.B) shows that half of the total pexiganan released is released within the first 24 hours. A secondary treatment 3-4 days post-surgery may better control the infection over a 7-day period.

The hydrosilylated porous silicon nanoparticles were chosen over the thermally oxidised porous silicon nanoparticles as they exhibited greater loading efficiency. This may be due to amide bonds forming between the carbonyl groups on the nanoparticles and the amine groups on the pexiganan. Unfortunately, these same bonds may be why so little pexiganan is being released from the nanoparticles. Improving the loading and release of pexiganan could be further investigated, with factors like increasing the pore size, changing the surface functionalisation, and altering the degradation rate of the nanoparticles being explored.

Additionally, the release of pexiganan from the porous silicon nanoparticles within a hydrogel should also be determined. This could be performed by simply incorporating the porous silicon nanoparticles loaded with pexiganan into the hydrogel and measuring the release of pexiganan into a medium (e.g. PBS) using a Nanodrop, similar to experiments conducted in this thesis.

The antibacterial and cellular effects of the porous silicon nanoparticles and the hydrogel, separately, could also be explored. A porous silicon nanoparticle only control was tested in the animal trial. However, with a n of 4 due to limitations on animal supply, the data confounded the results and therefore was not included.

In the animal trial, the positive effect of pexiganan on wound healing started to disappear by Day 6. This suggests that a second treatment or modifying the nanoparticles release profile to have more pexiganan released later may be needed. Additionally, the combined *in vitro* and *in vivo* work suggests that pexiganan may also have pro-wound healing properties through action on keratinocytes. With the proliferative phase beginning 3-4 days post-wounding [258], a secondary treatment may exacerbate these properties, producing significance in the histological measurements. The *in vitro* work could also be expanded to investigate effects on fibroblast function which may provide more insight into the Masson's and PCNA results observed in this trial. This histological staining could also be expanded to include the remaining animal samples. Further histological staining could investigate the effect of pexiganan on TNFα, nitric oxide (NO) and IL-6 secretion in the *in vivo* wound model, in alignment with previously published research.

The increased wound healing efficacy of pexiganan by pSiNPs may also be more significantly observed in a more chronic biofilm model of infection where the environment

is even more hostile and the difference between the treatments may be even more pronounced. This could be achieved with an *ex vivo* porcine biofilm wound model, or an *in vivo* biofilm excisional wound murine model.

In conclusion, the pSiNPs did not improve the antimicrobial properties of the antimicrobial peptide, pexiganan, highlighting the importance of a time and does dependent delivery system. However, the pSiNPs did improve the wound healing efficacy of pexiganan in an infected excisional wound model. Future directions will explore modifications to the pSiNP load/release properties, treatment dose and frequency, and animal model in order to further explore this therapy.

Chapter Five – Photodynamic Therapy Using Methylene Blue-Antibody Conjugates in an Infected Excisional Wound Model: A Pilot Study

5.1. Background

All wounds have some level of bacterial contamination which has the potential to progress to an infection [37-39]. Over 60% of chronic non-healing wounds having a biofilm and current treatment is primarily based on systemic antibiotics [42, 59]. Antibiotics are becoming increasingly ineffective with bacterial antimicrobial resistance on the rise and contributing to an estimated 4.95 million deaths in 2019 [53, 55]. Antibiotic-alternative methods for treating infected wounds are needed.

Photodynamic therapy (PDT) has been shown to be an effective treatment against a wide range of microorganisms utilising various photosensitisers and light sources. However, some bacteria (e.g. gram negative, biofilms) are harder to kill than others (e.g. gram positive, planktonic) and require higher doses and longer treatment regimens to achieve the same results [259]. While many photosensitisers have clinical uses unrelated to PDT, toxicity is a problem at high doses [241]. Additionally, while preferential uptake has been reported for certain photosensitisers, in general, photosensitisers do not discriminate between bacterial and mammalian cells [224, 260]. In the context of an infected wound, this means both the infection and the healthy tissue will be affected by PDT. This collateral damage to the healthy tissue can inhibit wound healing and may even prevent the immune system's ability to control any infection that may remain in the wound.

Methods for increasing the specificity of the photosensitisers are being investigated. One such method is the conjugation of photosensitisers to an antibody specific to bacteria, allowing the photosensitiser to select for bacteria over mammalian cells, improving the efficacy of the treatments and limiting the potential negative side effects [225]. Improving the specificity of the photosensitiser to allow for more targeted treatments may limit tissue damage and more easily disrupt biofilms. Increasing the specificity of the photosensitiser may also allow for lower doses of the photosensitiser to be used which may avoid the downfalls of using too much photosensitiser associated with increased toxicity and reduced efficacy of the treatment through photo-bleaching and self-shielding [225, 261, 262].

To date, Methylene Blue has not yet been conjugated to antibodies, though it has had its specificity increased through the use of nanoparticles [232-234, 236, 237]. Methylene Blue has previously shown efficacy against *S. aureus*, MRSA, and polymicrobial biofilms *in vitro* [239-242]. *In vivo*, MB has been successfully used to treat MRSA biofilms in mice [231].

In this chapter, Methylene Blue was conjugated to an antibody specific to *S. aureus* through EDC/NHS chemistry that involves an amide bond being created between an ester on Methylene Blue and a primary amine on the antibody. The photosensitisers Rose Bengal and Zinc Phthalocyanine were also briefly explored for the conjugation reactions. This was done due to the varying structures and properties between these three photosensitisers that may have resulted in different success rates with the conjugation chemistry or performed with different levels of efficacy in the *in vitro* and *in vivo* models. However, it was decided that Methylene Blue would be the photosensitiser of choice for the remainder of the study due to its more simplistic chemical structure as a proof of concept. The safety of MB-PDT on cells integral to the wound healing processes were explored utilising *in vitro* cellular assays and the safety of developed MB-Ab conjugates was tested in a pilot study of 12 mice utilising infected excisional wounds.

5.2. Methods

5.2.1. The LED Light

For the photodynamic therapy and photo-antibody treatments, an LED light from ThorLabs was procured through LasTek, setup shown in Figure 5.1, with the specifications in Table 5.1 for the wavelength emission of 660 nm. Briefly, the LED light was connected to the LED driver and then the power supply. The LED Light was set up using a stand and a clamp to the height required to achieve a 6 mm spot size. The output power was measured using the sensor head and the power meter, attached to a laptop. The output power was measured on the laptop using ThorLabs Optical Power Monitor program and was standardised to 150 mW.

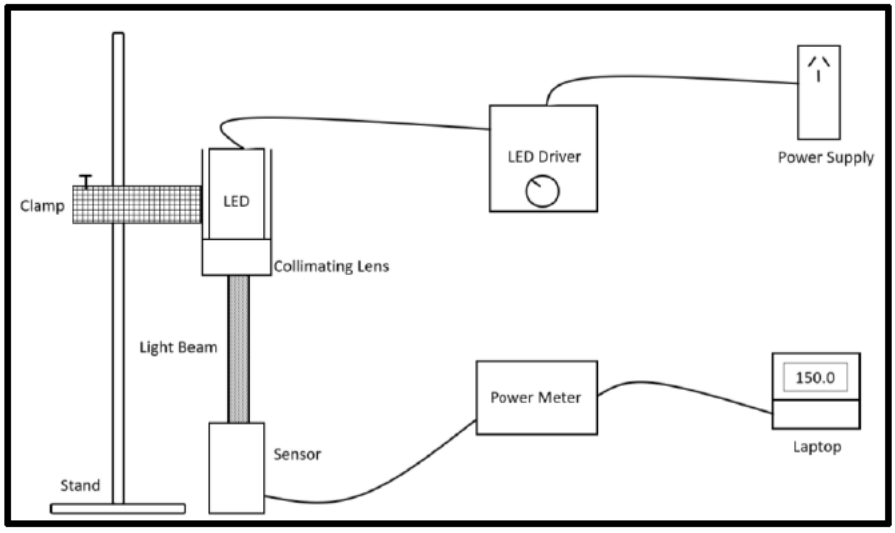

Figure 5.1. A diagrammatic representation of the LED setup used in this study.

Table 5.1. LED light equipment used in this study and their specifications. Purchased from ThorLabs (New Jersey, United States) through LasTek (Thebarton, SA, Australia).

Product Code	Product	Product Specifications
M660L4	660nm LED Light	940 mW, 1200 mA
PM100USB	Power Meter	with USB
LEDD1B	T-Cube LED Driver	1200 mA
S302C	Thermal Power Sensor Head	Surface Absorber, 0.19-25 µM, 2 W, Ø12 mm
KPS101	Power Supply Unit	15 V. 2.4 A with a 3.5 mm Jack Connector
ACL25416U-A	Aspheric Condenser Lens	Ø1". F=16 mm, NA=0.79, ARC: 350-700 nm
SM1L10	Lens Tube	1.00" Thread Depth with One Retaining Ring
YL-717HeNe	Safety Glasses	Lens Colour: Blue

For the *in vitro* assays, black 96-well plates with clear lids (Interpath, Somerton, Australia) were used to minimise irradiation between the wells. The following equations were used to calculate the light fluence to achieve the desired light fluence range from 5 J/cm^2 to 100 J/cm^2 for a 6 mm spot size (for both *in vitro* and *in vivo* work) (Figure 5.2. and Table 5.2).

Light Fluence = power density (W/cm^2) x time (seconds)

$$Power\ density = \frac{output\ power\ (W)}{spot\ size\ (cm^2)}$$

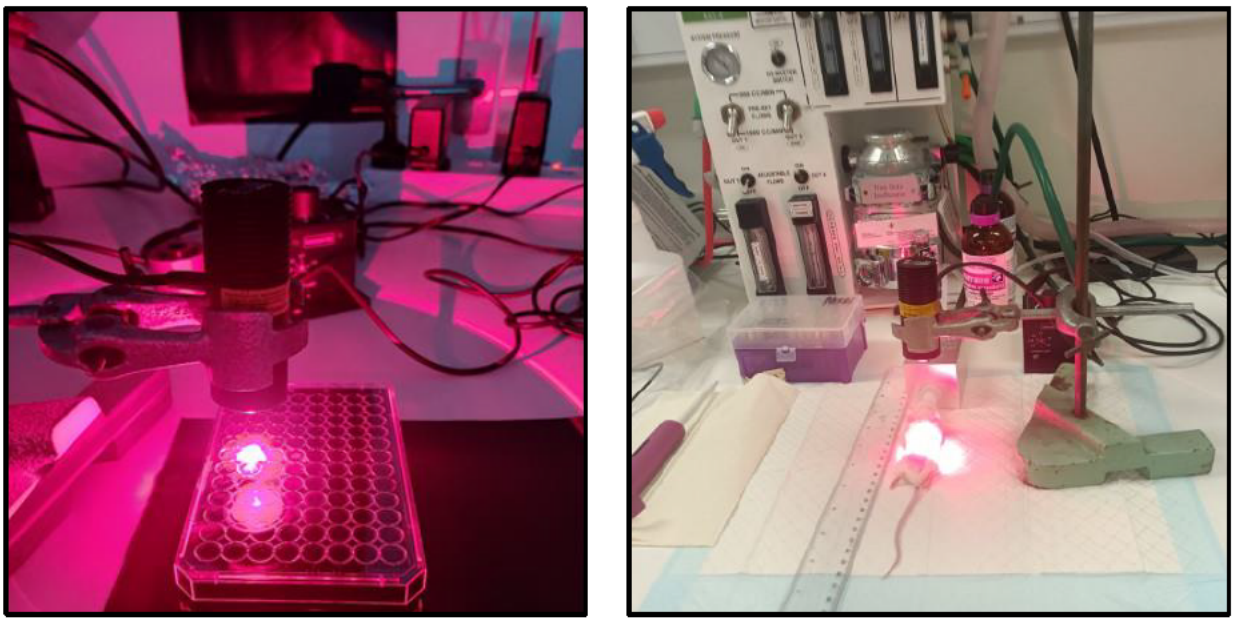

Figure 5.2. The LED light assembly for treating a 96-well plate (Left) and for treating mice (Right).

Table 5.2. The calculated exposure times for the various light fluences tested. Output power: 150 mW. Spot size: 6 mm. Wavelength: 660 nm.

Fluence (J/cm^2)	6 mm (0.29 cm^2)
5	10 secs
10	20 secs
20	39 secs
50	97 secs
100	194 secs

5.2.2. Conjugation

For the photosensitiser-antibody conjugates, two photosensitisers were chosen in addition to Methylene Blue; Rose Bengal and Zinc Phthalocyanine (Table 5.3.). Modified versions of these three photosensitisers were purchased as in Table 5.4. The antibody (polyclonal goat antibody to LTA, ab20001) used for the conjugation was specific to gram positive bacteria, ~150 kDa in size, and sourced from Abcam (Cambridge, United Kingdom). This anti-Gram-positive antibody binds with the lipoteichoic acid on the wall of Gram-positive bacteria (e.g. *S. aureus*).

Table 5.3. Selected photosensitisers for this study with their key characteristics.

	Methylene Blue	**Rose Bengal**	**Zinc Phthalocyanine**
Structure	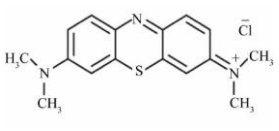	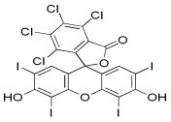	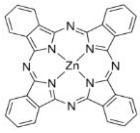
Activating Wavelength (nm)	664	550	690
Chemical Formula	$C_{16}H_{18}ClN_3S$	$C_{20}H_4Cl_4I_4O_5$	$C_{32}H_{16}N_8Zn$
Classification	Thiazine Dye	Xanthene Dye	Phthalocyanine
Charge	Cationic	Anionic	Cationic
Molar Mass (g/mol)	319.85	973.67	577.9
Water Solubility	Hydrophilic	Amphiphilic	Hydrophobic

Table 5.4. The modified photosensitisers purchased for the conjugation chemistry.

	Methylene Blue – NHS Ester	Rose Bengal Lactone	Zinc (II) 2, 9, 16, 23, - tetra (carboxyl) Phthalocyanine
Structure	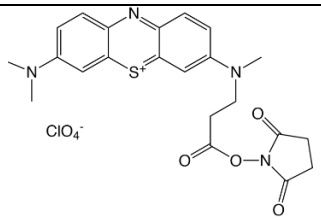	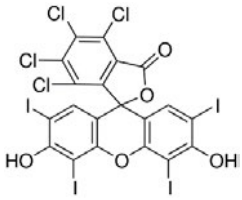	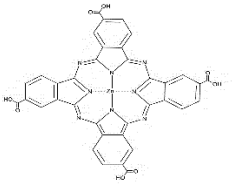
Chemical Formula	$C_{22}H_{23}N_4O_8SCl$	$C_{20}H_4Cl_4I_4O_5$	$C_{36}H_{16}N_8O_8Zn$
Molar Mass (g/mol)	538.96	973.67	793.95
Source	Glen Research (Sterling, Virginia, United States)	Sigma Aldrich (Castle Hill, NSW, Australia)	PorphyChem (Longvic, France)

The photosensitiser-antibody conjugates were created using EDC/NHS chemistry to form an amide bond between the two molecules. Methylene Blue (MB) and Rose Bengal (RB) had two esters, and Zinc Phthalocyanine (ZnPc) had 4, while the antibody had ~20 solvent accessible lysine residues capable of forming amide bonds with the photosensitisers.

RB-Lactone and ZnPc-COOH required an additional activation step prior to conjugation. This was achieved by incubating the photosensitisers with sulfo-NHS, EDC and DIPEA, at a 2:1 concentration ratio, in DMSO overnight at room temperature on a rocking platform. The photosensitisers were dissolved in DMSO and mixed with the antibody (polyclonal goat antibody to LTA, ab20001, Abcam) at the appropriate ratio overnight on a rocking platform at room temperature. The solution was then concentrated using VivaSpin Concentrators 10k Molecular Weight Cut Off (MWCO) which allowed for the unconjugated photosensitiser to filter out. This was achieved using a centrifuge at 12,000 x g for 5 minutes. The resulting solution was washed with PBS using a centrifuge at 12,000 x g for 5 minutes. The resulting solution was stored at 4°C. The conjugation was confirmed by detecting the presence of photosensitiser in the solution through fluorescent microscopy using an Olympus IX83 Fluorescence Microscope (Olympus, Tokyo, Japan), as the unconjugated photosensitiser was filtered out during the concentration step. The resulting MB-Ab conjugate is hereon referred to as MB-Ab alone, MB-Ab-PAT when used in conjugation with light or Inf MB-Ab-PAT when used in the infected animal trial. Photo-Antibody Therapy (PAT) refers to photodynamic therapy that utilises a photosensitiser conjugated to an antibody.

5.2.3. Western Blots

Solutions:

12.5% Running Gel: 5.25 mL 30% Acrylamide, 1.55 mL 3M Tris pH 8.9, 5.58 mL MilliQ Water, 125 µL 10% Sodium Dodecyl Sulfate (SDS), 100 µL 10% Ammonium Persulphate (APS), 6.25 µL Tetramethylethylenediamine (TEMED).

4% Stacking Gel: 0.5 mL 30% Acrylamide, 0.276 mL 0.5M Tris pH 6.8, 4.104 mL MilliQ Water, 50 µL 10% SDS, 40 µL 10% APS, 4 µL TEMED.

1x Running Buffer: 3.03 g Tris base, 14.4 g Glycine, 1 L MilliQ Water and 1 g SDS.

1x Transfer Buffer: 3.03 g Tris base, 14.4 g Glycine, 800 mL MilliQ Water and 200 mL Methanol.

Tris Buffered Saline (TBS): 100 mL Tris (10x), 100 mL NaCl (10x) and 800 mL MilliQ Water.

TTBS: 0.5 mL Tween 20 to every 100 mL TBS.

5x Loading Buffer: 2.5 mL 0.5 M Tris pH 6.8, 3.5 mL MilliQ Water, 0.5 g 5% SDS, 4 mL 40% Glycerol, 10 µL 0.1% Bromophenol Blue and 500 µL β-mercaptoethanol.

5% Skim Milk: 2.5 g Skim Milk Powder in 50 mL TTBS.

12% Skim Milk: 6 g Skim Milk Powder in 50 mL TTBS.

Making the gels: Approximately 6-7 mL of the 12.5% running gel was added to the 1.5 mm glass slides set up, topped with a few mL of MilliQ Water to prevent drying out and allowed to set at room temperature for approximately 30 minutes. The water was then poured off and the 4% stacking gel was pipetted on top of the running gel. The comb was inserted, and the gel allowed to set at room temperature for approximately 30 minutes.

The gels (12.5% running gel with 4% stacking gel) were set up in a gasket and placed into a running tank. The gaskets were first filled with 1x SDS Running Buffer, combs removed, and then the tank filled with 1x SDS Running Buffer from the gaskets. 20 µL (1 mg/mL) of Lipoteichoic Acid (LTA) mixed with an equal volume of MilliQ Water and 5x Loading Buffer and heated at 95˚C for 5 minutes before being loaded into the appropriate well. 5 µL BIORAD Kaleidoscope Precision Plus protein standard for ladder and 2 µL Loading Buffer

was added for blank wells. Once the gels were loaded, the tank was run at 100 V for 60 minutes.

The gel was removed from the glass chamber and soaked in cold Transfer Buffer, the sandwich was assembled with the white side down, 1 sponge, 2 pieces of blotting paper, the nitrocellulose membrane, the gel, 2 pieces of blotting paper, 1 sponge, black side of cassette. The holder was placed into a transfer tank with an ice pack and a magnet to stir the buffer to ensure an even temperature throughout. The tank was filled with cold Transfer Buffer run at 100 V for 60 minutes.

The membrane was blocked with 12% skim milk for 15 minutes on a rotating platform, and then incubated with the primary antibody (polyclonal goat antibody to LTA, ab20001, Abcam; either the antibody by itself or the Methylene Blue-Antibody (MB-Ab) conjugate) in 5% skim milk at room temperature for 2-3 hours and then stored overnight at 4°C. The membrane was then washed twice for 5 minutes in TTBS on a rotating platform and incubated with the secondary antibody (polyclonal rabbit antibody anti-goat Ig, Dako) in 5% skim milk. The membrane was washed twice for 5 minutes in TTBS, followed by an additional wash for 5 minutes in TBS. Equal volumes of the Thermo Fisher West Femto ECL Kit mixtures (Thermo Fisher Scientific, VIC, Australia) were combined immediately before administration to the blot for imaging in the Syngene G Box (Syngene, Australia).

5.2.4. The PAT Pilot Study

A pilot study of 12 mice was conducted to test the safety of the PDT/PAT therapies (Figure 5.3). The pilot study was approved by the UniSA animal ethics committee and carried out at the Core Animal Facility (CAF). The animal ethics number for this study was U19/20. The mice were obtained from Australian Bio Resources (ABR) and consisted of six female and six male balb/c mice, which were allocated evenly between four groups. Power calculations determined that a sample size of 6 mice per group will provide 95% power at the 5% level of significance to demonstrate an average reduction of 5 mm in wound size between infected and non-infected groups with a standard deviation of 2.3 mm, using an unpaired Student's t test. These power calculations were based on a reduction of 20% in wound size which has previously been determined to be biologically significant.

The four groups used in this study included, an uninfected group treated with a standard MB-PDT (100 µM and 100 J/cm^2) treatment (UnInf MB-PDT), an infected untreated group (Inf Untr), an infected group treated with a standard MB-PDT light treatment (100 µM and 100 J/cm^2) (Inf MB-PDT), and an infected group treated with the MB-Ab conjugate and light (5.3 µM and 100 J/cm^2) (Inf MB-Ab-PAT).

The infected excisional wound model was utilised as previously described in Section 2.3, with 6 mm wounds created. The mice were treated daily starting on Day 1, with the final treatment on Day 6. Treatments were applied topically in PBS, administered by pipette, followed immediately by LED light irradiation at 660 nm and 100 J/cm^2. The mice were humanely killed on Day 7, and the wounds excised. Half the wound was used for histology, and the remaining half for CFUs. Additionally, the heart, lungs, liver, spleen, and kidneys were also collected for histological staining to assess signs of toxicity to the organs.

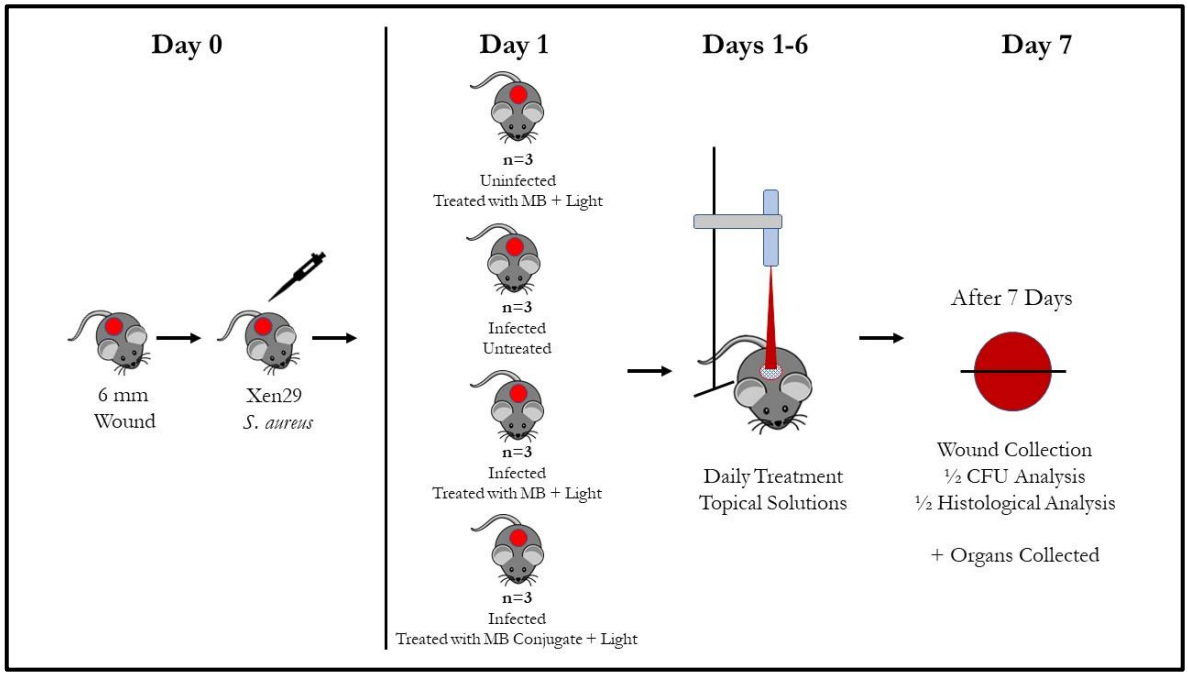

Figure 5.3. The timeline and treatment groups for the infected excisional wound model used in the Photo-Antibody Therapy pilot study.

5.3. Results

5.3.1. Conjugating Photosensitisers to an antibody specific to bacteria using EDC/NHS chemistry.

To create the photosensitiser (PS)-Ab conjugates, a nucleophile substitution reaction was used to create an amide bond between the photosensitiser and the antibody. A modified form of the photosensitisers was used – Methylene Blue with an ester attached, Rose Bengal Lactone, and Zinc Phthalocyanine with a carboxylic acid attached. Through EDC/NHS chemistry, this ester reacts with one of the many amines on the antibody to create an amide bond. Here, three ratios of PS:Ab are tested, 2:1, 4:1 and 8:1. This conjugation was proven successful for all three photosensitisers through the use of fluorescence microscopy, as the only photosensitiser that remains in the sample after the filtration process is photosensitiser that is attached to the antibody (Figure 5.4.A). A visual change in colour could also be seen (Figure 5.4.B). After the conjugation reactions, the mixture was centrifuged using VivaSpin concentrators (MWCO 10k) which removed any photosensitiser not attached to the antibody. So, any remaining Methylene Blue attached to the antibody. The presence of the photosensitiser was confirmed using fluorescence microscopy and quantified (Figure 5.4.C).

Antibodies have approximately 80 lysine residues throughout their structure, approximately 20 of these are solvent accessible. These lysine residues include primary amines that are capable of forming amide bonds with the photosensitiser. This means there is a chance that the photosensitiser binds to an antigen binding site, inhibiting the antibody's ability to bind to the bacteria. This risk increases as the PS:Ab ratio increases. To investigate whether the conjugation reaction caused a conformational change in the antibody, resulting in loss of function, Western blots were performed. In these Western blots, blots were created with lipoteichoic acid (LTA) run on the gel, and the conjugates were used as the primary antibody. As can be seen in the Figure 5.4.D, the MB-Ab conjugate still showed functional conformation by showing that the antibody was still capable of binding to the LTA after conjugation. The faint band was considered to be a reflection of the much lower concentration of the MB-Ab used as opposed to a decrease in function. The calculated dose of the MB-Ab conjugate based on the amount of photosensitiser and antibody used was 5.3 µM. The Rose Bengal and Zinc Phthalocyanine conjugates also showed functionality through the western blots (data not shown), however, the results

were variable, and it could not be determined if this reflected the methods or the photosensitiser. Going forward, only methylene blue was investigated.

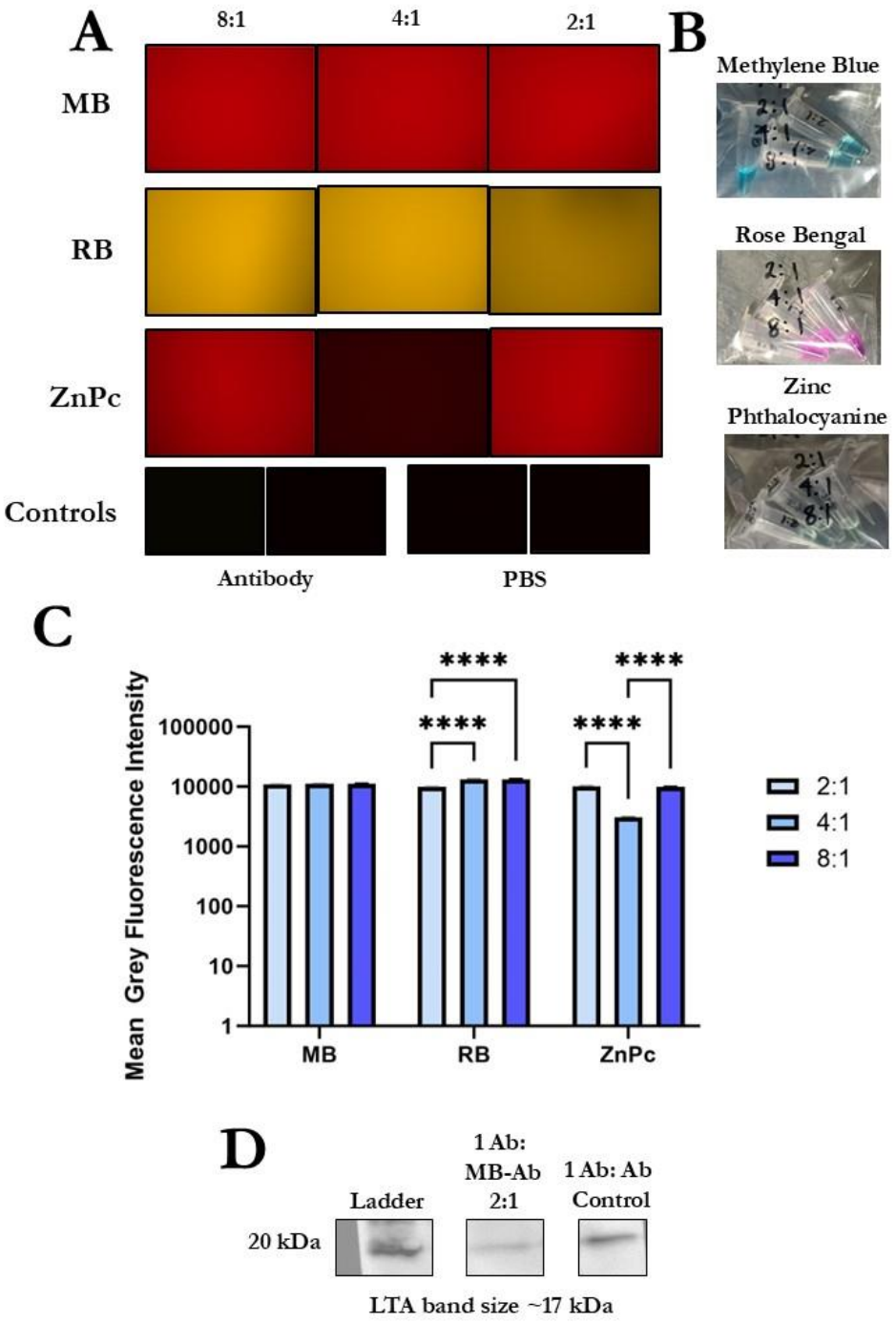

Figure 5.4. The creation of the photosensitiser-antibody conjugates. (A) Representative images of the fluorescent conjugates to confirm the success of the conjugation reactions in a 96-well plate using fluorescent microscopy. **(B)** Representative images of the conjugates in tubes **(C)** Fluorescent quantified as in (A) presented as Mean ± SEM **(D)** Western Blots confirming the functionality of the MB-Ab conjugate. Statistical significance was determined using a two-way ANOVA and Tukey's Multiple Comparisons test. **** = $p < 0.0001$.

5.3.2. Methylene Blue alone is not cytotoxic to keratinocytes or fibroblasts over a 2-hour period.

Before investigating the cytotoxicity of the conjugates in an infected wound model, the toxicity of the unconjugated Methylene Blue was first investigated *in vitro*. In a 96-well plate, where photosensitiser is administered to all wells followed by LED irradiation, there is a two-hour gap between the first well irradiated and the last well irradiated. To investigate the possible cytotoxic effects of MB alone on keratinocytes (HaCaTs) and fibroblasts (HFFs) during this two-hour incubation, resazurin assays were performed. 70% cell viability was determined as the minimum allowed for a treatment to not be considered cytotoxic in accordance with international guidelines [263].

As can be seen in Figure 5.5, while some cell death was observed, methylene blue did not cause cytotoxicity greater than 70% for either HaCaTs or HFFs. However, at high concentrations, methylene blue did gradually decrease viability by up to 29% to HaCaTs but had minimal effect on HFFs. The greatest decrease in cell viability to HaCaTs (Figure 5.5.A) was seen at 100 µM Methylene Blue after a 60-minute incubation where the population decreased to 71%, just narrowly avoiding the cytotoxic threshold. Several other concentrations and incubation times were also significantly reduced compared to the 0 µM control, with viability between 70-80%.

While there was no statistical significance found (Figure 5.5.B), HFFs appeared to increase in cell number initially with a 25% increase at 0.1 µM methylene blue after a 30-minute incubation. The greatest decrease in cell number observed was at 100 µM after a 60-minute incubation with a 12% decrease observed (Figure 5.5.B).

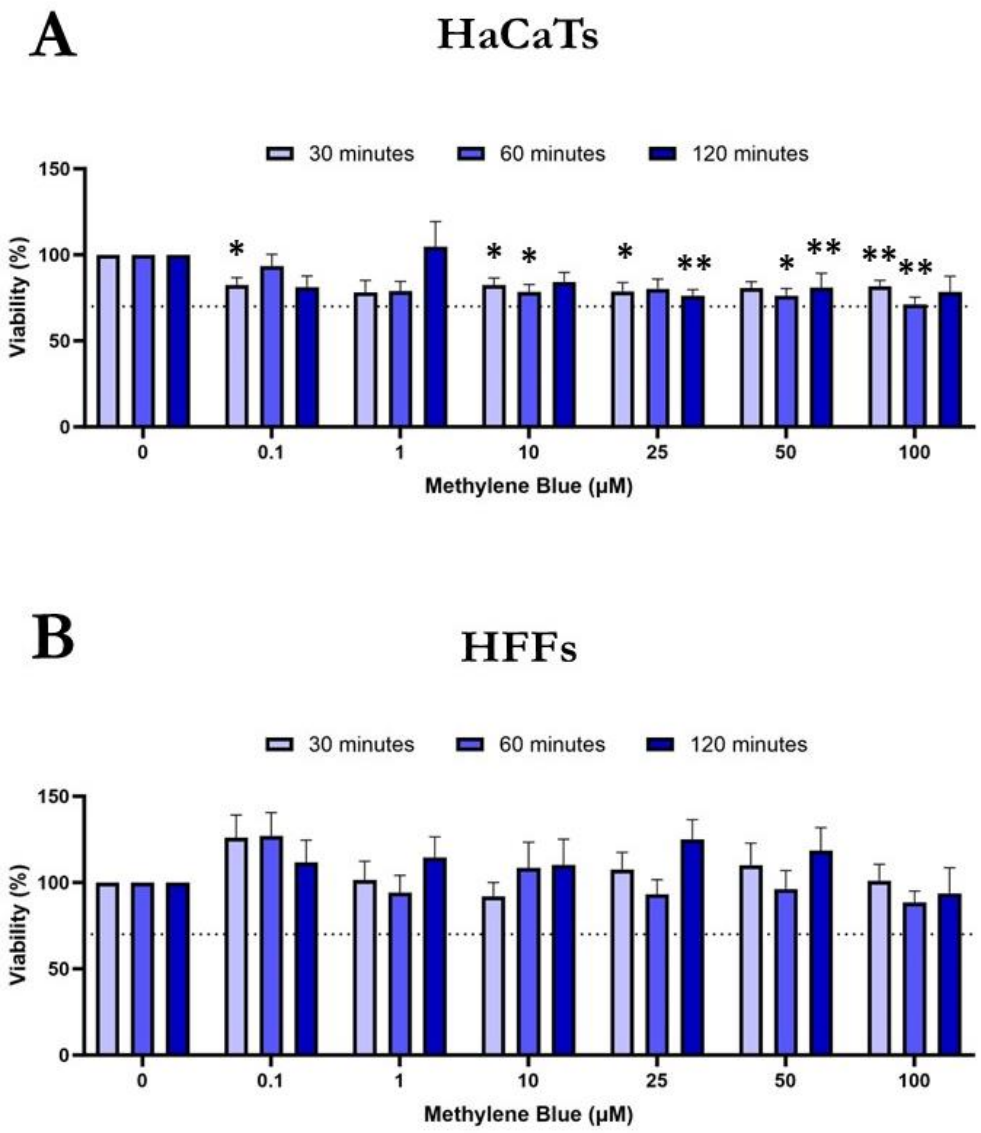

Figure 5.5. Effect of methylene blue on the viability of keratinocytes and fibroblasts two hours post-treatment. (A) HaCaTs **(B)** HFFs. Data is normalised to the cells only control and is presented as mean ± SEM. n = 3. Dashed line represents 70% cell viability. Statistics show significance compared to the 0 µM control. Statistical significance was determined using a two-way ANOVA and Tukey's Multiple Comparisons test. * = $p<0.05$, ** = $p<0.01$.

5.3.3. Methylene Blue only control shows toxicity to keratinocytes and fibroblasts after a 24-hour period while the light only control does not.

Before investigating the potential cytotoxicity of MB-PDT on keratinocytes and fibroblasts, it was necessary to investigate the two variables, Methylene Blue and light, separately. To determine the effects of Methylene Blue alone and light (660 nm) alone at a range of doses on HaCaTs and HFFs viability after 24-hours was investigated using a resazurin assay. The light alone had no cytotoxic effect on either the HaCaTs nor the HFFs (Figure 5.6.A and Figure 5.6.B). No effect of increasing fluence from 5 J/cm^2 to 100 J/cm^2 was observed. Increasing doses of Methylene Blue alone was more cytotoxic to the HaCaTs than the HFFs after 24 hours than was observed up to two hours (Figure 5.5). HaCaTs showed a decline in viability and reached 70% cell viability at 10 µM. All concentrations were statistically significant compared to the untreated control (Figure 5.6.C). HFFs were less affected by prolonged treatment and increased methylene blue concentrations with the only statistical significance found at 100 µM (Figure 5.6.D).

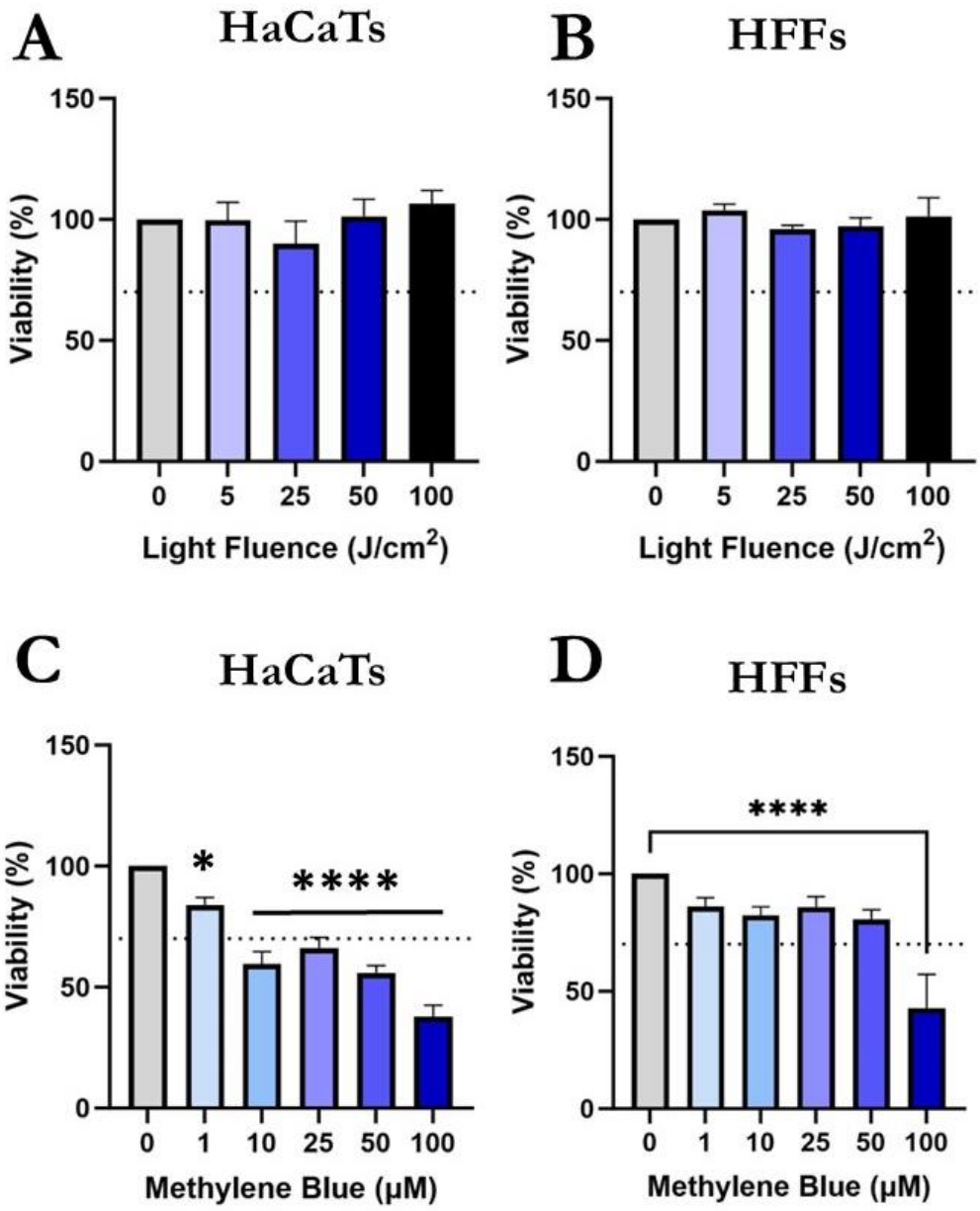

Figure 5.6. The effect of the LED light and methylene blue separately on keratinocytes and fibroblasts 24 hours post-treatment. (A) Light only on HaCaTs **(B)** Light alone on HFFs **(C)** Methylene blue only on HaCaTs **(D)** Methylene Blue alone on HFFs. Data is normalised to the cells only control and is presented as mean ± SEM. **(A)** and **(B)** n=3. **(C)** and **(D)** n=6. Dashed line represents 70% cell viability. Statistical significance was determined using a one-way ANOVA and (A) and (C) Dunnett's (B) and (D) Tukey's Multiple Comparisons test. * = $p < 0.05$, ** = $p < 0.01$, ****= $p < 0.0001$.

5.3.4. Determine safe dose of MB-PDT *in vitro.*

To investigate the cytotoxicity of the combined effect of Methylene Blue and light (MB-PDT) on HaCaTs and HFFs, a resazurin assay was performed 24 hours after treatment (Figure 5.7). The HaCaTs proved to be more vulnerable to the cytotoxic effects of MB-PDT than the HFFs. MB-PDT was shown to be cytotoxic to HaCaTs at 1 µM and 50 J/cm^2, with viability reducing to less than 25% for both the 50 J/cm^2 and 100 J/cm^2 for 10-100 µM Methylene Blue (Figure 5.7.A). MB-PDT proved to be cytotoxic to HFFs at 10 µM and 25 J/cm^2, with viability reducing to less than 15% for 50 J/cm^2 and 100 J/cm^2 for 10-100 µM Methylene Blue (Figure 5.7.B). Interestingly, MB-PDT produced a sharp decline in HFF viability between 1 and 10 µM, while the HaCaTs showed a slower decline in viability. As can be seen in Figures 5.7.A and 5.7.B, the light doses 5 J/cm^2 and 25 J/cm^2 trend very closely together for both the HaCaTs and the HFFs, as do 50 J/cm^2 and 100 J/cm^2. The addition of even just 5 J/cm^2 significantly increased the cytotoxic effects of the increasing concentrations of Methylene Blue.

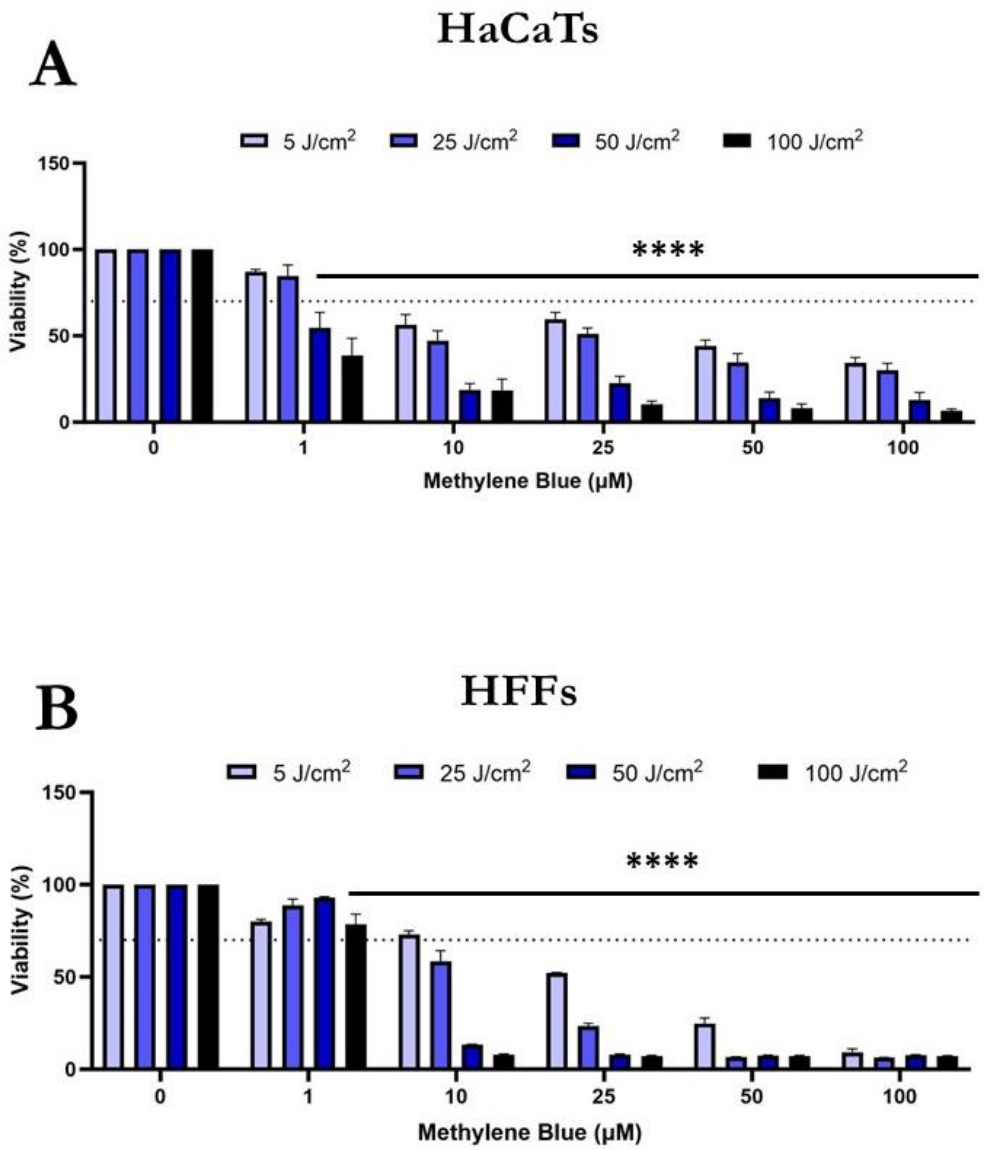

Figure 5.7. The effect of MB-PDT on the viability of keratinocytes and fibroblasts 24 hours post-treatment. (A) HaCaTs **(B)** HFFs. Data is normalised to the light only control and is presented as mean ± SEM. n = 3. Dashed line represents 70% cell viability. Statistical significance was determined using a two-way ANOVA and Tukey's Multiple Comparisons test. Statistical significance shown is compared to the 0 µM control. ****=p<0.001.

5.3.5. Photo-Antibody Therapy is a safe therapy for the treatment of infected wounds.

The main purpose of this pilot study was to determine the safety of this new therapy. A higher treatment dose is often needed *in vivo* than *in vitro* in order to achieve efficacy due to the increased complexity of a living biological organism. Due to this, for the controls, the upper limits of the light dose and photosensitiser concentration were tested in the pilot study to ensure safety and prevent the need for further pilot studies. This safety was largely indicated throughout the study by observing the appearance and behaviour of the mice. The mice were assessed daily for signs of pain or distress such as hunching, a reluctance to move, and skin irritation/redness. As can be seen in Figure 5.8.A, very few signs of pain or distress were observed and not for consecutive days. The skin irritation/redness observed on Day 1 was present prior to treatment and therefore due to the surgeries and infection on Day 0. No signs of stress or pain were observed in the Uninfected group treated with MB-PDT (UnInf MB-PDT) treatment group, indicating that the signs of distress/discomfort observed was due to infection and not the treatment applied.

Another important indicator of health in the mice is weight loss in response to 1 x 6 mm excisional wounds, mice typically lose weight in the first 24 hours then recovers in the following days. For this study, it was determined that if the mice exceeded 10% weight loss, buprenorphine would be administered and the UniVet notified. If the mice exceeded 15% weight loss, euthanasia would be considered in consultation with the UniVet. As can be seen in Figure 5.8.B, there was a slight trend for more weight loss in the PDT/PAT-treated groups regardless of infection, but this was not statistically significant. All groups averaged less than 10% weight loss during the trial. One mouse in the uninfected, MB-PDT treatment group reaching 10.35% weight loss at the end of the study. As this was the last day of the study with humane killing already planned, no action was taken. However, the weights of the infected, untreated (Inf Untr) group appear more stable, suggesting the treatments may be having a slight but not significant effect on weight loss in this model.

On Day 7 of the trial, after the wounds were collected, samples of five organs were also retrieved including: the heart, lungs, spleen, kidney and liver. The organs were processed and stained with H&E. As can be seen in Figure 5.9, none of the treatment groups displayed qualitative markers of tissue inflammation, toxicity or necrosis in any of these five organs. All of the organ samples maintained cellular structure, and showed no discolouration,

abnormal spacing, or infiltration of immune cells. This indicates there was no organ toxicity or build-up of the MB or MB-Ab in any of the organs over this timeframe.

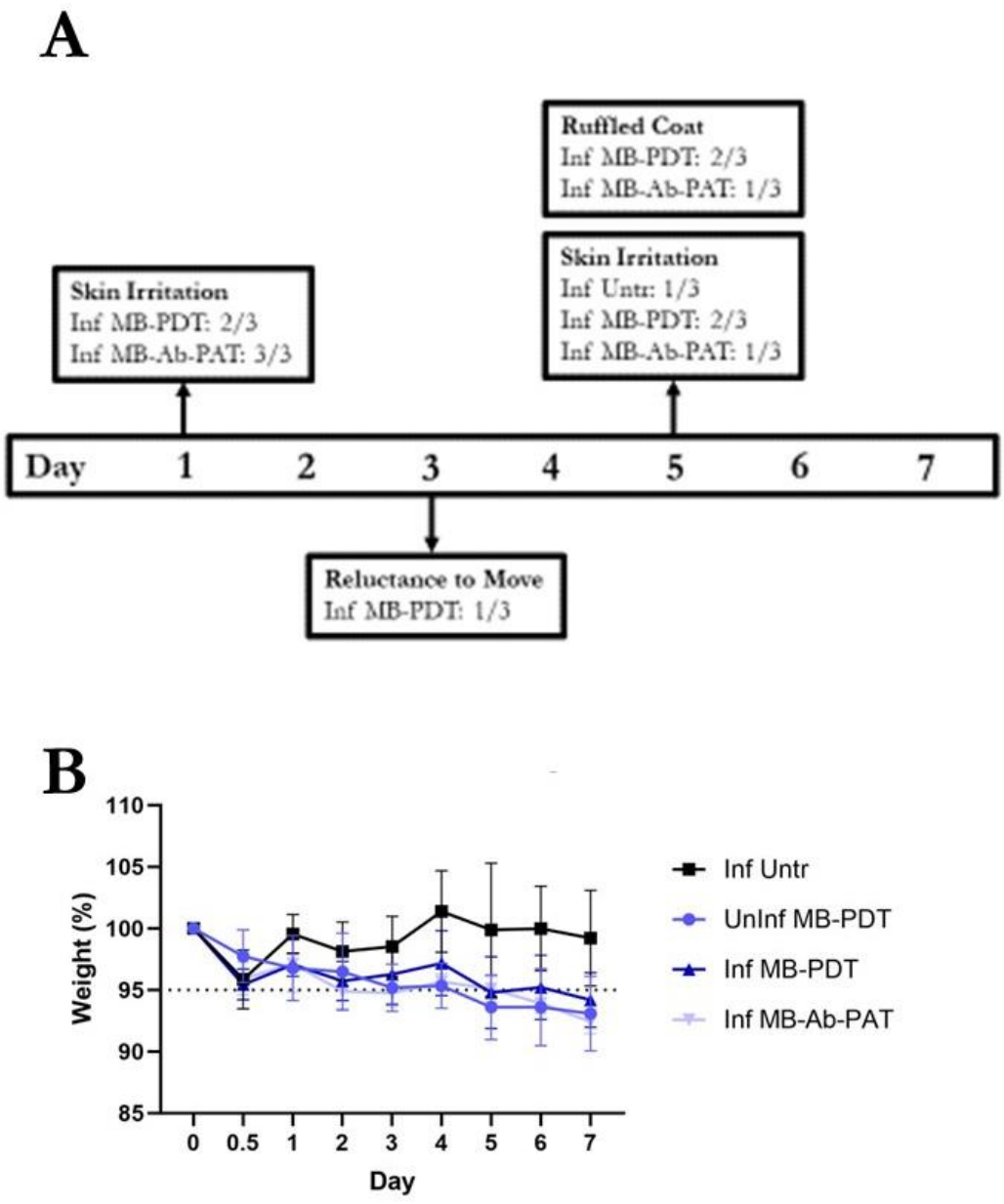

Figure 5.8. The health of the mice during the pilot study. (A) The appearance and behaviour of the mice as recorded in the CRS sheets **(B)** The weights of the mice over the 7-day trial. Data is baseline-corrected to Day 0. n = 3. Data is presented as Mean ± SD.

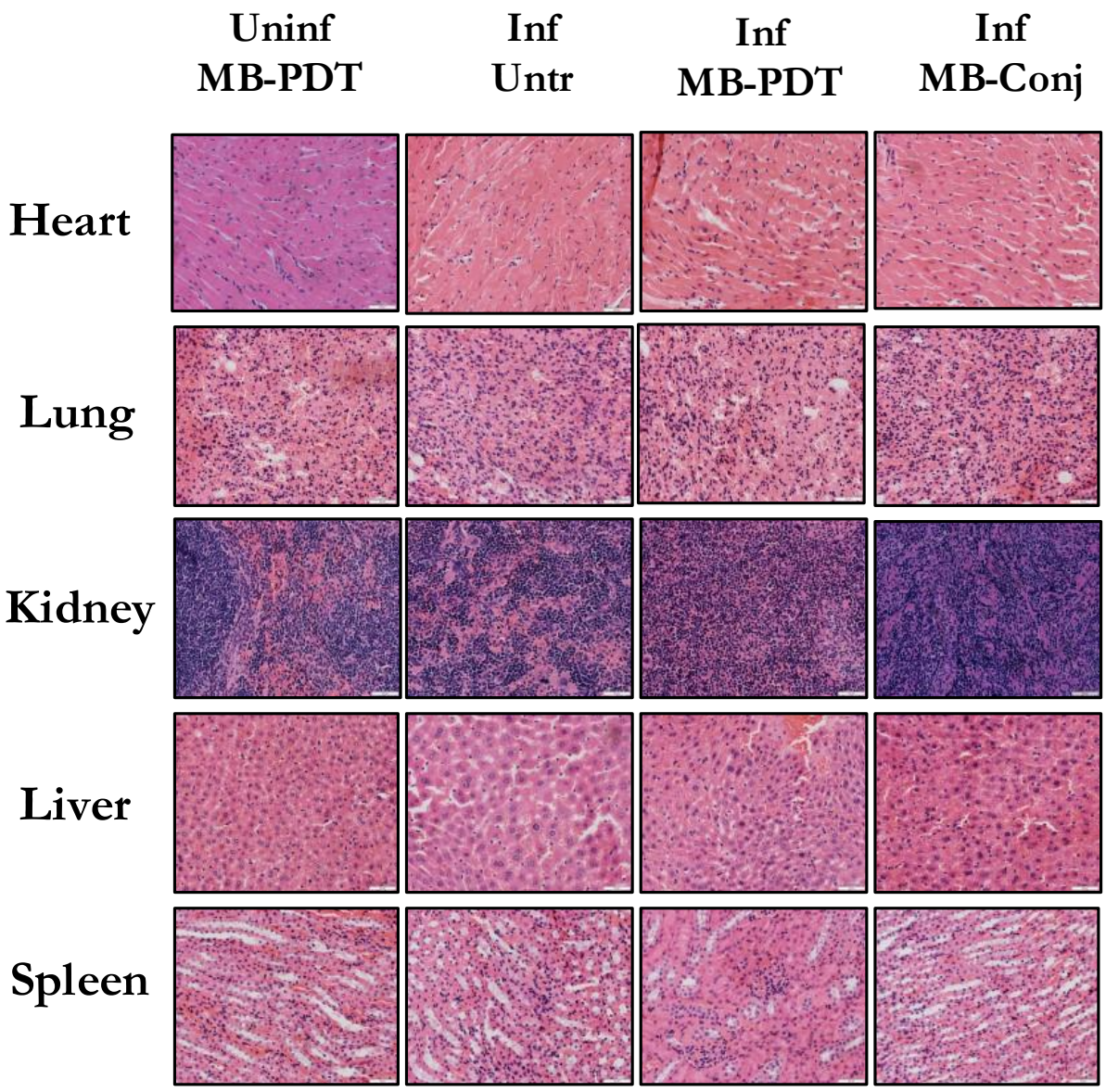

Figure 5.9. Representative histological sections of the five major organs taken at Day 7 of the trial and stained with H&E. Scale bar = 50 µM. (n = 3).

5.3.6. MB-Ab Photo-Antibody Therapy showed no significant effects on wound healing in infected excisional wounds in a pilot study of 12 mice.

Macroscopic measurements were taken daily starting immediately after surgery and finishing immediately after the study endpoint on Day 7 (Figure 5.10. and Figure 5.11.A). All mice started with no significant difference in wound gape or wound area on Day 0. A significant increase in the wound area of the Inf Untr group was observed between Day 0 and Day 1 prior to treatment (Figure 5.10). Due to this, and the results observed in Figure 5.11, the data is baseline-corrected to Day 1 – the day of treatment.

Both the wound area and gape decreased steadily over the course of the trial for all treatment groups regardless of infection (Figure 5.11.B and Figure 5.11.C). While not being statistically significant, the MB-Ab-PAT treatment group is trending towards smaller area/gape indicating improved healing compared to the other treatment groups on Day 4 and Day 7 (Figure 5.11.D and Figure 5.11.E).

The LED light treatment did not cause any redness or signs of irritation in the mice in or around the wounds (Figure 5.11.A). Some redness around the wound was observed, however it was only observed in the infected treatment groups, including the untreated group, and was not observed in the uninfected group that did undergo treatment. This indicates that any redness observed was due to the presence of infection in the wound. A much higher dose of methylene blue was used in the MB-PDT treatment groups than in the MB-Ab-PAT group. This difference can be seen visually in the macroscopic images where the MB-PDT treatments stained the wound a dark blue, while the MB-Ab-PAT treatment did not. This resulted in no adverse effects, as confirmed by the histological data.

On Day 7, the wounds were collected, and half used for histology. The wounds were wax-embedded, sectioned, and stained with Haematoxylin and Eosin (Figure 5.12.A). The histological assessment included the measurements of the wound length, dermal gape, epidermal thickness, and the percentage of re-epithelialisation (Figure 5.12.B-E). Unfortunately, given the low number of mice in the pilot study, no statistical significance was observed in any of the measurements between any of the treatments. However, the MB-PDT (UnInf/Inf) and MB-Ab-PAT treatment groups did appear to have smaller wound lengths, shorter dermal gapes, and a thicker epidermis than the untreated control.

The wounds excised on Day 7 of the trial were stained with Masson's Trichrome Total Collagen Stain to measure collagen deposition (Figure 5.13). Collagen deposition can be indicative of how far along the wound healing process has reached with more collagen being indicative of more rapid wound healing. No statistical significance was found between the treatment groups. However, there was a trend where the MB-Ab-PAT treatment group resulted in increased collagen deposition in the wound, indicating improved healing.

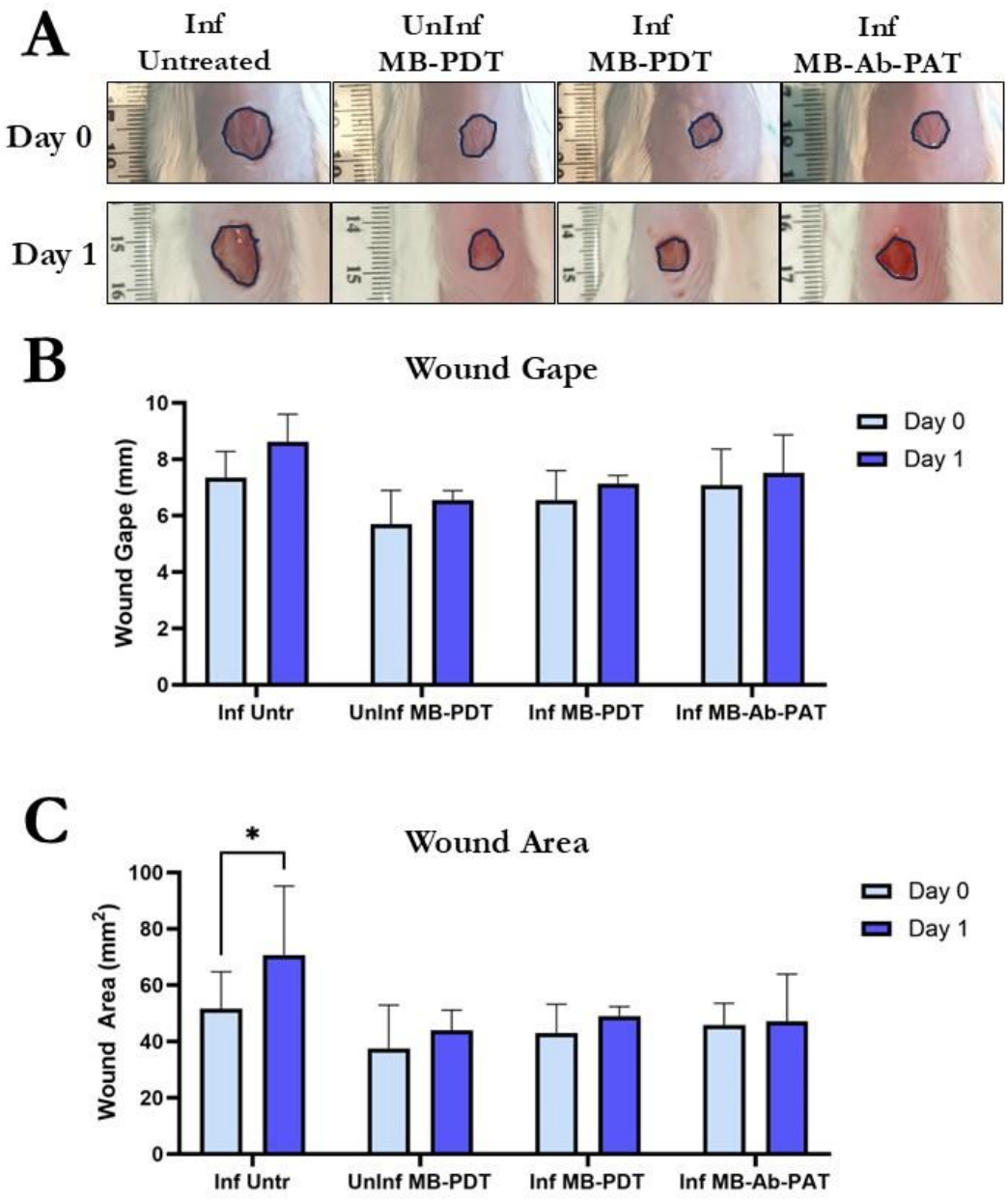

Figure 5.10. The initial macroscopic measurements of the wound gape and wound area on Day 0 and Day 1. (A) Representative images of the wounds on Day 0 and Day 1. **(B)** The Day 0 and Day 1 measurements for wound gape **(C)** The Day 0 and Day 1 measurements for the wound area. Data is presented as mean ± SD. n= 3. Statistical significance for (C) and (E) was determined using a two-way ANOVA and Tukey's Multiple Comparisons Test. * = $p < 0.05$.

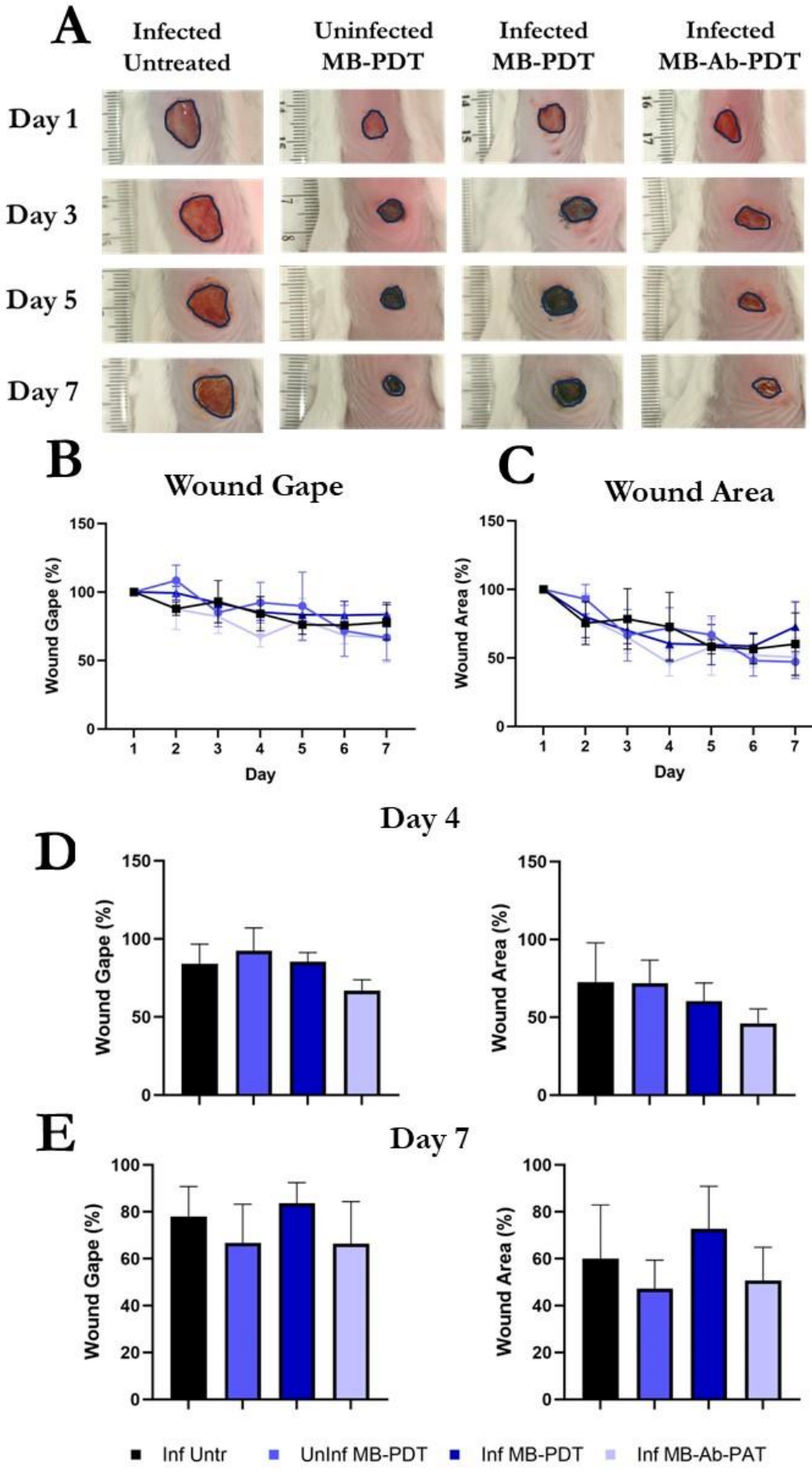
A
Infected Untreated
Uninfected MB-PDT
Infected MB-PDT
Infected MB-Ab-PDT
Day 1
Day 3
Day 5
Day 7
B
Wound Gape
Wound Gape (%)
Day
C
Wound Area
Wound Area (%)
Day
Day 4
D
Wound Gape (%)
Wound Area (%)
Day 7
E
Wound Gape (%)
Wound Area (%)
Inf Untr
UnInf MB-PDT
Inf MB-PDT
Inf MB-Ab-PAT

Figure 5.11. The macroscopic wound size over the 7-day trial. (A) Representative images of the wounds taken over the 7-day trial. **(B)** The wound gape baseline-corrected to Day 1 **(C)** The wound area baseline-corrected to Day 1 **(D)** The wound gape and wound area on Day 4. **(E)** The wound gape and wound area on Day 7. n=3. Data is baseline-corrected to the day of treatment – Day 1, and presented as mean ± SD.

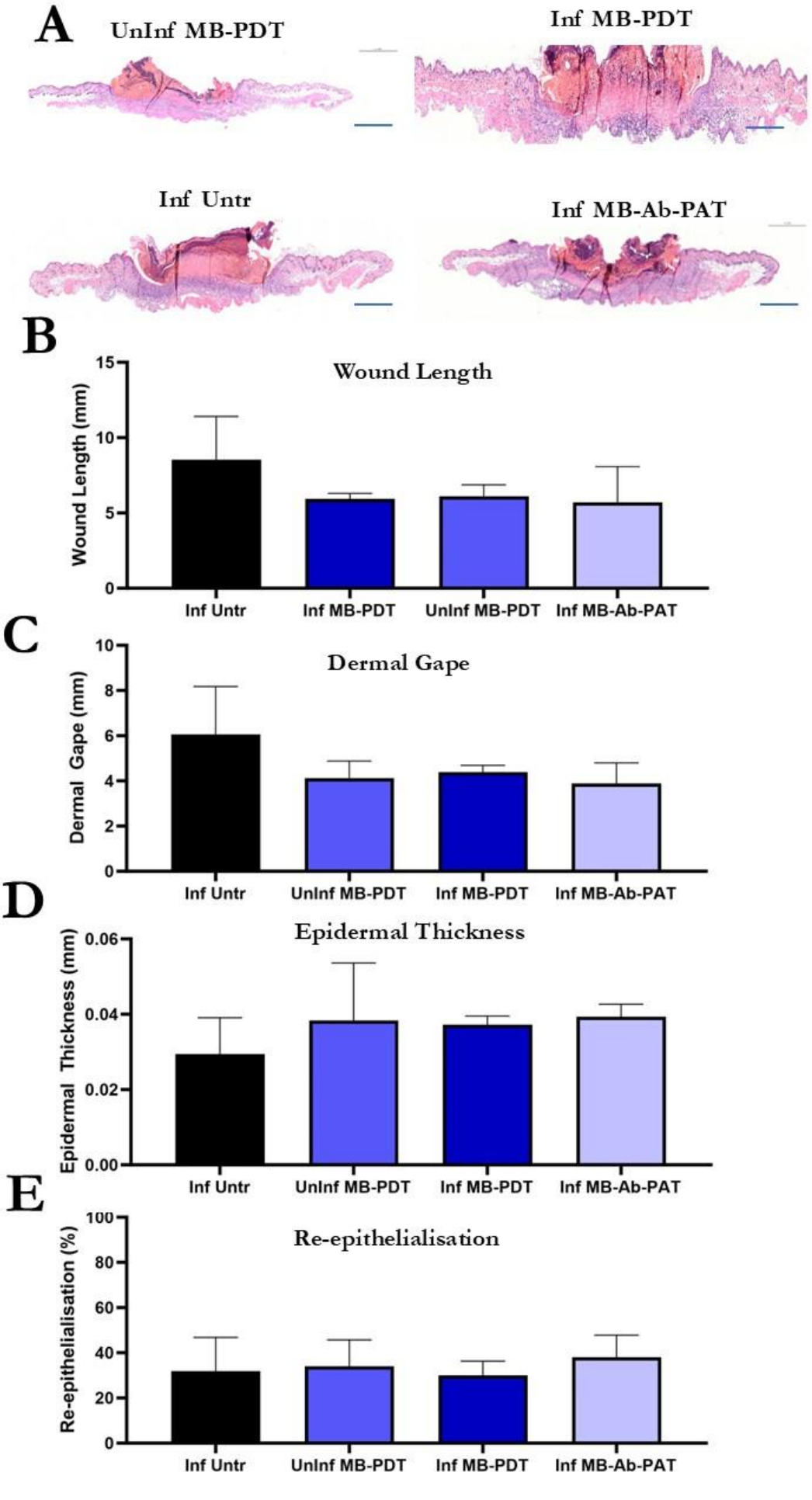
A
UnInf MB-PDT
Inf MB-PDT
Inf Untr
Inf MB-Ab-PAT
B
Wound Length
Wound Length (mm)
15
10
5
0
Inf Untr
Inf MB-PDT
UnInf MB-PDT
Inf MB-Ab-PAT
C
Dermal Gape
Dermal Gape (mm)
10
8
6
4
2
0
Inf Untr
UnInf MB-PDT
Inf MB-PDT
Inf MB-Ab-PAT
D
Epidermal Thickness
Epidermal Thickness (mm)
0.06
0.04
0.02
0.00
Inf Untr
UnInf MB-PDT
Inf MB-PDT
Inf MB-Ab-PAT
E
Re-epithelialisation
Re-epithelialisation (%)
100
80
60
40
20
0
Inf Untr
UnInf MB-PDT
Inf MB-PDT
Inf MB-Ab-PAT

Figure 5.12. The histological analysis of the wounds excised at Day 7. (A) Representative images of the H&E-stained wounds. Scale bar = 1 mm. **(B-E)** The histological measurements of the wounds. Data is presented as mean ± SD. n = 3.

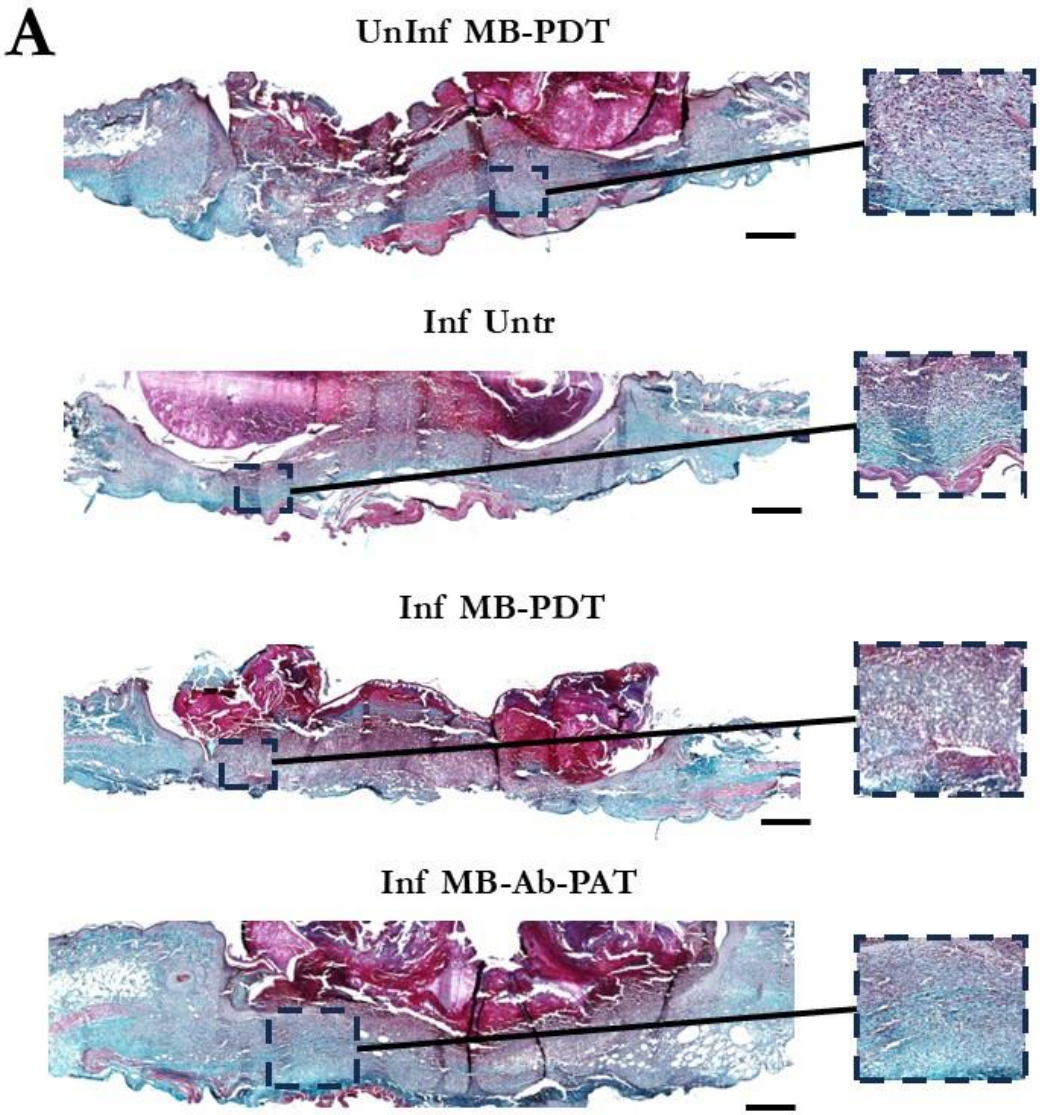

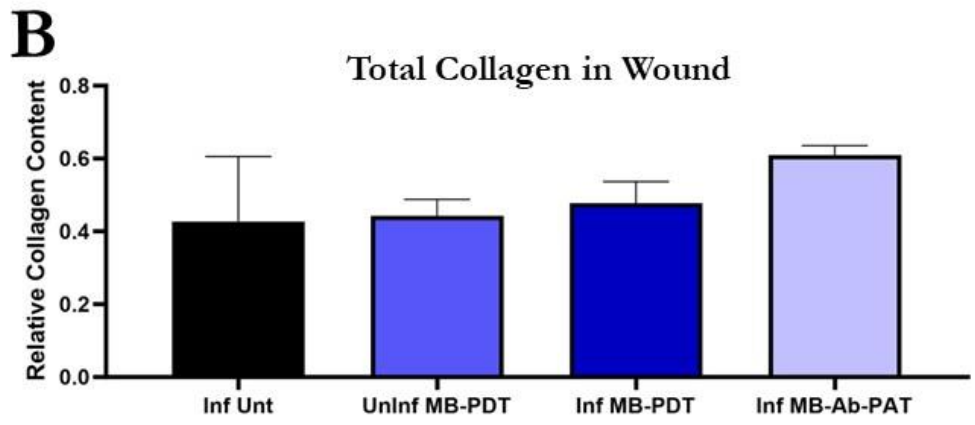

Figure 5.13. Masson's Trichrome Total Collagen Stain showing MB-AB-PAT had no effect on collagen deposition on Day 7. (A) Representative images of the excised wounds stained with Masson's Trichrome Total Collagen Stain **(B)** The total collagen in the wound measured using ImageJ. Data is presented as mean ± SD n=3. Scale bar = 1 mm.

5.3.7. MB-Ab Photo-Antibody Therapy showed no significant effects on wound infection using an infected excisional murine model.

The bacterial burden of the wound was measured daily in real time using the IVIS Live Imaging System (Figure 5.14 and Figure 5.15). All mice started on Day 0 with no significant difference in the initial inoculation of the wound. Bacterial growth was observed between Day 0 and 1 (Figure 5.14), the data was baseline corrected to Day 1 to account for this change as well as coinciding with the treatment start date.

As expected, the uninfected group showed no evidence of infection or bioluminescence above background (Figure 5.15.A). As can be seen in Figure 5.15.B, there was a large reduction in total flux at Day 2 in all groups, even untreated, which may be due to the bacteria getting acclimated to the new environment before recovering. No statistical significance between the infected treatment groups was found, however, both MB-PDT and MB-Ab-PAT trended towards improvement as seen by a decrease in the total flux. The non-infected treatment group remained uninfected through the course of the study (data not shown).

In addition to the daily IVIS imaging, half of the wound tissue was collected at the study's endpoint on Day 7 and was used to quantitate CFUs. The CFU analysis showed more bacteria in the MB-Ab-PAT group than the untreated group, though no statistical significance was found (Figure 5.15.C).

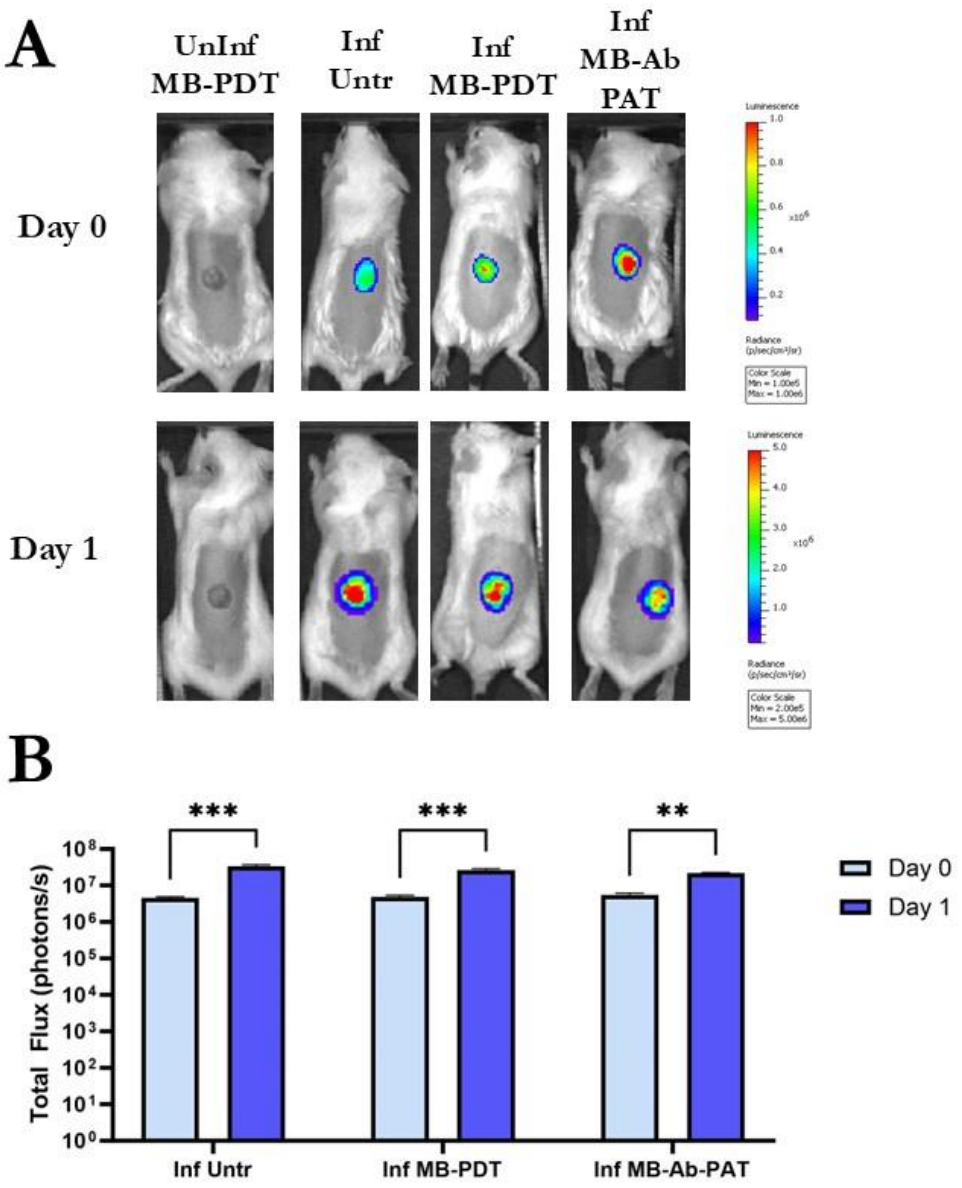

Figure 5.14. Bacterial burden significantly increased between the day of surgery (Day 0) and the following day prior to treatment (Day 1). (A) Representative images showing the bioluminescence of the wounds on Day 0. **(B)** The bacterial burden on Day 0 and Day 1. Data is presented as mean ± SD. * =p<0.05, ** =p<0.01, *** =p<0.001, **** =p<0.0001. Statistical significance was achieved using a two-way ANOVA and Sidak's Multiple Comparisons Test.

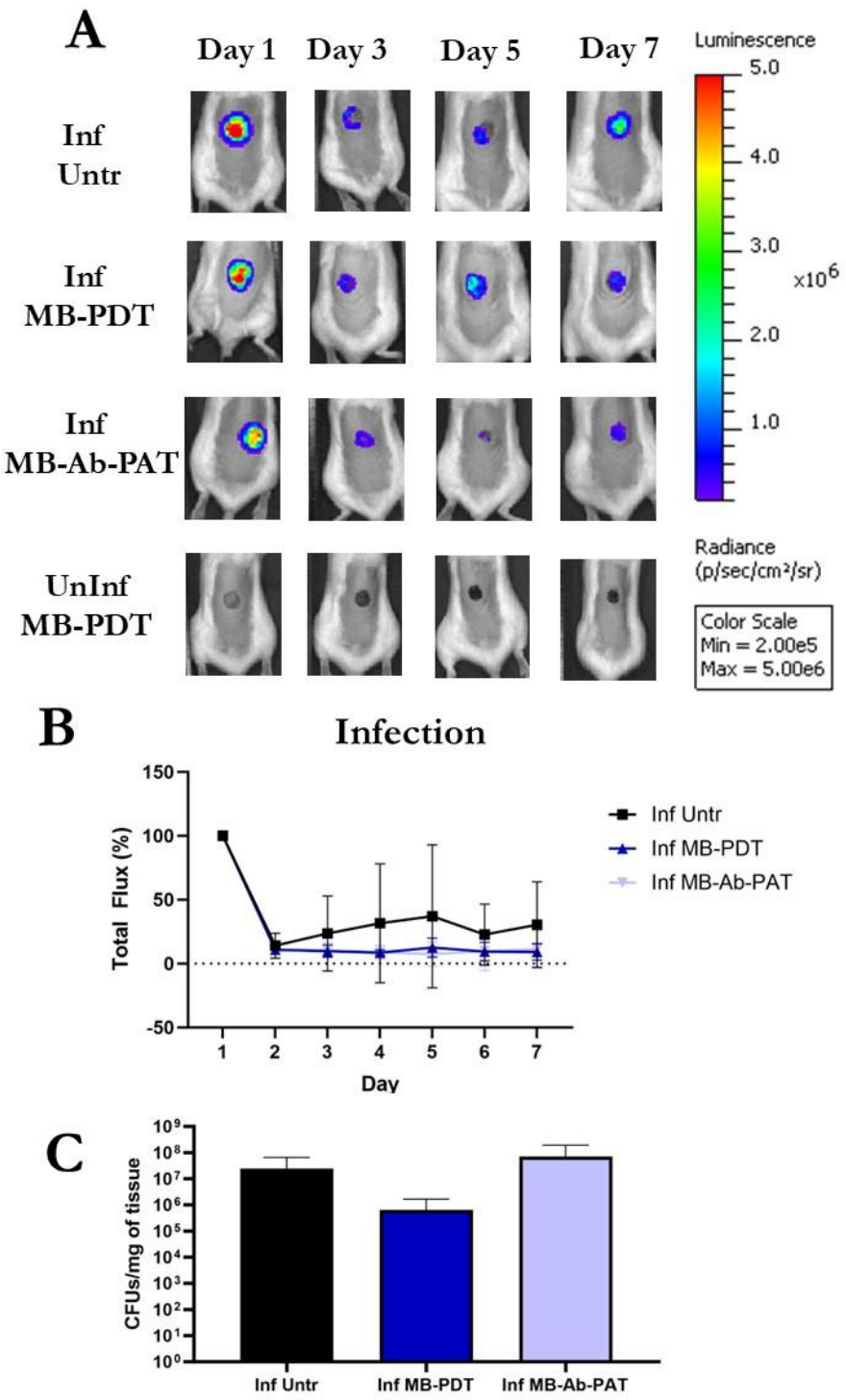

Figure 5.15. The bacterial burden over the course of the study. (A) Representative bioluminescent images taken by the IVIS over the course of the 7-day trial. **(B)** The quantified bacterial burden of the mice over the 7-day trial as measured by the IVIS baseline corrected to Day 1. **(C)** CFUs measured per mg of tissue at Day 7 from the excised wounds. Data is presented as mean ± SD. n = 3.

5.4. Discussion

Antibiotic resistance continues to rise around the world making antibiotic-alternative methods of clearing infection are of increasing necessity. Photodynamic therapy utilising Methylene Blue (MB-PDT) is a well explored method of killing micro-organisms, however, research into its effects on wound healing and mammalian cells is lacking.

In this chapter, the therapeutic effects of MB-PDT was explored both *in vitro* and *in vivo*. *In vitro*, Methylene Blue was confirmed to display cytotoxicity in skin cells, supporting the rationale to conjugate Methylene Blue to an antibody, and improving specificity to the bacteria present within wounds. Similar cytotoxic effects were also identified in these skin cells in response to MB-PDT treatment. However, due to the predicted increase in specificity of the photosensitiser we expect an antibacterial effect in response to a lower overall dose of Methylene Blue.

Both keratinocytes and fibroblasts are important for the later stages of wound repair. Fibroblasts are important for filling in the granulation tissue while keratinocytes are important for the re-epithelialisation of the wound. Previously, MB-PDT at 0.03% MB and 7.2 J/cm^2 has been shown to have no toxic effects to the epithelium on cilia in a 3D tissue model of human ciliated mucus [264]. On primary human fibroblasts, MB-PDT was found to reach 70% cell viability at 50 µg/mL Methylene Blue and 163.8 J/cm^2 24 hours post treatment. Additionally, the mitochondrial cell activity was reduced by 27% [265]. MB-PDT, at 100 µg/mL MB and 453.6 J/cm^2 caused a 1 log reduction in the population of H103 keratinocytes. The study also demonstrated the recovery rate of these keratinocytes, with the populations recovering by 85% and 48% just 6 hours post treatment with 151.2 J/cm^2 and 226.8 J/cm^2 respectively [266].

This study investigated if the standard MB-PDT treatment is toxic to either fibroblasts or keratinocytes over a 24-hour period *in vitro*. MB-PDT was cytotoxic to both the fibroblasts and the keratinocytes in a light dose and photosensitiser dose-dependent way. This indicates that standard MB-PDT treatments are harmful to mammalian cells critical for successful wound healing.

The dark toxicity (i.e. the toxicity of a photosensitiser in the absence of light) of the Methylene Blue may be of concern during an incubation time before irradiation or if not all the photosensitiser is activated in the wound. Previously, Methylene Blue has been shown

to be non-toxic to neutrophils at 100 µM after a 30-minute incubation [241]. The cell viability of primary human fibroblasts was reduced to 80% at 50 µg/mL after a 30-minute incubation [265]. In this study, the dark toxicity of Methylene Blue up to 100 µM was tested in both fibroblasts and keratinocytes. Some dark toxicity was found against the HaCaTs but this was not dose-dependent and did not reach 70% cell viability. This indicates that the dark toxicity of Methylene Blue over a 2-hour period is not of concern.

Red light alone (660 nm) showed no cytotoxicity against either the fibroblasts or the keratinocytes up to 100 J/cm^2. This agrees with previous studies that showed no negative effects on cell viability, proliferation, and migration on human gingival fibroblast (HGF-1) and murine L929 fibroblast cell lines. However, this study did only test up to 10.2 J/cm^2 [267] Conversely, in another study, the light alone showed a small cytotoxic effect on primary human fibroblasts at 54.6 J/cm^2 then recovery at 109.2 J/cm^2, then growth at 163.8 J/cm^2, 24 hours post treatment [265].

Previously, MB-PDT has been used *in vivo* to treat *C. albicans* at 450-500 µg/mL, and a MRSA biofilm at 100 µM and 50 J/cm^2 [231, 243]. In a murine model of bacterial arthritis using MRSA, MB-PDT was shown to decrease bacterial burden at 100 µM methylene blue and 50, 80 and 120 J/cm^2 (light fluences tested: 5-160 J/cm^2) with 50 J/cm^2 being the most effective and 160 J/cm^2 showing reduced antibacterial activity [231]. In my study, a "standard" treatment, based on this paper in particular, of 100 µM methylene blue and 100 J/cm^2 was used to treat both infected and uninfected wounds, though no significant decrease in *S. aureus* infection was observed.

Additionally, treating the mice with MB-PDT at 100 µM and 50 J/cm^2 one day prior to infection showed a reduction in bacterial burden over the seven-day period. This suggests that MB-PDT has the ability to suppress the development of an infection as a preventative treatment, further suggesting effects on wound healing independent of direct microbial killing [231]. While no significance was achieved, bacterial load as measured by the IVIS appears lower than the infected untreated group and prevented recovery.

Methylene Blue was successfully conjugated to an antibody specific to gram-positive bacteria using EDC/NHS chemistry in order to create a new Photo-Antibody Therapy (PAT) and the functionality of these conjugates was confirmed. This Photo-Antibody Therapy was then tested in a pilot study of 12 mice using an established infected excisional wound

model. This pilot study proved safety but with an n of 3 per group, was not statistically powered to achieve significance in regards to wound healing or infection outcomes.

The cytotoxicity studies with MB-PDT have shown a need for the improved specificity of the treatment. In this chapter, Methylene Blue was successfully conjugated to an antibody specific to gram-positive bacteria, to create a new Photo-Antibody Therapy. This Photo-Antibody Therapy has been proven to be safe in an infected excisional wound model. Rose Bengal and Zinc Phthalocyanine were successful conjugated to the antibodies, but the functionality of the conjugates was unable to be confirmed, and these conjugates were therefore not progressed to further *in vitro* and *in vivo* testing.

The pilot *in vivo* study showed that the MB-PDT and new PAT treatments were all safe in an infected excisional wound model. No adverse events were observed in the mice, and no excess weight loss occurred. A slight increase in weight loss was observed in the treated groups compared to the untreated group, though this may be due to the extended episodes of anaesthesia that accompanied the treatments. Another treatment control that could be included in the future is the administration of anaesthesia in the absence of treatment. This safety was re-affirmed with no signs of toxicity found in five major organs of the mice. While no statistical significance was found in the rate of wound healing or in the alleviation of the bacterial burden, several trends could be seen which warrant further investigation in larger studies. The macroscopic wounds were smaller for the MB-Ab-PAT treatment group on Days 4 and 7. On Day 7, both the MB-PDT and MB-Ab-PAT treatment groups showed smaller wound lengths, shorter dermal gapes, a thicker epidermis, and an increase in collagen deposition than the untreated control, indicating that the treatments may gain significance with a larger sample size. MB-PDT and MB-Ab-PAT treatment groups also displayed a trend towards less infection compared to the untreated group. This is suggestive of potential improved wound healing outcomes when Methylene Blue was used at lower concentrations but with increased specificity towards bacterial binding.

A limitation to this study is that this is a pilot study and has not yet progressed to a complete animal trial with an $n \geq 6$. A larger animal trial may clarify any differences between the treatment groups and provide more insight into the antimicrobial and wound healing effects of MB-Ab-PAT treatment approach. Extending the timeline beyond 7 days would also allow for any differences in the later stages of wound healing to be observed. Investigations could also extend to porcine wound models where the process of wound

healing is more similar to human skin. Increasing the concentration of the MB-Ab-PAT used may result in more pronounced effects, though it is interesting that the MB-Ab-PAT seemed to be as effective as the standard MB-PDT treatment in spite of a significantly lower dose being applied, highlighting the importance of targeted more specific treatment approaches that allows lower concentrations to have a similar effect without adverse effects on mammalian cells. Due to manufacturing limitations, for this pilot study, a 20-fold lower dose of MB-Ab conjugates was used compared to the standard methylene blue treatment. In the future, higher doses of the MB-Ab conjugates could also be explored.

Unfortunately, we identified a difference between the IVIS readings and the CFU measures of the bacterial load within the wound. This may be since the IVIS quantifies only metabolically active bacteria while CFUs measures all bacteria regardless of planktonic or biofilm state. Additionally, the IVIS measurements were focused on the whole wound over time, while CFUs are performed on only half the wound at the last day of trial, introducing potential variations to the interpretation of results as wounds may not have a uniform infection over the entire wound bed by the end of the trial.

Previous research has shown that MB-PDT may facilitate an increased neutrophil response to the site of treatment [241]. The tissue processing from the animal trial could be taken further to examine the effects of MB-PDT and PAT on the inflammatory phase by staining for neutrophils and macrophages. Additionally, while the functionality of the conjugates was confirmed in this study through western blots, further studies could investigate the conjugate specificity using western blots with lipopolysaccharide (LPS) instead of lipoteichoic acid (LTA) to determine specificity to gram positive bacteria over gram negative bacteria.

The binding of the conjugate to the bacteria could potentially be seen in real time, *in vitro* or *in vivo*, using a confocal or two-photon microscope. This could also provide insights into the incubation time necessary for the treatment to work, and potentially the colocalization of the photosensitiser/antibody.

Rose Bengal and Zinc Phthalocyanine were initially investigated alongside Methylene Blue, in addition to other conjugation ratios. These investigations stopped when the functionality tests using western blots yielded mixed results. This could be further investigated using western blots with additional controls. Densitometry could also be performed on the bands

to quantify the amount of protein in the sample and provide conjugation efficiency with each of the ratios.

In conclusion, Methylene Blue was successfully conjugated to an antibody specific to gram positive bacteria and its use in an infected excisional wound model showed no signs of adverse effects and promising bacteriostatic signs of antimicrobial efficacy. While no effects on wound healing or infection eradication could be observed, presented results warrant further investigation in larger animal studies.

Chapter Six –Discussion

6.1. Project Significance

Wound healing is a complex process that involves several carefully orchestrated phases and numerous cell types. If any of these phases get disrupted, wound healing may not progress appropriately and a chronic wound may form. Disruption to the skin integrity following tissue damage exposes the wound bed to bacterial contamination and potential development of clinical infection. Infection has been shown to impede wound healing by exacerbating inflammation and producing proteases which are detrimental to the mammalian cell function necessary for wound healing, as well as antimicrobial treatments. Eradication of infection or reduction of bacterial load within the wound bed can allow wound healing to recalibrate and successfully close.

Infected wounds are currently treated primarily with antibiotics. However, bacteria can develop resistance to antibiotics through a variety of mechanisms in response to exposure to antibiotics. Reducing antibiotic use is vital to combatting antimicrobial resistance. Antibiotic-alternative therapies for the treatment of infected wounds is necessary to aid in the reduction of the use of antibiotics, and to provide further treatment options for antibiotic-resistant infections.

In this thesis, several different innovative approaches were investigated to determine their effectiveness at treating infected wounds. The first approach was to improve healing and encourage wound repair so that may help the host's natural defence mechanisms to control the infection and heal despite of the infection. Therapeutic monoclonal antibodies bind proteins that contribute to disease and pathologies to inhibit their actions and improve outcomes [71]. Flightless I is a negative regulator of wound healing with under-expression improving wound healing and over-expression being detrimental to tissue repair and regeneration. Inhibiting Flightless I with the monoclonal antibody, Flightless neutralising antibody (FnAb), has been shown to improve wound healing though studies on Flightless I have not been extended to infected wounds. However, limiting its effectiveness is the protease rich environment of infected and diabetic wounds. Therefore, we packaged FnAb in porous silicon nanoparticles to protect it, whilst also facilitating a slow-release profile.

Two further approaches aimed to directly kill bacteria. First, the antimicrobial peptide, pexiganan, is an antimicrobial treatment that has been tested successfully in a human clinical trial of infected diabetic foot ulcers. However, pexiganan also displays evidence of cytotoxicity at high doses, thus we packaged pexiganan into slow release nanocarriers to mitigate any cytotoxic effects. Photodynamic therapy is another antimicrobial treatment that kills bacteria through reactive oxygen species using a photosensitiser and light. It has non-specific cytotoxicity, so we developed and tested a variation of photodynamic therapy where the photosensitiser is conjugated to an antibody to improve targeting and reduce dose.

These three antibiotic-alternative therapies in an infected excisional wound model looking for both antimicrobial and wound-promoting effects were therefore investigated. These therapies were also expanded upon by increasing their specificity or durability through chemical conjugation or the use of porous silicon nanoparticles as a delivery system.

6.2. Key Results and Discussion: FnAb

Chronic wounds have been found to have 100-fold increased protease load than equivalent acute wounds, and the presence of infection exacerbates this protease load [69-71]. This is made even worse by pathological conditions such as diabetes. Diabetic wounds are more prone to infection due to a variety of factors including hyperglycaemia, decreased vasculature, and comorbidities [84]. Combined, this creates an even more destructive environment than that of the infected wound alone, presenting an even greater challenge to treat. Treatments for infected diabetic wounds are quickly degraded in this hostile environment. Methods of protecting existing and novel treatments from degradation in the wound are being explored e.g. porous silicon nanoparticles as previously discussed. Therapies for infected wounds often focus on clearing the infection, however, promoting wound healing may allow the host's natural mechanisms to take care of the infection.

Monoclonal antibodies are a method of neutralising proteins detrimental to a biological process [71]. A protein important to wound healing is Flightless I. Flightless I is a negative regulator of wound healing with Flightless I expression upregulated in wounded skin, diabetic skin, and diabetic wounds. Reducing Flightless I expression has resulted in improved wound healing outcomes in incisional wounds, excisional wounds, burns, scars,

diabetic wounds and porcine wounds [136, 138, 140-147]. One method of reducing Flightless I expression is using the monoclonal antibody, Flightless neutralising antibody (FnAb). Monoclonal antibodies can be easily degraded by the hostile wound environment. Porous silicon nanoparticles have been shown to protect FnAb from proteolytic degradation in vitro and retained functional antibody release for up to 7 days post-treatment [145]. Previously, FnAb in porous silicon nanoparticles (FnAb pSiNPs) have been successfully used to treat excisional wounds in diabetic mice, functioning better than when FnAb was delivered alone [145]. However, FnAb pSiNPs was not assessed in diabetic wounds with an added burden of infection, which better represents the clinical population of these patients.

In this study, FnAb was delivered in porous silicon nanoparticles to infected diabetic wounds. Disappointingly, FnAb pSiNPs did not improve wound healing compared to naked FnAb or untreated controls. This is contrasted with an equivalent study performed in our lab that demonstrated FnAb pSiNPs to significantly improve diabetic wound healing in non-infected wounds compared to vehicle-treated controls (data not shown, unpublished). In that study, naked FnAb improved healing compared to treatment controls but not as effectively as FnAb pSiNPs. This suggests the delivery system is effective but will require optimisation to overcome the additional wound burden of infection and protease load. Since there was no dramatic effect of FnAb pSiNPs on wound healing, we did not anticipate an effect on infection. As expected, no effect on infection was observed.

Interestingly, a clear divide in the measure of infection was observed between the treatment groups that received porous silicon nanoparticles (FnAb pSiNPs, mIgG pSiNPs, pSiNPs) and the treatment groups that did not (FnAb, Saline). The treatment groups that received the nanoparticles showed signs of infection at the injection sites around the wound i.e. erythema, swelling, scabbing. Despite this, the FnAb pSiNPs appeared to control the infection the best out of the nanoparticle treatment groups based on the daily bioluminescence. FnAb alone did not affect wound healing compared to the saline control despite previous studies showing FnAb accelerating wound healing. This may be due to FnAb degrading in the hostile infected diabetic wound and demonstrates the need to protect FnAb from proteolytic degradation.

Future investigations would involve changing the method of delivery from intradermal injections to a topical application, possibly in a hydrogel. Antimicrobial and biofilm assays

would also be performed on the porous silicon nanoparticles to elucidate any direct effects on bacteria. While there was success in using the STZ-model of diabetes in male mice, as diabetic foot ulcers are more common in patients with Type II diabetes, a genetic model of db/db diabetic mice will also be utilised.

6.3. Key Results and Discussion: Pexiganan

Antimicrobial peptides are naturally occurring peptides produced by humans and animals to treat and prevent infection. One notable peptide is pexiganan, which was successfully used to treat infected diabetic foot ulcers in a clinical trial consisting of over 800 patients. In the clinical trial, pexiganan eliminated the infection and promoted wound closure, as well as the ofloxacin control, with no difference in the occurrence of side effects between the two treatments. One notable difference was that resistance to ofloxacin developed throughout the 42-day trial, but no resistance to pexiganan was observed [202, 203]. Despite this exciting outcome, subsequent follow up studies have been negligible, likely due to pexiganan failing to outperform the antibiotic and therefore not receiving FDA approval. Additionally, pexiganan has shown cytotoxicity to cell types crucial for wound healing at high concentrations.

As predicted, we found pexiganan was detrimental to keratinocyte viability and proliferation at concentrations higher than 40 µg/mL, and to migration at concentrations of 80 µg/mL. An increase in proliferation was observed at 1 and 5 µg/mL and no difference in migration was seen up to 80 µg/mL. Importantly, pexiganan was non-cytotoxic to keratinocytes at lower concentrations, and even resulted in an increase in cell proliferation at lower concentrations. With an MIC of 16 µg/mL, a low dose of pexiganan at 20 µg/mL was expected to be able to treat infection and potentially promote wound healing through effects on keratinocytes. The antimicrobial peptides, Tylotoin and Tiger 17, have been shown to increase the proliferation of keratinocytes and fibroblasts though the mechanism of action is currently unknown [180, 181].

Based on these *in vitro* wound studies, a safe and beneficial pexiganan dose was determined to be 20 µg per wound. Working closely with materials scientist, we are in a unique opportunity to overcome this limitation by packaging pexiganan into slow-release nano-carriers, which may allow us to overcome this toxicity, and further explore pexiganan

as a viable treatment option. As such, we proposed that the packaging of pexiganan in nanocarriers that limited the release of pexiganan so that the concentration does not exceed 20 μg/wound may provide antibacterial efficacy and without the cytotoxicity effects. An added advantage of nano-carriers is that ones can be specifically selected that are able to protect pexiganan from the hostile protease-enriched wound environment.

Infected wounds have a prolonged inflammatory response which result in a high protease load that is destructive to wound healing and any treatments applied [69-71]. Porous silicon nanoparticles are a biocompatible delivery system that involves encapsulating the treatment to protect it from the hostile environment of the wound. In this study, porous silicon nanoparticles were used to deliver pexiganan in an infected excisional wound model. Previously, collaborators loaded pexiganan into porous silicon nanoparticles functionalised through either thermal oxidation or hydrosilylation with the hydrosilylated nanoparticles showing greater loading efficiency, and a slow release over 150 hours. The pexiganan in the hydrosilylated porous silicon nanoparticles were shown to be non-cytotoxic to fibroblasts up to 50 μg/mL and showed antibacterial properties against both *S. aureus* and *P. aeruginosa*, both directly and indirectly. This preliminary *in vitro* data demonstrated that the nanoparticles are capable of carrying and releasing a therapeutic dose of pexiganan slowly over six days, making them an ideal delivery system in an infected wound model.

All treatments were delivered in a biocompatible pluronic F127 hydrogel that slowly releases the pexiganan and provides a moist environment that encourages wound healing [254]. Porous silicon nanoparticles increased the efficacy of pexiganan on wound healing in an infected excisional wound model compared to pexiganan alone. Treatment with a single dose of 'naked' pexiganan equivalent to the overall amount delivered by the porous silicon nanoparticles had a detrimental effect on wound healing compared to the hydrogel control. We identified that pexiganan delivered in porous silicon nanoparticles had no effect on infection but there was a positive effect on wound healing in an infected excisional murine wound model compared to pexiganan alone. This may be because pexiganan may need to be applied at higher concentrations in order to be antibacterial while the wound healing benefits are only seen at lower doses. The nanoparticles could be optimised to release the pexiganan more quickly to eradicate the infection e.g. larger pore sizes, functionalisation, faster degradation. With half the loaded pexiganan released within

48 hours, a higher concentration could result in higher dose initially to control the infection, and then a slow release of the remaining half for the rest of the trial for the wound healing benefits. Even two variations of porous silicon nanoparticles could be used, one with a quick release of contents at the beginning, and one with a slower release later. Due to the wide variation observed in the infection data in the animal trial, the animal trial may need to be further optimised for more consistent results.

6.4. Key Results and Discussion: Photodynamic Therapy

Photodynamic therapy is an antibiotic-alternative method of killing bacteria that works through the production of reactive oxygen species. A photosensitiser is applied which passively enters the bacterial cell and is then activated by light of a certain wavelength to produce reactive oxygen species and singlet oxygen which cause damage. This damage is localised to where the photosensitiser is, and an accumulation of the photosensitiser is often needed to produce enough damage to kill the bacteria, however, adverse effects to mammalian cells is a common problem of this approach.

Photodynamic therapy is not specific to bacterial cells over mammalian cells, causing damage to the surrounding healthy tissue in addition to the infection. Methods of increasing specificity are being researched [225]. Our novel approach for the treatment of infected wounds is through antibody conjugation, i.e. Photo-Antibody Therapy, which involves conjugating a photosensitiser to an antibody specific to its target to increase the specificity of the photosensitiser to bacteria over healthy tissue, allowing for a more efficient photodynamic therapy treatment of infected wounds.

The photosensitiser used in this study was Methylene Blue; a common blue dye, activated by red light, with previous clinical uses [268]. Photodynamic therapy using Methylene Blue has been used to treat and prevent infection in murine models [231] but not in an infected excisional wound and antibody-conjugation for this photosensitiser for the treatment of infection had not been previously explored.

In this study, an antibody specific to lipoteichoic acid on gram positive bacteria was attached to Methylene Blue using EDC/NHS conjugation chemistry. The chemistry required extensive trial and error with great difficulties trying to confirm the success of the conjugation through mass spectrometry, even utilising outside labs, to no success. In place of the originally intended mass spectrometry, fluorescence microscopy was used to confirm

the conjugation reactions, and western blots to confirm the antibody was still functional. This photosensitiser-antibody conjugate, MB-Ab, was tested for safety in a pilot study of 12 mice.

Prior to the pilot study, MB-PDT was found to be cytotoxic to keratinocytes and fibroblasts at higher doses after 24 hours which demonstrated a need to increase the specificity to avoid damage to cells integral to wound healing. While a standard MB-PDT treatment regimen used in previous animal trials was used, a 20-fold lower dose of MB-Ab conjugates was utilised. The MB-Ab conjugates that we selected showed safety in the pilot study with no signs of skin toxicity observed at the macroscopic or microscopic level, or in any of the organs collected. This suggested we chose a dosing regimen that was safe for the experimental animals. While no statistical significance was found in the assessment of wound healing or infection, the treated groups showed smaller wounds than the untreated control. Additionally, both the MB-Ab conjugate and MB alone appeared to control the infection better than the untreated control. Repeatedly, there seemed to be minimal difference between the MB-Ab and MB treatment groups despite a lower dose of the MB-Ab conjugate being used indicating that the antibody conjugation increased the efficacy of MB. The observation of a trend towards improved healing and reduced infection suggests plausibility for this treatment approach in infected wounds but supports further optimisation, which will be discussed below.

Photo Antibody Therapy has not been investigated in the context of infection but has been explored as a cancer treatment. Other methods of increasing the specificity of the photosensitiser include conjugating the photosensitiser to peptides, oligonucleotides, and chitosan, however, these have had limited efficacy. Nanoparticles have also been explored, as well as quantum dots, which can be effective but can also introduce other variables such as loading efficiency, release, and without further modifications does not increase specificity.

The next step in this research is to conduct a full animal trial using the same model and treatments. Using real-time microscopy to observe colocalization and microbial killing between the treatments and the bacteria would provide more insight into the incubation times required for an effective treatment, as would antimicrobial assays.

6.5. Porous silicon nanoparticles cannot be intradermally injected in the presence of infection

An unexpected complication arose during the real time assessment of infection using the IVIS. In the FnAb trial, porous silicon nanoparticles were intradermally injected around the infected wound on Day 1. Bioluminescence was detected at the injection sites 24 hours later by the IVIS and remained there throughout the trial, but only in the mice treated with nanoparticles. This complication was not observed in the Pexiganan trial where porous silicon nanoparticles were topically applied. Different surface functionalisation methods are used to give porous silicon nanoparticles different properties [157]. The porous silicon nanoparticles used in the FnAb trial were thermally oxidised, while the porous silicon nanoparticles used in the Pexiganan trial were hydrosilylated. In this case, the different functionalisation methods were chosen based on loading and release assays for their target treatment. Porous silicon nanoparticles are reported to have auto luminescent properties that can be exacerbated by thermal oxidation while hydrosilylation is reported to have no effect on auto luminescence [154, 155, 160, 161].

To determine if the bioluminescence observed in the FnAb trial was caused by the bioluminescent bacteria or whether it was auto luminescence from the nanoparticles, porous silicon nanoparticles were intradermally injected into scavenged mice posthumously and imaged using the IVIS. No auto luminescence was detected from the intradermally injected nanoparticles, indicating that the bioluminescence seen throughout the trial was due to bacteria and not the nanoparticles. This indicates that the infection may have migrated from the wound to the injection sites within 24 hours of treatment and continued to migrate over the course of the trial but only in the treatment groups that received porous silicon nanoparticles. The remaining treatment groups that were also intradermally injected did not show signs of infection in this study. This indicates that it is the combination of the nanoparticles and the intradermal injection and not the intradermal injection alone that caused the infection to spread.

Medical devices and implants are prone to infection and biofilm development [269, 270]. It is possible that the nanoparticles similarly provided the bacteria with a hospitable surface on which to grow. Porous silicon nanoparticles do degrade, though the rate of degradation varies, and with the added bacteria so close to the injection sites, it is possible the nanoparticles were not able to degrade before infection migrated to the injection sites and

managed to establish itself. Intradermal injection may not be an appropriate delivery system for porous silicon nanoparticles in the presence of infection. Sterilising the nanoparticles through UV irradiation before application may be a method of limiting infection worthy of exploring in future trials.

Both the FnAb and pexiganan trials utilised porous silicon nanoparticles, however, the bioluminescent pattern was only observed in the FnAb trial where the nanoparticles were intradermally injected and not in the pexiganan trial where the nanoparticles were topically applied. The main differences between the porous silicon nanoparticles used in the FnAb trial and the pexiganan trial, is that the pexiganan nanoparticles were functionalised through hydrosilylation as opposed to thermal oxidation. Hydrosilylation is not expected to enhance the luminescent properties of porous silicon nanoparticles. The porous silicon nanoparticles used in the FnAb trial were smaller but with larger pores (particle size: 161 nm, pore size: 33 nm) which may have allowed the bacteria to enter the nanoparticles and provided a niche environment for them to flourish. While the porous silicon nanoparticles used in the pexiganan trial had smaller pores (pore size: 10 nm), they are larger particles (particle size: 340 nm) which could provide the bacteria with a larger surface area to form a biofilm. Nanoparticles with inherent antimicrobial properties, such as gold and silver, may not have this complication, while contributing positive synergistic effects. It is possible that the nanoparticles used in the pexiganan trial did exhibit some luminescence during the trial but went unnoticed due to the nanoparticles residing along with the bioluminescent bacteria in the wound. In the future, a control group of mice administered nanoparticles topically in the absence of infection would elucidate this and could allow for any effects from the nanoparticles to be investigated and accounted for.

In dead mice that were posthumously administered porous silicon nanoparticles, auto luminescence was detected from the nanoparticles that were topically applied to the mice. While this luminescence was minimal compared to infection, this may indicate that thermally oxidised porous silicon nanoparticles should not be topically applied without the appropriate controls to account for the baseline auto luminescence.

6.6. Limitations and Future Directions

6.6.1. Optimising the Wound Model

This study used infected excisional murine models with minimal deviation between each other. However, the infected wound model is not representative of an infected human wound, but rather an investigation into the wound healing process in the presence of infection. Human wounds are extremely varied. While this model utilises excisional wounds, other wounds like burns and pressure ulcers could be explored. Currently, creating a chronic infected excisional wound murine model has not been achieved. Though, STZ-induced diabetic models are considered to be models of delayed wound healing [271].

A wound size of 6 mm was used for the Photo Antibody Therapy pilot study, while the pexiganan and FnAb trials used 10 mm excisional wounds. The 6 mm pilot study wounds healed significantly faster over the course of 7 days than the 10 mm trials. However, with smaller wound sizes, the wound area was reduced more rapidly within 24 hours due to contraction, and it can be more difficult for the infection to take hold. Excisional wounds can be held open through the use of splints to discourage wound healing through contraction, however, this introduces another variable and foreign material into the wound, is technically challenging, and only has limited efficacy [272].

While wound size decreased steadily over a seven-day period for the Photo Antibody Therapy and Pexiganan trials, more significant results may be seen by extending the study to 10 or 14 days. The Pexiganan trial in particular at 10 mm barely decreased by the end of the 7 days, growing slightly during the trial due to scab formation. Extending the Pexiganan trial long enough that the scabs fall off revealing the true wound size underneath may provide a more accurate view of the wound healing processes underneath.

This study used bioluminescent *S. aureus* to infect the excisional wounds. Infected wound development in humans often begins with *S. aureus* contamination due to this bacteria being a commensal on the skin. As the infection develops, it often becomes polymicrobial, with gram-negative bacteria like *Pseudomonas aeruginosa* becoming a prominent population in the wound [43]. Investigations should begin with *S. aureus* but should then expand into the harder to kill, *P. aeruginosa*, and then polymicrobial infections. Short term infection and wound healing studies do not reflect the long-term progression of human

chronic wounds. This infected wound model is an excellent starting point for its simplicity while using complex biological systems.

The wound healing process varies between strains of mice, as well as sex [273]. Due to this, wound healing studies will often begin with one sex, usually female, and then expand into the other. The pexiganan trial followed this standard by using all female mice. The PAT pilot study utilised both male and female mice to ensure there were no sex-based side effects of the treatment and only one safety study need be conducted. The Flii trial diverged from this as sex-based complications arose with the STZ-model of diabetes. Diabetes was successfully induced through the STZ method in 100% of male mice with almost no mortality, while the female mice had only a 5% induction rate. For this reason, this study utilised all male mice while the causes behind this sex-based difference was explored.

Female mice have been shown to be less sensitive STZ [123, 250]. While the exact mechanisms for this are unknown, estrogens have been shown to reduce the sensitivity of male rats to STZ-induced diabetes, indicating that estrogen plays a protective role against STZ [123, 274]. Higher doses of STZ may be needed to induce diabetes in female mice using STZ, with one study using 100 mg/kg, compared to the 50 mg/kg used in this study [275].

6.6.2. Optimising Treatments

For the Pexiganan and FnAb trials, the mice were treated once on Day 1, 24 hours post-surgery and infection, while the mice in the Photo Antibody Therapy trial were treated every day. Treating on Day 1 is treating in the early stages of wound healing when inflammation and infection are establishing. This is fine for antibacterial treatments that can work by preventing the infection from establishing but pro-wound healing effects may not be seen at this time. This study showed that pexiganan may be able to promote wound healing by acting on keratinocytes. FnAb works by neutralising Flii which is crucial for the early stages of wound healing but detrimental to the later stages of wound healing. Timing these two treatments later, perhaps on Day 3 or 4, may better target the later stages of wound healing. Repeated treatments, on Days 1 and 4 or every day, could yield more significant results. The treatment dose could also be increased, or the nanoparticles optimised to carry more treatment or release the treatment faster or slower. In another trial conducted concurrently with the FnAb trial (data not shown), FnAb delivered in porous

silicon nanoparticles were successfully used to treat excisional wounds in the absence of infection. This supports the possibility that the increased hostility of infection may require an increased dose or treatment schedule.

6.6.3. Delivery method

In this study three delivery methods were utilised: topical application, topical application of hydrogel, and intradermal injection. For the Photo Antibody Therapy trial, the treatments were delivered topically via a pipette. This allowed for quick absorption and direct contact with the bacteria which was necessary for photodynamic therapy to work. Due to this is, neither hydrogels nor intradermal injections were optimal delivery methods. Though incubation times between the administration of the photosensitiser and its activation by light could be explored to give the photosensitiser more time to enter the bacterial cells before activation.

In the Pexiganan trial, the treatments were also delivered topically via a pipette but in a hydrogel. Hydrogels promote wound healing and allow for a slow drug release [254]. In this study, all wounds were left uncovered which can leave the wound open for further bacterial contamination and can dry the wound out. The hydrogels provide some coverage and provide a moist environment ideal for wound healing but may be rubbed off by the mice moving around. While the hydrogels were not apparent by Day 3 of the trial, further studies could be conducted into the degradation rate of the hydrogel, as well as the release of the porous silicon nanoparticles from the hydrogel, and the release of pexiganan from the nanoparticles within the hydrogel. Wound healing and antimicrobial assays could also be performed to investigate the effects of this vehicle directly.

Treatments were intradermally injected around the wound for the FnAb trial. Intradermal injections provide more instant results as the treatment is delivered directly to the skin around the wound [145]. However, this is not often clinically relevant as clinically, a topical treatment is more often used.

Due to the results found in the FnAb trial, porous silicon nanoparticles should not be intradermally injected in the presence of infection due to the infection moving from the wound into the injection sites. Topical application of porous silicon nanoparticles may affect the luminescence read by the IVIS. However, this would be dependent on the

functionalisation method used and the baseline could be accounted for with the appropriate controls.

6.6.4. IVIS vs CFUs

Consistently throughout the studies, the bioluminescence measured at the end of the trial did not match the CFUs measured directly from the wound. This could be a few reasons. First, the IVIS only measures metabolically active bacteria. This is a potential issue particularly for biofilm models where bacteria are metabolically inert and therefore won't be bioluminescent [131]. In this regard, the CFUs are a more accurate measure of the bacterial burden but only at the end of the trial. In order to get similar results from the CFUs, more animals would need to be used and the end points staggered throughout the trial (e.g. Days 1, 3, 5, and 7). The daily IVIS measurements reduces this animal burden and allows for more refined care of the animals throughout the study.

Additionally, the CFUs taken at the end of the trial are determined from using only a portion of the wound, while the IVIS captures the whole wound. It is possible that the CFUs are reflective of only the portion of wound taken and not the whole wound. In this case, using half of the wound for CFUs, as was done in the Photo-Antibody Therapy animal trial, is more preferable than using only a quarter of the wound, as was done for the Pexiganan and FnAb trials. Though variation across the two halves of the wound could still exist.

The discrepancy between the IVIS readings and the CFUs can be seen in other published studies [276, 277]. One study graphed the correlation between the two metrics; graphing the log values of the CFUs relative to the *in vivo* bioluminescence measured by the IVIS [278]. The study that needs to be conducted is a simple *in vitro* biofilm assay measured daily using the IVIS, where samples are taken daily for CFUs. This way, the two metrics can be seen side by side, and the time at which a biofilm begins to form could be determined. This could also allow a type of calibration curve to be formed for use in future studies.

Additional measures of the bacterial burden could be taken to further supplement this data. For instance, LIVE/DEAD staining could be performed on a quarter of the wound to quantify the biofilm biomass. Using the LIVE/DEAD BacLight Bacterial Viability Kit, wounds are rinsed of the planktonic bacteria, and the wound stained and Z stack imaged. This would provide information on the biofilm, while the IVIS provides information on the planktonic

bacteria, while the CFUs ideally measure both. A limitation of CFUs is that the bacteria in a biofilm struggle to separate from the matrix or detach from the tissue and can aggregate. To separate the bacteria from the tissue, the infected tissue is vortexed and sonicated repeatedly though this method can also affect bacterial viability [279]. Gram stains could also be performed on the sample of wound collected for histological staining and the infection quantified. Histological staining could be expanded to investigate host responses to infection such as inflammasomes, caspases, and apoptosis, to determine if the treatments are promoting inflammation, apoptosis, pyroptosis, or necrosis.

6.6.5. Additional wound models

In this study, infected excisional murine models were used, however, other models of infection could be explored. *In vitro*, the antibacterial properties of Photo Antibody Therapy and Pexiganan could be explored on planktonic bacteria using minimum inhibition concentration (MIC) and time-kill assays, and on biofilms using a crystal violet assay or an *in vitro* biofilm wound assay that involves biofilms grown on membranes. Antibacterial investigations could then be expanded into an *ex vivo* porcine infected wound model which utilises a piece of pig skin to hold infection and then treatment which can then be analysed similarly to an *in vivo* model [280].

A current limitation of infected wound models is the difficulty to consistently form biofilms, a key recurring feature in chronic wounds [42, 59]. One method currently being explored is the transfer of established biofilms into excisional wounds. In diabetic mice, *P. aeruginosa* biofilms were developed on membranes were transferred to excisional wounds two days post-surgery and covered in a dressing. None of these wounds managed to heal within four weeks, 64% healed within six weeks, and all wounds had healed by eight weeks [281, 282].

A variation of the murine infected excisional wound model used in this study that could be explored is the biofilm model where the infected wounds are covered with dressings and left untreated for 3-4 days to allow a biofilm to develop before beginning treatment. A polymicrobial biofilm model could also be explored where a polymicrobial biofilm is developed *in vitro* and then transferred to an animal model.

Murine models were used in this study as they are a common first step to clinical use due to being small, inexpensive and easily researched. However, there are significant

differences between the physiology of mice and that of humans. A key difference is that murine wounds heal mostly through contraction while human wounds heal through re-epithelialisation and granulation. Porcine physiology is more similar to humans in this way with full thickness wounds healing through contraction, and partial thickness wounds healing through re-epithelialisation and granulation [283]. In order for any of the treatments to progress to human clinical trials, research using porcine wound models would need to be conducted.

No diabetic model encapsulates the entirety of the disease, but rather each model represents an aspect. The inducible STZ model of diabetes was used in the FnAb trial which is a model of Type I diabetes. However, higher doses of STZ may be needed to induce diabetes in female mice [275]. As, this treatment is intended to be used in patients with Type II diabetes and so a genetic db/db model will next be investigated. If the investigations continue into pigs, the STZ model will need to be used again.

6.6.6. COVID-19

The COVID 19 pandemic was a great delay for research worldwide and this study was no different. Delays in importing the LED light and modified photosensitisers internationally led to delays in the Photo Antibody Therapy work which led to the expansion of this study into other therapies. The pandemic led to closure of the core animal facility which delayed many animal trials and caused a backlog. This led to only a pilot study of the Photo Antibody Therapy trial being conducted and not managing to take the study to a full trial in time for this thesis.

6.7. Conclusion

In summary, this thesis explored three antibiotic-alternative therapies for the treatment of infected wounds. Neither FnAb nor FnAb delivered in porous silicon nanoparticles improved wound healing in the presence of infection. However, this data is clouded by the infection moving from the excisional wound to the intradermal injection sites around the wound in the presence of nanoparticles. The pexiganan trial showed that pexiganan had a detrimental effect on wound healing while pexiganan delivered in porous silicon nanoparticles marginally improved wound healing. Pexiganan had no effect on infection regardless of delivery method. This indicates that porous silicon nanoparticles are a desirable delivery system for pexiganan though optimisation is needed to see an effect on infection. A methylene blue-antibody conjugate was created to be used as a Photo Antibody Therapy. In mice wounds, promising results were found with indicators of safety and the conjugate performing equal to or better than the unconjugated methylene blue. Overall, this study demonstrated how complicated infection makes the wound healing process and how difficult finding new treatments for infected wounds is.

References

1. Wong, R., et al., *The dynamic anatomy and patterning of skin.* Experimental dermatology, 2016. **25**(2): p. 92-98.
2. Ramadon, D., et al., *Enhancement strategies for transdermal drug delivery systems: Current trends and applications.* Drug delivery and translational research, 2021: p. 1-34.
3. MacNeil, S., *Progress and opportunities for tissue-engineered skin.* Nature, 2007. **445**(7130): p. 874-880.
4. Arda, O., N. Göksügür, and Y. Tüzün, *Basic histological structure and functions of facial skin.* Clinics in dermatology, 2014. **32**(1): p. 3-13.
5. Roig-Rosello, E. and P. Rousselle, *The human epidermal basement membrane: a shaped and cell instructive platform that aging slowly alters.* Biomolecules, 2020. **10**(12): p. 1607.
6. Aleemardani, M., et al., *The importance of mimicking dermal-epidermal junction for skin tissue engineering: a review.* Bioengineering, 2021. **8**(11): p. 148.
7. Driskell, R.R., et al., *Defining dermal adipose tissue.* Experimental dermatology, 2014. **23**(9): p. 629-631.
8. Boateng, J.S., et al., *Wound healing dressings and drug delivery systems: a review.* Journal of pharmaceutical sciences, 2008. **97**(8): p. 2892-2923.
9. Trinh, X.-T., et al., *A comprehensive review of natural compounds for wound healing: targeting bioactivity perspective.* International Journal of Molecular Sciences, 2022. **23**(17): p. 9573.
10. Jespersen, J., *Pathophysiology and clinical aspects of fibrinolysis and inhibition of coagulation. Experimental and clinical studies with special reference to women on oral contraceptives and selected groups of thrombosis prone patients.* Danish Medical Bulletin, 1988. **35**(1): p. 1-33.
11. George Broughton, I., J.E. Janis, and C.E. Attinger, *The basic science of wound healing.* Plastic and reconstructive surgery, 2006. **117**(7S): p. 12S-34S.
12. Pitchford, S., D. Pan, and H.C. Welch, *Platelets in neutrophil recruitment to sites of inflammation.* Current opinion in hematology, 2017. **24**(1): p. 23-31.
13. Bielefeld, K.A., S. Amini-Nik, and B.A. Alman, *Cutaneous wound healing: recruiting developmental pathways for regeneration.* Cellular and Molecular Life Sciences, 2013. **70**: p. 2059-2081.
14. Theoharides, T.C., et al., *Mast cells and inflammation.* Biochimica et Biophysica Acta (BBA)-Molecular Basis of Disease, 2012. **1822**(1): p. 21-33.
15. Juráňová, J., J. Franková, and J. Ulrichová, *The role of keratinocytes in inflammation.* Journal of Applied Biomedicine, 2017. **15**(3): p. 169-179.
16. Werner, S., T. Krieg, and H. Smola, *Keratinocyte–fibroblast interactions in wound healing.* Journal of investigative dermatology, 2007. **127**(5): p. 998-1008.
17. Kim, M.-H., et al., *Dynamics of neutrophil infiltration during cutaneous wound healing and infection using fluorescence imaging.* Journal of Investigative Dermatology, 2008. **128**(7): p. 1812-1820.
18. Ellis, S., E.J. Lin, and D. Tartar, *Immunology of wound healing.* Current dermatology reports, 2018. **7**: p. 350-358.
19. Wilgus, T.A., S. Roy, and J.C. McDaniel, *Neutrophils and wound repair: positive actions and negative reactions.* Advances in wound care, 2013. **2**(7): p. 379-388.
20. Wang, X.-J., et al. *Role of TGFβ-mediated inflammation in cutaneous wound healing*. in *Journal of Investigative Dermatology Symposium Proceedings*. 2006. Elsevier.
21. Ueno, C., T.K. Hunt, and H.W. Hopf, *Using physiology to improve surgical wound outcomes.* Plastic and reconstructive surgery, 2006. **117**(7S): p. 59S-71S.
22. Rodrigues, M., et al., *Wound healing: a cellular perspective.* Physiological reviews, 2019. **99**(1): p. 665-706.
23. Wynn, T.A. and K.M. Vannella, *Macrophages in tissue repair, regeneration, and fibrosis.* Immunity, 2016. **44**(3): p. 450-462.

24. Ballas, C.B. and J.M. Davidson, *Delayed wound healing in aged rats is associated with increased collagen gel remodeling and contraction by skin fibroblasts, not with differences in apoptotic or myofibroblast cell populations.* Wound Repair and Regeneration, 2001. **9**(3): p. 223-237.
25. Ferrante, C.J. and S.J. Leibovich, *Regulation of macrophage polarization and wound healing.* Advances in wound care, 2012. **1**(1): p. 10-16.
26. Li, J., Y.P. Zhang, and R.S. Kirsner, *Angiogenesis in wound repair: angiogenic growth factors and the extracellular matrix.* Microscopy research and technique, 2003. **60**(1): p. 107-114.
27. Hong, W.X., et al., *The role of hypoxia-inducible factor in wound healing.* Advances in wound care, 2014. **3**(5): p. 390-399.
28. Hayakawa, T., et al., *Changes in type of collagen during the development of human post-burn hypertrophic scars.* Clinica Chimica Acta, 1979. **93**(1): p. 119-125.
29. Eriksen, H.A., et al., *Increased content of type III collagen at the rupture site of human Achilles tendon.* Journal of Orthopaedic Research, 2002. **20**(6): p. 1352-1357.
30. Rohani, M.G. and W.C. Parks, *Matrix remodeling by MMPs during wound repair.* Matrix biology, 2015. **44**: p. 113-121.
31. Bahar-Shany, K., A. Ravid, and R. Koren, *Upregulation of MMP-9 production by TNFα in keratinocytes and its attenuation by vitamin D.* Journal of cellular physiology, 2010. **222**(3): p. 729-737.
32. Baum, J. and H.S. Duffy, *Fibroblasts and myofibroblasts: what are we talking about?* Journal of cardiovascular pharmacology, 2011. **57**(4): p. 376-379.
33. Bond, J.S., et al., *Scar redness in humans: how long does it persist after incisional and excisional wounding?* Plastic and reconstructive surgery, 2008. **121**(2): p. 487-496.
34. Toy, L., *Matrix metalloproteinases: their function in tissue repair.* Journal of wound care, 2005. **14**(1): p. 20-22.
35. McDougall, S., et al., *Fibroblast migration and collagen deposition during dermal wound healing: mathematical modelling and clinical implications.* Philosophical Transactions of the Royal Society A: Mathematical, Physical and Engineering Sciences, 2006. **364**(1843): p. 1385-1405.
36. Landis, S.J., *Chronic wound infection and antimicrobial use.* Advances in skin & wound care, 2008. **21**(11): p. 531-540.
37. Powers, J.G., et al., *Wound healing and treating wounds: Chronic wound care and management.* Journal of the American Academy of Dermatology, 2016. **74**(4): p. 607-625.
38. Negut, I., V. Grumezescu, and A.M. Grumezescu, *Treatment strategies for infected wounds.* Molecules, 2018. **23**(9): p. 2392.
39. Swanson, T., et al., *IWII wound infection in clinical practice consensus document 2016 update.* Wound Practice & Research: Journal of the Australian Wound Management Association, 2016. **24**(4): p. 194-198.
40. Diban, F., et al., *Biofilms in chronic wound infections: innovative antimicrobial approaches using the in vitro Lubbock chronic wound biofilm model.* International journal of molecular sciences, 2023. **24**(2): p. 1004.
41. Edwards, R. and K.G. Harding, *Bacteria and wound healing.* Current opinion in infectious diseases, 2004. **17**(2): p. 91-96.
42. Suleman, L., *Extracellular bacterial proteases in chronic wounds: a potential therapeutic target?* Advances in wound care, 2016. **5**(10): p. 455-463.
43. Puca, V., et al., *Microbial species isolated from infected wounds and antimicrobial resistance analysis: Data emerging from a three-years retrospective study.* Antibiotics, 2021. **10**(10): p. 1162.
44. Glik, J., et al., *The impact of the types of microorganisms isolated from blood and wounds on the results of treatment in burn patients with sepsis.* Polish Journal of Surgery, 2012. **84**(1): p. 6-16.
45. Huszczynski, S.M., J.S. Lam, and C.M. Khursigara, *The role of Pseudomonas aeruginosa lipopolysaccharide in bacterial pathogenesis and physiology.* Pathogens, 2019. **9**(1): p. 6.

46. Falcone, M., et al., *Challenges in the management of chronic wound infections.* Journal of global antimicrobial resistance, 2021. **26**: p. 140-147.
47. Mahmoudi, M. and L.J. Gould, *Opportunities and challenges of the management of chronic wounds: a multidisciplinary viewpoint.* Chronic Wound Care Management and Research, 2020: p. 27-36.
48. Percival, S.L., et al., *Antiseptics for treating infected wounds: efficacy on biofilms and effect of pH.* Critical reviews in microbiology, 2016. **42**(2): p. 293-309.
49. CARE, I.I.W., *Use of wound antiseptics in practice.* 2023.
50. Lineback, C.B., et al., *Hydrogen peroxide and sodium hypochlorite disinfectants are more effective against Staphylococcus aureus and Pseudomonas aeruginosa biofilms than quaternary ammonium compounds.* Antimicrobial Resistance & Infection Control, 2018. **7**: p. 1-7.
51. Dadgostar, P., *Antimicrobial resistance: implications and costs.* Infection and drug resistance, 2019: p. 3903-3910.
52. De Oliveira, D.M., et al., *Antimicrobial resistance in ESKAPE pathogens.* Clinical microbiology reviews, 2020. **33**(3): p. 10.1128/cmr. 00181-19.
53. Marston, H.D., et al., *Antimicrobial resistance.* Jama, 2016. **316**(11): p. 1193-1204.
54. Naghavi, M., et al., *Global burden of bacterial antimicrobial resistance 1990–2021: a systematic analysis with forecasts to 2050.* The Lancet, 2024. **404**(10459): p. 1199-1226.
55. Murray, C.J.L., et al., *Global burden of bacterial antimicrobial resistance in 2019: a systematic analysis.* The Lancet, 2022. **399**(10325): p. 629-655.
56. Christaki, E., M. Marcou, and A. Tofarides, *Antimicrobial resistance in bacteria: mechanisms, evolution, and persistence.* Journal of molecular evolution, 2020. **88**(1): p. 26-40.
57. Lee, J.-H., *Perspectives towards antibiotic resistance: from molecules to population*. 2019, Springer. p. 181-184.
58. Donlan, R.M. and J.W. Costerton, *Biofilms: survival mechanisms of clinically relevant microorganisms.* Clinical microbiology reviews, 2002. **15**(2): p. 167-193.
59. Malone, M., et al., *The prevalence of biofilms in chronic wounds: a systematic review and meta-analysis of published data.* Journal of wound care, 2017. **26**(1): p. 20-25.
60. Grande, R., V. Puca, and R. Muraro, *Antibiotic resistance and bacterial biofilm.* Expert Opinion on Therapeutic Patents, 2020. **30**(12): p. 897-900.
61. Howell-Jones, R., et al., *A review of the microbiology, antibiotic usage and resistance in chronic skin wounds.* Journal of antimicrobial chemotherapy, 2005. **55**(2): p. 143-149.
62. Blanco-Fernandez, B., et al., *Nanotechnology approaches in chronic wound healing.* Advances in wound care, 2021. **10**(5): p. 234-256.
63. Han, G. and R. Ceilley, *Chronic wound healing: a review of current management and treatments.* Advances in therapy, 2017. **34**: p. 599-610.
64. Siddiqui, A.R. and J.M. Bernstein, *Chronic wound infection: facts and controversies.* Clinics in dermatology, 2010. **28**(5): p. 519-526.
65. Zahedi, P., et al., *A review on wound dressings with an emphasis on electrospun nanofibrous polymeric bandages.* Polymers for Advanced Technologies, 2010. **21**(2): p. 77-95.
66. Australia, W., *5 Point Plan to Solve Australia's Chronic Wound Problem.* 2024.
67. Armstrong, D.G., et al., *Diabetic Foot Ulcers: A Review.* JAMA, 2023. **330**(1): p. 62-75.
68. Raziyeva, K., et al., *Immunology of acute and chronic wound healing.* Biomolecules, 2021. **11**(5): p. 700.
69. Schreml, S., et al., *The impact of the pH value on skin integrity and cutaneous wound healing.* Journal of the European Academy of Dermatology and Venereology, 2010. **24**(4): p. 373-378.
70. Tarnuzzer, R.W. and G.S. Schultz, *Biochemical analysis of acute and chronic wound environments.* Wound Repair and Regeneration, 1996. **4**(3): p. 321-325.

71. Turner, C.T., et al., *Therapeutic Potential of Inorganic Nanoparticles for the Delivery of Monoclonal Antibodies.* Journal of Nanomaterials, 2015. **2015**(1): p. 309602.
72. MacLeod, A.S. and J.N. Mansbridge, *The innate immune system in acute and chronic wounds.* Advances in wound care, 2016. **5**(2): p. 65-78.
73. FrykbergRobert, G., *Challenges in the treatment of chronic wounds.* Advances in wound care, 2015.
74. Krzyszczyk, P., et al., *The role of macrophages in acute and chronic wound healing and interventions to promote pro-wound healing phenotypes.* Frontiers in physiology, 2018. **9**: p. 419.
75. Zhao, R., et al., *Inflammation in chronic wounds.* International journal of molecular sciences, 2016. **17**(12): p. 2085.
76. Hesketh, M., et al., *Macrophage phenotypes regulate scar formation and chronic wound healing.* International journal of molecular sciences, 2017. **18**(7): p. 1545.
77. Burgess, J.L., et al., *Diabetic wound-healing science.* Medicina, 2021. **57**(10): p. 1072.
78. Park, H.Y., et al., *A long-standing hyperglycaemic condition impairs skin barrier by accelerating skin ageing process.* Experimental dermatology, 2011. **20**(12): p. 969-974.
79. Lai, C., et al., *Comparison of transepidermal water loss and skin hydration in diabetics and nondiabetics.* Clinical and Experimental Dermatology, 2021. **46**(1): p. 58-64.
80. Sakai, S., et al., *Functional properties of the stratum corneum in patients with diabetes mellitus: similarities to senile xerosis.* British Journal of Dermatology, 2005. **153**(2): p. 319-323.
81. Ibuki, A., et al., *Aging-like physiological changes in the skin of Japanese obese diabetic patients.* SAGE Open Medicine, 2018. **6**: p. 2050312118756662.
82. Deng, L., et al., *The role of oxidative stress and antioxidants in diabetic wound healing.* Oxidative medicine and cellular longevity, 2021. **2021**(1): p. 8852759.
83. Dworzański, J., et al., *Glutathione peroxidase (GPx) and superoxide dismutase (SOD) activity in patients with diabetes mellitus type 2 infected with Epstein-Barr virus.* Plos one, 2020. **15**(3): p. e0230374.
84. Jagadeesh, A.T., et al., *Culture characterization of the skin microbiome in type 2 diabetes mellitus: a focus on the role of innate immunity.* Diabetes Research and Clinical Practice, 2017. **134**: p. 1-7.
85. Eming, S.A., P. Martin, and M. Tomic-Canic, *Wound repair and regeneration: mechanisms, signaling, and translation.* Science translational medicine, 2014. **6**(265): p. 265sr6-265sr6.
86. Sindrilaru, A., et al., *An unrestrained proinflammatory M1 macrophage population induced by iron impairs wound healing in humans and mice.* The Journal of clinical investigation, 2011. **121**(3): p. 985-997.
87. Beidler, S.K., et al., *Inflammatory cytokine levels in chronic venous insufficiency ulcer tissue before and after compression therapy.* Journal of vascular surgery, 2009. **49**(4): p. 1013-1020.
88. Doupis, J., et al., *Microvascular reactivity and inflammatory cytokines in painful and painless peripheral diabetic neuropathy.* The Journal of Clinical Endocrinology & Metabolism, 2009. **94**(6): p. 2157-2163.
89. Morey, M., et al., *Hyperglycemia acts in synergy with hypoxia to maintain the pro-inflammatory phenotype of macrophages.* PloS one, 2019. **14**(8): p. e0220577.
90. Montanaro, M., et al., *Macrophage activation and M2 polarization in wound bed of diabetic patients treated by dermal/epidermal substitute Nevelia.* The International Journal of Lower Extremity Wounds, 2022. **21**(4): p. 377-383.
91. Zykova, S.N., et al., *Altered cytokine and nitric oxide secretion in vitro by macrophages from diabetic type II-like db/db mice.* Diabetes, 2000. **49**(9): p. 1451-1458.
92. Dinh, T. and A. Veves, *Microcirculation of the diabetic foot.* Current pharmaceutical design, 2005. **11**(18): p. 2301-2309.
93. Beckman, J.A., M.A. Creager, and P. Libby, *Diabetes and atherosclerosis: epidemiology, pathophysiology, and management.* Jama, 2002. **287**(19): p. 2570-2581.

94. Novosyadlyy, R., et al., *Crosstalk between PDGF and IGF-I receptors in rat liver myofibroblasts: implication for liver fibrogenesis.* Laboratory investigation, 2006. **86**(7): p. 710-723.
95. Catrina, S.-B., et al., *Hyperglycemia regulates hypoxia-inducible factor-1α protein stability and function.* Diabetes, 2004. **53**(12): p. 3226-3232.
96. Yang, D.-R., et al., *Endothelial dysfunction in vascular complications of diabetes: a comprehensive review of mechanisms and implications.* Frontiers in Endocrinology, 2024. **15**: p. 1359255.
97. Xu, S., et al., *Endothelial dysfunction in atherosclerotic cardiovascular diseases and beyond: from mechanism to pharmacotherapies.* Pharmacological reviews, 2021. **73**(3): p. 924-967.
98. Lima, A.L., et al., *Cutaneous manifestations of diabetes mellitus: a review.* American Journal of Clinical Dermatology, 2017. **18**: p. 541-553.
99. Andrade, T.A.M., et al., *Skin changes in streptozotocin-induced diabetic rats.* Biochemical and biophysical research communications, 2017. **490**(4): p. 1154-1161.
100. Kim, J.H., et al., *Impaired permeability and antimicrobial barriers in type 2 diabetes skin are linked to increased serum levels of advanced glycation end-product.* Experimental dermatology, 2018. **27**(8): p. 815-823.
101. Caley, M.P., V.L.C. Martins, and E.A. O'Toole, *Metalloproteinases and Wound Healing.* Advances in Wound Care, 2015. **4**(4): p. 225-234.
102. Lobmann, R., et al., *Expression of matrix metalloproteinases and growth factors in diabetic foot wounds treated with a protease absorbent dressing.* Journal of Diabetes and its Complications, 2006. **20**(5): p. 329-335.
103. Wan, R., et al., *Diabetic wound healing: The impact of diabetes on myofibroblast activity and its potential therapeutic treatments.* Wound Repair and Regeneration, 2021. **29**(4): p. 573-581.
104. Feng, X., et al., *Fibrin and collagen differentially but synergistically regulate sprout angiogenesis of human dermal microvascular endothelial cells in 3-dimensional matrix.* International journal of cell biology, 2013. **2013**(1): p. 231279.
105. Health, A.I.o. and Welfare, *Diabetes: Australian facts*. 2024, AIHW: Canberra.
106. Wounds, A., *Pre-Budget Submission to fight Australia's chronic wound epidemic.* 2022.
107. Vuorlaakso, M., et al., *Major amputation profoundly increases mortality in patients with diabetic foot infection.* Frontiers in surgery, 2021. **8**: p. 655902.
108. Armstrong, D.G., et al., *Five year mortality and direct costs of care for people with diabetic foot complications are comparable to cancer.* Journal of foot and ankle research, 2020. **13**: p. 1-4.
109. Costantini, E., et al., *Type 2 diabetes mellitus and sepsis: state of the art, certainties and missing evidence.* Acta Diabetologica, 2021. **58**(9): p. 1139-1151.
110. Schuetz, P., P. Castro, and N.I. Shapiro, *Diabetes and sepsis: preclinical findings and clinical relevance.* Diabetes care, 2011. **34**(3): p. 771-778.
111. Stacey, H.J., et al., *The prevalence of methicillin-resistant Staphylococcus aureus among diabetic patients: a meta-analysis.* Acta diabetologica, 2019. **56**: p. 907-921.
112. Wang, Z., et al., *Association between diabetes mellitus and outcomes of patients with sepsis: A meta-analysis.* Medical science monitor: international medical journal of experimental and clinical research, 2017. **23**: p. 3546.
113. Frydrych, L.M., et al., *Obesity and type 2 diabetes mellitus drive immune dysfunction, infection development, and sepsis mortality.* Journal of leukocyte Biology, 2018. **104**(3): p. 525-534.
114. Esper, A.M., M. Moss, and G.S. Martin, *The effect of diabetes mellitus on organ dysfunction with sepsis: an epidemiological study.* Critical care, 2009. **13**: p. 1-6.
115. King, A. and J. Bowe, *Animal models for diabetes: understanding the pathogenesis and finding new treatments.* Biochemical pharmacology, 2016. **99**: p. 1-10.

116. Kottaisamy, C.P.D., et al., *Experimental animal models for diabetes and its related complications—a review.* Laboratory animal research, 2021. **37**(1): p. 23.
117. Pearson, J.A., F.S. Wong, and L. Wen, *The importance of the Non Obese Diabetic (NOD) mouse model in autoimmune diabetes.* Journal of autoimmunity, 2016. **66**: p. 76-88.
118. Hu, P., et al., *Type 1 diabetic Akita mice have low bone mass and impaired fracture healing.* Bone, 2021. **147**: p. 115906.
119. Wang, J., et al., *A mutation in the insulin 2 gene induces diabetes with severe pancreatic β-cell dysfunction in the Mody mouse.* The Journal of clinical investigation, 1999. **103**(1): p. 27-37.
120. Zakaria, Z.Z., M.N. Ahmad, and N.A. Qinna, *Animal models in type 2 diabetes mellitus research: pros and cons.* Jordan Journal of Agricultural Sciences, 2021. **17**(4): p. 425-440.
121. Asrafuzzaman, M., et al., *Animal models for assessing the impact of natural products on the aetiology and metabolic pathophysiology of Type 2 diabetes.* Biomedicine & Pharmacotherapy, 2017. **89**: p. 1242-1251.
122. Denroche, H.C., F.K. Huynh, and T.J. Kieffer, *The role of leptin in glucose homeostasis.* Journal of diabetes investigation, 2012. **3**(2): p. 115-129.
123. Furman, B.L., *Streptozotocin-Induced Diabetic Models in Mice and Rats.* Current Protocols in Pharmacology, 2015. **70**(1): p. 5.47.1-5.47.20.
124. Kahanovitz, L., P.M. Sluss, and S.J. Russell, *Type 1 diabetes—a clinical perspective.* Point of care, 2017. **16**(1): p. 37-40.
125. Nørgaard, S.A., et al., *Softened food reduces weight loss in the streptozotocin-induced male mouse model of diabetic nephropathy.* Laboratory animals, 2018. **52**(4): p. 373-383.
126. Etuk, E., *Animals models for studying diabetes mellitus.* Agric Biol JN Am, 2010. **1**(2): p. 130-134.
127. Heydemann, A., *An overview of murine high fat diet as a model for type 2 diabetes mellitus.* Journal of diabetes research, 2016. **2016**(1): p. 2902351.
128. Sami, D.G., H.H. Heiba, and A. Abdellatif, *Wound healing models: A systematic review of animal and non-animal models.* Wound Medicine, 2019. **24**(1): p. 8-17.
129. Wilhelm, K.P., D. Wilhelm, and S. Bielfeldt, *Models of wound healing: an emphasis on clinical studies.* Skin Research and Technology, 2017. **23**(1): p. 3-12.
130. Kopecki, Z. and A. Cowin, *Fighting chronic wound infection-one model at a time.* Wound Practice & Research: Journal of the Australian Wound Management Association, 2017. **25**(1): p. 6-13.
131. Ogunniyi, A.D., et al., *Bioluminescent murine models of bacterial sepsis and scald wound infections for antimicrobial efficacy testing.* Plos one, 2018. **13**(7): p. e0200195.
132. Strudwick, X.L. and A.J. Cowin, *Multifunctional Roles of the Actin-Binding Protein Flightless I in Inflammation, Cancer and Wound Healing.* Front Cell Dev Biol, 2020. **8**: p. 603508.
133. Campbell, H., et al., *The Drosophila melanogaster flightless-I gene involved in gastrulation and muscle degeneration encodes gelsolin-like and leucine-rich repeat domains and is conserved in Caenorhabditis elegans and humans.* Proceedings of the National Academy of Sciences, 1993. **90**(23): p. 11386-11390.
134. de Couet, H.G., et al., *Molecular and mutational analysis of a gelsolin-family member encoded by the flightless I gene of Drosophila melanogaster.* Genetics, 1995. **141**(3): p. 1049-1059.
135. Straub, K.L., M.C. Stella, and M. Leptin, *The gelsolin-related flightless I protein is required for actin distribution during cellularisation in Drosophila.* Journal of cell science, 1996. **109**(1): p. 263-270.
136. Ruzehaji, N., et al., *Attenuation of flightless I improves wound healing and enhances angiogenesis in a murine model of type 1 diabetes.* Diabetologia, 2014. **57**(2): p. 402-12.
137. Adams, D.H., et al., *Gender specific effects on the actin-remodelling protein Flightless I and TGF-beta1 contribute to impaired wound healing in aged skin.* Int J Biochem Cell Biol, 2008. **40**(8): p. 1555-69.

138. Ruzehaji, N., et al., *The influence of Flightless I on Toll-like-receptor-mediated inflammation in a murine model of diabetic wound healing.* Biomed Res Int, 2013. **2013**: p. 389792.
139. Campbell, H.D., et al., *Fliih, a gelsolin-related cytoskeletal regulator essential for early mammalian embryonic development.* Molecular and cellular biology, 2002. **22**(10): p. 3518-3526.
140. Cowin, A.J., et al., *Flightless I deficiency enhances wound repair by increasing cell migration and proliferation.* J Pathol, 2007. **211**(5): p. 572-581.
141. Turner, C.T., et al., *Delivery of Flightless I siRNA from Porous Silicon Nanoparticles Improves Wound Healing in Mice.* ACS Biomater Sci Eng, 2016. **2**(12): p. 2339-2346.
142. Adams, D.H., et al., *Attenuation of Flightless I, an actin-remodelling protein, improves burn injury repair via modulation of transforming growth factor (TGF)-beta1 and TGF-beta3.* Br J Dermatol, 2009. **161**(2): p. 326-36.
143. Lin, C.H., et al., *Decreased expression of Flightless I, a gelsolin family member and developmental regulator, in early-gestation fetal wounds improves healing.* Mamm Genome, 2011. **22**(5-6): p. 341-52.
144. Turner, C.T., et al., *Fibroblast-specific upregulation of Flightless I impairs wound healing.* Exp Dermatol, 2015. **24**(9): p. 692-7.
145. Turner, C.T., et al., *Delivery of Flightless I Neutralizing Antibody from Porous Silicon Nanoparticles Improves Wound Healing in Diabetic Mice.* Adv Healthc Mater, 2017. **6**(2).
146. Cameron, A.M., et al., *Flightless I is a key regulator of the fibroproliferative process in hypertrophic scarring and a target for a novel antiscarring therapy.* Br J Dermatol, 2016. **174**(4): p. 786-94.
147. Mills, S.J., et al., *Flightless I Negatively Regulates Macrophage Surface TLR4, Delays Early Inflammation, and Impedes Wound Healing.* Cells, 2022. **11**(14).
148. Kopecki, Z., et al., *Flightless I regulates hemidesmosome formation and integrin-mediated cellular adhesion and migration during wound repair.* J Invest Dermatol, 2009. **129**(8): p. 2031-45.
149. Yang, G.N., et al., *Effect of flightless I expression on epidermal stem cell niche during wound repair.* Advances in Wound Care, 2020. **9**(4): p. 161-173.
150. Jackson, J.E., et al., *In vitro analysis of the effect of Flightless I on murine tenocyte cellular functions.* J Orthop Surg Res, 2020. **15**(1): p. 170.
151. Thomas, H.M., et al., *Attenuation of Flightless I Increases Human Pericyte Proliferation, Migration and Angiogenic Functions and Improves Healing in Murine Diabetic Wounds.* Int J Mol Sci, 2020. **21**(16).
152. Chan, H., et al., *Cytoskeletal protein flightless I differentially affects TGF-beta isoform expression in both in vitro and in vivo wound models.* Wound Practice & Research: Journal of the Australian Wound Management Association, 2014. **22**(3): p. 169-181.
153. Jackson, J.E., et al., *Flii neutralizing antibodies improve wound healing in porcine preclinical studies.* Wound Repair Regen, 2012. **20**(4): p. 523-36.
154. Lee, S.H., J.S. Kang, and D. Kim, *A mini review: recent advances in surface modification of porous silicon.* Materials, 2018. **11**(12): p. 2557.
155. Sailor, M.J., *Chemical reactivity and surface chemistry of porous silicon.* Handbook of Porous silicon, 2014: p. 355-380.
156. Kang, R.H., et al., *Systematic degradation rate analysis of surface-functionalized porous silicon nanoparticles.* Materials, 2019. **12**(4): p. 580.
157. Jung, Y., Y. Huh, and D. Kim, *Recent advances in surface engineering of porous silicon nanomaterials for biomedical applications.* Microporous and Mesoporous Materials, 2021. **310**: p. 110673.
158. Bimbo, L.M., et al., *Biocompatibility of Thermally Hydrocarbonized Porous Silicon Nanoparticles and their Biodistribution in Rats.* ACS Nano, 2010. **4**(6): p. 3023-3032.
159. Park, J.-H., et al., *Biodegradable luminescent porous silicon nanoparticles for in vivo applications.* Nature Materials, 2009. **8**(4): p. 331-336.

160. Zeng, Q., et al., *Degradable and self-luminescence porous silicon particles as tissue adhesive for wound closure, monitoring and accelerating wound healing.* Journal of Colloid and Interface Science, 2022. **607**: p. 1239-1252.
161. Park, Y., et al., *Photoluminescent and biodegradable porous silicon nanoparticles for biomedical imaging.* Journal of Materials Chemistry B, 2019. **7**(41): p. 6271-6292.
162. Heinrich, J.L., et al., *Luminescent colloidal silicon suspensions from porous silicon.* Science, 1992. **255**(5040): p. 66-68.
163. Godefroo, S., et al., *Classification and control of the origin of photoluminescence from Si nanocrystals.* Nature nanotechnology, 2008. **3**(3): p. 174-178.
164. Wilson, W.L., P. Szajowski, and L. Brus, *Quantum confinement in size-selected, surface-oxidized silicon nanocrystals.* Science, 1993. **262**(5137): p. 1242-1244.
165. Stojanovic, V., et al., *Potential of porous silicon nanoparticles as an emerging platform for cancer theranostics.* Journal of Materials Chemistry B, 2016. **4**(44): p. 7050-7059.
166. Quignard, S., et al., *Silica nanoparticles as sources of silicic acid favoring wound healing in vitro.* Colloids and Surfaces B: Biointerfaces, 2017. **155**: p. 530-537.
167. Öri, F., et al., *Silicon-dioxide− polyvinylpyrrolidone as a wound dressing for skin defects in a murine model.* Journal of Cranio-Maxillofacial Surgery, 2017. **45**(1): p. 99-107.
168. Naderi, N., et al., *Nanoparticles in wound healing; from hope to promise, from promise to routine.* Front. Biosci, 2018. **23**: p. 1038-1059.
169. Miao, F., et al., *Antimicrobial Peptides: The Promising Therapeutics for Cutaneous Wound Healing.* Macromol Biosci, 2021. **21**(10): p. e2100103.
170. Hassan, M., et al., *Natural antimicrobial peptides from bacteria: characteristics and potential applications to fight against antibiotic resistance.* Journal of applied microbiology, 2012. **113**(4): p. 723-736.
171. Chung, P.Y. and R. Khanum, *Antimicrobial peptides as potential anti-biofilm agents against multidrug-resistant bacteria.* Journal of Microbiology, Immunology and Infection, 2017. **50**(4): p. 405-410.
172. Huan, Y., et al., *Antimicrobial peptides: classification, design, application and research progress in multiple fields.* Frontiers in microbiology, 2020. **11**: p. 582779.
173. Mba, I.E. and E.I. Nweze, *Antimicrobial peptides therapy: an emerging alternative for treating drug-resistant bacteria.* The Yale journal of biology and medicine, 2022. **95**(4): p. 445.
174. Di Somma, A., et al., *Antimicrobial and antibiofilm peptides.* Biomolecules, 2020. **10**(4): p. 652.
175. Mukhopadhyay, S., et al., *Antimicrobial peptide polymers: No escape to ESKAPE pathogens—A review.* World Journal of Microbiology and Biotechnology, 2020. **36**: p. 1-14.
176. Wu, Y., et al., *In vitro pharmacodynamics and bactericidal mechanism of fungal defensin-derived peptides NZX and P2 against Streptococcus agalactiae.* Microorganisms, 2022. **10**(5): p. 881.
177. Ramos, R., et al., *Wound healing activity of the human antimicrobial peptide LL37.* Peptides, 2011. **32**(7): p. 1469-1476.
178. Teixeira, M.A., et al., *Antibacterial and hemostatic capacities of cellulose nanocrystalline-reinforced poly(vinyl alcohol) electrospun mats doped with Tiger 17 and pexiganan peptides for prospective wound healing applications.* Biomater Adv, 2022. **137**: p. 212830.
179. Gomes, A., et al., *Wound-Healing Peptides for Treatment of Chronic Diabetic Foot Ulcers and Other Infected Skin Injuries.* Molecules, 2017. **22**(10).
180. Tang, J., et al., *A Small Peptide with Potential Ability to Promote Wound Healing.* PLOS ONE, 2014. **9**(3): p. e92082.
181. Mu, L., et al., *A potential wound-healing-promoting peptide from salamander skin.* FASEB J, 2014. **28**(9): p. 3919-29.
182. Jung Kim, D., et al., *Efficacy of the designer antimicrobial peptide SHAP1 in wound healing and wound infection.* Amino acids, 2014. **46**: p. 2333-2343.

183. Huang, H.-N., et al., *Use of the antimicrobial peptide Epinecidin-1 to protect against MRSA infection in mice with skin injuries.* Biomaterials, 2013. **34**(38): p. 10319-10327.
184. Liu, H., et al., *A short peptide from frog skin accelerates diabetic wound healing.* The FEBS journal, 2014. **281**(20): p. 4633-4643.
185. Chen, S., et al., *Cathelicidin-WA polarizes E. coli K88-induced M1 macrophage to M2-like macrophage in RAW264. 7 cells.* International Immunopharmacology, 2018. **54**: p. 52-59.
186. Pena, O.M., et al., *Synthetic cationic peptide IDR-1018 modulates human macrophage differentiation.* PloS one, 2013. **8**(1): p. e52449.
187. Mohamed, M.F., A. Abdelkhalek, and M.N. Seleem, *Evaluation of short synthetic antimicrobial peptides for treatment of drug-resistant and intracellular Staphylococcus aureus.* Scientific reports, 2016. **6**(1): p. 29707.
188. Thangamani, S., et al., *Antibacterial activity and therapeutic efficacy of Fl-PRPRPL-5, a cationic amphiphilic polyproline helix, in a mouse model of staphylococcal skin infection.* Drug design, development and therapy, 2015: p. 5749-5754.
189. Huang, H.-N., et al., *Epinecidin-1 protects against methicillin resistant staphylococcus aureus infection and sepsis in pyemia pigs.* Marine Drugs, 2019. **17**(12): p. 693.
190. Puthia, M., et al., *A dual-action peptide-containing hydrogel targets wound infection and inflammation.* Science translational medicine, 2020. **12**(524): p. eaax6601.
191. Liu, H., et al., *A potential wound healing-promoting peptide from frog skin.* The international journal of biochemistry & cell biology, 2014. **49**: p. 32-41.
192. Di Grazia, A., et al., *The frog skin-derived antimicrobial peptide esculentin-1a (1-21) NH2 promotes the migration of human HaCaT keratinocytes in an EGF receptor-dependent manner: a novel promoter of human skin wound healing?* PloS one, 2015. **10**(6): p. e0128663.
193. Di Grazia, A., et al., *Temporins A and B stimulate migration of HaCaT keratinocytes and kill intracellular Staphylococcus aureus.* Antimicrobial agents and chemotherapy, 2014. **58**(5): p. 2520-2527.
194. Chereddy, K.K., et al., *PLGA nanoparticles loaded with host defense peptide LL37 promote wound healing.* Journal of Controlled Release, 2014. **194**: p. 138-147.
195. Pfalzgraff, A., et al., *Synthetic antimicrobial and LPS-neutralising peptides suppress inflammatory and immune responses in skin cells and promote keratinocyte migration.* Scientific reports, 2016. **6**(1): p. 31577.
196. Zhu, Y., et al., *Potent laminin-inspired antioxidant regenerative dressing accelerates wound healing in diabetes.* Proceedings of the National Academy of Sciences, 2018. **115**(26): p. 6816-6821.
197. Sommer, A., et al., *Melittin modulates keratinocyte function through P2 receptor-dependent ADAM activation.* Journal of Biological Chemistry, 2012. **287**(28): p. 23678-23689.
198. Tomioka, H., et al., *Novel anti-microbial peptide SR-0379 accelerates wound healing via the PI3 kinase/Akt/mTOR pathway.* PloS one, 2014. **9**(3): p. e92597.
199. Ma, Z., et al., *Membrane-active amphipathic peptide WRL3 with in vitro antibiofilm capability and in vivo efficacy in treating methicillin-resistant Staphylococcus aureus burn wound infections.* ACS infectious diseases, 2017. **3**(11): p. 820-832.
200. Zasloff, M., *Magainins, a class of antimicrobial peptides from Xenopus skin: Isolation, characterization of two active forms, and partial cDNA sequence of a precursor.* Journal of Ethnopharmacology, 1988. **23**(2-3): p. 360.
201. Gottler, L.M. and A. Ramamoorthy, *Structure, membrane orientation, mechanism, and function of pexiganan--a highly potent antimicrobial peptide designed from magainin.* Biochim Biophys Acta, 2009. **1788**(8): p. 1680-6.
202. Lamb, H.M. and L.R. Wiseman, *Pexiganan Acetate.* Drugs, 1998. **56**(6): p. 1047-1052.
203. Lipsky, B.A., K.J. Holroyd, and M. Zasloff, *Topical versus systemic antimicrobial therapy for treating mildly infected diabetic foot ulcers: a randomized, controlled, double-blinded, multicenter trial of pexiganan cream.* Clin Infect Dis, 2008. **47**(12): p. 1537-45.

204. Ge, Y., et al., *In Vitro Antibacterial Properties of Pexiganan, an Analog of Magainin.* Antimicrob Agents Chemother, 1999. **43**(4): p. 782-788.
205. Ghazvini, K., A. Neshani, and H. Farsiani, *Preparation and evaluation of antibacterial properties of Pexiganan, a Magainin analogue with Broadly-Spectrum Antimicrobial Activity.* Pakistan Journal of Medical and Health Sciences, 2021. **15**(6): p. 1778-1784.
206. Gomes, D., et al., *Pexiganan in Combination with Nisin to Control Polymicrobial Diabetic Foot Infections.* Antibiotics (Basel), 2020. **9**(3).
207. Chaiarwut, S., et al., *Surface immobilization of PCL electrospun nanofibers with pexiganan for wound dressing.* Journal of Polymer Research, 2021. **28**(9).
208. Durao, J., et al., *Nitric Oxide Release from Antimicrobial Peptide Hydrogels for Wound Healing.* Biomolecules, 2018. **9**(1).
209. Hancock, R.E., *Peptide antibiotics.* The lancet, 1997. **349**(9049): p. 418-422.
210. Jacob, L. and M. Zasloff. *Potential therapeutic applications of magainins and other antimicrobial agents of animal origin*. in *Ciba Foundation Symposium 186-Antimicrobial Peptides: Antimicrobial Peptides: Ciba Foundation Symposium 186*. 2007. Wiley Online Library.
211. Gopinath, D., et al., *Pexiganan-incorporated collagen matrices for infected wound-healing processes in rat.* J Biomed Mater Res A, 2005. **73**(3): p. 320-31.
212. Thapa, R.K., D.B. Diep, and H.H. Tonnesen, *Topical antimicrobial peptide formulations for wound healing: Current developments and future prospects.* Acta Biomater, 2020. **103**: p. 52-67.
213. Kulkarni, M.M., et al., *Design of protease-resistant pexiganan enhances antileishmanial activity.* Parasitol Res, 2014. **113**(5): p. 1971-6.
214. Zhang, X.L., et al., *The synthetic antimicrobial peptide pexiganan and its nanoparticles (PNPs) exhibit the anti-helicobacter pylori activity in vitro and in vivo.* Molecules, 2015. **20**(3): p. 3972-85.
215. Elnaggar, M.G., et al., *Antibacterial nanotruffles for treatment of intracellular bacterial infection.* Biomaterials, 2020. **262**: p. 120344.
216. Boltes Cecatto, R., et al., *Methylene blue mediated antimicrobial photodynamic therapy in clinical human studies: The state of the art.* Photodiagnosis Photodyn Ther, 2020. **31**: p. 101828.
217. Li, X., et al., *Clinical development and potential of photothermal and photodynamic therapies for cancer.* Nat Rev Clin Oncol, 2020. **17**(11): p. 657-674.
218. Clement, S. and J.Y. Winum, *Photodynamic therapy alone or in combination to counteract bacterial infections.* Expert Opin Ther Pat, 2024: p. 1-14.
219. Songca, S.P. and Y. Adjei, *Applications of antimicrobial photodynamic therapy against bacterial biofilms.* International journal of molecular sciences, 2022. **23**(6): p. 3209.
220. Huang, L., et al., *Type I and Type II mechanisms of antimicrobial photodynamic therapy: an in vitro study on gram-negative and gram-positive bacteria.* Lasers in surgery and medicine, 2012. **44**(6): p. 490-499.
221. Mojzisova, H., S. Bonneau, and D. Brault, *Structural and physico-chemical determinants of the interactions of macrocyclic photosensitizers with cells.* European Biophysics Journal, 2007. **36**: p. 943-953.
222. Boyle, R.W. and D. Dolphin, *Structure and biodistribution relationships of photodynamic sensitizers.* Photochemistry and photobiology, 1996. **64**(3): p. 469-485.
223. Oleinick, N.L., R.L. Morris, and I. Belichenko, *The role of apoptosis in response to photodynamic therapy: what, where, why, and how.* Photochemical & Photobiological Sciences, 2002. **1**(1): p. 1-21.
224. Castano, A.P., T.N. Demidova, and M.R. Hamblin, *Mechanisms in photodynamic therapy: part one—photosensitizers, photochemistry and cellular localization.* Photodiagnosis and photodynamic therapy, 2004. **1**(4): p. 279-293.
225. Pye, H., et al., *Antibody-Directed Phototherapy (ADP).* Antibodies, 2013. **2**(2): p. 270-305.

226. Hamblin, M.R., *Upconversion in photodynamic therapy: plumbing the depths.* Dalton Trans, 2018. **47**(26): p. 8571-8580.
227. Dai, T., et al., *Photodynamic therapy for methicillin-resistant Staphylococcus aureus infection in a mouse skin abrasion model.* Lasers Surg Med, 2010. **42**(1): p. 38-44.
228. Simonetti, O., et al., *Effectiveness of antimicrobial photodynamic therapy with a single treatment of RLP068/Cl in an experimental model of Staphylococcus aureus wound infection.* Br J Dermatol, 2011. **164**(5): p. 987-95.
229. Shiratori, M., et al., *Open study of photodynamic therapy for skin ulcers infected with MRSA and Pseudomonas aeruginosa.* Photodiagnosis and Photodynamic Therapy, 2021. **36**.
230. Lambrechts, S.A., et al., *Photodynamic therapy for Staphylococcus aureus infected burn wounds in mice.* Photochem Photobiol Sci, 2005. **4**(7): p. 503-9.
231. Tanaka, M., et al., *Photodynamic therapy can induce a protective innate immune response against murine bacterial arthritis via neutrophil accumulation.* PLoS One, 2012. **7**(6): p. e39823.
232. Darabpour, E., et al., *Fast and effective photodynamic inactivation of 4-day-old biofilm of methicillin-resistant Staphylococcus aureus using methylene blue-conjugated gold nanoparticles.* Journal of Drug Delivery Science and Technology, 2017. **37**: p. 134-140.
233. Tawfik, A.A., J. Alsharnoubi, and M. Morsy, *Photodynamic antibacterial enhanced effect of methylene blue-gold nanoparticles conjugate on Staphylococcal aureus isolated from impetigo lesions in vitro study.* Photodiagnosis Photodyn Ther, 2015. **12**(2): p. 215-20.
234. Khan, S., et al., *Gold nanoparticles enhance methylene blue-induced photodynamic therapy: a novel therapeutic approach to inhibit Candida albicans biofilm.* Int J Nanomedicine, 2012. **7**: p. 3245-57.
235. Belekov, E., et al., *Improved antimicrobial properties of methylene blue attached to silver nanoparticles.* Photodiagnosis Photodyn Ther, 2020. **32**: p. 102012.
236. Hah, H.J., et al., *Methylene blue-conjugated hydrogel nanoparticles and tumor-cell targeted photodynamic therapy.* Macromol Biosci, 2011. **11**(1): p. 90-9.
237. Khan, S., et al., *Photoinactivation of multidrug resistant bacteria by monomeric methylene blue conjugated gold nanoparticles.* J Photochem Photobiol B, 2017. **174**: p. 150-161.
238. Jahnchen, J., M.G. Purwanto, and K. Weisz, *NMR studies on self-complementary oligonucleotides conjugated with methylene blue.* Biopolymers, 2005. **79**(6): p. 335-43.
239. Miyabe, M., et al., *Effect of photodynamic therapy on clinical isolates of Staphylococcus spp.* Braz Oral Res., 2011. **25**(3): p. 230-234.
240. Biel, M.A., et al., *Antimicrobial photodynamic therapy treatment of chronic recurrent sinusitis biofilms.* Int Forum Allergy Rhinol, 2011. **1**(5): p. 329-34.
241. Tanaka, M., et al., *Optimal photosensitizers for photodynamic therapy of infections should kill bacteria but spare neutrophils.* Photochem Photobiol, 2012. **88**(1): p. 227-32.
242. Biel, M.A., et al., *Reduction of Endotracheal Tube Biofilms Using Antimicrobial Photodynamic Therapy.* Lasers Surg Med, 2011. **43**(7): p. 586-590.
243. Teichert, M.C., et al., *Treatment of oral candidiasis with methylene blue-mediated photodynamic therapy in an immunodeficient murine model.* Oral Surg Oral Med Oral Pathol Oral Radiol Endod, 2002. **93**(2): p. 155-60.
244. Tardivo, J.P., et al., *A clinical trial testing the efficacy of PDT in preventing amputation in diabetic patients.* Photodiagnosis and photodynamic therapy, 2014. **11**(3): p. 342-350.
245. Aspiroz, C., et al., *Photodynamic Therapy With Methylene Blue for Skin Ulcers Infected With Pseudomonas aeruginosa and Fusarium spp.* Actas Dermo-Sifiliográficas (English Edition), 2017. **108**(6): p. e45-e48.
246. Embleton, M.L., et al., *Selective lethal photosensitization of methicillin-resistant Staphylococcus aureus using an IgG-tin (IV) chlorin e6 conjugate.* J Antimicrob Chemother, 2002. **50**(6): p. 857-64.
247. Embleton, M.L., et al., *Antibody-Directed Photodynamic Therapy of Methicillin-Resistant Staphylococcus aureus.* Microbial Drug Resistance, 2004. **10**(2).

248. Gad, F., et al., *Effects of growth phase and extracellular slime on photodynamic inactivation of gram-positive pathogenic bacteria.* Antimicrob Agents Chemother, 2004. **48**(6): p. 2173-8.
249. Kennedy, D.J., et al., *Central Role for the Cardiotonic Steroid Marinobufagenin in the Pathogenesis of Experimental Uremic Cardiomyopathy.* Hypertension, 2006. **47**(3): p. 488-495.
250. Kolb-Bachofen, V., et al., *Low-Dose Streptozocin-Induced Diabetes in Mice: Electron Microscopy Reveals Single-Cell Insulitis Before Diabetes Onset.* Diabetes, 1988. **37**(1): p. 21-27.
251. Moura, L.I.F., et al., *Neurotensin-loaded collagen dressings reduce inflammation and improve wound healing in diabetic mice.* Biochimica et Biophysica Acta (BBA) - Molecular Basis of Disease, 2014. **1842**(1): p. 32-43.
252. Larouche, J., et al., *Immune regulation of skin wound healing: mechanisms and novel therapeutic targets.* Advances in wound care, 2018. **7**(7): p. 209-231.
253. Carretero, M., et al., *In vitro and in vivo wound healing-promoting activities of human cathelicidin LL-37.* Journal of Investigative Dermatology, 2008. **128**(1): p. 223-236.
254. Gioffredi, E., et al., *Pluronic F127 hydrogel characterization and biofabrication in cellularized constructs for tissue engineering applications.* Procedia Cirp, 2016. **49**: p. 125-132.
255. Diniz, I.M., et al., *Pluronic F-127 hydrogel as a promising scaffold for encapsulation of dental-derived mesenchymal stem cells.* Journal of Materials Science: Materials in Medicine, 2015. **26**: p. 1-10.
256. Flamm, R.K., et al., *In vitro spectrum of pexiganan activity when tested against pathogens from diabetic foot infections and with selected resistance mechanisms.* Antimicrob Agents Chemother, 2015. **59**(3): p. 1751-4.
257. Cohen, H., et al., *Interaction of Pexiganan (MSI-78)-Derived Analogues Reduces Inflammation and TLR4-Mediated Cytokine Secretion: A Comparative Study.* ACS Omega, 2023. **8**(20): p. 17856-17868.
258. Reinke, J. and H. Sorg, *Wound repair and regeneration.* European surgical research, 2012. **49**(1): p. 35-43.
259. F Sperandio, F., Y.-Y. Huang, and M. R Hamblin, *Antimicrobial photodynamic therapy to kill Gram-negative bacteria.* Recent patents on anti-infective drug discovery, 2013. **8**(2): p. 108-120.
260. Castano, A.P., T.N. Demidova, and M.R. Hamblin, *Mechanisms in photodynamic therapy: Part three—Photosensitizer pharmacokinetics, biodistribution, tumor localization and modes of tumor destruction.* Photodiagnosis and photodynamic therapy, 2005. **2**(2): p. 91-106.
261. Kruger, C.A. and H. Abrahamse, *Utilisation of targeted nanoparticle photosensitiser drug delivery systems for the enhancement of photodynamic therapy.* Molecules, 2018. **23**(10): p. 2628.
262. Shrestha, A. and A. Kishen, *Polycationic chitosan-conjugated photosensitizer for antibacterial photodynamic therapy.* Photochem Photobiol, 2012. **88**(3): p. 577-83.
263. Standardization, I., *Biological evaluation of medical devices.* Part 5: Tests for in vitro cytotoxicity, 2009: p. 1-34.
264. Biel, M.A., et al., *The effect of antimicrobial photodynamic therapy on human ciliated respiratory mucosa.* Laryngoscope, 2012. **122**(12): p. 2628-31.
265. Kashef, N., G. Ravaei Sharif Abadi, and G.E. Djavid, *Photodynamic inactivation of primary human fibroblasts by methylene blue and toluidine blue O.* Photodiagnosis Photodyn Ther, 2012. **9**(4): p. 355-8.
266. Zeina, B., et al., *Cytotoxic effects of antimicrobial photodynamic therapy on keratinocytes in vitro.* British Journal of Dermatology, 2002. **146**: p. 568-573.
267. Kim, M.-S., et al., *Effect of 660 nm Light-Emitting Diode on the Wound Healing in Fibroblast-Like Cell Lines.* International Journal of Photoenergy, 2015. **2015**: p. 1-9.

268. Tardivo, J.P., et al., *Methylene blue in photodynamic therapy: From basic mechanisms to clinical applications.* Photodiagnosis Photodyn Ther, 2005. **2**(3): p. 175-91.
269. Costerton, J., L. Montanaro, and C.R. Arciola, *Biofilm in implant infections: its production and regulation.* The International journal of artificial organs, 2005. **28**(11): p. 1062-1068.
270. Arciola, C.R., D. Campoccia, and L. Montanaro, *Implant infections: adhesion, biofilm formation and immune evasion.* Nature reviews microbiology, 2018. **16**(7): p. 397-409.
271. Tan, M.L.L., et al., *Challenges faced in developing an ideal chronic wound model.* Expert Opinion on Drug Discovery, 2023. **18**(1): p. 99-114.
272. Ansell, D.M., et al., *A statistical analysis of murine incisional and excisional acute wound models.* Wound Repair and Regeneration, 2014. **22**(2): p. 281-287.
273. Ashcroft, G.S., et al., *Estrogen accelerates cutaneous wound healing associated with an increase in TGF-ß1 levels.* Nature medicine, 1997. **3**(11): p. 1209-1215.
274. Paik, S., et al., *Induction of insulin-dependent diabetes by streptozotocin Inhibition by estrogens and potentiation by androgens.* Diabetes, 1982. **31**(8): p. 724-729.
275. Guo, R., et al., *Female mouse model of diabetes mellitus induced by streptozotocin and high-carbohydrate high-fat diet.* Polish Journal of Veterinary Sciences, 2022: p. 547-555-547-555.
276. Deshmukh, M., et al., *Utilization of In Vivo Imaging System to Study Staphylococcal Sepsis and Septic Arthritis Progression in Mouse Model.* Pathogens, 2024. **13**(8): p. 652.
277. Cronin, M., et al., *In vivo bioluminescence imaging of intratumoral bacteria.* Bacterial Therapy of Cancer: Methods and Protocols, 2016: p. 69-77.
278. Baban, C.K., et al., *Bioluminescent bacterial imaging in vivo.* Journal of visualized experiments: JoVE, 2012(69): p. 4318.
279. Welch, K., Y. Cai, and M. Strømme, *A method for quantitative determination of biofilm viability.* Journal of Functional Biomaterials, 2012. **3**(2): p. 418-431.
280. Andersson, M.Å., et al., *Development of an experimental ex vivo wound model to evaluate antimicrobial efficacy of topical formulations.* International journal of molecular sciences, 2021. **22**(9): p. 5045.
281. Zhao, G., et al., *Time course study of delayed wound healing in a biofilm-challenged diabetic mouse model.* Wound Repair and Regeneration, 2012. **20**(3): p. 342-352.
282. Zhao, G., et al., *Delayed wound healing in diabetic (db/db) mice with Pseudomonas aeruginosa biofilm challenge: a model for the study of chronic wounds.* Wound Repair and Regeneration, 2010. **18**(5): p. 467-477.
283. Grada, A., J. Mervis, and V. Falanga, *Research techniques made simple: animal models of wound healing.* Journal of Investigative Dermatology, 2018. **138**(10): p. 2095-2105. e1.